DocuSign Envelope ID: BF76729B-E49B-4A11-80D2-38AC0C4692E3

Submission ID 14973806 Submitted Nov 01, 2023 05:19 PM
IP 165.123.225.48 Browser Chrome (113.0.0.0) Referrer

Question	Response
Title of ETD:	Chemical Tools to Control Protein Expression, Function, and Degradation
Name of Author	Kristie Elaine Darrah
Describe the Correction(s):	Figure 1-19 contained images that were repeated in Figure 1-40. Additionally, three of the reagent recipes in the Expanded Methods chapter were listed wrong. The new version of this ETD PDF contains the correct images that correspond to the data presented in the Figure 1-19 and the corrected reagent recipes.
File Upload	kdarrah_etd with revised figure 1-19.pdf

Question	Response
Assistant Director of Graduate Studies	DocuSigned by: Jessica Layne A63891E7DEB5435... 11-02-2023 | 9:09 AM EDT
Professor-Vice Provost	DocuSigned by: Amanda Godley A505BB26B34544B... 11-07-2023 | 4:12 PM EST

Chemical Tools to Control Protein Expression, Function, and Degradation

by

Kristie Elaine Darrah

B.S. Chemistry-Biochemistry, Bloomsburg University, 2014

Submitted to the Graduate Faculty of the

Dietrich School of Arts and Sciences in partial fulfillment

of the requirements for the degree of

Doctor of Philosophy

University of Pittsburgh

2021

UNIVERSITY OF PITTSBURGH

DIETRICH SCHOOL OF ARTS AND SCIENCES

This dissertation was presented

by

Kristie Elaine Darrah

It was defended on

July 28, 2021

and approved by

Dr. W. Seth Childers, Assistant Professor, Department of Chemistry

Dr. Paul Floreancig, Professor, Department of Chemistry

Dr. Thomas S. Leyh, Professor, Department of Microbiology and Immunology, Albert Einstein College of Medicine

Thesis Advisor/Dissertation Director: Dr. Alexander Deiters, Department of Chemistry

Copyright © by Kristie Elaine Darrah

2021

Chemical Tools to Control Protein Expression, Function, and Degradation

Kristie Elaine Darrah, PhD

University of Pittsburgh, 2021

The precise timing and localization of the complex interactions among small molecules and biomacromolecules during cellular biological processes directly correlate to larger changes that can have long withstanding impacts on overall human health. Chemical tools to discreetly investigate the individual contribution of key cellular events or signaling pathways are vital to uncovering answers to many of the questions within the realm of chemical biology. Herein, I describe my contributions towards developing and applying oligonucleotide- and small molecule-based chemical tools to the fields of developmental biology, sulfotransferase biology, and targeted protein degradation.

Using morpholino oligonucleotide antisense agents, I have developed conditionally activated, cyclic morpholino reagents responsive to enzyme catalysis or small molecule treatment and have applied them in controlling endogenous gene expression in zebrafish embryos. In combination with current optically controlled technologies, these reagents can be used to silence expression of individual genes within multi-gene networks. I have also synthesized the first synthetic, allosteric small molecule inhibitor of any sulfotransferase enzyme. This work uncovered the sulfotransferase active site cap as an entirely novel allosteric pocket that can be exploited for small molecule regulation. The inhibitors presented in this work have laid the groundwork for a potentially novel approach to treating major depression disorder. Finally, I have contributed to implementing a broadly applicable approach for the optical activation of small molecule-induced

protein degradation. By utilizing a general photocaging strategy, the approach presented in this work permits spatiotemporal control over PROTAC-mediated protein degradation.

Table of Contents

List of Tables

List of Figures

Preface

I would like to thank my advisor, Dr. Alexander Deiters, for his continued guidance and support throughout my time in graduate school. Your high expectations and enthusiasm for science have helped shape me into a more confident and creative scientist over these last few years. I would also like to thank my committee members, Dr. W. Seth Childers, Dr. Paul Floreancig, and Dr. Thomas Leyh for their support through my graduate education.

I would like to thank all past and present members of the Deiters lab for the insightful scientific discussions and comradery. I would like to extend a special thank you to Anirban Bardhan, Mary Cacace, Taylor Courtney, Cole Emanuelson, Chasity Hankinson, and Amy Ryan. Not every day in graduate school has been sunshine and rainbows, and I thank all of you for your kindness, friendship, and support in the form of ridiculous (sometimes hardly appropriate, "liiiiiiiine") inside jokes, coffee walks, ice cream, cubby talks, margaritas, etc. as we've navigated not only the trials and tribulations of research and failures, but also the general unexpected "life" happenings (including a global freaking pandemic) over the past 5 years. I value the unique friendships I've built with each of you and want to thank you for giving me fond memories to look back on.

Finally, I would like to dedicate this work to my mother, Kendra, and in memory of my father, William. Mom, I am so fortunate to have grown up having the perfect example of a strong, female scientist to look up to. To my dad, Bill, though you didn't get to see the end of this journey, this was for you. I love you both and thank you for everything.

1.0 Conditional Control of Protein Expression

1.1 Introduction to Antisense Oligonucleotide-Based Control of Protein Expression

Nucleic acid-based regents are broadly applicable tools that have found widespread application in the investigation of biological mechanisms, in particular gene function and gene regulation.[1-5] Chemical modifications to enhance the stability and delivery of nucleic acid-based technologies have propelled these tools beyond basic research to receive significant attention as therapeutics, e.g., antisense agents, guide RNAs, and mRNA vaccines. A significant advantage of nucleic acids as probes is that these reagents can be utilized in a highly programmable and predictable manner based on hybridization rules and sequence information.

One class of synthetic nucleic acid tools that has been widely used to successfully regulate gene expression includes antisense oligonucleotides (ASOs).[6] ASOs are short, (typically 8-30 nucleotides in length) single stranded oligonucleotides that can regulate gene expression by sequence-specifically binding to the sense strand of endogenous RNA targets.[7-9] ASOs find their target RNAs independent of protein chaperones, as there is no cellular machinery to assist in antisense recognition.[7] Once bound to the target sequence, these reagents can repress protein expression via RNase H-mediated mRNA knockdown or steric blocking of the translational machinery. Further, ASOs can also be used to regulate protein expression through manipulation of alternative splicing patterns.[3] These agents have shown much success in controlling gene expression in several systems including mammalian tissue culture, mice, *Xenopus laevis* (frog), sea urchins, chicks, and *Danio rerio* (zebrafish).[6, 10, 11]

Research efforts surrounding ASOs have focused on altering their structural chemistry to improve their stability *in vivo.*[12] Unmodified ASOs suffer from fast turnover due to degradation by endogenous endo- and exonucleases which, in turn, can affect their ability to achieve effective intracellular concentrations.[13] Second generation ASOs include modifications to the phosphate backbone, ribose sugar, or a combination of both to increase stability against nucleases and confer favorable pharmacokinetic properties (Figure 1-1). Modifications to the backbone include the replacement of a non-bridging oxygen atom with a sulfur (phosphorothioate) or methyl (methylphosphonate) to avoid nuclease binding to ASO reagents thereby preventing their degradation. These structural alterations increase nuclease resistance and improve tissue distribution as a result of increased binding to serum proteins.[14] Furthermore, phosphorothioate modifications significantly increase the half-lives of DNA or RNA-based oligonucleotides from times lengths of minutes to days.[2] However, there remains a functional sacrifice as backbone modified ASOs can also exhibit reduced binding affinity towards its respective nucleic acid target. Additionally, replacement of an oxygen atom in the phosphate group introduces a chiral center leading to formation of diastereomeric oligonucleotides. Thereby, introduction of multiple modification will lead to a mixture of diastereomeric oligonucleotides exhibiting differential target binding affinities resulting in variable therapeutic properties.[15]

Nuclease resistance can also be enhanced through the incorporation of modifications within the ribose sugar. Substitutions at the 2'-position with groups that remove or mask the nucleophilic hydroxyl, including fluoro- (2'-F), methoxy- (2'-OMe), and methoxyethyl (2'-O-MOE), impact the hydrogen bonding properties and the overall stability of the oligonucleotide helical structure.[16, 17] The ribose sugar has also previously been modified to generate locked nucleic acids (LNA) where the sugar pucker is conformationally restricted or "locked" through the incorporation of a

methylene bridge between the 2'-O and the 4'-C of the ribose sugar. This modification locks the sugar in a conformation that is entropically favorable for Watson-Crick base pairing which enhances thermal stability and allows for stronger binding interactions in the ASO-target duplex as usually determined from increased melting temperatures (T_m).[18-20]

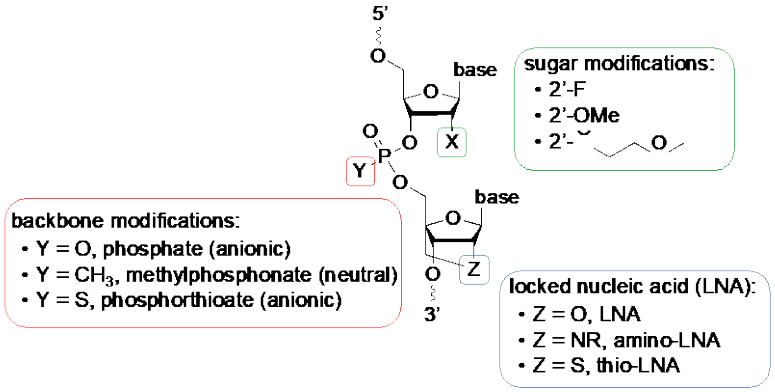

Figure 1-1: Chemical modifications to ASOs
The incorporation of chemical modifications within the backbone and sugar moieties of the nucleic acid structure can enhance functional properties of these reagents. Figure was adapted from Ochoa *et. al*., *Molecules*, **2020**, 25, 4659.[12]

Third generation ASOs include phosphorodiamidate morpholino oligonucleotides (MOs) and peptide nucleic acids (PNAs) which contain a combination of the aforementioned chemical modifications (Figure 1-2). MOs contain a neutrally charged phosphorodiamidate backbone in which the ribose-based sugar is replaced with a six-membered morpholine ring.[21-24] PNAs contain a backbone entirely composed of polyamide ("peptide") linkages, with nucleobases attached via a methyl carbonyl linker.[25, 26] Due to their overall neutral charge and unnatural backbone structures, these agents maintain a high affinity for RNA targets and are less susceptible to engage in non-specific interactions with cellular proteins, decreasing the likelihood of off-target effects or degradation by nucleases and/or proteases.[27] However, PNA reagents exhibit poor water solubility and decreased intracellular uptake which has led to the development of several chemically-modified versions including cationic PNAs, α-/γ-PNAs, lysine-modified PNAs, and negatively

charged PNAs (ncPNAs).[28] Morpholinos have been extensively utilized in developmental biology research which is discussed in more detail in Section 1.2.

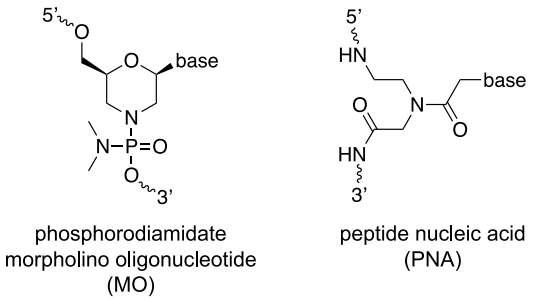

Figure 1-2: Structures of MO- and PNA-based antisense agents

The mechanism by which ASOs function, whether through RNase H-mediated cleavage of transcripts or steric blocking of the cellular translational machinery can be dictated by the nucleic acid structure (Figure 1-3).[2] Modified DNA-based ASOs form a DNA/RNA heteroduplex upon target binding. This DNA/RNA duplex is recognized as a substrate for the endogenous nuclease RNase H, which is recruited to the duplex, and induces hydrolytic cleavage and subsequent degradation of the mRNA transcript. In cases where transcript degradation is not the desired outcome (e.g., splice-switching antisense oligonucleotides, SSOs), the antisense reagents are strategically designed to contain modifications within the sugar ring. As a result, the SSO/pre-mRNA heteroduplex formed upon target binding is less likely to be recognized as a substrate for RNase H, thereby circumventing mRNA degradation. Instead, the splice switching occurs through an RNase H-independent mechanism in which the ASO sterically blocks the spliceosomal machinery from the splice junction and permits translation of a dominant-negative or gain-of-function splice variant protein.[7, 29] Together, these features provide interesting opportunities to

fine-tune the function of a particular synthetic oligonucleotide tool through modification of its chemical composition.[2]

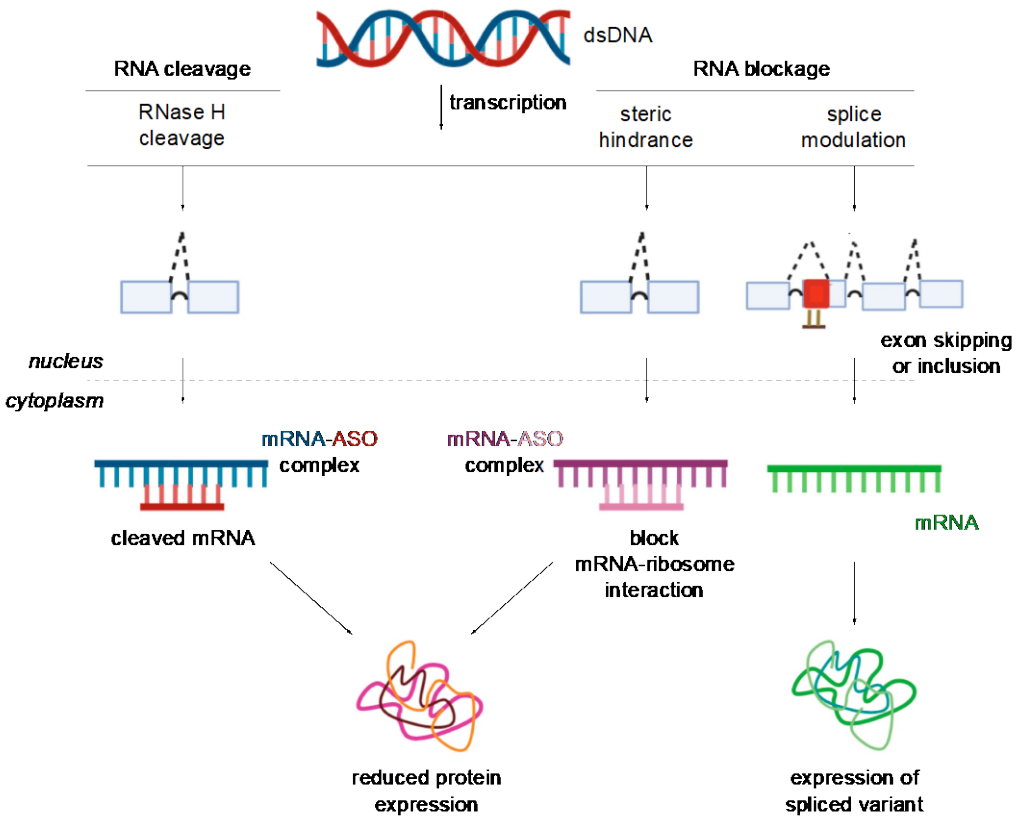

Figure 1-3: Mechanism of antisense oligonucleotide-mediated control of gene expression
ASOs can control gene expression by either (1) inducing RNase H-mediated degradation of the mRNA transcript or (2) sterically blocking the RNA through target hybridization. In the case of RNA cleavage, formation of the ASO/mRNA heteroduplex recruits the RNase H enzyme which hydrolytically cleaves the mRNA transcript. Alternatively, when modified ASOs are utilized, the resulting mRNA-ASO duplex is not recognized as a substrate by RNase H. The ASO blocks the ribosome from accessing the mRNA for translation. Through this same mechanism, ASOs can be targeted to bind to splice junctions (represented as a red square) which can undergo alternative splicing through exon skipping or exon inclusion to alter the mRNA reading frame and translate a spliced protein variant. Figure was adapted from Dhuri *et. al.*, *J. Clin. Med.*, **2020**, 9, 2004.[25]

ASOs have also received attention as novel therapeutic strategies against rare, genetic disorders that are not be amenable to treatment with traditional small molecule drugs.[25] However, a significant limitation to the clinical use of therapeutic oligonucleotides is cellular delivery. Efforts towards overcoming this hurdle encompass an entire division of oligonucleotide research.[30-32] Lipid nanoparticles are the most widely used vehicles in oligonucleotide delivery but

are typically modified with neutral polymers such as PEG to increase biodistribution and avoid rapid clearance from the bloodstream.[33] Polymeric nanocarriers such as poly(lactic-co-glycolic acid) (PLGA)[34] and complexation with cationic polymers, such as cell penetrating peptides,[35] have also shown promise but have not yet advanced into clinical settings. Despite this limitation, numerous antisense drugs have received approval from the United States Food and Drug Administration (FDA) and several are currently being evaluated in clinical trials for cardiovascular, neuromuscular, inflammatory, and infectious diseases.[36, 37]

1.2 Morpholinos as Gene Silencing Agents in Zebrafish

Over the last 20 years, morpholino antisense oligonucleotides have served as valuable tools for developmental biologists by providing key insight into the molecular mechanisms of gene expression, regulation, and function in various model organisms. MOs allow for specific interrogation of a single gene without genetic manipulation of the organism under study. One animal model that has been particularly successful for morpholino antisense-related applications is *Danio rerio*, or zebrafish. Zebrafish have proven to be an important biomedical research model for human development and disease especially in the context of understanding the mechanisms that govern gene regulation during these processes.[38-40] The zebrafish genome is fully sequenced and shares remarkable homology with humans as 70% of human genes have a related zebrafish ortholog.[41] While they are relatively cheap and easy to maintain, zebrafish breed year-round and one pair of adult zebrafish can produce as many as 200-300 eggs at a time, making this vertebrate model amenable to large-scale screens that are not easily achieved with other animal model systems. Furthermore, zebrafish embryos are fertilized and develop rapidly *ex utero*. By 24 hours

post-fertilization (hpf), most of the primary organ systems (eyes, heart, brain, muscles) are formed.[42] The optical transparency of the embryo allows for real-time visualization of these early developmental processes as well as manipulation with non-invasive optical tools. Due to their small size and the relative simplicity of their native environment, they are cheaper and considered low maintenance as compared to other animal models (ex. rodents). Taken together, the numerous advantages of zebrafish nicely address the shortcomings of mammalian-based vertebrate model systems and position this organism to make fundamental contributions in advancing drug discovery and biomedical research programs.

As discussed in Section 1.1, MOs are ideal for use in complex, multicellular organisms like zebrafish embryos because they are resistant to enzymatic degradation by nucleases, have fewer non-specific interactions with proteins (due to their neutral charge), and have an enhanced affinity for complementary nucleic acids to that of native oligonucleotides.[24, 43] MOs are the most commonly used antisense reagents in zebrafish, as they allow for rapid loss-of-function studies and have been successfully used in studying both maternal and zygotic gene function throughout embryonic development.[44-46] Furthermore, these reagents are commercially available from GeneTools, LLC (Philomath, OR) making them readily accessible to developmental biologists.

Synthetic oligonucleotides containing phosphorothioate DNA or 2'-OMe RNA have shown significant toxicity to the developing embryos at concentrations as low as 500 femtomole (fmol) per embryo.[47, 48] This is likely due to irreversible triggering of DNA damage checkpoints that ultimately lead to cell cycle arrest. Other modified reverse genetic tools, such as PNAs have also been applied to zebrafish embryos with varying success.[47, 49] PNAs are relatively insoluble due to the pseudo-peptide backbone making it difficult to achieve effective concentrations *in vivo*. To circumvent the solubility issues, hydrophilic, negatively charged PNAs (ncPNAs) have been

generated and successfully utilized for silencing gene expression in embryos with comparable efficacies to MO-based reagents.[47, 50, 51] However, very few ncPNAs have been reported. Those that have been published have only been used to study genes expressed in the early stages of embryonic development, suggesting these reagents may also be limited by their *in vivo* stability.

MOs are typically 25-bases in length and are injected into the yolks of early stage (1-8 cell stage) embryos.[52] The cytoplasmic bridges between the yolk and blastomeres enable rapid diffusion of the hydrophilic MOs and ensure ubiquitous delivery to the cells.[53] Following injection, MOs silence gene expression globally and immediately through steric blocking of translational start sites and intron-exon splice junctions in target mRNAs, the effects of which can persist up to 5 days post-fertilization (dpf).[10, 43] MOs have also been successfully applied to inhibiting the function of endogenous noncoding RNAs by blocking miRNA binding sites in endogenous transcripts, inhibiting pri- and pre-mRNA processing, or sequestering mature miRNAs.[54-56]

While the discovery of MOs has had a transformative effect on developmental biology research, they are not perfect and come with their own set of challenges. MOs are designed to perfectly complement their intracellular target sequences, however these reagents can still bind, albeit weakly, to unintended targets or to homologous sequences containing as many as 2-4 base mismatches.[47, 52, 57] The phenotypes that result from these nonspecific interactions are difficult to reliably distinguish from those that result from specific target engagement.[58] Furthermore, embryo toxicity and phenotypic artifacts in the anterior neural tissue and notochord can also stem from the morpholino alone. It has been previously shown that 15-20% of MOs can induce upregulation of the p53 apoptosis pathway, the mechanism of which remains elusive.[59, 60] To circumvent this MO-mediated p53 activation, experimental MOs are co-injected with a p53 MO to counteract the

upregulation. However, a major caveat to this experimental work is that the phenotypic analysis is then evaluated in a p53-deficient background as opposed to a wild-type embryo.

As a result of these observations, the following experimental guidelines for morpholino use in zebrafish embryos have been established in the field in order to validate that the observe morphant phenotype is solely the result of morpholino-induced silencing:[60, 61] (1) MOs should be dosed to establish and score the morphological defects, as well as, evaluate the threshold for toxicity, (2) target gene knockdown should be validated experimentally using an antibody against the protein of interest, RT-PCR, reporter constructs, etc., (3) the phenotype established in the dose response should be validated using a second MO of independent sequence, preferably non-overlapping with the MO sequence of interest, (4) Rescue of the wild-type phenotype through co-injection of the experimental MO with synthetic, MO-resistant mRNA expressing the target of interest should also be demonstrated, (5) morphant phenotypes should be compared to the corresponding genetic mutant that was generated using a complementary mutagenesis tool (CRISPR/Cas9, TALENs, etc.). It should be noted that for novel MOs, the final criterion is especially important as the discrepancies that have been observed between morphant and mutant phenotypes remain a major point of contention in the zebrafish community.[62]

1.3 Optically Controlled Morpholinos

Investigations of biological processes are often complicated by the inherent complexity of the timing, dynamics, and localization of regulatory events exemplified in gene regulatory networks. The study of gene expression and related functions *in vivo* requires tools equipped with elements that enable equally precise control. Until recently, methods for regulating endogenous

gene expression in early development have been limited, as silencing of essential genes in the earliest stages of development may prove lethal, precluding studies of the contribution of a particular gene or gene function at later developmental stages. Furthermore, investigations into localized gene expression activity in specific regions or organs systems are complicated as a result of global silencing with currently available tools. Gene editing tools such as CRISPR and TALEN-based methodologies typically require multiple animal generations for full implementation and have significant limitations for conditional control. One strategy to address this methodology gap has been the development of caged morpholinos oligomers (cMOs) which are unable to bind their target sequences until exposure to a trigger, releasing active the MO.

Light has proven to be an excellent conditional stimulus, as it is non-invasive, can be applied with spatial and temporal precision, and can be easily tuned by its wavelength and amplitude. The application of light-triggered cMOs in zebrafish zygotes is particularly attractive due to the optical transparency the developing embryo which allows light to efficiently penetrate the embryo to photoactivate these tools. As a result, various photochemically triggered cMO approaches have been validated in zebrafish zygotes.[48, 63-70]

1.3.1 Photocleavable Inhibitory MO Strands

The first generation cMOs, pioneered by the Chen lab (Stanford University), incorporated a short, inhibitory oligomer tethered to a 25-base MO via a photolabile linker.[63, 64] The inhibitory oligomer hybridizes to the MO prohibiting binding to target mRNAs. Light-induced cleavage of the linkers results in dissociation of the duplex, target mRNA hybridization, and inhibition of gene function during zebrafish embryogenesis (Figure 1-4A). This duplex-based design has been validated with linkers containing dimethoxynitrobenzyl (DMNB) (**1** and **2**) and 8-bromo-7-

hydroxyquinolinyl (BHQ) chromophores (**3**) which are cleaved using UV- and two-photon irradiation, respectively. It is also worth noting that this cMO approach is quite versatile and has been successfully adapted for photocontrolling ncPNA activity using a nitrobenzyl-based linker (**4**) in zebrafish embryos.[51] The expression of various developmentally-relevant genes including *no tail a* (*ntla*), *heart of glass* (*heg*), *floating head* (*flh*), *endothelial-specific variant gene 2* (*etv2*), and *spadetail* (*spt*) have been efficiently regulated following light irradiation.[63, 64] While successful, these structures must be carefully designed to maintain a suitable difference in activity between the caged and decaged forms. Improved caging efficiency has been demonstrated with inhibitory oligomers that anneal to the terminal end of the MO ("blunted"), rather than to the middle of the MO sequence ("staggered") (Figure 1-4A).[64] Additionally, photocleavage of the inhibitory oligomers has the potential to induce unwanted off-target effects.[66]

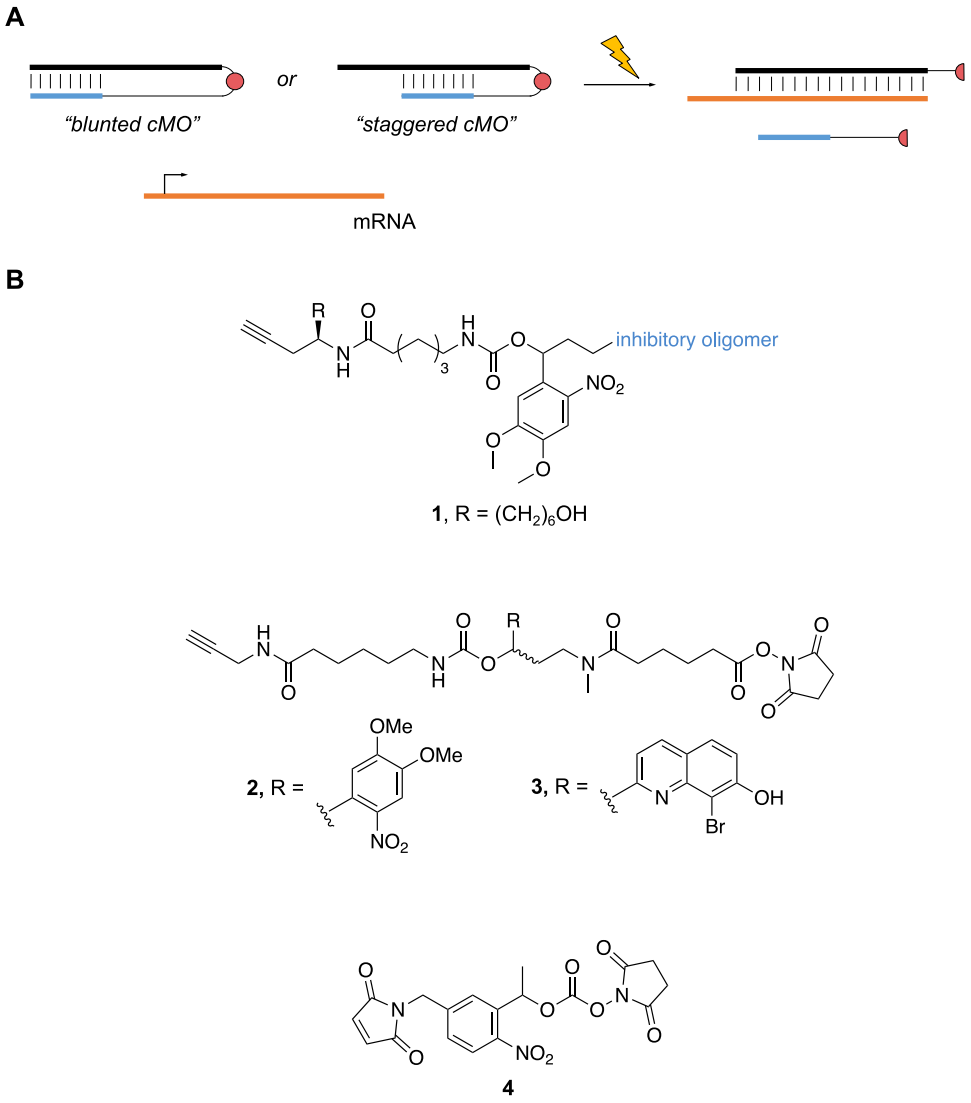

Figure 1-4: MO caging with photolabile inhibitory duplexes
Inhibitory duplexes formed via covalent tethering of an oligomers that anneal to either the terminal (blunt) or middle (staggered) of the MO sequence via a photolabile linker (red circle) prevent target hybridization until light-induced cleavage of the linker. B) Structures of photocleavable linkers that have been applied to this caging approach.

A second design, containing two inhibitory oligomers that are joined by a photocleavable linker (**5**), the entirety of which covers the full length of the MO. Following irradiation with light, the inhibitory oligomer is fragmented into smaller oligonucleotides that are incapable of re-annealing to the released, active MO (Figure 1-5A). While these duplexes have shown to be easier to prepare, they do not circumvent the toxicity induced by the inhibitor strands. Furthermore, these

full length duplexes have demonstrated some instability when applied *in vivo*.[48, 71] Caged MOs of this design were made commercially available from GeneTools, LLC, dubbed "PhotoMorphs", but were later discontinued due to stringent design parameters, time-consuming optimization, and differential efficacies that varied with the MO sequence. Additionally, an analogous design has been utilized for light-induced deactivation of MO function by incorporating the nitrobenzyl-based linker within the backbone of the MO sequence (Figure 1-5B). Upon irradiation, the MO fragments and is no longer able to bind to its target mRNA, restoring normal gene expression. Light induced deactivation of MO function was applied to dissecting the temporal dynamics of *sox10* in neural crest development in zebrafish embryos.[71]

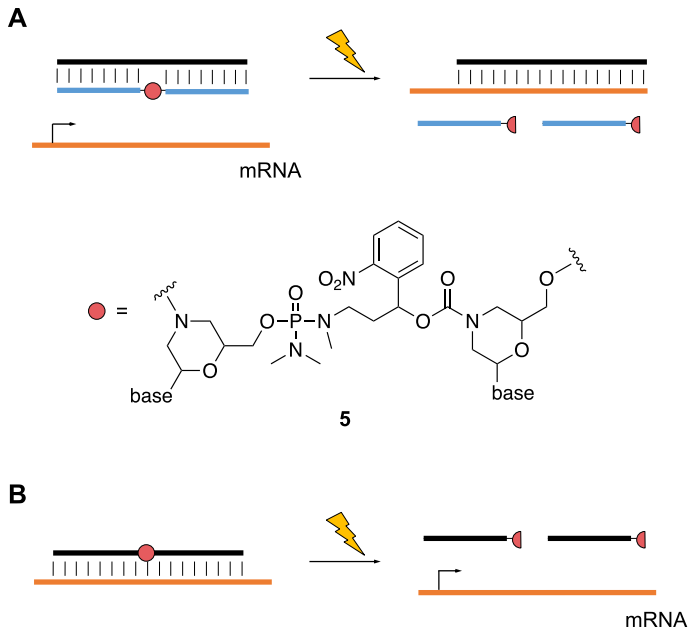

Figure 1-5: MO caging by inhibitory duplexes with internal photolabile linkers
A) Incorporation of a nitrobenzyl-photocleavable linker within the complementary oligomer inhibits MO function until light irradiation induces fragmentation, thereby destroying the duplex, and permitting target mRNA hybridization. B) Use of a photocleavable linker within the MO sequence can be used as a suitable strategy to obtain photodeactivation of MO antisense function.

1.3.2 Nucleobase-caged MOs

A second attractive strategy to optically control ASO activity is the sequence specific introduction of photocaged nucleobases.[72] The installation of caging groups at key H-bonding sites on the nucleobase disrupts the Watson-Crick binding interface providing an efficient means of controlling nucleic acid function. Full blocking of hybridization between oligonucleotides and their complement strands is achieved through even distribution of photocaging groups every 4-6 bases throughout the sequence (Figure 1-6A).[73] Irradiation restores the native nucleobase structure, permitting hybridization through the natural Watson-Crick hydrogen bonding interactions. While this approach overcomes the stringent design requirements of caged inhibitory duplexes and obviates the need for potentially toxic inhibitory oligomers, the synthetic installation of the base-caged monomers can be challenging. However, this approach ensures minimal background activity of the caged reagent prior to light exposure. The Deiters group has applied this approach utilizing the 6-nitropiperonyloxymethylene (NPOM) caging group to mask thymidine (Figure 1-6B) and photochemically regulate ASOs in mammalian cell culture.[74, 75] Subsequently, nucleobase caging strategies have also been successfully translated to MOs for regulating gene expression in various organisms including zebrafish and *Xenopus*.[65] More recently, nucleobase caged morpholinos have been applied to sea urchin models to temporally regulate the expression of *vegf3* and *kirrelL* ,two essential genes with distinct roles in skeletogenesis.[76]

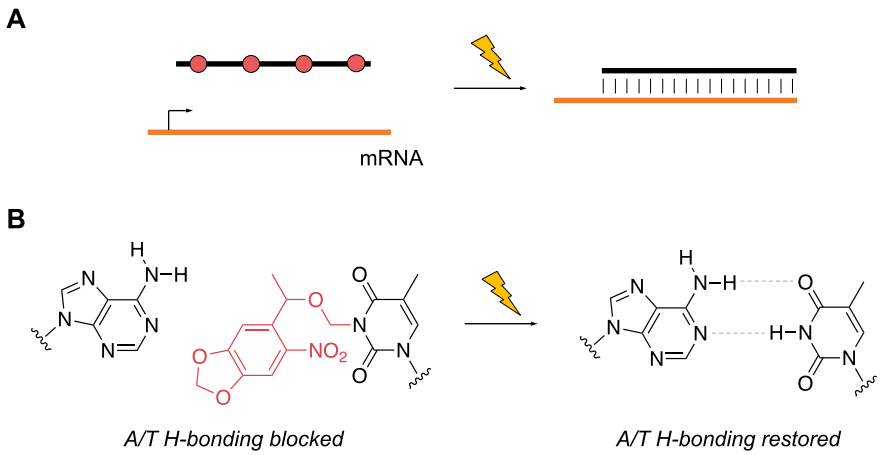

Figure 1-6: Nucleobase caging of MOs
A) The incorporation of 4-6 evenly spaced photocaged nucleobases blocks the Watson-Crick binding interface of the MO, thereby impeding formation of the MO/target mRNA hetroduplex until light irradiation. B) Installation of an NPOM photocaging group at N-3 on thymine prevents blocks hydrogen bonding interactions with adenine until light exposure.

1.3.3 Circular Caged MOs

Building on previous cMO successes, the Chen group designed an alternative caging approach by utilizing conformationally gated, cyclized MOs to overcome the stringent design requirements of inhibitory duplexes and avoid the potential toxicity that results from inhibitory accessory oligonucleotides. The curvature induced by end-to-end macrocyclization of the MO with photocleavable linkers diminishes the binding to the target mRNAs. Light activation of the cyclic cMO relies on a single photolysis step that cleaves the linker, linearizes the cMO, thereby restoring hybridization to target mRNAs and resulting in gene silencing activity (Figure 1-7A). These linkers can be used to cyclize any MO that is equipped with the proper reactive handles in relatively few synthetic steps, making this a highly modular approach that is compatible with commercially available oligomers. While moderate basal activity (~ 20%) of the cyclized 25mer cMOs has been reported, increasing the curvature by shortening the sequence to 21 or 23 bases has been shown to

decrease the this background activity. However, shortening the sequence sacrifices the silencing activity of linear MO due to diminished RNA interactions.[66]

This approach has been validated using photolabile linkers containing nitrobenzyl- (**6**-**8**)[66, 68] coumarin- (**9**-**10**),[67] and BHQ- (**11**), and 8-cyano-7-hydroxylquinolin-2-yl (CyHQ, **12**)- based[70] chromophores. The modularity of this design is well validated as nearly all linker structures contain N-hydroxysuccinimide (NHS) and chloroacetamide reactive handles for bioconjugation to 5'-amino and 3'-disulfide terminally modified MOs (Figure 1-7B). Photocleavable cMOs have been used to interrogate *ntla*, *pancreas transcription factor 1a* (*ptf1a*), *beta catenin-2*, *flh*, and *spt* expression within the first 24 hours of embryo development. The Dore lab (NYU Abu Dhabi) showcased the *in vivo* stability of BHQ- and CyHQ cyclic cMOs, as embryos injected with these cMOs developed similarly to wild-type embryos. However, when irradiated at later stages of development (24 hpf), recapitulation of the neurological and craniofacial defects that result from the of silencing *glutamic acid decarboxylase 1b* expression were evident, suggesting the cyclic cMOs remained stable and functionally inert until light exposure.[70]

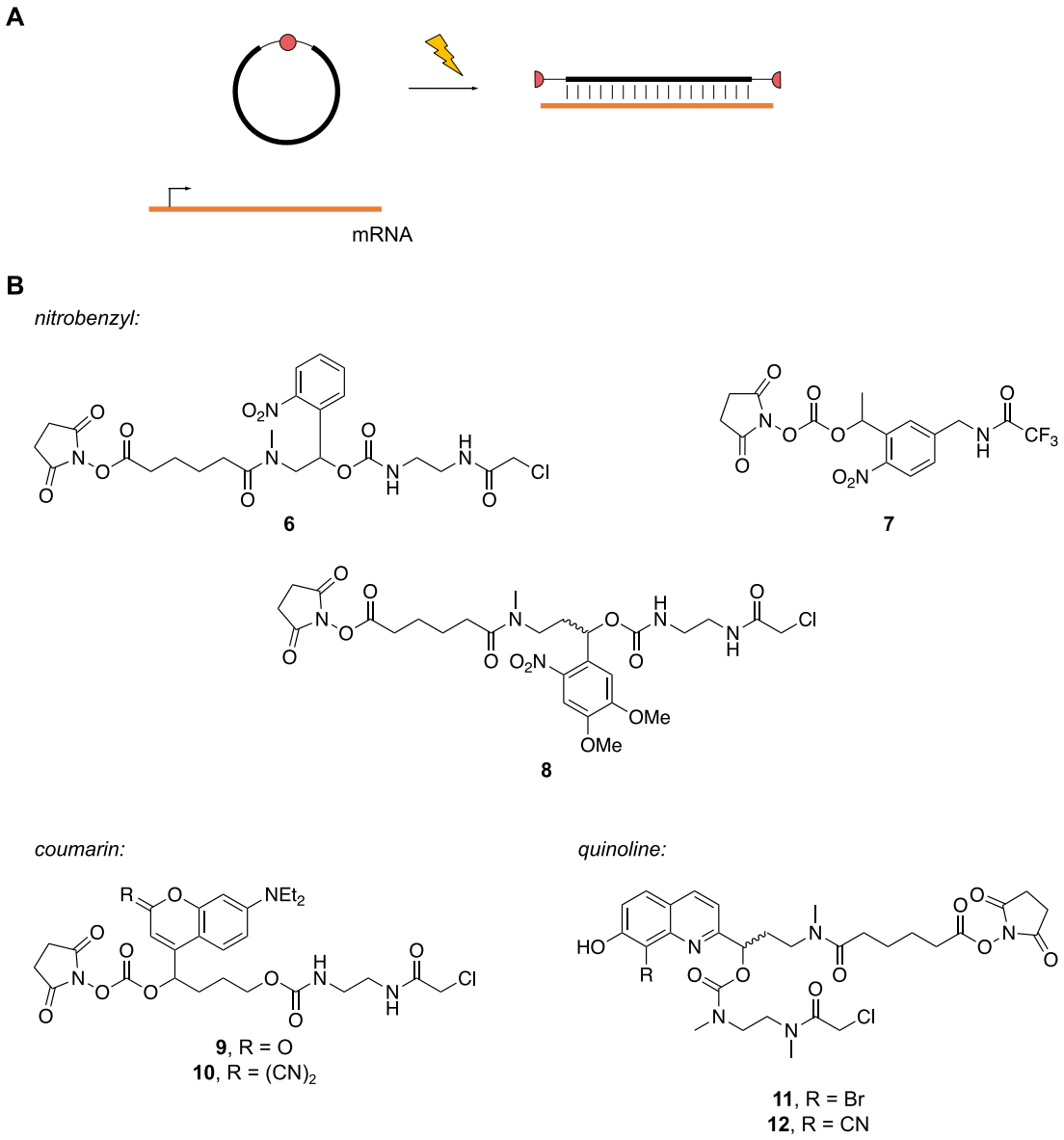

Figure 1-7: MO caging through cyclization
End-to-end macrocyclization of a terminally modified linear MO with a photolabile linker generates an inactive, cyclic oligonucleotide unable to bind mRNA targets. Light irradiation induces photolysis of the linker, linearization of the cMO, and restoration of MO function. B) Structures of the various photocleavable linkers that have been reported for cyclic cMO strategies.

Using spectrally differentiated nitrobenzyl- and coumarin-based cyclic cMOs, Chen and Deiters demonstrated sequential, wavelength-specific silencing of gene expression and applied these cMOs in probing dynamics of axial muscle development in zebrafish embryos (Figure 1-8).[67, 77] The authors utilized nitrobenzyl- and diethylaminocoumarin (DEACM)-containing

linkers (**6** and **9**, respectively) to cyclize cMOs targeting *spt* and *flh*, respectively, both of which are key components in a small gene regulatory network controlling *myod1* expression during mesoderm development in zebrafish embryogenesis. The nitrobenzyl caging group can be efficiently decaged following irradiation with UV light, while the electron donating ability of the C-7 diethylamino group induces a bathochromic shift allowing for efficient photolysis of DEACM caging groups with wavelengths greater than 400 nm.[78] The blue-shifted absorbance maxima of the nitrobenzyl chromophore makes it less susceptible to photolysis at wavelengths greater than 400 nm. Zebrafish embryos co-injected with both cyclic nitrobenzyl *spt* and DEACM *flh* cMOs followed by irradiation with either 405 or 470 nm light exhibited a phenotype consistent with *flh* knockdown, indicating only the DEACM cMO, and not the nitrobenzyl cMO, was activated. However, when co-injected embryos were sequentially irradiated with 405 or 470 nm light and then 365 nm light, a *spt* morphant phenotype was observed, suggesting efficient activation of the nitrobenzyl *spt* cMO. Temporally resolved photoactivation of these spectrally distinct MOs were used to analyze the timing of axial muscle development directed by *spt* function in *flh* null embryos, revealing the developmental stage at which *spt* functions to direct muscle cell fate.

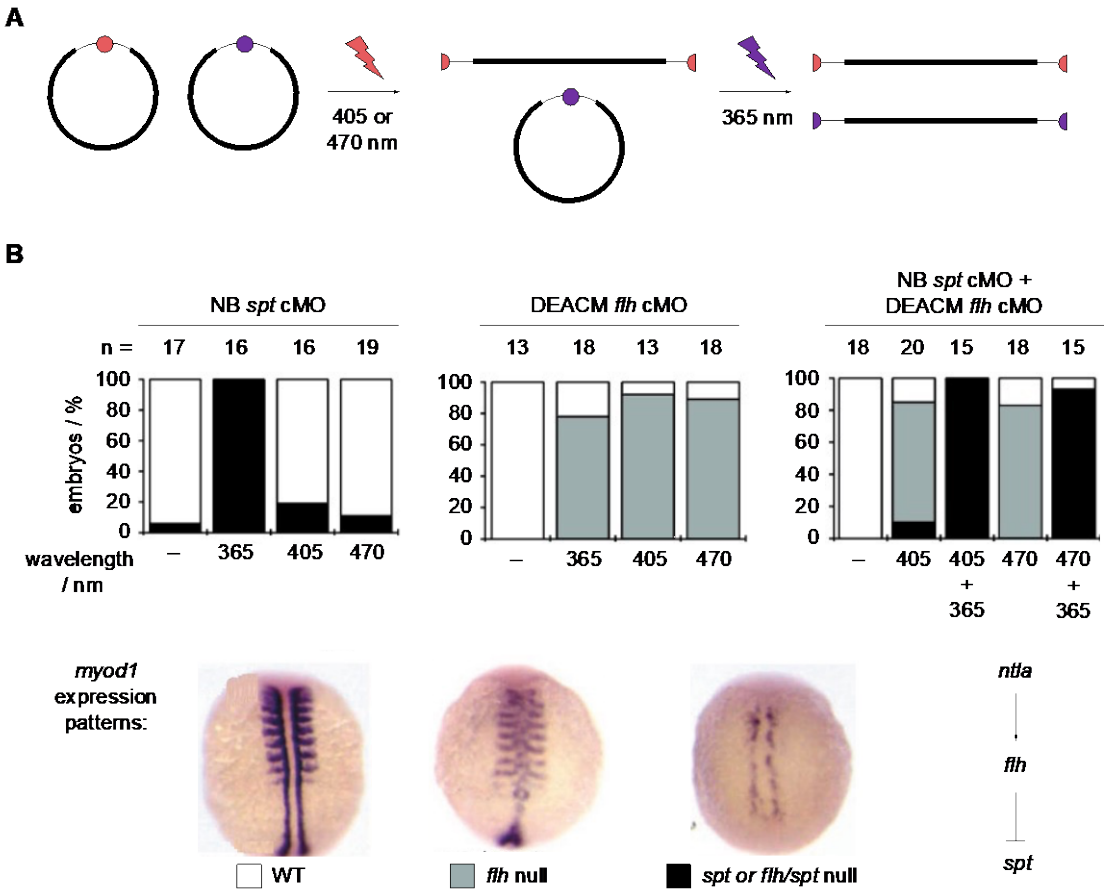

Figure 1-8: Sequential activation of spectrally-differentiated cyclic cMOs
A) Schematic of wavelength-specific activation of DEACM- (pink) and NB- (purple) caged, cyclic cMOs. B) Quantification of phenotypes for embryos injected with the photocaged cMOs and subjected to the indicated irradiation conditions. Representative images of *myod1* expression patterns from non-injected (white), *flh* null (gray), and *spt* null (black) embryos, as determined by in situ hybridization experiments. Figure was adapted from Yamazoe *et. al.*, *Angew. Chem. Int. Ed.*, **2014**, 53, 10114.[67]

Since the demonstration of combinatorial control over gene expression, efforts towards advancing cyclic cMOs have been focused around optimizing linker synthesis and expanding the repertoire of conditional triggers towards chromophores that can be activated using light in the near-IR or visible regions (Figure 1-9). Photoactivation with longer wavelengths of light minimizes phototoxicity associated with UV light and allows for deeper tissue penetration.[79, 80] To this end, the Dmochowski group (University of Pennsylvania) synthesized a visible light-responsive ruthenium-polypyridyl linker (RuBEP, **13**) that decages rapidly via a ligand-solvent

exchange.[69] When incorporated into an MO targeting *chordin* (*chd)*, the RuBEP cMO-injected embryos displayed a strong phenotype only when irradiated with 450 nm light. More recently, the Dore lab has optimized the synthesis of a CyHQ- cMO linker which, like RuBEP, can undergo photolysis with one- or two-photon excitation. This second-generation CyHQ linker **14** linker contains an alkyne handle permitting click conjugation to azide-modified MOs. As mentioned previously, cyclic cMOs containing these chromophores have been successfully activated using two-photon excitation for spatially resolved gene silencing *in vivo.* The high extinction coefficients and quantum yields of these caging groups makes them attractive candidates for linker preparation.

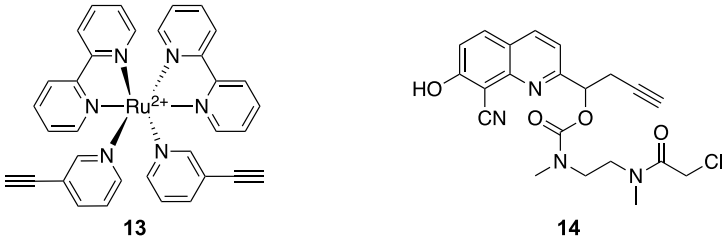

Figure 1-9: Red-shifted cMO linkers

1.4 Development of Conditionally Controlled cMO Technologies

While light gated methodologies provide spatial and temporal control of MO function, few near-IR or 2-photon activatable photolabile groups have been applied in cMO technologies necessitating the use of other triggers to activate MOs in deep tissues or non-transparent organisms. Further, light-triggered technologies require specialized optical equipment that cannot be applied to more than one embryo at a time. Despite the significant progress that has been achieved with optically controlled methodologies, the manipulation and investigation of genetic networks with external, conditional control remains challenging. We sought to address this methodology gap by

building on the principles established with light controlled cyclic cMOs to expand the repertoire of biorthogonal triggers to small molecule- and enzymatically responsive linkers. We have designed linkers containing the proper reactive handles for end-to-end macrocyclization of the MO reagent. Based on the success of the photoactivatable cyclic cMOs discussed previously, we anticipate that these conditionally triggered cMOs will be highly effective as the linkers have been designed to rely on a single cleavage event to restore MO function. Taken together, these light-, enzyme-, and small molecule-controlled reagents can be used in tandem to independently control gene expression and function and afford a new level of genetic control in live organisms.

1.5 Enzymatically Triggered cMOs

The cyclic cMO caging approach can be easily adapted to accommodate enzymatically cleavable linkers, so long as these linkers are equipped with reactive handles suitable for end-to-end cyclization. Enzymatic triggers hold advantages that complement the limitations of the current suite of optically controlled cyclic cMOs. As an example, the structural complexity and physical movement of cells and whole organisms make precise irradiation in a live animal nearly impossible. Enzymatic cMO activation can convey spatially controlled gene silencing regardless of the complexity of the tissue morphology when placed under control of a tissue-specific promoter for inducible expression of the triggering enzyme.

This concept has been previously validated by the Chen lab to control endogenous gene expression in live zebrafish embryos through utilization of the *Escherichia coli* nitroreductase NfsB to trigger cleavage of a 4-nitrobenzyl cMO targeting *ntla* (Figure 1-10A).[81] Previously applied in a gene-directed enzyme prodrug therapy (GDEPT) in transgenic mouse models, the

nitroreductase enzyme was harnessed to activate the antitumor drug CB1954 in selectively killing luminal epithelial cells within the mouse mammary glands.[82] In the absence of the anti-tumor prodrug, the enzyme showed no adverse effects against closely associated myoepithelial cells, adipocytes, or fibroblasts, thereby circumventing the "bystander effect" and demonstrating the orthogonality of the enzyme. Additionally, this strategy has been utilized to generate a model for beta cell regeneration in zebrafish embryos, which has larger implications in discovering pharmacological and genetic modifiers of this pathway within vertebrate organisms.[83]

The NfsB nitroreductase catalyzes conversion of the 4-nitro group on the linker **15** to form a 4-hydroxylaminophenyl intermediate that self-immolates via a 1,6-elimination and decarboxylation sequence, thereby generating the linear MO. Embryos co-injected with cMO and synthetic mRNA expressing mCherry-tagged NfsB exhibited a dose-dependent phenotypic response by 24 hpf, as the strength of the *ntla* loss-of-function phenotype directly correlated with the amount of NfsB mRNA injected (Figure 1-10B). Further, the authors utilize the NfsB-activatable cMOs to induce localized knockdown *pancreatic and duodenal homeobox 1* (*pdx1*) and *motor neuron and pancreas homeobox 1* (*mnx1*) in insulin producing cells using a transgenic zebrafish line *Tg(insulin:CFP-nfsB)* that stably expresses the triggering enzyme under a tissue-specific promoter. MO-mediated knockdown of these transcription factors inhibits endocrine differentiation leading to β-cell ablation and a loss of insulin producing cells. Wild-type embryos co-injected with NfsB *pdx1* and NfsB *mnx1* cMOs exhibited normal β-cell differentiation, suggesting the NfsB cMOs remained intact and functionally inert. The corresponding transgenic fish exhibited inhibition of endocrine formation, with 70% exhibiting partial or complete loss of insulin producing β-cells, confirming successful tissue-specific cMO activation and silencing of target gene expression. Additionally, the Dmochowki group recently developed a caspase-3

activatable PNA-based oligonucleotide sensor to probe apoptosis in a cellular model.[84] Together, these results provide initial proof-of-concept validation of our approach. Expansion of this class of cMOs to additional enzyme/substrate pairs will enable fast and independent control multi-gene networks with a degree of orthogonality that is difficult to achieve with the current suite of light-controlled cMO linkers.

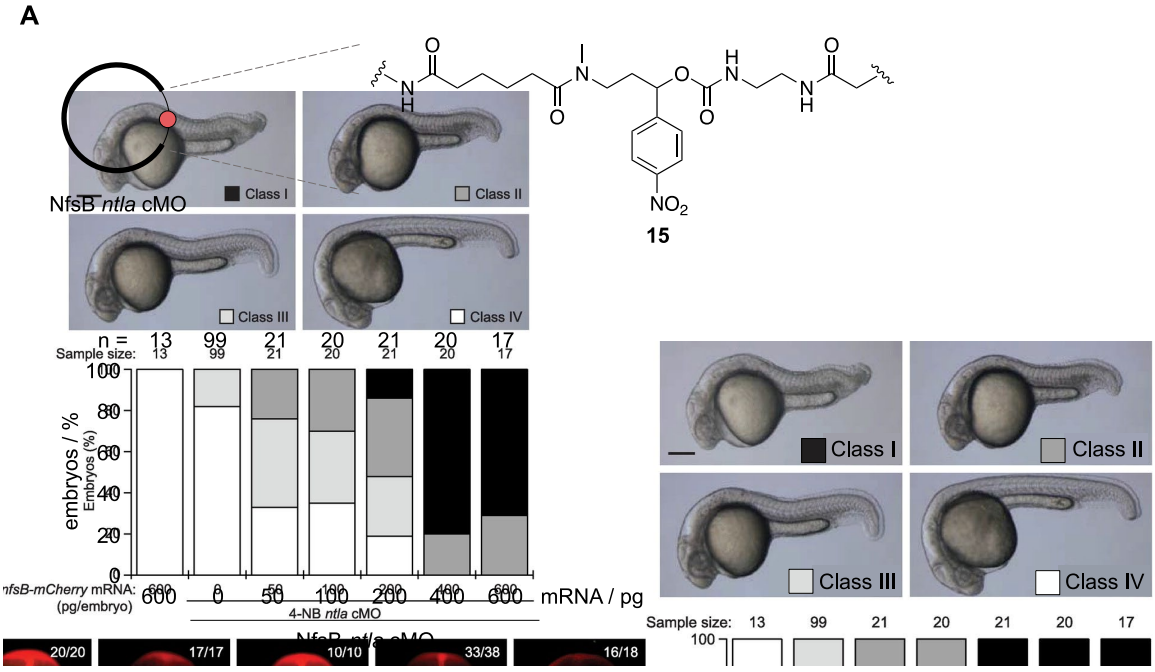

Figure 1-10: Nitroreductase-cleavable cMO
A) Structure of the 4-nitrobenzyl containing linker that is cleaved via NfsB catalyzed reduction. B) Zebrafish embryos co-injected with the Nfsb *ntla* cMO and synthetic mRNA expressing Nfsb-mCherry demonstrate a dose-dependent phenotypic response. Figure was adapted from Yamazoe *et. al.*, *ACS Chem. Biol.*, **2014**, 9, 1985.[81]

1.5.1 β-Lactamase Cleavable cMO

β-Lactam antibiotics revolutionized the field of medicine following the initial discovery of penicillin by Alexander Fleming in 1929.[85] More than 80 years after penicillin was introduced into the clinic, numerous β-lactam antibiotics have received FDA approval and remain one of the most

prescribed drugs for treatment against bacterial infection. There are four classes of β-lactam antibiotics currently in clinical use including cephalosporins, which are bicyclic structures consisting of a strained cyclic amide fused to a dihydrothiazine heterocycle (Figure 1-11).[86, 87] Structure activity studies revealed that modifications to the C-3 and C-7 positions of cephalosporins were tolerated and also retained bacteriocidal activity, leading to further development of these drugs.[86]

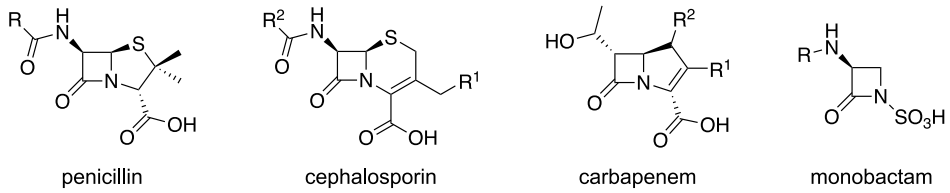

Figure 1-11: General core structural scaffolds of β-lactam-based antibiotics
R groups (R, R^1, and R^2) represent regions of functionalization on each core scaffold.

Following commercial development, several diverse β-lactam-type antibiotics emerged. However, a major consequence of this progress was the increased selective pressure on the bacteria which eventually evolved to overcome antibiotic treatment by adapting resistance mechanisms. In the case of β-lactam antibiotics, secretion of degradation-inducing enzymes, known as β-lactamases, by gram-negative and gram-positive bacteria remains the primary mechanism of resistance.[88] β-Lactamase enzymes are separated into four different classes, three of which follow a classical acylation/de-acylation catalytic mechanism analogous to that observed in the serine protease family (Figure 1-12A). Class B β-lactamase enzymes consist of metallo-β-lactamases which utilize zinc to drive antibiotic hydrolysis (Figure 1-12B).[89] First, a nucleophilic active site serine attacks the carbonyl carbon of the lactam amide bond. The acyl-enzyme intermediate is then quenched following nucleophilic attack by water to form the hydrolyzed, inactive antibiotic and

regenerate the active β-lactamase enzyme.[86] In clinical practice today, β-lactamase inhibitors are often co-administered with β-lactam antibiotics to combat this resistance mechanism.[88, 90-92]

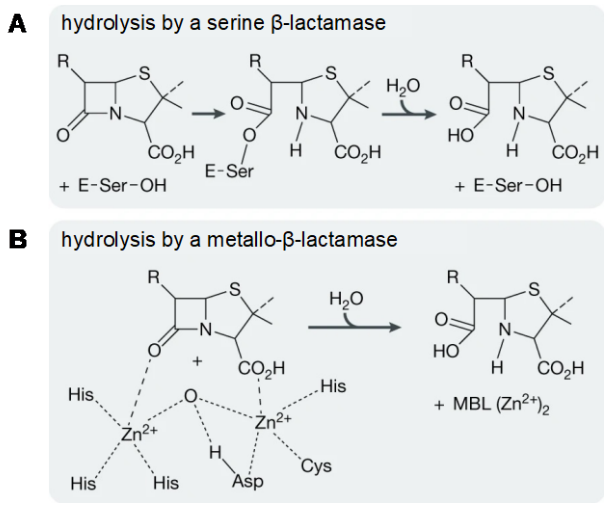

Figure 1-12: Mechanism of β-lactam hydrolysis by β-lactamase enzymes
Figure was adapted from Bush et. al., *Nat. Rev. Microbiol.*, **2019**, 17, 295.[88]

Taking advantage of this highly specific interaction, β-lactamase enzymes have also been heavily utilized in directed enzyme prodrug therapeutic (DEPT) strategies.[93-95] This strategy exploits the interaction between a substrate-enzyme pair in overcoming the adverse effects of chemotherapeutic activity following global distribution by limiting activation only in tissues that express the enzyme. Generally, bacterial enzymes have several properties that make them favorable for DEPT applications including stability, catalytic efficiency, and ease of manufacturing when compared to human enzymes. Additionally, their enzymatic function is often unique to bacterial systems, resulting in minimal disruption to the mammalian system.[96] Specifically, β-lactamase enzymes have been used to spatially control the therapeutic effects of several cancer drugs including doxorubicin,[97] taxol,[98] and paclitaxel[99] and have also been applied as antibody-fusions to generate tumor-targeted therapies.[96, 100, 101] The success of the β-lactamase

enzyme as an orthogonal, locally-activated therapeutic strategy, also make this an attractive candidate as a research tool for studying biological processes with spatial control.

Previously, the Tsien lab has exploited the very selective cleavage of cephalosporins by the β-lactamase enzyme to generate a fluorogenic cephalosporin-based sensor to measure gene expression with high sensitivity in real time.[102] The sensor, **CCF2**, contained two fluorophores, fluorescein and 6-chloro-7-hydroxycoumarin, installed at the C-3 and C-7 positions on the cephalosporin scaffold, respectively. In proximity, these fluorophores exhibit efficient fluorescence resonance energy transfer (FRET). When the sensor is intact, excitation of the 6-chloro-7-hydroxycoumarin (donor) with 409 nm light results in emission of fluorescein (acceptor), exhibiting green fluorescence (em. 520 nm). In the presence of β-lactamase, the lactam ring is hydrolyzed generating a free amino group that triggers spontaneous elimination of any good leaving group attached at the exocyclic methylene (Figure 1-13A).[103, 104] β-lactamase-mediated cleavage of **CCF2**, triggers release of the acceptor (fluorescein), and when excited with 409 nm light, re-establishes longer-wavelength (em. 447 nm) blue fluorescence from the 6-chloro-7-hydroxycoumarin donor molecule. Using an esterified derivative of **CCF2**, the authors demonstrate efficient permeability and subsequent activation of the sensor in mammalian cells either transfected with a β-lactamase expression construct or engineered to stably express β-lactamase under a glucocorticoid-responsive promoter (Figure 1-13B).

Soon after this initial report, the authors applied **CCF2** as a marker for gene expression in live zebrafish embryos.[105] Following microinjection at the 1-cell stage, **CCF2** exhibited a stable, green fluorescent signal until the tail bud stage (10 hpf), at which point slight blue fluorescence was observed around the embryo yolk (Figure 1-13C). This visualization of blue fluorescence suggests that the sensor is cleaved at these later stages of development, the mechanism of which

remains elusive, indicating that the **CCF2** probe is only an effective marker for gene expression during pre-somitic stages of development (1-10 hpf). Despite this limitation, the authors were able to demonstrate spatially resolved activation of **CCF2** in pre-somitic embryos. Sensor activation was observed at ~ 5 hpf (30% epiboly) after global distribution of the sensor and co-injection of β-lactamase mRNA and a rhodamine-dextran dye at 2 hpf (64-cell stage). Activation of **CCF2** is observed only in cells that also exhibit rhodamine fluorescence (Figure 1-13D) suggesting β-lactamase is not only expressed and active, but also has no detrimental effects on embryo viability during the pre-somitic stages of embryo development. Overall, this demonstrates that β-lactamase is a suitable enzyme-based trigger for cyclic cMO activation in live zebrafish embryos.

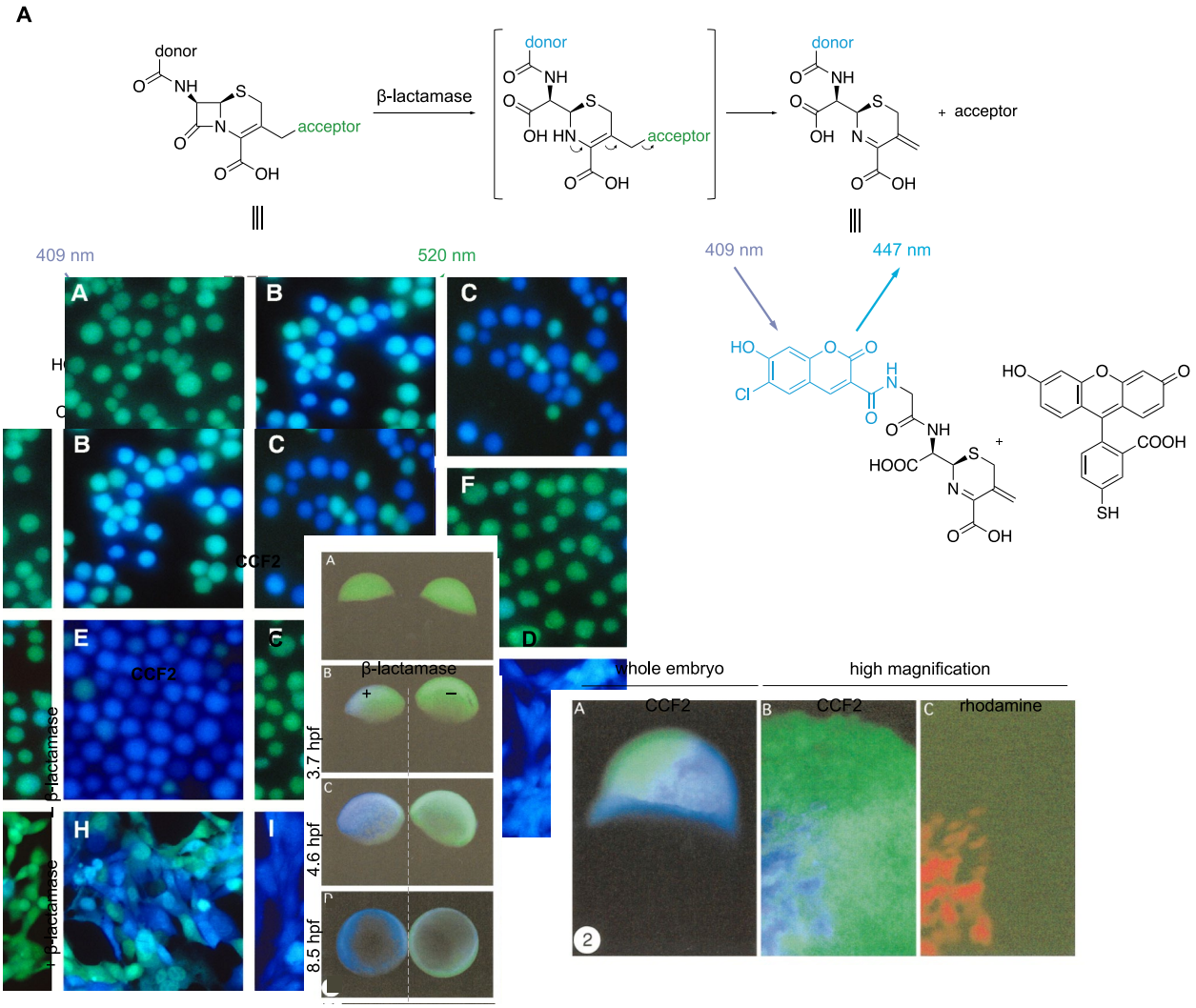

Figure 1-13: Cephalosporin-based marker of gene expression in cells and zebrafish embryos
A) Structure of FRET-based cephalosporin sensor **CCF2**. Hydrolysis of the cephalosporin core by β-lactamase induces induces fragmentation of the sensor resulting in a substantial change in fluorescent signal from 520 nm (fluorescein, acceptor, green) to 447 nm (6-chloro-7-hydroxycoumarin, donor, blue). B) Baby hamster kidney (BHK) cells engineered to stably express TEM-1 β-lactamase under a glucocorticoid-responsive promoter exhibit **CCF2** activation following induction of expression. C) **CCF2** can be used as a marker for gene expression in developing zebrafish embryos through pre-somitic development (~ 10 hpf), after which non-specific activation of the sensor occurs as evidenced by light blue fluorescence at the margin of the embryo yolk. D) Spatially resolved **CCF2** activation in zebrafish embryos. High magnification images reveal blue fluorescence only in cells that also show rhodamine fluorescence suggesting β-lactamase mRNA is delivered and express an active enzyme when injected at later developmental stages. Figure was adapted from Zlokarnik *et. al.*, *Science*, **1998**, 279, 84 and Raz *et. al.*, *Dev. Bio.*, **1998**, 203, 290.[102, 105]

1.5.1.1 Synthesis of β-lactamase-activatable Cyclic cMOs

As a first step towards achieving β-lactamase-mediated control over MO function, we designed a cMO linker utilizing the cephalosporin core scaffold. As mentioned previously, the C-

3 and C-7 positions on the cephalosporin scaffold are most accessible for functionalization,[86] therefore the orthogonal azido- and chloroacetamide- handles necessary for bioconjugation to the MO were installed at these positions. Leaving groups attached to the C-3 position of the cephalosporin ring via a methylene linkage can undergo spontaneous elimination following hydrolysis of the β-lactam ring.[103, 104] Taking this into consideration in our linker design, we strategically installed a carbamate linkage at this position. Analogous to the **CCF2** sensor discussed above, we anticipate that linearization of the cMO will occur following β-lactamase-induced hydrolysis of the lactam ring, forming the corresponding amine, which will then undergo self-immolation via the carbamate linkage. This elimination reaction will release the 5'-end of the MO and regenerate the active, linear MO which can hybridize to endogenous target mRNAs and induce gene silencing (Figure 1-14A). The linker was synthesized by Dr. Rohan Kumbhare (Deiters lab) and the synthetic scheme is depicted in Figure 1-14B.

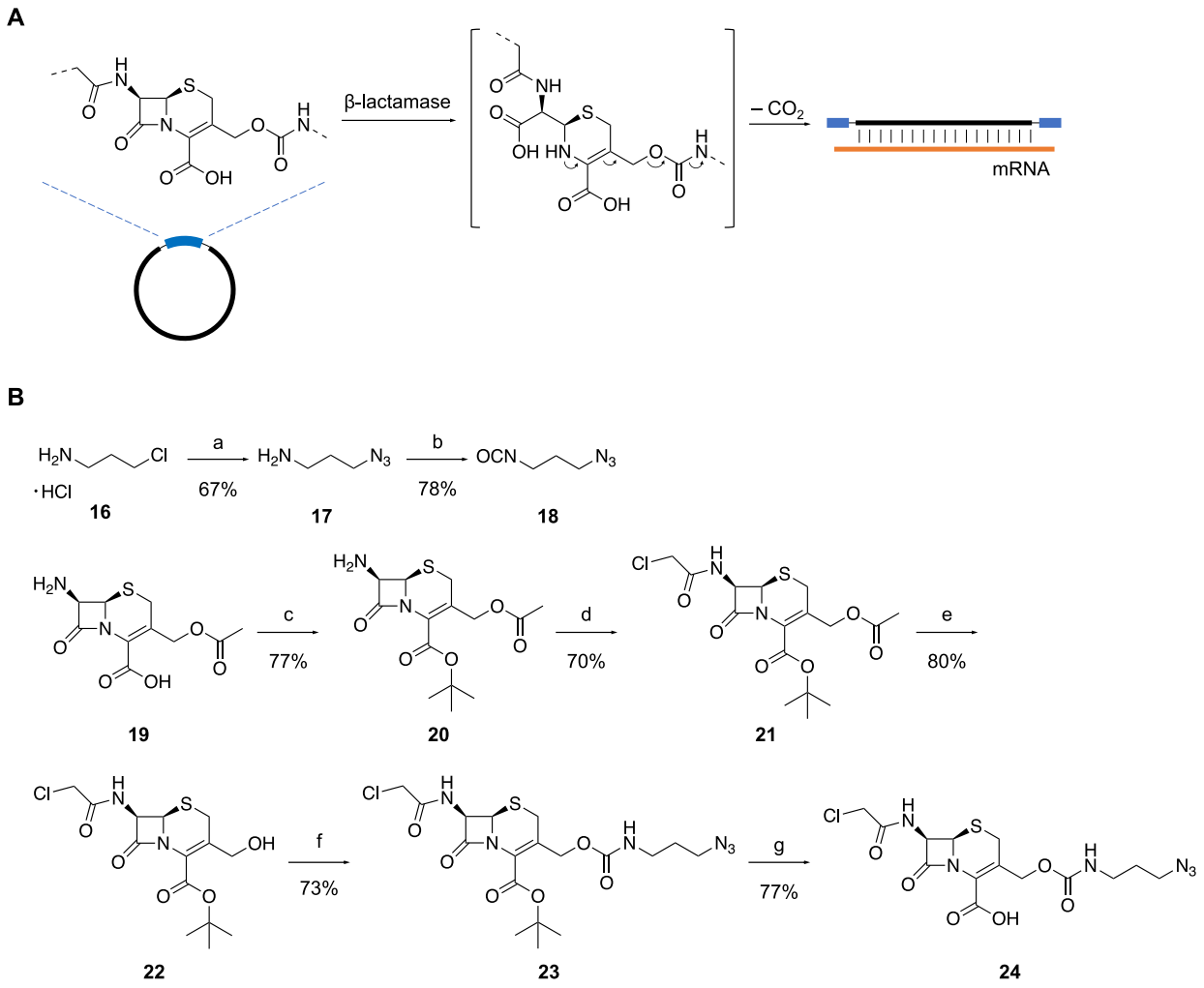

Figure 1-14: Synthesis and cleavage mechanism of β-lactamase-activated cMO.
A) Proposed mechanism of β-lactamase-mediated cMO linearization. B) Synthesis scheme of cephalosporin-containing cMO linker **24**. Reagents and conditions: a) NaN_3, H_2O, 67%; b) diphosgene, sat. $NaHCO_3$/DCM (1:1), 78%; c) TsOH, H_2SO_4, t-butyl acetate, 77%; d) 2-chloroacetyl chloride, sat. $NaHCO_3$/DCM (1:1), 70%; e) Candida antarctica Lipase B, THF/hexanes (1:9), s-butanol, 4Å moleular sieves, 80%; f) **18**, dibutyltin dilaurate, toluene/DCM, 73%; g) triethylsilane, TFA/DCM, 77%. Synthesis was completed by fellow lab member Dr. Rohan Kumbhare (Deiters lab).

The linker **24** was then used to prepare cyclic cephalosporin cMO targeting the T-box transcription factor *ntla* (5'-GACTTGAGGCAGACATATTTCCGAT-3', anti-start codon is underlined). The *ntla* MO (**27**) was purchased from Gene Tools, LLC (Philomath, OR) and terminally modified with 5'-amine and 3'-disulfide handles to allow for macrocyclization. To install the necessary alkyne handle for reaction with the azide on linker **24**, 4-pentynoic acid (**25**)

was reacted with *N, N, N', N'*-tetramethyl-*O*-(*N*-succinimidyl)uranium tetrafluoroborate (TSTU) to generate the corresponding NHS ester **26**. The *ntla* MO was reacted with **26** in 0.1 M Tris-HCl buffer pH 8.5 to yield the alkyne functionalized *ntla* MO **28**. The linker **24** was then clicked to the terminal alkyne **28** via a copper(I)-catalyzed alkyne-azide cycloaddition (CuAAC) following previously reported conditions.[106] However, when the reaction was analyzed by MALDI-TOF mass spectrometry, a mass was observed that was not consistent with the expected clicked product **29** (Figure 1-15A). To troubleshoot the reaction, a test click reaction utilizing the same conditions was performed with simple alkyne **25** and monitored by liquid chromatography-mass spectrometry (LCMS). The test reaction was successful and a mass consistent with the expected clicked product **30** was observed (Figure 1-15B). However, in subsequent click reactions with the alkyne-modified MO **28**, the formation of this same unknown product was observed and could not be assigned to any conceivable reaction intermediate or potential product.

To circumvent issues with the carboxylic acid containing linker **24**, we tested the click reaction of the *ntla* MO **27** with the *tert*-butyl ester intermediate **23** (Figure 1-15C). A CuAAC conjugation of the alkyne modified MO with the *tert*-butyl ester linker **23** under the same reaction conditions successfully yielded the corresponding triazole product **31**. The MO-linker conjugate was then treated with resin-immobilized tris(2-carboxyethyl)phopshine (TCEP) to reduce the 3'-dithiol and generate the free thiol. The reduced product then underwent a spontaneous, intramolecular cyclization through reaction with the chloroacetamide handle on **23** to form the cyclized cMO product **32**. To remove any unreacted, linear MO species, the cMO **32** was further purified using iodoacetyl- and NHS-functionalized resins and purification by HPLC.

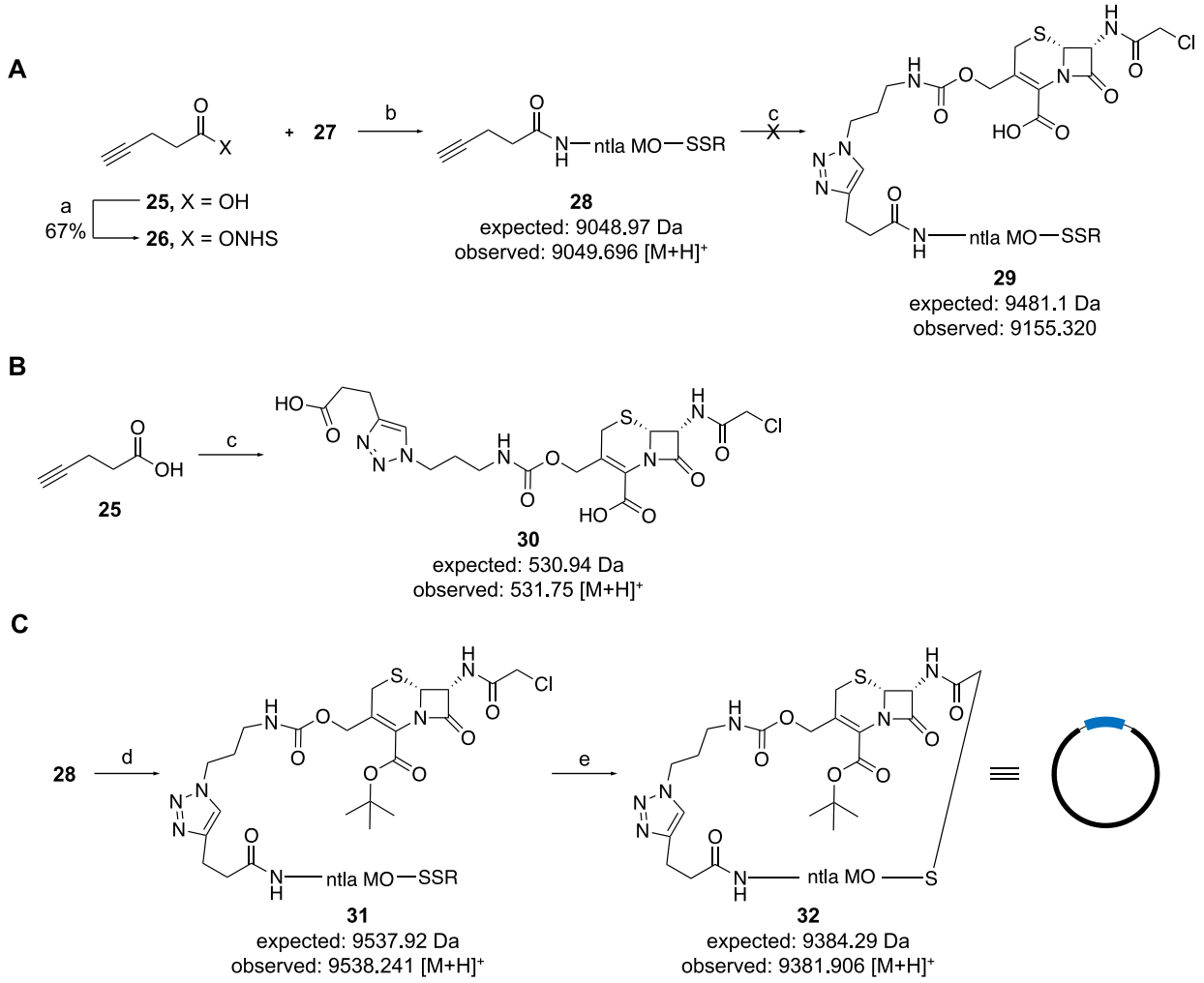

Figure 1-15: Synthesis of cephalsporin-containing cyclic cMO
A) Attempted cyclization of *ntla* MO (NH_2-*ntla* MO-SSR, **27)** with cephalosporin linker **24**. B) Test click reaction of **24** with simple alkyne **25**. Reaction was analyzed by LCMS. C) Cyclization of *ntla* MO **27** with cephalosporin linker **23**. Reagents and conditions: a) TSTU, TEA, ACN, 94%; b) 0.1 M Tris pH 8.5 buffer, 10% DMSO; c) **24**, Cu(II)-TBTA, sodium ascorbate, 10% DMSO, H_2O; d) **23**, Cu(II)-TBTA, sodium ascorbate, 10% DMSO, H_2O; e) resin immobilized TCEP, 0.1 M Tris pH 8.5 buffer.

While the protection of the C-4 carboxylic acid with a *tert*-butyl ester is a popular choice for the synthesis of cephalosporins and related analogs, there have been no studies that have directly explored β-lactamase reactivity toward the C-4 carboxylic acid-protected analogs. However, there are few reports where the bactericidal activity of these analogs has been screened and if a specific bacterial strain is resistant, then it could be hypothesized that the analog is susceptible to β-lactamase-mediated inactivation.[107, 108] To ensure that the presence of the *tert*-

butyl ester protecting group does not hinder β-lactamase-mediated cleavage, cleavage of the linker by recombinant *E. coli* β-lactamase (Novus Biologicals) was monitored by LCMS (Figure 1-16). The linker **23** was diluted to 1 mM in 50 mM sodium phosphate buffer. Recombinant β-lactamase (1 μg) was added to the reaction mixture, and the reaction was incubated at 30 ºC for 24 hours. At the indicated time point, an aliquot of the reaction mixture was removed and analyzed by LCMS. Considerable disappearance of the linker was observed after 3 hours at 30 ºC, with complete disappearance after overnight incubation. A mass consistent with the anticipated elimination product **33** was observed, suggesting that the presence of the *tert*-butyl protecting group on the cephalosporin core does not impact the accessibility of the enzyme to the cleavage site. Further, the linker was not hydrolyzed in the absence of enzyme, suggesting it is stable and the cleavage observed is entirely due to β-lactamase activity.

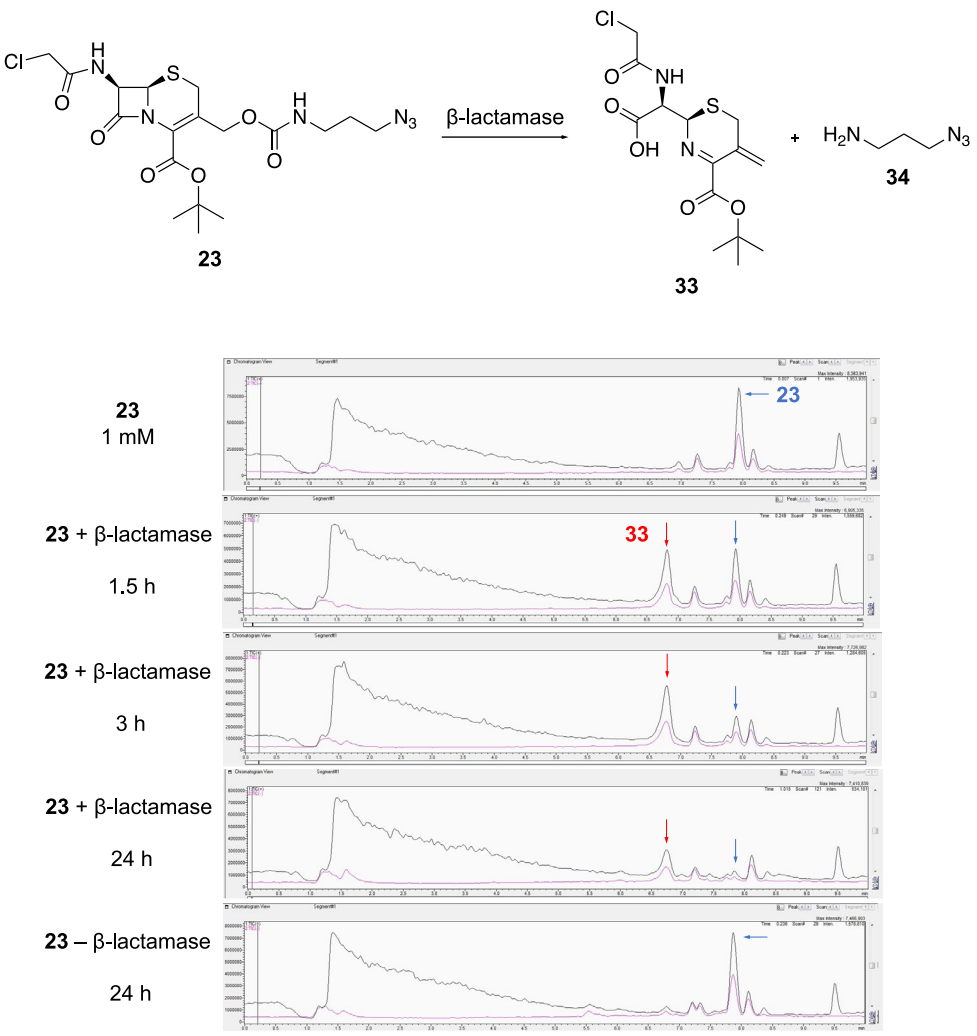

Figure 1-16: LCMS studies of *t*Bu-cephalosporin linker cleavage by recombinant β-lactamase enzyme
Linker **23** (1 mM, indicated by the blue arrow) was incubated with recombinant β-lactamase (1 µg) in 50 mM sodium phosphate buffer. At each time point, an aliquot of the reaction was removed an analyzed by LCMS (ESI). After 1.5 hr incubation, detection of the elimination product (indicated by the red arrow) is observed. The linker **23** remains stable in the absence of enzyme for 24 hours.

1.5.1.2 Evaluation of β-lactamase Expression and Activity

Having validated cleavage of the *t*Bu-cephalosporin linker *in vitro*, and successfully synthesizing the cephalosporin-based cMO, we next focused our efforts in generating a β-lactamase expression construct. For optimal expression in zebrafish, the coding sequence of β-lactamase was adapted from previous reports[109] and codon optimized for mammalian expression

(Table 1-1). An HA-tag was cloned to the N-terminus to allow for detection of protein expression by western blot. The HA-β-lactamase sequence was purchased as a gene fragment from Twist. The gene fragment was amplified by PCR using primers P1 and P2 and ligated into the BamHI and XhoI restriction sites of the pCS2+ backbone.

The pCS2-HA-β-lactamase construct was then used to validate enzyme expression and activity in cells. HEK293T cells were transfected with pCS2-HA-β-lactamase, incubated for 24 hours, and then protein expression was analyzed by an anti-HA western blot (Figure 1-17B). Expression of HA-β-lactamase was confirmed in transfected lysates, while no HA-signal was detected in untransfected lysates, suggesting the enzyme is efficiently expressed in mammalian cells. To determine if the enzyme that is being expressed also maintains serine hydrolase activity, we utilized nitrocefin (**35**), a chromogenic β-lactamase substrate with a cephalosporin core.[110] When intact, nitrocefin is yellow (λ_{max} = 390 nm at pH 7). However, following β-lactamase-mediated hydrolysis of the cephalosporin core, a color change from yellow to red (λ_{max} = 486 nm at pH 7) is observed (Figure 1-17A). When incubated with recombinant β-lactamase (0.5 μg) in 50 mM sodium phosphate buffer, full cleavage of nitrocefin is observed in ~ 12 minutes (Figure 1-17C). HEK293T cells were transfected with varying amounts of pCS2-HA-β-lactamase (100 ng) and incubated for 24 hours. Following incubation, the cells were lysed and the nitrocefin substrate was added to the lysates. Following addition of **35**, the expected color change was observed almost immediately as indicated by the 3-fold increase in absorbance at 486 nm (Figure 1-17D). These results validate both the expression and activity of the β-lactamase enzyme in mammalian cells.

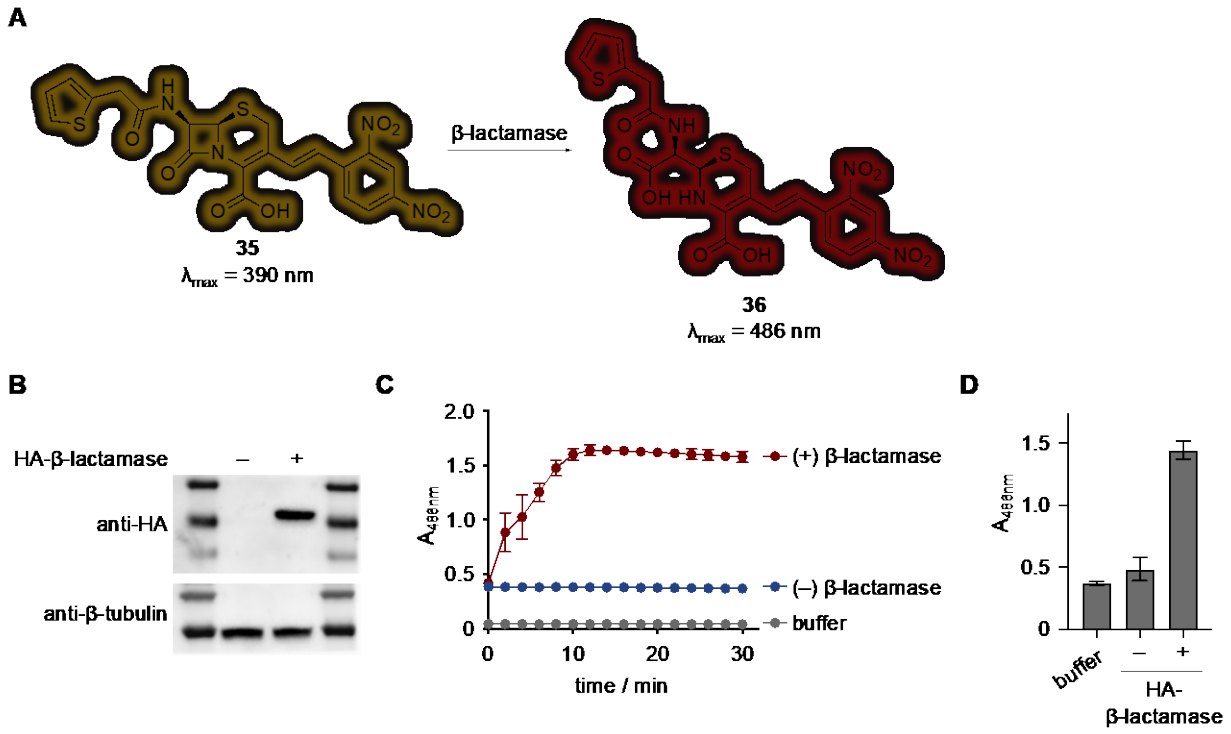

Figure 1-17: Evaluation of β-lactamase activity in vitro and in mammalian cell culture
A) Structure of chromogenic β-lactamase substrate nitrocefin (**35**). After β-lactamase-mediated hydrolysis generates **36**, the substrate exhibits an obvious yellow to red color change. B) Western blot analysis of HEK293T cell lysates confirms expression of HA-tagged β-lactamase in cells transiently transfected with pCS2-HA- β-lactamase. C) Nearly full hydrolysis of nitrocefin (1 mM) is observed following incubation with recombinant β-lactamase (0.5 μg) in 50 mM sodium phosphate buffer. D) HEK293T cell lysates transfected with pCS2-HA-β-lactamase were incubated with **35** for 2 minutes before absorbance at 486 nm was measured.

Next, we sought to evaluate whether β-lactamase would be expressed and maintain activity *in vivo*. In order to induce overexpression of β-lactamase in zebrafish embryos, synthetic HA- β-lactamase mRNA was generated through *in vitro* transcription and injected (400 pg) into the yolk sac of 1- to 4-cell stage zebrafish embryos.[111] At 24 hpf, the wild-type (WT) and the mRNA-injected embryos were pooled (n = 100 embryos/condition), and were lysed for western blot analysis. Gratifyingly, analysis of mRNA-injected lysates indicates that the enzyme is expressed (Figure 1-18A). We next utilized the nitrocefin assay to determine whether the expressed enzyme maintains function. Zebrafish embryos at the 1- to 4-cell stage were injected with increasing doses of HA-β-lactamase mRNA (0-1000 pg). At 24 hpf, embryos were pooled (n = 41

embryos/condition) and lysed by homogenization. Embryo lysates were mixed with nitrocefin substrate and enzyme activity was monitored over 80 minutes. Based on these results, there is an obvious dose-dependent correlation in β-lactamase activity, suggesting the extent of enzymatic activity can be finely tuned based on the mRNA injection amount. Further, the minimum amount of HA-β-lactamase required to meet maximal activity is 500 pg (Figure 1-18B). The initial linear rate of nitrocefin hydrolysis (Figure 1-18C) also demonstrates a clear positive correlation between the amount of mRNA injected into the zebrafish embryos and the rate of enzymatic activity. It is also important to note that overexpression of β-lactamase in early-stage embryos does not induce any obvious toxicity or developmental defects (Figure 1-18D).

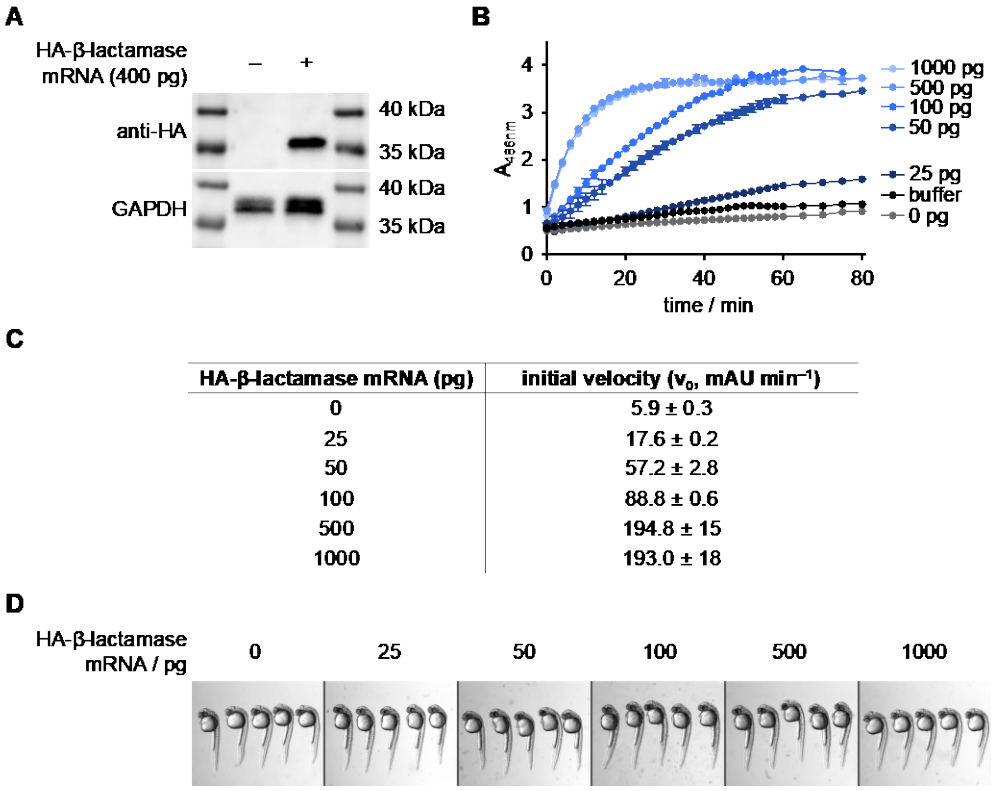

Figure 1-18: Evaluation of β-lactamase *in vivo*
A) Western blot analysis of wild-type zebrafish embryos or zebrafish embryos injected with 400 pg HA-β-lactamase mRNA. B) Zebrafish embryos were injected with increasing amounts of HA-β-lactamase mRNA. Embryos were lysed at 24 hpf and lysates were incubated with nitrocefin. Nitrocefin hydrolysis was monitored by measuring absorbance at 486 nm over 80 minutes. C) Initial velocity of β-lactamase-mediated conversion of nitrocefin to its corresponding

hydrolyzed product. Initial velocities were determined through a linear regression analysis of the first 10 minutes of the data presented in panel B. D) Representative images of 24 hpf embryos injected with the indicated amount of HA-β-lactamase mRNA exhibit no developmental defects due to overexpression of the enzyme.

1.5.1.3 Evaluation of cMO Activation *in vivo*

To determine if we could induce enzymatic activation of MO function *in vivo*, we utilized our cyclic cephalosporin-based cMO targeting endogenous gene *ntla* (**32**). Silencing of *ntla* expression during early embryo development induces distinct morphological defects that are evident by 24 hpf including a loss of notochord cells, posterior truncation, and misshapen somites (Figure 1-19A).[112, 113] We and others have investigated conditional silencing of *ntla* expression with optically- and enzymatically-triggered cMOs, making this an excellent candidate for *in vivo* studies.[63, 64, 66, 67, 81]

Zebrafish embryos were microinjected with 300 pg of either a standard control MO, the linear *ntla* MO, or the cyclic cephalosporin-based cMO **32**. Where indicated, embryos were co-injected with 400 pg of the HA-β-lactamase mRNA. Injected embryos were incubated to 24 hpf and analyzed for the *ntla* loss-of-function phenotype (Figure 1-19B). Embryos injected with the cyclic cephalosporin-based cMO alone exhibited minimal phenotypic defects. The extent of background gene silencing is consistent with what has been previously reported for other cyclic cMOs.[66, 69] However, when cMO is co-injected with HA-β-lactamase mRNA, full rescue of strong *ntla* phenotype is observed, comparable to that observed in embryos injected with the linear *ntla* MO. Further, embryos injected with either the control MO alone or with HA-β-lactamase mRNA exhibit no obvious phenotypic defects, indicating the phenotype observed with the cMO can be specifically credited to *ntla* MO-induced gene silencing that results from enzymatic decaging.

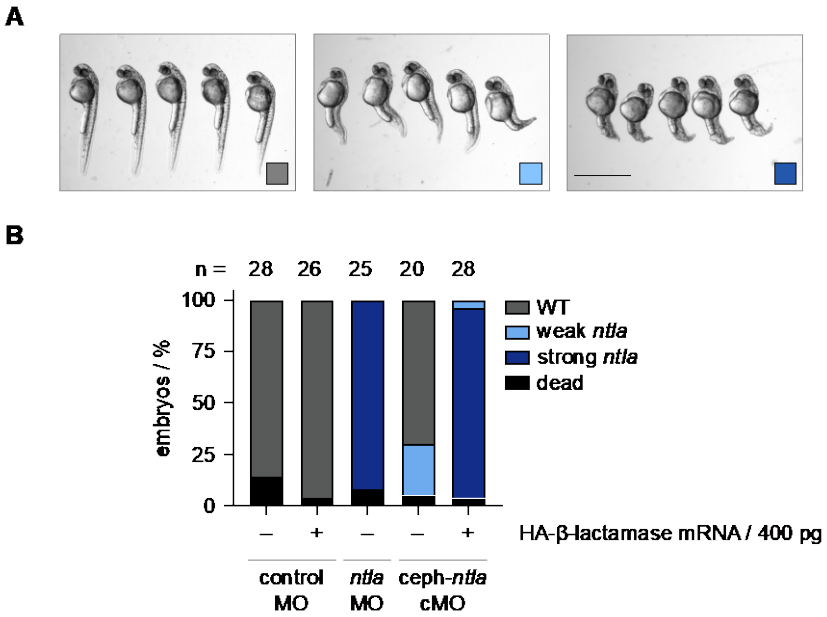

Figure 1-19: β-lactamase-mediated activation of MO function *in vivo*
A) Representative images of *ntla* morphant phenotype. "Weak" phenotype (light blue) exhibits all hallmark indicators of the *ntla* loss-of-function phenotype but only demonstrates mild posterior truncation, as evidence by the slightly longer tail lengths. "Strong" phenotype (dark blue) exhibits loss of notochord cells, U-shaped somites, and posterior truncation. Scale bar equals 1 mm. B) Phenotypic scoring of 24 hpf zebrafish embryos injected with the indicated morpholino reagents (300 pg) and where indicated, mRNA expressing HA-β-lactamase (400 pg).

1.5.1.4 Summary and Future Directions

Herein, we utilize enzyme-mediated antibiotic resistance mechanisms in the development of a β-lactamase-activatable cMO tethered by a cephalosporin-based linker. A cMO linker containing a cephalosporin core-scaffold and two reactive handles was synthesized and used to successfully cyclize a terminally modified *ntla* MO. While the cephalosporin linker **23** contains a *t*Bu ester adjacent to the scissile site, we validated this modification does not impact β-lactamase reactivity through LCMS studies. Following confirmation of cleavage *in vitro*, an HA-tagged β-lactamase expression construct was generated. The expression and activity of β-lactamase was validated in mammalian cells and in live zebrafish embryos through probing of the corresponding lysates by western blot and utilization of chromogenic β-lactamase substrate, nitrocefin,

respectively. Finally, efficient MO-mediated silencing of endogenous gene expression was demonstrated in live zebrafish embryos co-injected with the cyclic cephalosporin-based cMO **32** and mRNA expressing the triggering enzyme.

Ongoing efforts are focused on reproducing these promising results in embryos and optimizing the injection amounts in order to reduce the background gene silencing that is observed in the absence of the enzyme trigger. We are currently working towards demonstrating tunability of the phenotypic strength through dosing the amounts of mRNA injected. Additionally, while we and others have successfully demonstrated enzyme-triggered silencing of the *ntla* gene, we would like to demonstrate the modularity of this approach by targeting other endogenous genes, including *spadetail*.

1.5.1.5 Materials and Methods

Reagents. Recombinant *E. coli* β-lactamase protein was purchased from Novus Biologicals (Cat. No. NBP2-59641) as a 1 mg/mL solution. Anti-HA antibodies were purchased from either Cell Signaling Technologies (mouse 2367S or rabbit 3724S). Anti-beta tubulin (10068-1-AP) and anti-GAPDH (mouse, 60004-1-Ig) were purchased from ProteinTech. HRP-linked anti-rabbit (SA00001-2) and anti-mouse (SA00001-1) secondary antibodies were purchased from ProteinTech. All antibodies were diluted following the manufacturer's recommendation unless otherwise indicated. Chromogenic β-lactamase substrate nitrocefin (484400-5MG) was purchased from Sigma and used without further purification.

1.5.1.5.1 Synthetic Protocols

General chemical protocols. All starting materials were purchased from commercial suppliers and used without further purification. Anhydrous reaction solvents were purchased from commercial suppliers and were kept on sieves as provided by the manufacturer. All reactions were performed in flame dried glassware under and inert atmosphere and stirred magnetically. ^{1}H and ^{13}C NMR spectra were recorded on a Bruker Ultrashield 300 MHz, 400 MHz, or 500 MHz instrument. Analytical LC-MS data were collected on a Shimadzu LCMS-2020 and a ThermoScientific Q-Exactive Orbitrap. Samples analyzed by LC-MS were resolved on a Hypersil GOLD C18 column (1.9 µm, 2.1 x 100 mm, ThermoScientific) at 40 ºC eluting with a gradient of 5-95% acetonitrile + 0.1% formic acid in water + 0.1% formic acid. HPLC purifications were performed using a Shimadzu LC-20AD equipped with a SP-20AD UV/Vis detector as outlined in Section 4.3.4. All morpholino compounds were prepared, purified, and analyzed by MALDI-TOF MS as outlined in Section 4.3.3.

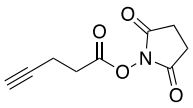

2,5-Dioxopyrrolidin-1-yl pent-4-ynoate (26). 4-Pentynoic acid (25 mg, 0.26 mmol) was dissolved in anhydrous acetonitrile (2.55 mL). Triethylamine (89 µL, 0.64 mmol, non-anhydrous) was added dropwise at room temperature while stirring. The reaction was cooled to 0 ºC in an ice bath while stirring for 15 minutes. Then, the septum was removed and TSTU (84.3 mg, 0.28 mmol) was added to the reaction mixture while stirring on ice. The vial was capped with the septum again and the reaction vessel was purged with a nitrogen balloon for 15 minutes. The reaction mixture

was stirred at 0 ºC in an ice bath for 30 minutes, at which point the ice bath was removed, and then the reaction mixture was gradually warmed to room temperature over 2 hours. The solvent was removed under reduced pressure and the crude material was dried under high vacuum for ~ 4 hours. The crude residue was dissolved in dichloromethane (500 µL) and purified on silica gel by flash column chromatography using 3% methanol in dichloromethane as the eluent. The NHS-ester **26** was obtained in 94% yield as a white solid. ^{1}H NMR (400 MHz, $CDCl_3$) δ 2.85 (m, 6H), 2.60 (m, 2H), 2.04 (t, J = 2.8 Hz, 1H). The analytical data matched previous literature reports.[114]

Alkyne-functionalized *ntla* MO (28). Linear *ntla* MO **27** (100 µL, 1 mM, 100 nmol) was diluted with 0.1 M sodium borate pH 8.5 buffer (894 µL) at room temperature in a 1.7 mL Eppendorf tube and was vortexed briefly to mix. The NHS-activated alkyne **26** (6 µL, 100 mM in DMSO, 6 eq) was added. The tube was vortexed briefly to mix and the reaction was incubated at room temperature overnight. The next morning, the crude reaction mixture was analyzed by MALDI-TOF MS (expected: 9048.97, observed: 9047.885) as outlined in Section 4.3.3. The alkyne-modified linear *ntla* MO **28** was purified by HPLC as outlined in Section 4.3.4. The purified MO fractions were pooled, diluted with water, and lyophilized to dryness.

Cephalosporin linker-*ntla* conjugate (31). The dry, purified, alkyne-functionalized *ntla* MO was resuspended in water (100 µL) and the concentration was determined on the ND-1000 NanoDrop spectrophotometer following the protocol outlined in Section 4.3.2 (GeneTools, 1:20 and 1:10 in 0.1 N HCl, 265 nm, constant = 34). The typical concentration range can vary depending on the scale of the reaction but is usually between 100-300 µM. The click reaction was performed following a previously reported protocol provided from the manufacturer.[106] The alkyne functionalized *ntla* MO **28** (100 µL, 281 µM, 10.2 nmol) was diluted with water (265 µL) and DMSO (28 µL, final 10%) to a final concentration of 50 µM. The cephalosporin linker **23** (28 µL,

5 mM in DMSO, 51 nmol) was added to the reaction mixture and the reaction was briefly vortexed to mix. In a separate tube, a 5 mM solution sodium ascorbate was freshly prepared by dissolving solid sodium ascorbate (~ 5-10 mg) in milliQ water (~5.1-10.2 mL, depending on the amount of solid weighed). Then, the aqueous sodium ascorbate solution (112 µL, 5 mM in water, 204 nmol) was added to the reaction mixture which was briefly vortexed to mix. In separate tubes, a 40 mM solution of $CuSO_4$ in water and a 40 mM solution of tris[(1-benzyl-1H-1,2,3-triazol-4-yl)methyl]amine (TBTA) in DMSO were freshly prepared. Then, equal volumes (20 µL) of each solution, the $CuSO_4$ and TBTA solutions, were combined and mixed by pipetting to generate a 20 mM $CuSO_4$-TBTA solution in 50% DMSO. A portion of this 20 mM $CuSO_4$-TBTA solution (28.1 µL, 204 nmol) was added to the linker and alkyne-MO reaction mixture and vortexed briefly to mix. The final concentration of the MO in the reaction mixture was 50 µM. The reaction was incubated overnight at room temperature. The next morning, a small aliquot of the crude reaction mixture was removed and co-spotted with sinapinic acid (SA) matrix and analyzed by MALDI-TOF MS (expected: 9537.92, observed: 9537.424) following the protocol outlined in Section 4.3.3. After confirmation of reaction completion, the cephalosporin *ntla* MO clicked product **31** was purified by HPLC using a 20 minute gradient of 5-50% acetonitrile in 0.1M triethylammonium acetate (TEAA) buffer as outlined in Section 4.3.4. The conjugated MO product elutes as a single, broad peak between 10-13 minutes. The purified MO fractions were pooled and lyophilized to dryness.

Cyclic cephalosporin *ntla* cMO (32). The purified cephalosporin *ntla* MO conjugate **31** was dissolved in water (150 µL) and diluted with 0.1 M Tris pH 8 buffer (150 µL). Immobilized TCEP slurry (200 µL) was pipetted into a Pierce spin cup filter and mixed with 0.1 M Tris pH 8 buffer (400 µL). The spin cup filter was centrifuged for 2 minutes at 2,000 rpm and the flow-

through was discarded. The immobilized TCEP resin was rinsed twice more with 0.1 M Tris pH 8 buffer (400 µL). Following the final rinse, the resuspended MO solution (300 µL) was added directly to the resin. The tube was inverted to mix and incubated at room temperature overnight. The next morning, the spin cup filter was centrifuged at 2,000 rpm for 2 minutes and a portion of the crude cyclization reaction mixture (2 µL) was co-spotted with sinapic acid (6 µL) and analyzed by MALDI-TOF MS (expected: 9384.29, observed: 9384.991) as outlined in Section 4.3.3. Following confirmation of reaction completion, the crude cyclization reaction was purified by HPLC following the protocol specified in Section 4.3.4. The cyclized cephalosporin *ntla* cMO elutes as a broad peak between 9-11 minutes. Fractions containing purified cMO were pooled and lyophilized to dryness overnight. The cMO was subject to additional purifications with NHS-activated agarose and SulfoLink resins to ensure complete removal on any linear MO impurities. Purifications are outlined in Sections 4.3.5 and 4.3.6, respectively.

Following the final, purification step the purified, dried cMO was resuspended in water (40 µL) and the concentration was determined by measuring absorbance at 265 nm on the NanoDrop following GeneTools recommended protocol. The purified cMO solution was diluted in 0.1 N HCl (1:10 and 1:5) and the concentration (ng/µL) of each solution was measured in triplicate as outlined in Section 4.3.2. The three measurements for each diluted solution were averaged and then multiplied by the corresponding dilution factor (10 or 5), and then averaged to determine the actual concentration of the MO solution (typically < 300 ng/µL). If needed, the MO was further diluted with milliQ water to a working concentration of ~ 150-200 ng/µL, and stored as 1-3 uL aliquots at –20 ºC.

1.5.1.5.2 Molecular and Cell Biology Protocols

Cleavage of the cephalosporin linker 23 *in vitro*. Linker **23** was prepared as a 5 mM stock in DMSO and stored at –20 ºC as 10 µL aliquots. In two separate reactions, an aliquot of linker **23** was thawed and diluted to 1 mM in 50 mM sodium phosphate buffer pH 8 (40 µL). Where indicated, recombinant β-lactamase enzyme (0.5 µL, 1 mg/mL) was added to the reaction and the reaction was incubated at 30 ºC. At the indicated time point (0.5, 1.5, 3, 17, 24 h) a 20 µL aliquot was removed from the reaction mixture and linker cleavage as assessed by on a Shimadzu LC-MS-2020 (ESI DUIT, 10 minutes, 100-1000 MHz, 5 µL injection volume) eluting with a gradient of 5-95% acetonitrile + 0.1% formic acid in water + 0.1% formic acid. Screenshots of the mass spectrum for each time point were exported and are presented in Figure 1-16.

Cloning of pCS2-HA-β-lactamase. The coding sequence of β-lactamase was obtained from the sequence specified for the pET15-Beta-Lactamase construct on Addgene (Plasmid #62729). The coding sequence of an HA tag was inserted upstream of the β-lactamase so that a proper detection handle was included in the sequence. The entire HA-β-lactamase coding sequence was codon optimized for humans using the IDT codon optimization tool.[115] This sequence was then ordered as a gene fragment from Twist Biosciences (San Francisco, CA) and the coding sequence is specified in Table 1-1 below. The gene fragment was used as a template for PCR amplification with primers P1 and P2 (see Table 1-1 for a list of primer sequences) in a standard Phusion PCR amplification (see Section 4.1.1). The amplicon was electrophoresed on an agarose gel and purified by gel extraction with the E.Z.N.A Gel Extraction kit (Omega BioTek, 101318-972). The pCS2+ vector was obtained from former lab member Dr. Jihe Liu. Both, the purified HA-β-lactamase amplicon and the pCS2+ vector, were restriction digested with BamHI and XhoI

(NEB) and purified by gel extraction. The HA-β-lactamase insert was then ligated into the pCS2+ vector using T4 DNA ligase (NEB) following the protocol in Section 4.1.3. Plasmid sequence was confirmed by Sanger sequencing (Genewiz) using the provided SP6 forward primer and M13-48REV sequencing primers.

Table 1-1: List of gene fragments and primers used for generating pCS2-HA-β-lactamase
Restriction site sequences are indicated in **bold.**

Primer	Sequence (5' → 3')
P1	ATATC**GGATCC**ATGGGTTCTAGCTATCC
P2	TGAAT**CTCGAG**TTACCAGTGCTTGATCAAG
human codon optimized HA-β-lactamase	ATGGGTTCTAGCTATCCGTATGATGTGCCTGACTACGCTA GTTCAGGTCTCGTACCGCGGGGCTCTCATGGTGGGGGTTC TGCTGCCGCCATGCACCCAGAGACACTGGTTAAGGTGAAG GACGCGGAAGATCAGCTTGGTGCCCGAGTGGGCTACATTG AACTTGATCTGAATTCCGGGAAGATCCTTGAAAGTTTCCGG CCGGAAGAAAGATTCCCGATGATGTCCACTTTCAAAGTACT TCTCTGTGGTGCCGTGCTGTCACGGATAGACGCCGGGCAGG AACAACTGGGCCGAAGAATTCATTATTCCCAGAATGATCTT GTCGAATACAGTCCGGTTACGGAGAAACATTTGACGGATGG TATGACGGTCCGAGAACTCTGTTCAGCCGCAATCACTATGAG TGATAACACTGCTGCTAACCTGCTTTTGACCACCATCGGGGGT CCCAAGGAGCTGACCGCTTTTCTTCATAACATGGGCGACCATG TCACACGACTCGACCGATGGGAGCCCGAGCTCAATGAAGCTAT CCCTAATGACGAACGAGATACCACAATGCCTGTGGCTATGGCT ACAACCCTCAGAAAGTTGCTGACCGGTGAGCTTCTCACGCTTG CGTCACGGCAACAGTTGATTGATTGGATGGAGGCCGACAAGG TAGCGGGTCCTTTGCTGCGATCTGCCTTGCCTGCGGGCTGGTT CATTGCGGATAAAAGCGGGGCTGGTGAGAGGGGATCACGAG GAATCATAGCCGCCCTTGGACCGGACGGAAAACCGAGCAGGA TTGTAGTCATCTACACTACAGGATCTCAAGCTACAATGGACGA GCGCAACAGGCAGATAGCCGAAATAGGCGCGAGCTTGATCAA GCACTGGTAA

Western blot analysis of HA-β-lactamase expression in cells. HEK293T cells were plated in a translucent, 12-well plate pre-treated with poly-D-lysine (MP Biomedicals, 1 mg/mL, see Section 4.2.2) at a cell density of 150k cells/well in DMEM supplemented with 10% fetal bovine serum (FBS) (1 mL/well) and incubated overnight. The next day, cells were transiently

transfected with pCS2-HA-β-lactamase (200 ng/well) using Lipofectamine 2000 as outlined in Section 4.2.3. The next morning, the transfection media (1.2 mL) was removed from cells and replaced with fresh DMEM containing 10% of FBS (1 mL). Cells were incubated an for additional 24 hours at 37 ºC. Three identical wells were transfected to ensure a sufficient amount of lysate would be obtained for western blot analysis.

The following day, media was removed, and cells were carefully rinsed with cold PBS (500 µL) so as to not lift any of the cells from the bottom of the well. While still on ice, chilled RIPA buffer supplemented with Halt protease inhibitor cocktail (150 µL, ThermoScientific 78429) was added to each well and the plate was shaken on ice at 4 ºC for 20 minutes. Lysate was removed from each well and cellular debris was pelleted by centrifugation at max speed at 4 ºC for 10 minutes. Following centrifugation, the supernatant was removed, and lysates were mixed with 4X Laemlli buffer supplemented with 10% β-mercaptoethanol (50 µL) (125 µL lysate and 40 µL buffer). Samples were incubated at 95 ºC for 10 minutes and stored at –20 ºC. Lysates (25 µL) were resolved on a 12% SDS-PAGE gel topped with a 4% stacking gel as outlined in Section 4.1.11. and the western blot was run according to the protocol outlined in Section 4.2.5. Following transfer, the membrane was cut using the molecular weight markers as guides, such that the protein of interest (in this case, HA-β-lactamase) and the loading control could be analyzed using the same membrane. The membrane was blocked for 2 hours in either 5% [w/v] non-fat milk in TBST (0.1% Tween-20 in TBS) or 5% BSA [w/v] in TBST blocking buffers. The choice of blocking buffer was dependent on the manufacturer's specific recommendation for the primary antibody. The membrane was probed with either an anti-HA antibody (CST, 3724S) diluted 1:1000 in 5% [w/v] BSA (protein-of-interest) or an anti-β-tubulin antibody (ProteinTech 10068-1-AP) diluted 1:4000 in 5% [w/v] non-fat milk in TBST. Primary antibodies were incubated at 4 ºC overnight while

rocking. The following morning, membranes were washed with TBST and the membrane was probed with the HRP-linked goat anti-rabbit IgG secondary antibody (ProteinTech, SA00001-2) diluted 1:5000 in TBST for 90 minutes at room temperature. Following incubation, the secondary antibody was removed, the membrane was rinsed with TBST, and the blots were developed with SuperSignal West Pico PLUS Chemiluminescent Substrate (ThermoScientific, 34580) for 5 minutes, and imaged following the protocol outlined in Section 4.2.5.

Nitrocefin assay. Nitrocefin (**35**) was obtained as a solid stock from Sigma. Nitrocefin (5 mg) was dissolved in 194 µL sterile-filtered DMSO to generate a 50 mM DMSO stock. The stock was stored as 10 µL aliquots at –80 ºC. For activation with recombinant β-lactamase enzyme (Novus Biologicals), nitrocefin (10 µL from 50 mM stock in DMSO) was diluted in 50 mM sodium phosphate buffer (490 µL) to a final concentration of 1 mM. The nitrocefin solution (50 µL) was pipetted into a transparent 96-well plate. Where indicated, recombinant β-lactamase enzyme (0.5 µL, 1 mg/mL) was added to the nitrocefin solution. Absorbance was measured at 390 nm (absorbance maxima for nitrocefin) and 486 nm (absorbance maxima for hydrolyzed product) every 2 minutes for 30 minutes on a Tecan M1000 plate reader. The raw absorbance values were plotted as a function of time in PRISM.

For activation by enzyme that was expressed in cells, HEK293T cells (40k/well) were plated in a white, 96-well plate pre-treated with poly-D-lysine in DMEM containing 10% FBS (100 µL) and incubated overnight at 37 ºC. The next day, cells were transiently transfected with pCS2-HA-β-lactamase (100 ng) using Lipofectamine 2000 according to the protocol outlined in Section 4.2.3. The next morning, the transfection media (150 µL) was removed and replaced with fresh DMEM (10% FBS). Cells were incubated for an additional 24 hours. Following incubation, the media was removed, and cells were rinsed with PBS (500 µL). Passive lysis buffer (500 µL,

5X, Promega E1941) was diluted to 1X in milliQ water (2 mL) and 20 µL was added to each well. The cells were lysed at room temperature while shaking for 20 minutes. Following lysis, 50 mM sodium phosphate buffer was added to the lysed cells (30 µL) to a final volume of 50 µL. Nitrocefin (50 µL, 1 mM in 50 mM sodium phosphate buffer) was added and the reaction mixtures were incubated at room temperature for 2 minutes. Absorbance at 390 nm and 486 nm was measured on the TECAN M1000 plate reader.

1.5.1.5.3 Zebrafish Protocols

Zebrafish aquaculture, breeding, and embryo microinjection are outlined in Section 4.4. Embryos from the natural mating of wild-type adult AB* zebrafish were collected and used for all injections.

HA-β-lactamase mRNA microinjections. The HA-β-lactamase mRNA injection solution was prepared such that the final desired amount of mRNA could be attained following a 2 nL injection. Zebrafish embryos (n = 40) at the 1- to 2-cell stage were injected in the yolk with HA-β-lactamase mRNA (2 nL). The injection solution was prepared Following injection, embryos were incubated at 29 ºC until 24 hpf.

Nitrocefin assay with zebrafish embryos lysate. mRNA injected embryos were removed from the incubator at 24 hpf and transferred to 35 mm petri dishes. The embryos were manually dechorionated using forceps, anesthetized with tricaine in E3 water (2.5 mL), and imaged on the Leica MZ16 stereoscope following the imaging protocol outlined in Section 4.4.4. Embryos were pooled and transferred to Eppendorf tubes (n = 41 embryos/tube). Excess E3 water was removed by careful pipetting. Embryos were centrifuged at 5k rpm at 4 ºC for 5 minutes an excess E3 water

was removed by pipetting and discarded. Embryos were resuspended in passive lysis buffer (100 µL, Promega E1941) and lysed following the protocol specified in Section 4.4.5. Embryos were homogenized for 60 seconds on ice and then centrifuged at 5k rpm for 2 min at 4 ºC.

Nitrocefin (10 µL, 50 mM) was diluted to 2 mM in 50 mM sodium phosphate buffer (240 µL) and pipetted into a white, 384-well plate (15 µL). An equal volume of either buffer (negative control reaction) or embryo lysate (15 µL) was added to each well for a final nitrocefin concentration of 1 mM (30 µL total volume). The absorbance at 390 nm and 486 nm was measured every 2 minutes for 60 minutes, and then every 5 minutes until 90 minutes on the Tecan M1000 plate reader. The raw absorbance values were plotted as a function of time in PRISM. Initial velocity rates were calculated by performing a linear regression analysis of the absorbance values measured between 0 and 10 minutes. The slope of the line corresponds to the initial velocity as AU/min. All R^2 values were between 0.96-0.99 indicating a good linear fit.

Western blot analysis of zebrafish embryo lysate. Zebrafish embryos at the 1- to 4-cell stage were injected with 400 pg HA-β-lactamase mRNA. Embryos were incubated to 24 hpf at 29 ºC. At 24 hpf, embryos were pooled into batches of 100 and manually dechorionated using forceps. Embryos were deyolked on ice in embryo deyolking buffer by vigorous pipetting with a P1000 tip until the solution was milky white in color. Embryos were centrifuged at max speed at 4 ºC for 10 minutes, resulting in a relatively big, light brown pellet. Supernatant was discarded. The pellet was washed with deyolking buffer on ice and centrifuged again. The wash was discarded. The pellet was resuspended in lysis buffer (~ 2 µL per embryo, 20 mM Tris, 150 mM NaCl, 1 mM EDTA, 1 mM EGTA, 1% Triton X-100) on ice by vigorous pipetting. Once resuspended, the deyolked embryos were lysed by homogenization using Pellet Pestel Cordless Motor (Fisher 12-141-361) equipped with an RNase-free disposable pellet pestle (Fisher 12-141-364). Embryos were

homogenized on ice for 2 minutes. Once fully homogenized, the lysates were centrifuged at max speed for 10 minutes at 4 ºC. Protein concentration of embryo lysates was determined via a Bradford assay. *Note: in the course of this work, a more efficient lysis protocol was optimized (see Section 4.4.6) and is the preferred lysis protocol for analyzing embryo lysates by western blot.*

Samples (50 µg) were resolved on a 12% SDS-PAGE gel topped with a 4% stacking gel run at 60V for 20 minutes and then increased to 180V for 60 minutes. Lysates were analyzed by western blot following the protocol outlined in Section 4.2.5. The membrane was probed with either an anti-HA antibody (CST, 2367S) diluted 1:1000 in 5% [w/v] non-fat milk (protein of interest) or an anti-GAPDH antibody (ProteinTech 60004-1-Ig) diluted 1:8000 in 5% [w/v] non-fat milk in TBST. Primary antibodies were incubated at 4 ºC overnight while rocking. The following morning, the membranes were washed with TBST and then the membrane was probed with the HRP-linked goat anti-mouse IgG secondary antibody (ProteinTech, SA00001-1) diluted 1:2500 in TBST for 90 minutes at room temperature. Following incubation, the secondary antibody was removed, and the membrane was rinsed with TBST. The blot(s) were developed and imaged following the protocol outlined in Section 4.2.5.

β-lactamase-mediated cMO activation. MO and cMO solutions were diluted to either 150 pg/nL (control MO and *ntla* MO, stored at room temperature) or 100 pg/nL (cephalosporin *ntla* cMO **32**, aliquot stored at –20 ºC was thawed) in water. MO solutions were heated to 65 ºC for 90 seconds to dissociate MO aggregates. Where indicated, injection solutions were diluted with HA-β-lactamase mRNA (stock ~ 1 µg/nL) to a final concentration of 200 pg/nL (co-injection with the control and *ntla* MO) or 133 pg/nL (co-injection with cephalosporin cMO). The final volume of all injection solutions was 3-5 µL. Phenol red was added to a final concentration of 0.05% in each solution and used as a tracer dye for embryo injections. Embryos at the 1-to 4-cell stage were

injected with either 2 nL (control and *ntla* MO) or 3 nL (cephalosporin cMO **32**) in the yolk directly under the blastomere following the microinjection protocol specified in Section 4.4.3. Unfertilized embryos were removed at 3 hpf. All other zebrafish embryos were incubated at 29 ºC until 24 hpf for phenotypic analysis and imaging as specified in Section 4.4.4.

1.5.2 TEV Protease Activatable cMO

The Tobacco etch virus nuclear-inclusion-a endopeptidase (TEVp) is a 27 kDa protease encoded by the Tobacco Etch Virus, a single stranded RNA plant virus.[116] TEVp is structurally homologous to cellular serine-type proteases, such as trypsin or chymotrypsin. However, unlike serine-type proteases which utilize serine as a catalytic nucleophile, TEVp contains a nucleophilic cysteine as its catalytic nucleophile.[117, 118] TEVp recognizes a specific, 7 amino acid peptide consensus sequence ExxYxQ-(S/G) (labeled P6 to P1/P1') and catalyzes hydrolysis of the peptide bond between the Q/S or Q/G residues. The amino acids at the P6, P3, P1, and P1' positions are necessary for recognition and cleavage by the protease.[119] All other residues merely dictate the rate of catalytic activity.[120, 121]

One of the most popular applications of TEVp has been towards the production and purification of recombinant proteins.[120] Often, affinity or epitope tags are engineered onto the termini of the protein of interest to aid in monitoring or purifying recombinant proteins. However, in some cases the tag may impact protein folding or activity. Enzymatic removal with TEVp has remained a particularly appealing method for affinity tag removal as the protease maintains its specific, proteolytic activity under various buffering conditions, pH, and temperatures.[120] While already a very efficient protease, TEVp has also served as a model protease for directed evolution approaches to engineer site-specific proteases to recognize and cleave alternative consensus

sequences.[122-124] These systems seek to build highly specific proteases with enhanced and tunable catalytic efficiency to build a broadly applicable platform that can be used to modulate the activity of a desired protein target. Additionally, TEVp has also been engineered as a split-enzyme system to assay protein-protein interactions in cells.[125, 126]

While much of the research surrounding TEVp has remained focused on optimizing protein expression, solubility, and stability as it applies to bacterial systems,[127-129] there have been limited reports of TEVp utilized in model organisms. Previously, TEVp has been applied in *Drosophila* as a method for manipulating protein function.[130, 131] Using fruit flies engineered to conditionally express TEVp, Harder *et. al.* demonstrate TEVp-mediated inactivation of protein function *in vivo* through site-specific cleavage of engineered targets containing the TEVp consensus sequence.[130] Furthermore, there were no detrimental developmental effects or toxicity in the transgenic flies engineered to conditionally express TEVp using tissue-specific or inducible promoters, suggesting the protein is both safe to the organism and there are no proteins susceptible to TEVp cleavage within the *Drosophila* proteome. TEVp-induced protein inactivation has been applied by Pauli *et al.* in investigations into the role of the protein complex cohesin within post-mitotic neuronal cells in *Drosophila.*[131] Based on the successful expression and activity of TEVp in a live model organism, and its orthogonality to the *Drosophila* proteome, it was concluded that this highly specific protease could serve as a potentially useful orthogonal enzymatic trigger for cMO activation in live zebrafish embryos.

1.5.2.1 Synthesis of TEV Protease-activated cMO

Towards developing a TEVp-activatable cyclic cMO, we designed a peptide-based linker containing the TEVp consensus cleavage site equipped with two reactive handles for conjugation the terminal ends of the modified MO oligomer (Figure 1-20). The canonical recognition sequence

that is most efficiently cleaved by TEVp is ENLYFQ(S/G).[121, 132, 133] We used microwave-assisted Fmoc-based solid phase peptide synthesis to prepare cMO linker **37**. The peptide-based cMO linker was designed to contain a C-terminal azido-modified lysine residue, for click conjugation to the alkyne-modified MO **28** (used previously in the preparation of the β-lactamase-activatable cyclic cMO), and an N-terminal chloroacetamide for conjugation to the 3'-thiol on the MO. A beta-alanine spacer was incorporated between glycine (G) and the azido-lysine in an attempt to circumvent any steric interference by the MO that could restrict accessibility of the enzyme to the cleavage site.

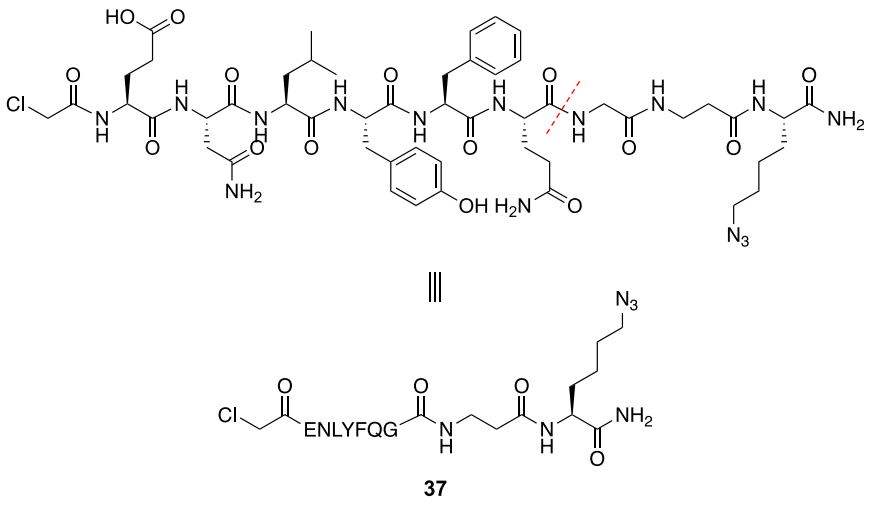

Figure 1-20: Structure of the TEV-cleavable cMO linker 37
TEV protease preferentially hydrolyzes the peptide bond between Q and G in the consensus sequence (represented by a red dashed line).

Prior to macrocyclization of the MO, we first validated cleavage of the linker *in vitro*. The linker **37** (100 µg) was incubated with recombinant TEV protease (1 µg, BioVision) and cleavage of the peptide was monitored by HPLC (Figure 1-21). Peaks were collected and analyzed by MALDI-TOF mass spectrometry. Nearly full disappearance of the peptide linker **37** was observed after 30 minutes at 37 ºC and formation of the expected, cleaved peptide fragment was confirmed.

Taken together, these results validate that our linker is cleaved by TEVp and follows the anticipated enzymatic mechanism.

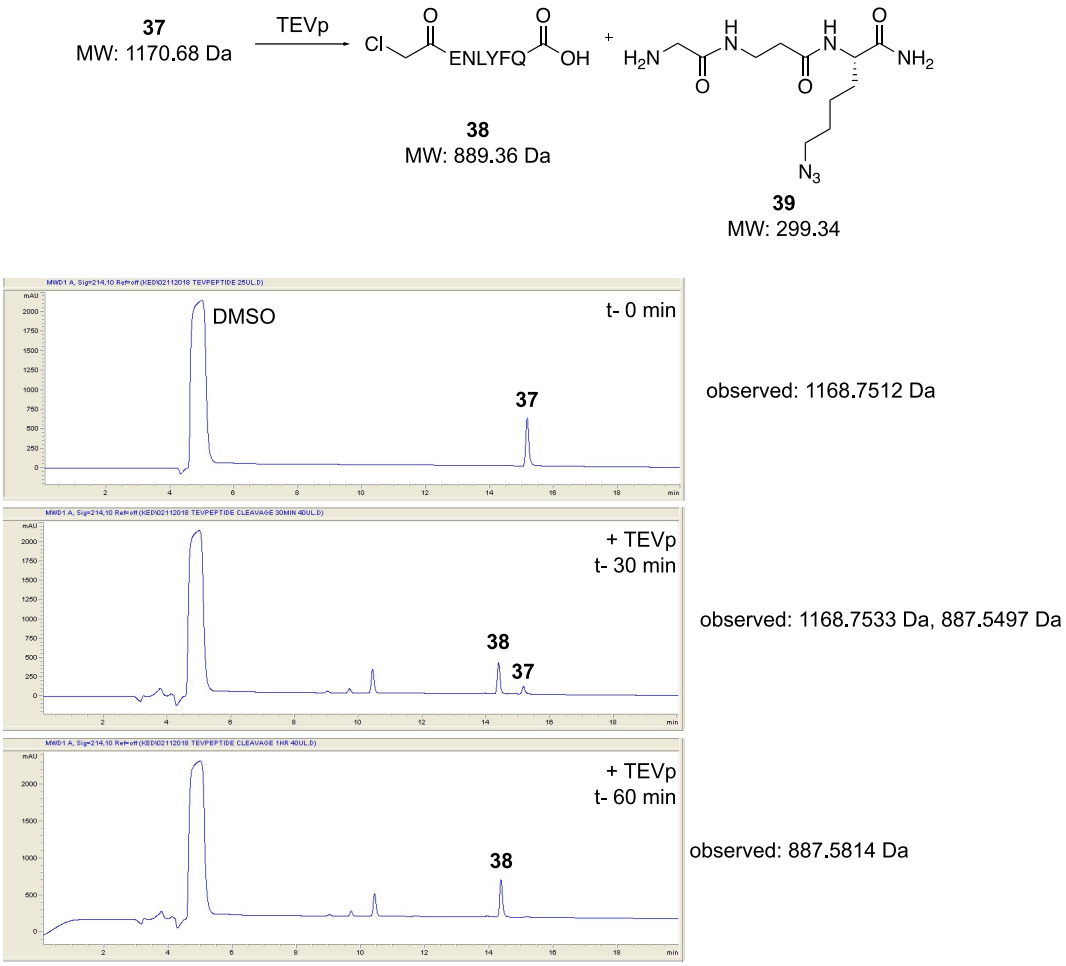

Figure 1-21: HPLC studies of TEVp cMO linker cleavage *in vitro*

The peptide-based linker **37** was then conjugated to the terminal ends of the modified *ntla* MO to generate a TEVp-activatable cyclic cMO (Figure 1-22). Using alkyne-modified *ntla* MO **28**, the C-terminal azido-lysine was clicked onto the terminal alkyne of the MO via a CuAAC reaction following the same protocol that was successful in the preparation of the β-lactamase cyclic cMO.[106] The peptide-MO conjugate **40** was then incubated with resin-immobilized TCEP to generate the free 3'-thiol. Reaction of the free thiol with the N-terminal chloroacetamide on the

peptide cMO linker **37** induces macrocyclization of the MO, generating the cyclic TEVp-activatable cMO product, **41**.

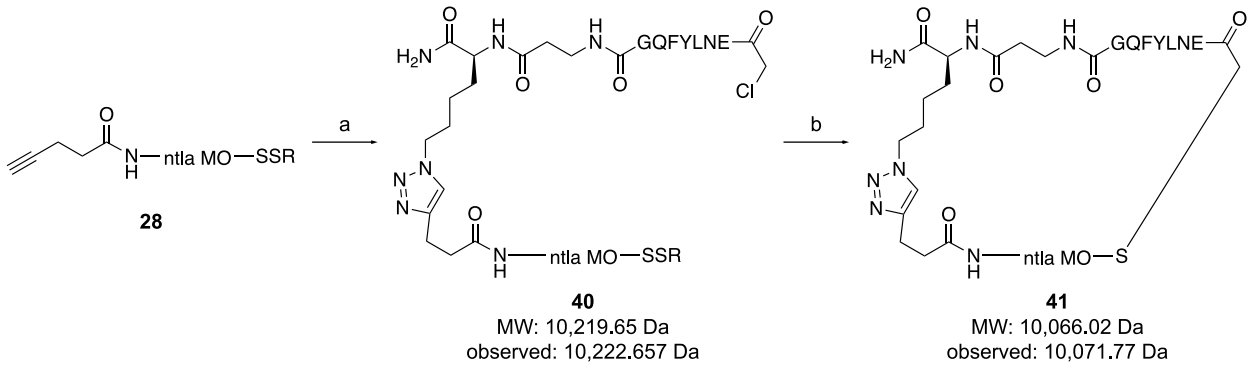

Figure 1-22: Synthesis of *ntla*-TEV cyclic cMO
Reagents and conditions: a) **37**, Cu(II)-TBTA, sodium ascorbate, 10% DMSO, H_2O; b) resin immobilized TCEP, 0.1 M Tris pH 8.5 buffer.

1.5.2.2 Evaluation of TEV Protease Expression and Activity

In an effort to validate TEVp expression and function in live zebrafish embryos, we next cloned a TEVp expression construct. The coding sequence for TEVp was PCR amplified from a mammalian expression plasmid pCI-TEVp from Dr. Kalyn Brown using primers P3 and P4 was ligated into the 5'-BamHI and 3'-EcoRI restriction sites of the pCS2+ backbone. To ensure maximal efficiency of the enzyme, we utilized the TEVp S219V mutant which prevents autolytic deactivation of the enzyme.[134, 135] To allow for detection of TEVp expression by western blot, PCS2-TEVp-HA was cloned concurrently. The coding sequence of TEVp-HA was PCR amplified from mammalian expression plasmid pCI-TEVp-HA from fellow lab member Dr. Jihe Liu using primers P5 and P6 and ligated into the 5'-BamHI and 3'-EcoRI restriction sites of the pCS2+ backbone.

Prior to translation into zebrafish, these TEVp expression vectors were then used to evaluate TEVp expression and function in mammalian cell culture. Western blot analysis of lysates

from HEK293T cells transfected with pCS2-TEVp-HA confirmed TEVp-HA expression via probing with an anti-HA antibody, indicating efficient expression from the pCS2+ construct (Figure 1-23A). To evaluate whether the expressed protein retains proteolytic activity, we utilized a TEVp-GloSensor assay (Promega). GloSensor is a circularly permuted luciferase, in which a TEVp cut site is engineered between the N- and C-termini of luciferase. Cleavage of the cut site by TEVp induces a conformational shift and a large increase in luminescence that directly correlates with proteolytic activity (Figure 1-23B). In HEK293T cells transfected with pTriEx-GloSensor (from Dr. Kalyn Brown) and either pCS2-TEVp or pCS2-TEVp-HA a nearly 3-fold increase in luminescence was observed (Figure 1-23C), indicating that the TEVp that is expressed from either construct is functional. Further, luminescent signal remains low in cells transfected with pTriEx-GloSensor alone, or co-transfected with catalytically dead TEVp mutant pCI-TEVp-Y175F-C152A (from Dr. Jihe Liu), indicating the increase in luminescence observed is solely the result of a catalytically active TEVp enzyme.

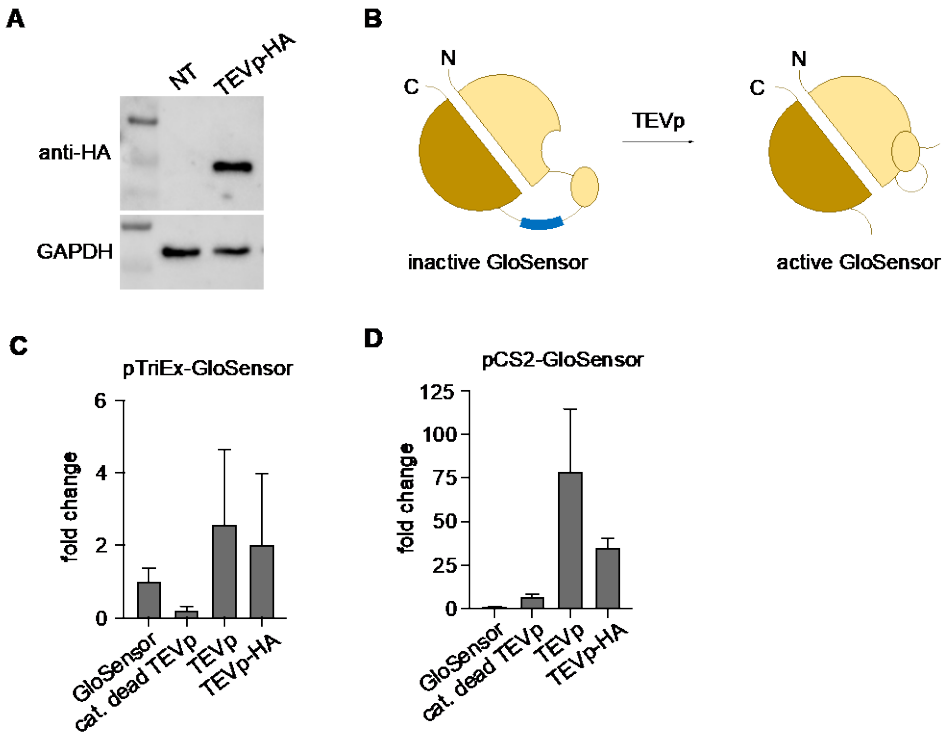

Figure 1-23: Evaluation of TEVp expression and activity in cells
A) Western blot analysis of TEVp expression in HEK293T cells. B) Schematic of GloSensor activation by TEVp. C and D) Evaluation of TEVp activity in HEK293T cells transfected with the indicated TEVp plasmid and either pTriEx-GloSensor (C) or PCS2-Glosensor (D). Error bars represent standard deviations from the average of three independent experiments.

In order to make the GloSensor assay amenable to zebrafish studies, the coding sequence of GloSensor was PCR amplified from pTriEx-GloSensor using primers P7 and P8 and was ligated into the 5'-BamHI and 3'-EcoRI restriction sites of the pCS2+ backbone. To confirm that expression from the pCS2+ vector would not interfere with the sensor activation, the assay was repeated using pCS2-GloSensor. Gratifyingly, a 75-fold increase was observed in cells co-transfected with pCS2-TEVp and a nearly 50-fold increase was observed in cells co-transfected with pCS2-TEVp-HA (Figure 1-23D). We speculate that the inconsistencies between assays are primarily a result of transfection efficiency, however, it cannot be ruled out that GloSensor may be expressed more efficiently from the pCS2+ vector than from the pTriEx vector. Regardless, these results indicate pCS2-TEVp and pCS2-TEVp-HA express a functional enzyme.

In order to overexpress TEVp in zebrafish embryos, synthetic mRNA expressing TEVp-HA was prepared via *in vitro* transcription. Zebrafish embryos were injected with the TEVp-HA mRNA (400 pg) and cultured to 24 hpf, at which point they were lysed. Lysates were analyzed for TEVp expression via an anti-HA western blot (Figure 1-24A). Unfortunately, no HA-tagged proteins were detected in lysates from injected embryos. To rule out any potential issues with the mRNA stock, the expression of the synthetic mRNA stock was tested using a rabbit reticulocyte *in vitro* translation kit (Promega) and the lysate was analyzed by western blot (Figure 1-24B). Gratifyingly, the HA-tagged TEVp was detected in the lysate system, suggesting the TEVp-HA mRNA is translationally competent. To determine if the observed lack of TEVp expression was due to an inherent flaw during embryo lysis or the western blot procedure, TEVp activity was assayed using the GloSensor assay. Synthetic mRNA expressing GloSensor (200 pg) was co-injected with increasing amounts of TEVp mRNA (50 – 600 pg). Embryos were incubated to 24 hpf, lysed, and then luminescence was measured (Figure 1-24C). Unfortunately, no increase in luminescence was observed with any amount of mRNA injection, corroborating results observed by western blot. Furthermore, zebrafish injected with synthetic mRNA expressing firefly luciferase exhibited raw luminescence values orders of magnitude higher than those observed with the GloSensor assay (data not shown), suggesting the GloSensor may also not be reliably expressed in embryos.

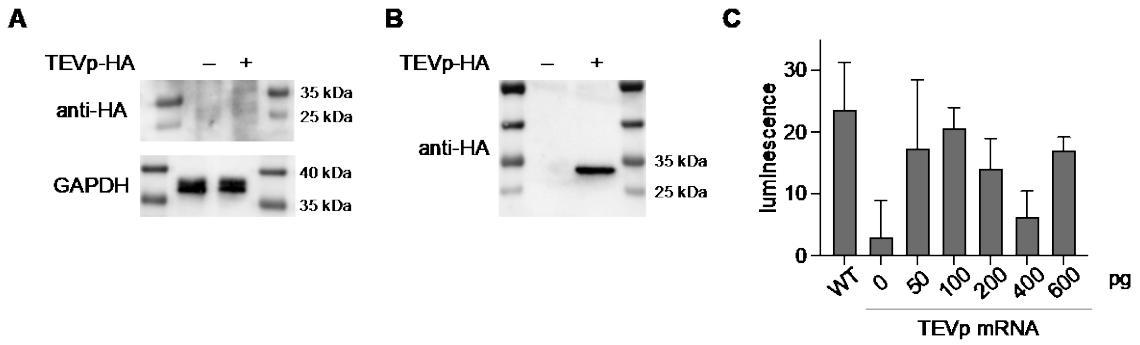

Figure 1-24: Evaluation of TEVp expression *in vivo*
A) Western blot analysis of 24 hpf zebrafish lysates for TEVp-HA (MW: 29 kDa) expression. B) Western blot analysis of TEVp-HA expression in a rabbit reticulocyte in vitro translation lysate system. C) GloSensor assay in zebrafish embryos. Error bars represent standard deviations from the average of three independent experiments (n = 15 embryos/condition).

In efforts to troubleshoot TEVp expression *in vivo*, we cloned a fluorescent TEVp fusion construct. Using this construct, TEVp expression can be monitored by fluorescence imaging which can give more insight as to whether the TEVp is being expressed and/or rapidly degraded in the developing zebrafish environment. Taking guidance from the nitroreductase-activatable cMO report,[81] a TEVp-mCherry construct was designed in which the mCherry was cloned directly onto the C-terminus of TEVp. The pCS2-TEVp-mCherry construct was constructed by Gibson assembly of pCS2-TEVp (using primers P9 and P10) and mCherry (amplified from pmCherry-N1 (from Dr. Taylor Courtney) using primers P11 and P12). Concurrently, a construct containing a self-cleavable P2A linker between TEVp and mCherry was also cloned (pCS2-TEVp-P2A-mCherry) to ensure direct fusion of mCherry would not interfere with TEVp activity, while still remaining an indicator of protein expression.[136] The construct pCS2-TEVp-P2A-mCherry was generated through Gibson assembly of pCS2-TEVp (using primers P13 and P14) and P2A-mCherry (amplified from pUb-K-EGFP-P2A-mCherry from fellow lab member Amy Ryan, using primers P15 and P16).

The expression and activity of the mCherry-tagged TEVp constructs was first evaluated in mammalian cell culture. HEK293T cells were transfected with either mCherry, pCS2-TEVp-mCherry, or pCS2-TEVp-P2A-mCherry followed by fluorescence imaging, and the corresponding lysates were analyzed for expression by western blot with an anti-mCherry antibody (Figure 1-25A). While efficient expression of mCherry and TEVp-mCherry constructs were observed, a very faint signal consistent with mCherry was observed in lysates transfected with pCS2-TEVp-P2A-mCherry, suggesting expression may not be as efficient. Additionally, the expression of these constructs was validated by fluorescence imaging (Figure 1-25B). Next, the proteolytic activity of each construct was evaluated using the GloSensor system previously described (Figure 1-25C). Despite the diminished expression observed by western blot and fluorescence imaging, both TEVp-mCherry and TEVp-P2A-mCherry exhibited comparable activity to that of wild type TEVp in the GloSensor assay indicating proteolytic activity is unaffected by either the direct fusion of the fluorescent protein or the fusion through the self-cleavable P2A linker.

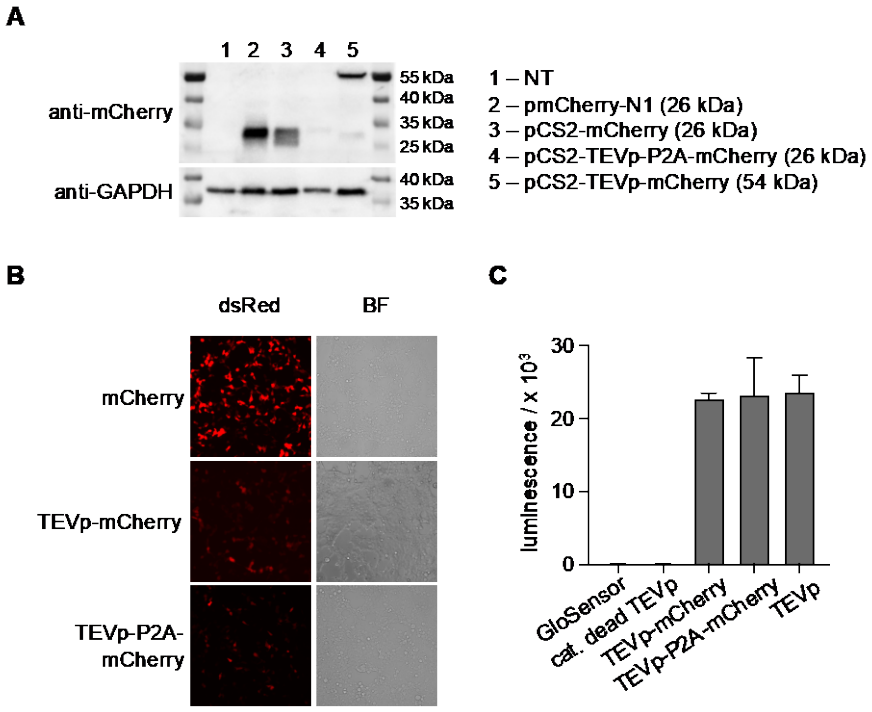

Figure 1-25: Evaluation of TEVp-mCherry constructs in cells
A) Western blot analysis of TEVp-mCherry and TEVp-P2A-mCherry expression in HEK293T cell lysates probed with an anti-mCherry antibody. B) Flurorescence imaging of HEK293T cells transfected with the indicated TEVp-mCherry expression construct. C) Evaluation of TEVp proteolytic activity as monitored through luminescence activation of GloSensor. Error bars represent standard deviations from the average of three independent experiments.

With promising results of TEVp expression and proteolytic activity in cells, we next evaluated these constructs in zebrafish embryos. In order to obtain optimal expression in embryos, the coding sequence of TEVp-mCherry was codon optimized for *Danio rerio*. The codon optimized sequence was ordered as gene fragment (Twist) and cloned into the BstBI and XhoI sites of the pCS2+ vector using P17 and P18. Synthetic mRNAs expressing codon-optimized TEVp-mCherry and the TEVp-P2A-mCherry constructs were prepared by *in vitro* transcription. The mRNAs were microinjected into 1-cell stage zebrafish embryos and protein expression was monitored through fluorescence imaging (Figure 1-26A-B). Unfortunately, no mCherry fluorescence was observed at any of the time points imaged (2-26 hours post-injection, hpi). Injected embryos were lysed and were probed with an anti-mCherry antibody via western blot

(Figure 1-26C). Consistent with the fluorescence imaging results, a very faint signal was detected in TEVp-mCherry and TEVp-P2A-mCherry mRNA injected embryos. However, it is obvious the TEVp fusions were not as efficiently expressed as the mCherry construct. To rule out any potential issues regarding translation of the mRNA stock, the expression of the codon optimized TEVp-mCherry was assessed using the rabbit reticulocyte *in vitro* translation system (Figure 1-26D). Codon optimized TEVp-mCherry was detected via western blot suggesting the mRNA is translationally competent. We hypothesize that the lack of protein expression observed with TEVp is potentially due to an inherent issue with the TEVp coding sequence that either prevents expression exclusively in the zebrafish embryonic environment or signals non-specific degradation of the mRNA template before TEVp can be translated.

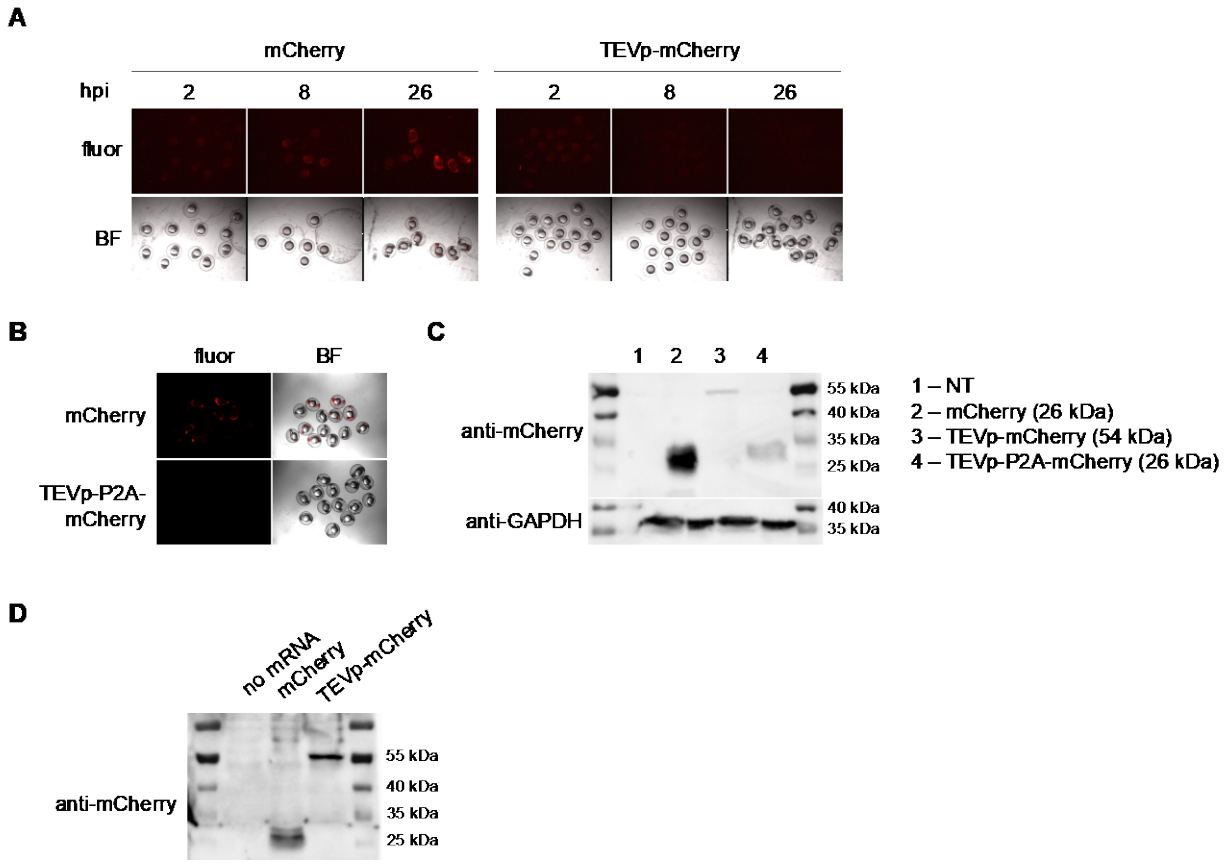

Figure 1-26: Evaluation of TEVp-mCherry constructs in zebrafish embryos
A) Fluorescence imaging of zebrafish embryos injected with codon optimized TEVp-mCherry at varying stages of embryonic development. B) Representative images of zebrafish embryos injected with TEVp-P2A-mCherry mRNA at 24 hpf. C) Western blot analysis of lysed zebrafish embryos injected with the indicated fluorescent fusion TEVp construct. D) Western blot analysis of codon optimized TEVp-mCherry translated using a lysate-based *in vitro* translation system.

1.5.2.3 Development of a GFP-based Fluorogenic TEVp Sensor

Although the GloSensor system served as an efficient means to measure TEVp proteolytic activity in mammalian cells, these results did not directly translate when the luminescent reporter system was modified for use in zebrafish embryos. Based on the poor *in vivo* results with GloSensor and the overall lack of appropriate tools to survey TEVp activity *in vivo*, we sought to develop a fluorogenic GFP-based sensor to monitor TEVp activity. Previously, Shu *et. al.* demonstrated the utility of a fluorogenic GFP sensor to assay protease activity in mammalian cell

culture and live zebrafish embryos.[137] Their design, dubbed ZipGFP, entails a modified split GFP reporter engineered with heterodimerizing coiled coils connected via a TEV peptide linker. The "zipping" of the coiled coils inhibit assembly of the split GFP, preventing chromophore maturation, and fluorescence activation (Figure 1-27A). Upon TEVp-mediated cleavage, the coiled coils are "unzipped" and permit self-assembly, resulting in a 10-fold increase in GFP fluorescence when applied in cells (Figure 1-27B). Although initial proof-of-concept studies with this fluorogenic sensor were performed using TEVp as the activating enzyme, the authors never utilized this sensor in studying TEVp activity in developing zebrafish embryos. Instead, the recognition sequence was altered to monitor executioner caspase activity and the induction of apoptosis in mammalian cell culture and developing zebrafish embryos.

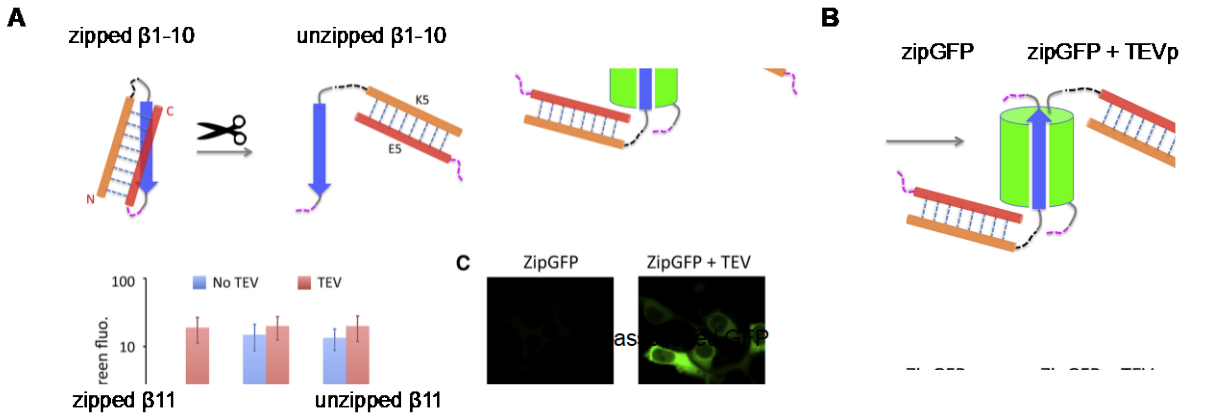

Figure 1-27: Fluorogenic zipGFP TEVp sensor
A) Cartoon schematic of zipGFP TEV sensor. A split GFP protein consisting of β-strands 1-10 and 11 were "zipped" with heterodimeric coiled coils attached via a TEV peptide cleavable linker. Following TEVp-mediated cleavage, the coiled coils are cleaved and permit self assembly of the split GFP system, resulting in increased GFP fluorescence. B) HEK293T cells co-transfected with plasmids expressing zipped β-strands 1-10, zipped β-strand 11, and TEVp exhibit a significant increase in GFP fluorescence as a result of sensor activation. Figure was adapted from Shu et. al., *Cell Chem. Biol*., **2016**, 23(7), 875.[137]

Based on the previous success of using a fluorogenic GFP-based sensor to study protease activity in developing zebrafish embryos, we designed our own GFP-based fluorogenic sensor

modeling the design off of a second, previously reported caspase sensor.[138] Unlike ZipGFP, the sensor utilizes a one-protein and thus one-plasmid system in which a 27 amino acid peptide derived from the proton channel domain of the influenza M2 protein was linked to the C-terminus of GFP through a consensus caspase cut site.[139] We adapted this design to include a TEVp cleavage site between GFP and the peptide. In the absence of TEVp, the peptide quenches fluorescence of GFP by inhibiting chromophore maturation and the sensor remains dark. Following TEVp-mediated hydrolysis of the peptide linker, the peptide is released and GFP fluorescence is restored (Figure 1-28A). The TEVp activatable GFP sensor (TEVa-GFP) was constructed by replacing the caspase recognition peptide sequence in the reported sensor (DEVD) with the TEVp consensus peptide sequence (ENLYFQG). The cleavage site was replaced by Gibson assembly using primers P19 and P20, generating the sensor pmKate-2-C-TEVa-GFP.

With sensor in hand, we next validated activation in mammalian cells. HEK293T cells were transfected with pmKate-2-C-TEVa-GFP alone or co-transfected with sensor and a TEVp expression construct (pCS2-TEVp or pCS2-TEVp-HA). Cells were incubated overnight, and sensor activation was assessed through fluorescence imaging (Figure 1-28B). Gratifyingly, a significant increase in GFP fluorescence is observed following co-transfection with pCS2-TEVp or pCS2-TEVp-HA. Further, in the absence of TEVp, background fluorescence remains minimal which is encouraging since the length of the peptide linker is slightly elongated due to the difference in lengths between the caspase peptide recognition sequence (4-mer) and the TEVp peptide recognition sequence (7-mer). This indicates the quenching peptide can efficiently quench GFP fluorescence regardless of the added flexibility in the peptide linker.

In order to make the sensor amenable for studying TEVp activity in zebrafish embryos, the TEVa-GFP sensor was cloned into the pCS2+ vector. The TEVa-GFP coding sequence was PCR

amplified using primers P21 and P22 and ligated into the BamHI and EcoRI sites of the pCS2+ vector. To ensure the sensor functions efficiently when expressed from the pCS2+ backbone, sensor activation was assessed in HEK293T cells transfected with pCS2-TEVa-GFP alone or co-transfected with a TEVp expression construct (Figure 1-28C). As expected, the extent of activation is analogous to that observed with the native, reported plasmid backbone. A significant increase in GFP fluorescence is observed only in cells that were co-transfected with pCS2-TEVp or pCS2-TEVp-HA, while cells transfected with pCS2-TEVa-GFP alone exhibit minimal GFP fluorescence.

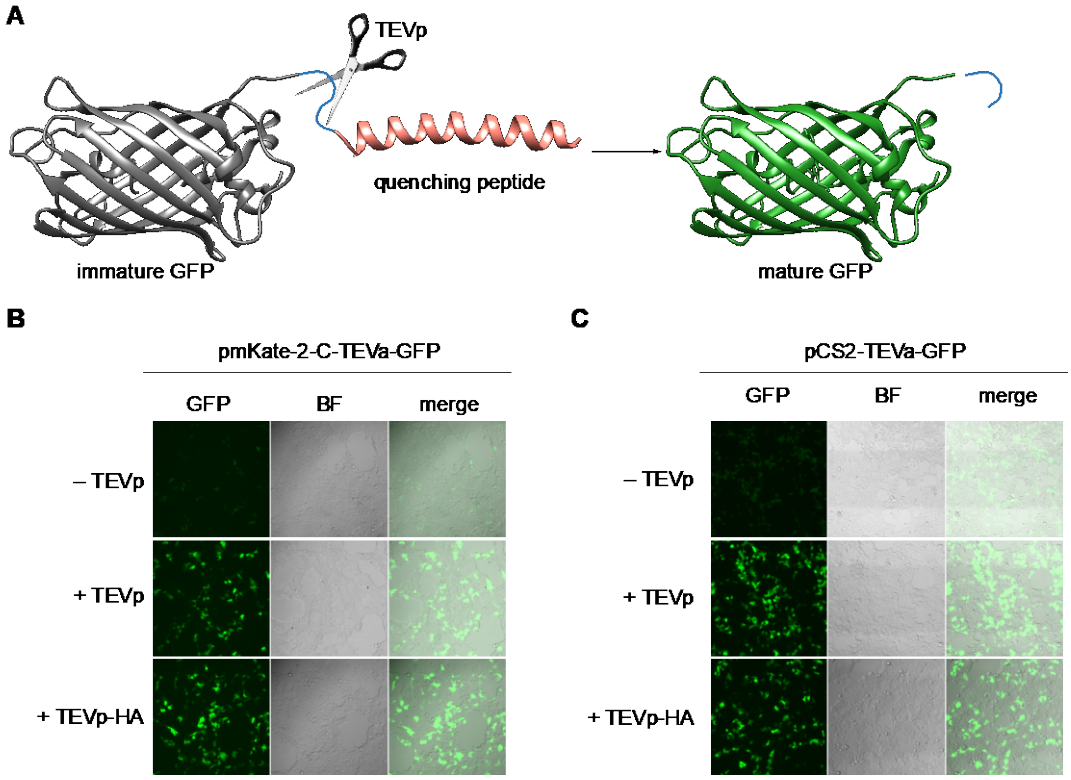

Figure 1-28: Development of a fluorogenic GFP-based TEVp sensor
A) Schematic of the protein-based fluorogenic GFP sensor, TEVa-GFP. Direct fusion of a quenching peptide to the C-terminus of GFP via a TEV peptide linker inhibits chromophore maturation and GFP fluorescence until TEVp-mediated cleavage of the TEV linker removes the quenching peptide and restores GFP fluorescence. B and C) Evaluation of the TEVa-GFP in HEK293T cells. Cells were transfected with either pmKate-2-C-TEVa-GFP (B) or pCS2-TEVa-GFP (C) alone or in the presence of a TEVp expression construct.

With promising results of the sensor in mammalian cell culture, we next sought to assess the utility of the TEVa-GFP sensor in live zebrafish embryos. Synthetic mRNA expressing the TEVa-GFP sensor was prepared through *in vitro* transcription of the pCS2-TEVa-GFP construct. Although no translation of the various TEVp mRNAs was observed by western blot analysis and fluorescence imaging of zebrafish embryos, we first attempted to evaluate sensor activation in zebrafish embryos through co-injection of the sensor mRNA with TEVp mRNA. Unfortunately, no GFP fluorescence was observed in any of the embryos (Figure 1-29A), possibly due to a lack of sensor expression, confirming our previous results. Since the issues regarding TEVp expression in zebrafish embryos may be inherent to the stability or translation of the mRNA transcript, we sought to circumvent expression by co-injecting the recombinant TEVp protein (BioVision) into zebrafish embryos. We performed injection with increasing amounts of recombinant TEVp and followed sensor activation at various time points during development (Figure 1-29B). Following co-injection of 1 ng of TEVp, the maximal amount that could be attained given the concentration of the recombinant protein stock, unfortunately, no sensor activation in embryos was observed. The integrity and activity of the recombinant TEVp was confirmed *in vitro* using a FRET-based peptide sensor by Dr. Taylor Courtney (data not shown), suggesting the TEVp is either inactive or degraded when introduced into the developing embryo environment.

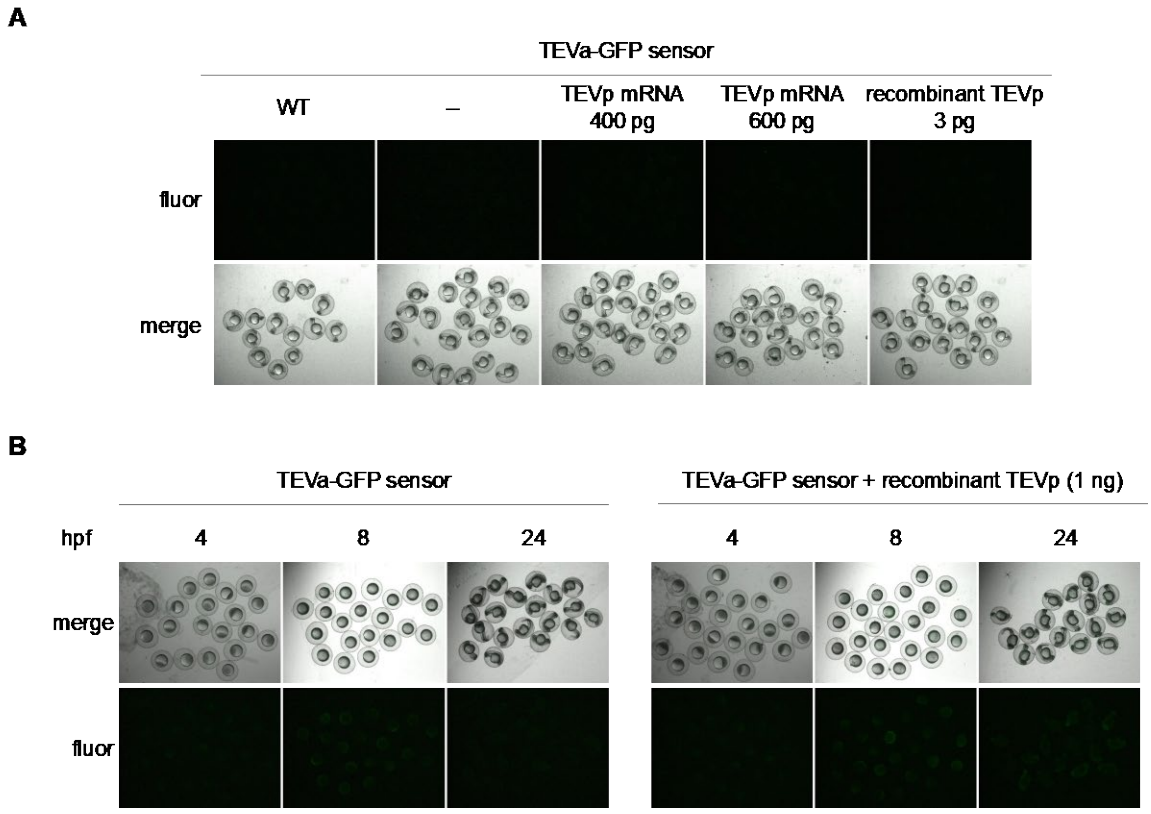

Figure 1-29: Evaluation of TEVa-GFP sensor activation *in vivo*
A) Representative images of 24 hpf zebrafish embryos microinjected with mRNA expression TEVa-GFP and either mRNA expressing TEVp or recombinant TEVp protein. No sensor activation is observed by 24 hpf. B) Representative images of zebrafish embryos injected with TEVa-GFP and recombinant TEVp and imaged at varying time points throughout development.

With the current design of the TEVp sensor, it cannot be ruled out that the lack of sensor activation in embryos could be credited to translation of the mRNA template. In order to validate transfection/injection of the sensor construct into cells and zebrafish embryos, we mimicked the previously reported design for the original caspase sensor by including the red fluorescent protein mLumin, downstream of the TEVa-GFP sequence.[138] Separated by an internal ribosome entry site (IRES), the modified construct should constitutively express TEVa-GFP and mLumin, which will serve as a distinct, internal fluorescent control. Further, the IRES sequence is derived from the encephalomyocarditis virus (EMCV) and has been shown to be an effective means for dicistronic gene expression in developing zebrafish embryos.[140] However, to validate translation from a single

translational start site, direct fusion or linkage via a self-cleaving P2A peptide of the mLumin fluorescent to the GFP sensor is needed.

Using the previously reported caspase activatable GFP sensor with the downstream IRES-mLumin sites (pT-CA-GFP-IRES-mLumin), the caspase sensor was cut out using NheI and EcoRI restriction enzymes, and replaced with the TEVa-GFP sensor, amplified from pCS2-TEVa-GFP using P23 and P24, generating pT-TEVa-GFP-IRES-mLumin. To validate sensor function in cells, HEK293T cells were transfected with either the modified TEVa-GFP sensor alone or co-transfected with a TEVp expression construct (Figure 1-30A) and sensor expression and activation were monitored by fluorescence imaging. Gratifyingly, all transfected cells exhibited uniform mLumin fluorescence indicating uniform transfection efficiency and expression of the sensor. No green fluorescence was observed in cells transfected with sensor alone or co-transfected with a plasmid expressing a catalytically dead TEVp. However, in the presence of active TEVp (pCS2-TEVp and pCS2-TEVp-HA), and significant increase in green fluorescence is observed suggesting efficient activation of the modified sensor construct in mammalian cells.

In order to utilize the sensor in zebrafish embryos, the TEVa-GFP-IRES-mLumin coding sequence was cloned into the pCS2+ backbone. TEVa-GFP-IRES-mLumin was amplified using P25 and P26 and the pCS2+ vector was amplified using P27 and P28. The two fragments were ligated using Gibson assembly to generate the pCS2-TEVa-GFP-IRES-mLumin construct. To validate sensor integrity and function when expressed from the pCS2+ vector, HEK293T cells were transfected with either pCS2+-TEVa-GFP-IRES-mLumin or a TEVp expression construct (pCS2-TEVp or pCS2-TEVp-HA). The experiment presented in Figure 1-30B was performed by Savannah Albright (Deiters Lab). As expected, sensor expression and activation was identical to that observed with the pT-TEVa-GFP-IRES-mLumin construct.

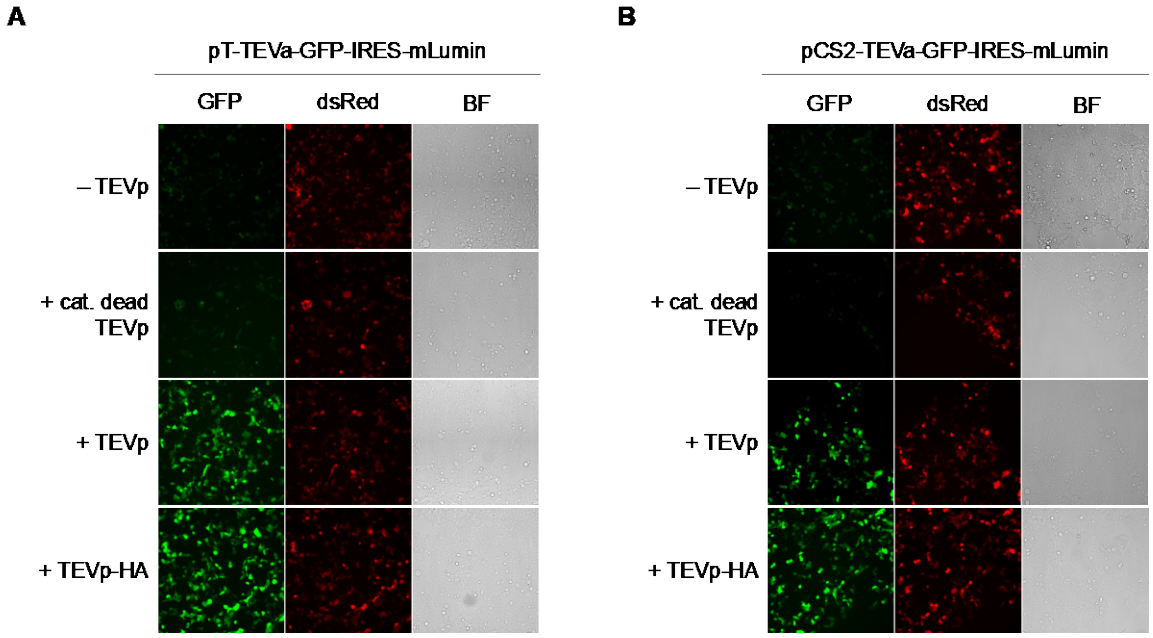

Figure 1-30: Evaluation of the TEVa-GFP-IRES-mLumin sensor in cells
HEK293T cells were transfected with either the pT-TEVa-GFP-IRES-mLumin (A) or pCS2-TEVa-GFP-IRES-mLumin (B) sensor alone or co-transfected with a TEVp expression construct. Sensor is efficiently expressed in all transfected cells and sensor activation is observed only in the presence of active TEVp.

The expression of an adapted sensor construct containing an internal mLumin fluorescent control will allow for normalization of the fluorescent sensor output in live zebrafish embryos. However, instead of the IRES-containing sensor that was adapted from the original caspase-activatable sensor, a modified sensor construct that is either directly fused or linked through a self-cleaving peptide would be preferential to confirm translation from a single translational start site in the *in vivo* system. Once resolved, this sensor will be the first one-plasmid system that can be used to assay TEVp activity in live zebrafish embryos. Furthermore, we envision that with modification of the cleavage site, that this sensor could be utilized as a general assay for studying protease activity throughout embryo development.

1.5.2.4 Summary and Future Directions

Herein, we attempted to exploit the highly specific interaction between TEVp and its consensus cleavage site to generate an enzymatically triggered cMO reagent to add to the current repertoire of orthogonal enzymatic triggers. A peptide-based linker containing the key recognition sequence was synthesized and successfully used to cyclize an MO antisense agent targeting endogenous *ntla*. Cleavage of the peptide-based linker by recombinant TEV protease was validated in biochemical assays suggesting it could be a suitable trigger for cMO activation *in vivo*. TEVp expression and activity was validated by western blot and two distinct, reporter assays in cells. Unfortunately, these results were not translated when evaluated in zebrafish embryo models. Through various troubleshooting efforts, we hypothesize that either an aspect innate to the TEVp coding sequence potentially triggers non-specific degradation of the mRNA transcript prior to expression in live embryos. Furthermore, while TEVp has been a widely used biochemical tool in bacterial and cell-based systems, there are limited reports of its utility in live model systems. As a result, there are also few reliable assays to survey TEVp activity *in vivo*. While we plan to continue to troubleshoot TEVp expression and activity *in vivo*, the TEVp-mediated activation approach can be applied to control antisense function of DNA-based reagents or other oligonucleotide tools in a cell-based setting.

In attempts to troubleshoot TEVp expression *in vivo*, we generated a fluorogenic TEVp activatable GFP-based sensor to assay TEVp proteolytic activity. The sensor design is based on a previously reported dark-to-bright caspase sensor,[138] and we replaced the caspase recognition site with the TEV recognition site. We validated the utility of the sensor in cell-based assays, and additionally cloned a modified version that contains a distinct, internal mLumin fluorescent protein control. While the TEVa-GFP sensor worked well in cell-based models, we were unable to

demonstrate its activation in zebrafish embryos as a result of issues encountered either with TEVp expression, or expression of the sensor itself. We are currently working towards validating sensor expression *in vivo* using the modified mLumin-containing construct, in addition to concurrently cloning a self-cleavable peptide between the sensor and the internal mLumin fluorescent control. Unlike other fluorogenic protease sensors that have been previously applied to zebrafish,[137] this sensor is expressed using a simple, one-plasmid system. Furthermore, the consensus cleavage site can be engineered to accommodate any consensus protease sequence and can therefore be applied to assessing protease activity during development more broadly defined.

1.5.2.5 Materials and Methods

Reagents. EZ Cut recombinant TEV protease was purchased from BioVision (Cat. No. 78471000). The anti-HA and anti-GAPDH antibodies were purchased from ProteinTech (51064-2-AP and 10494-1-AP, respectively). Anti-mCherry was purchased from BioVision (5993-30T). HRP-linked anti-rabbit (SA00001-2) and anti-mouse (SA00001-1) secondary antibodies were purchased from ProteinTech. All antibodies were diluted following the manufacturer's recommendation unless otherwise indicated.

1.5.2.5.1 Synthetic Protocols

General chemical protocols. All reagents used in solid phase peptide synthesis including Fmoc-protected amino acids, Rink amide resin, solvents, coupling agents, and additives were purchased from commercial sources and used without further purification. Analytical LC-MS data were collected on a Shimadzu LCMS-2020 and a ThermoScientific Q-Exactive Orbitrap. HPLC

purification were performed using a Shimadzu LC-20AD equipped with a SP-20AD UV/Vis detector. All peptides were co-spotted with either 1 mg/mL alpha-cyano-4-hydroxycinnamic acid (CHCA, Proteochem Inc P9100) or sinapic acid (SA, Proteochem Inc 9102) matrices on a MSP 96 target ground steel BC MALDI plate (Bruker Daltonics, Part No. 8280799) and analyzed on a Bruker Daltonics UltrafleXtreme MALDI TOF-mass spectrometer in either the reflectron positive or linear positive mode.

Solid phase peptide synthesis. All peptide synthesis was performed using a CEM Discovery microwave synthesizer equipped with a fiber optic temperature probe covered with a glass sheath (University of Pittsburgh Glass Shop) in order to protect the probe from kinking or breaking the fiber optic probe cord. The microwave unit was housed in a fume hood and operated in open-vessel mode using the fiber optic probe to measure temperature and control power output. All microwave reactions were stirred magnetically. The synthesizer was connected to an air input line which to cool the reaction vessel following microwave assisted heating.

The TEV peptide linker was synthesized using microwave assisted Fmoc-based solid phase methods on the CEM Discover system using H-Rink amide resin (ChemImpex 02900). Synthesis was carried out using 50 – 75 μmol scale reaction (150 – 225 mg resin) in 10 mL fritted syringe reaction vessels (Torviq) equipped with a microflea magnetic stir bar. The rink amide resin was swelled in DMF (5 mL) while stirring at room temperature for 20 minutes. Since the rink amide resin is Fmoc-protected, the resin was deprotected in 20% [v/v] 4-methyl piperidine in DMF (1 mL). The reaction vessel was fitted with a cap and vigorously stirred. The reaction vessel was loaded into the microwave reactor and deprotected at 50 ºC for 2 minutes. Following initial deprotection of the resin, the synthesis of the peptide was performed as follows: 1. Coupling – A 1.7 mL Eppendorf tube was loaded with solid Fmoc-protected amino acid (4 eq). The amino acid

was dissolved in a 0.3 M solution of *O*-(1H-6-chlorobenzotriazole-1-yl)-1,1,3,3-tetramethyluronium hexafluorophosphate (HCTU, 4 eq) solution of *N*-methyl-pyrrolidine (1 mL), followed by immediate addition of *N*,*N*'-diisopropylethylamine (6 eq, volume varies with reaction scale). The amino acid was vortexed until complete dissolution of the solid amino acid was observed (usually about 1 minute). Following complete solubilization, the amino acid solution was incubated at room temperature for ~ 2 minutes. The reaction vessel containing the dried, swelled resin was capped and the entire amino acid solution (~ 1 mL) was added directly to the resin. The reaction vessel was stirred over a magnetic stir plate prior to loading into the microwave reactor. The fiber optic probe was gently placed into the reaction vessel. The coupling reaction was carried out in temperature mode at 70 ºC for 3 minutes (maximum allowable power 75 W). Following completion of the coupling reaction, the reaction vessel was removed from the microwave reactor and the coupling solution was drained via a vacuum manifold. The resin was washed at least 3 times with DMF (5 mL per rinse) under nitrogen bubbling to mix. Following the washes, the resin was mixed with deprotection solution (20% [v/v] 4-methyl piperidine in DMF, 1 mL) and mixed over a magnetic stir plate before loading into the microwave reaction vessel. Once loaded, the fiber optic probe was gently placed in the reaction vessel and the coupled amino acid was deprotected following the same method as described for initial deprotection of the resin. Following deprotection, the resin was washed with DMF three times (5 mL per rinse) under nitrogen gas. The reaction scheme of coupling, wash, deprotection, wash was repeated until all residues were coupled to the growing peptide chain.

Periodically during synthesis, a microcleavage of the resin was performed to evaluate reaction progression and ensure synthesis integrity. For microcleavage reactions, the tip of a 5 ¾" glass pipette was gently dipped into the dry resin bed. The pipette tip, loaded with a small portion

of the resin, was mixed with global deprotection solution (25 µL, 95% [v/v] trifluoroacetic acid, 2.5% [v/v] water, 2.5% [v/v] triisopropylsilane (TIPS) and incubated at room temperature for minimum 15 minutes. The cleaved peptide was precipitated from the aliquot of the globally deprotected solution (10 µL) with ice cold diethyl ether (200 µL) and briefly centrifuged to pellet the peptide. The diethyl ether was removed by pipetting and the resulting small, peptide pellet was resuspended in a 50% [v/v] acetonitrile in water solution (10 µL). Microcleaved peptides were co-spotted with either alpha-cyano-4-hydroxycinnamic acid (CHCA, peptides < 2 kDa) or sinapic acid (SA, peptides > 1.5 kDa) matrices and analyzed directly by MALDI-TOF mass spectrometry. After coupling of the final residue, the resin was washed with DMF (5 mL) twice and then dichloromethane (5 mL) three times under nitrogen bubbling. The resin was dried on the vacuum manifold for ~ 10-15 minutes. The syringe plunger was used to push all resin against the fritted filter and a needle was capped onto the end of the syringe. The global cleavage cocktail (95% [v/v] TFA, 2.5% [v/v] water, 2.5% [v/v] TIPS) was pulled up through the needle until the solution covered the entire resin bed (volume varies with reaction scale, typically 1-3 mL). Then, the needle was removed, and the syringe was capped. The syringe was rocked end-over-end on the shaker for up to 4 hours at room temperature. The peptide was precipitated into ice cold diethyl ether (~ 100 mL). The precipitated peptide was then pelleted through centrifugation at 7k rpm for 10 minutes at 4 ºC. The peptide pellet was resuspended in a solution of 50% [v/v] acetonitrile in water + 0.1% [v/v] TFA (varies with peptide composition but typically no more than 5 mL). When solubility of the peptide was problematic, DMSO was added to the crude peptide mixture at a final concentration no greater than 25%. Insoluble particulates were removed by syringe filtering through a 0.45 µm PTFE syringe filter. Peptides were purified by reversed phase HPLC on the Shimadzu LC-20AD using a gradient of 5-95% acetonitrile + 0.1% [v/v] TFA in water + 0.1%

[v/v] TFA on a Zorbax 5 µm SB-C18 SemiPrep column (9.5 x 250 mm, PN 880975-202). In some cases, the gradient was adjusted to better dial in on the polarity of the desired peptide. Confirmation of peptide integrity was confirmed by MALDI-TOF mass spectrometry. Following purification, fractions containing pure peptide were combined and lyophilized to dryness. Syntheses typically yielded anywhere from 5-10 mg pure TEV peptide linker.

The dry peptide was dissolved in minimal DMSO (~ 50 – 100 µL) and then the concentration was determined by measuring the absorbance at 280 nm on the TECAN M200. The peptide was diluted into PBS (1:100) and the absorbance of the diluted peptide mixture and a corresponding DMSO blank (1:100 in DMSO in PBS) were measured in triplicate. The absorbance of the blank was substracted from the absorbance of the peptide mixture. The concentration of the peptide can then be calculated using the following equation: concentration (mg/mL) = ((A_{280}*dilution factor*molecular weight/(n*ε_{Trp} + n* ε_{Tyr} + n* ε_{Phe})). The extinction coefficients (ε) for the aromatic amino acids at 280 nm are as follows: ε_{Trp} = 5500 M^{-1} cm^{-1}, ε_{Tyr} = 1490 M^{-1} cm^{-1}, ε_{Phe} = 200 M^{-1} cm^{-1}.

TEVp linker-*ntla* conjugate (40). The dry, purified alkyne-functionalized *ntla* MO was dissolved in water (50 µL) and the concentration was determined on the ND-1000 NanoDrop spectrophotometer following the protocol outlined in Section 4.3.2 (GeneTools, 1:20 and 1:10 in 0.1 N HCl, 265 nm, constant = 34). The click reaction was performed following a previously reported protocol provided from the manufacturer.[106] The alkyne functionalized *ntla* MO **28** (50 µL, 111 µM, 5.5 nmol) was diluted with water (28 µL) and DMSO (6 µL, final conc. 10%). The TEV peptide linker **37** (6 µL, 5 mM in DMSO, 30 nmol) was added to the reaction mixture and the reaction was briefly vortexed to mix. In a separate tube, a 5 mM solution sodium ascorbate was freshly prepared by dissolving solid sodium ascorbate (~ 5-10 mg) in water (~ 5-11 mL,

depending on amount of solid sodium ascorbate weighed out). Then, the aqueous sodium ascorbate solution (24 μL, 5 mM in water, 120 nmol) was added to the reaction mixture which was briefly vortexed to mix. In separate tubes, a 40 mM solution of $CuSO_4$ in water and a 40 mM solution of tris[(1-benzyl-1H-1,2,3-triazol-4-yl)methyl]amine (TBTA) in DMSO were freshly prepared. Then equal volumes (10 μL) of each solution, the $CuSO_4$ and TBTA solutions, were combined and mixed by pipetting to generate a 20 mM $CuSO_4$-TBTA solution in 50% DMSO. A portion of this 20 mM $CuSO_4$-TBTA solution (6 μL, 120 nmol) was added to the click reaction mixture and vortexed briefly to mix. The final concentration of the MO in the reaction mixture is 50 μM. The reaction was incubated overnight at room temperature. The next morning, a small aliquot of the crude reaction mixture was removed and co-spotted with sinapic acid matrix and analyzed by MALDI-TOF MS (expected: 10219.65, observed: 10222.657) as outlined in Section 4.3.3. After confirmation of reaction completion, the TEVp *ntla* MO clicked product 40 was purified on the Shimadzu LC20-AD HPLC using a gradient of 5-50% acetonitrile in 0.1 M triethylammonium acetate (TEAA) buffer over 20 minutes following the protocol outlined in Section 4.3.4, eluting as a single, broad peak between 9 – 11 minutes. The purified MO fractions were pooled and lyophilized to dryness.

Cyclic TEVp *ntla* cMO (41). The purified TEVp *ntla* MO conjugate **40** was dissolved in water (60 μL) and diluted with 0.1 M Tris pH 8 buffer (140 μL). Immobilized TCEP slurry (150 μL) was pipetted into a Pierce spin cup filter and mixed with 0.1 M Tris pH 8 buffer (200 μL). The spin cup filter was centrifuged for 2 minutes at 2k rpm and the flow through was discarded. The immobilized TCEP resin was rinsed twice more with 0.1 M Tris pH 8 buffer (200 μL) and centrifuged. Following the final rinse, the resuspended MO solution (200 μL) was added directly to the rinsed, dry resin. The tube was inverted to mix and incubated at room temperature overnight.

The next morning, the spin cup filter was centrifuged at 2k rpm for 2 minutes and a portion of the crude cyclization reaction was analyzed by MALDI-TOF MS (expected: 10066.02, observed: 10070.931) as specified in Section 4.3.3. Following confirmation of reaction completion, the crude cyclization reaction was purified on the Shimadzu LC-20AD HPLC following the protocol in Section 4.3.4, eluting the purified cMO as a single, broad peak between 9-11 minutes. Fractions containing purified cMO were pooled and lyophilized to dryness overnight. The cyclic cMO product was subject to purification with NHS-activated agarose resin and SulfoLink resin following the protocol outlined in Section 4.3.5 and 4.3.6, respectively.

1.5.2.5.2 Molecular and Cell Biology Protocols

Cleavage of TEV peptide linker by recombinant TEV protease *in vitro*. TEV peptide linker (17 µL, 100 µg, from 5 mM stock in DMSO) was mixed with EZ Cut recombinant TEV protease (Biovision, 1 µg) in TEVp cleavage buffer (80 µL, 50 mM Tris-HCl pH 8.0, 0.5 mM EDTA, 1 mM DTT) at 37 ºC. At the indicated time point, an aliquot (25 µL) of the reaction was removed, spun in a 10 kDa spin column, and the filtrate was analyzed by absorbance at 280 nm on the Agilent HPLC (5-95% acetonitrile + 0.1% [v/v] TFA in water + 0.1% [v/v] TFA) using a gradient of 1 mL/min. Eluted peaks were manually collected, co-spotted with CHCA matrix, and analyzed by MALDI-TOF MS.

Cloning of new plasmids. All cloning was performed using chemically competent Top10 cells. The pCS2+ backbone was obtained from Dr. Jihe Liu (Deiters lab). All plasmid sequences were confirmed by Sanger sequencing (Genewiz) using their available SP6 forward and M13-

48REV reverse sequencing primers. Protocols for restriction digest, ligation, and Gibson isothermal assembly are outlined in Sections 4.1.2, 4.1.3, and 4.1.4, respectively.

The coding sequence of the S219V TEVp mutant was amplified from pCI-TEVp, obtained from Dr. Kalyn Brown (Deiters lab) using primers P3 and P4 (see Table 1-2 for list of all primer sequences) and ligated into the BamHI and XhoI sites of pCS2+ to generate pCS2-TEVp. The HA-tagged construct was PCR amplified from pCI-TEVp-HA, obtained from Dr. Jihe Liu (Deiters lab), using primers P5 and P6 and ligated into the BamHI and EcoRI sites of pCS2+ to generate pCS2-TEVp-HA. The fluorescent fusion pCS2-TEVp-mCherry construct was cloned through a 2-fragment Gibson assembly of pCS2-TEVp amplified from the corresponding plasmid template using P9 and P10, with an mCherry fragment PCR amplified from pmCherry-N1, obtained from fellow lab member Taylor Courtney, using plasmids P11 and P12. PCR amplification and subsequent Gibson assembly was performed following the protocols outlined in Sections 4.1.1 and 4.1.4, respectively. A version of the fluorescent fusion construct containing a self-cleavable P2A linker was also cloned via a 2-fragment Gibson assembly of the pCS2-TEVp fragment amplified from the corresponding plasmid using primers P13 and P14, with the P2A-mCherry fragment, amplified from pUb-K-EGFP-P2A-mCherry, obtained from fellow lab member Amy Ryan, using P15 and P16. The coding sequence of TEVp-mCherry was codon optimized for *Danio rerio* using the IDT codon optimization tool.[115] This sequence was then ordered as a gene fragment from Twist Biosciences (San Francisco, CA). The sequence of the gene fragment can be found in Table 1-3. The gene fragment was used as a template and PCR amplified using primers P17 and P18 and ligated into the BstBI and XhoI sites of the pCS2+ backbone.

The coding sequence of GloSensor was amplified from pTriEx-Glosensor, obtained from Dr. Kalyn Brown (Deiters lab), using primers P7 and P8 and ligated into the BamHI and EcoRI sites of the pCS2+ vector.

Caspase activatable sensor pCA-GFP (Addgene #32748) was a gift from Dr. Jeanne Hardy's lab. The caspase site was replaced using P19 and P20 via 1-fragment Gibson assembly, generating the pmKate-2-C-TEVa-GFP plasmid. The coding sequence of the TEVa-GFP sensor was PCR amplified using P21 and P22 and ligated into the BamHI and EcoRI cut sites of the pCS2+ backbone. For cloning of the modified sensor containing a downstream internal, fluorescent protein (mLumin) control, pT-CA-GFP-IRES-mLumin (Addgene #32749) was obtained as a gift from Dr. Jeanne Hardy's lab. The coding sequence of TEVa-GFP was amplified from pCS2-TEVa-GFP using P23 and P24. The caspase activatable sensor was cut out of pT-CA-GFP-IRES-mLumin following restriction digest with NheI and EcoRI and the TEVa-GFP sensor was ligated into this site to generate pT-TEVa-GFP-IRES-mLumin. The optimized TEVa-GFP-IRES-mLumin sensor was cloned into the pCS2+ vector following PCR amplification from pT-TEVa-GFP-IRES-mLumin using P25 and P26, and PCR amplification of the pCS2+ backbone with P27 and P28. The two fragments were cloned via Gibson assembly as outlined in Section 4.1.4.

Table 1-2: List of primers used to generate new plasmid constructs
Restriction sites are indicated in **bold.**

Primer	Sequence (5' to 3')
P3	GAATAT**GGATCC**ATGGGCGAGAGCCTGTTC
P4	GTTTAT**GAATTC**TTACCGGCGCCTCCTGC
P5	ATTGA**GGATCC**ATGGGCGAGAGCCTGTTC
P6	TCCACG**GAATTC**TTAAGCGTAATCTGGAACATCGT
P7	GAATAT**GGATCC**ATGGACACCGCTATCCTCAG
P8	GCCAT**GAATTC**ACAACGGGGATGATCTGGTT
P9	GTTCTTTTTGCAGGATCCATGGGCGAGAGCCTGTTCAAGG
P10	CGCCCTTGCTCACCATTCCGGAGCCCCGGCGCCTCCTGCG
P11	CGCAGGAGGCGCCGG GGCTCCGGAATGGTGAGCAAGGGC G
P12	CGAGAGGCCTTGAATTCTTACTTGTACAGCTCGTCCATG
P13	GAGCTGTACAAGTAA GAATTCAAGGCCTCTCGAGCCTCT
P14	AGTAGCTCCGGAGCCCCGGCGCCTCCTGCGAT
P15	CGCAGGAGGCGCCGGGGCTCCGGAGCTACTAACTTCAGCCTGC
P16	GAGAGGCCTTGAATTCTTACTTGTACAGCTCGTCC
P17	ATGCA**TTCGAA**ATGGGGGAGTCATTGTTTAA
P18	GTCAT**CTCGAG**TTACTTATAAAGCTCGTCCA
P19	GAAAATCTCTACTTCCAGAGTTTTCAGGGGCCATGC
P20	ACTCTGGAAGTAGAGATTTTCCTTGTACAGCTCGTCC
P21	ATTCT**GGATCC**GCCACCATGGTGAGCAAG
P22	CAGCCT**GAATTC**CTTACAGACGATCCAGAATCCAC
P23	AATA**GCTAGC**ATGGTGAGCAAGGGCGAGGA
P24	CAGT**GAATTC**TTACAGACGATCCAGAATCCACAG
P25	TTCTTTTTGCA**GGATCC**GCTAGCATGGTGAGCAAGGG
P26	TAGTTCTAGAGG**CTCGAG**TTATCTGTGCCCCAGTTTGC
P27	GCAAACTGGGGCACAGATAA**CTCGAG**CCTCTAGAACTA
P28	CTTGCTCACCATGCTAGC**GGATCC**TGCAAAAAGAACAAG

Table 1-3: Sequence of zebrafish codon-optimized TEVp-mCherry

Construct	Sequence (5' to 3')
zebrafish codon optimized TEVp-mCherry	ATGGGGGAGTCATTGTTTAAAGGCCCTAGGGATTATAACCCGA TATCTAGTTCCATTTGTCATCTCACAAACGAATCCGACGGACAT ACAACCTCACTGTACGGTATCGGCTTTGGTCCTTTCATAATCAC TAACAAACACCTTTTCCGCCGAAATAATGGGACGCTCCTTGTAC AATCTCTTCATGGCGTATTTAAAGTCAAAGACACTACGACCTTG CAGCAACACCTCGTTGACGGTAGAGATATGATTATTATTCGGA TGCCAAAGGACTTTCCCCCTTTTCCACAGAAGCTTAAGTTCCGT GAGCCCCAAAGGGAAGAGAGGATATGTCTGGTTACAACCAATT TCCAAACTAAGAGCATGTCTAGTATGGTGTCAGATACGTCTTGC ACATTCCCGTCTTCCGACGGCATATTCTGGAAACATTGGATCCA GACAAAGGATGGTCAGTGTGGTTCTCCTCTGGTCTCCACACGTGA TGGATTTATAGTAGGGATCCATAGTGCGAGTAATTTCACTAATAC TAACAACTATTTCACGTCTGTACCTAAAAATTTTATGGAACTGCT GACTAACCAGGAGGCGCAACAGTGGGTCAGCGGCTGGAGACTTA ATGCTGACTCAGTTTTGTGGGGGGGACATAAGGTGTTCATGGTCA AGCCAGAGGAACCGTTCCAACCTGTGAAAGAAGCCACCCAGCTGA TGAATCGACGCAGACGCCGCGGGAGTGGCATGGTTAGCAAGGGAG AAGAAGATAATATGGCGATTATTAAGGAATTCATGAGATTCAAGGT TCATATGGAAGGATCAGTCAATGGACATGAGTTCGAGATTGAAGGC GAGGGGGAGGGACGGCCATATGAGGGAACACAGACTGCGAAACTC AAGGTAACGAAAGGCGGACCTCTGCCATTCGCATGGGATATACTCT CTCCTCAGTTCATGTACGGGAGTAAGGCTTATGTGAAACACCCCGC GGATATCCCAGATTACCTCAAACTCTCTTTCCCCGAAGGATTCAAAT GGGAACGGGTAATGAACTTTGAGGACGGCGGAGTTGTCACTGTGAC CCAGGATTCTAGTCTCCAGGACGGGGAATTCATATATAAGGTTAAG TTGCGGGGTACAAACTTTCCTTCCGATGGACCTGTGATGCAGAAAA AGACGATGGGGTGGGAAGCGTCCAGCGAGCGTATGTACCCCGAGG ACGGTGCACTGAAGGGGGAAATTAAACAACGACTGAAATTGAAGG ACGGGGGTCACTATGACGCCGAAGTAAAGACGACCTATAAAGCGA AAAAGCCGGTCCAACTTCCAGGAGCTTATAATGTCAATATTAAATT GGACATAACGAGCCATAACGAAGATTACACTATCGTTGAACAGTA CGAGCGAGCGGAAGGTAGGCACAGTACGGGGGGGATGGACGAG CTTTATAAGTAA

General cell culture and transfection. All cells were maintained according to the protocol outlined in Section 4.2.1. In the TEVp activity assays (Glosensor and TEVa-GFP sensor activation), a 96-well format and 100 µL media was used.

Western blot analysis of TEVp expression in cells. HEK293T cells were plated in a translucent, 12-well plate at a cell density of 200k cells/well in DMEM supplemented with 10%

FBS (1 mL/well) and incubated overnight. The next day, cells were transiently transfected with either pCS2-TEVp-HA, pCS2-mCherry, pCS2-TEVp-mCherry, pmCherry-N1, or pCS2-TEVp-P2A-mCherry overnight using Lipofectamine 2000 following the protocol outlined in Section 4.2.3. The next morning, transfection media (1.2 mL) was removed from cells and replaced with fresh DMEM + 10% FBS (1 mL). Cells were incubated an additional 24 hours at 37 ºC.

The following day, media was removed, and cells were carefully rinsed with cold 1X PBS (500 µL) so as to not lift any of the cells from the bottom of the well. While still on ice, chilled RIPA buffer supplemented with 1X Halt protease inhibitor cocktail (100 µL, ThermoScientific 78429) was added to each well and the plate was shaken on ice at 4 ºC for 20 minutes. Lysate was removed from each well by pipetting and the cellular debris was pelleted by centrifugation at max speed at 4 ºC for 10 minutes. Following centrifugation, the supernatant was removed and lysates (100 µL) were mixed with Laemlli buffer supplemented with 10% β-mercaptoethanol (35 µL). Samples were heated at 95 ºC for 10 minutes and stored at –20 ºC.

Lysates (15 µL) was resolved on a 10% SDS-PAGE gel topped with a 4% stacking gel run at 60V for 20 minutes and then increased to 150V for 90 minutes and then analyzed by western blot following the protocol outlined in Section 4.2.5. The membrane was probed with either an anti-HA antibody (ProteinTech, Cat. No. 51064-2-AP) diluted 1:5000 in 5% [w/v] non-fat milk in 1X TBST, an anti-mCherry antibody (BioVision, 5993-30T) diluted 1:1000 in 5% [w/v] non-fat milk in 1X TBST, or an anti-GAPDH antibody (ProteinTech 10494-1-AP) diluted 1:5,000 in 5% [w/v] non-fat milk in 1X TBST. Primary antibodies were incubated at 4 ºC overnight while rocking. The following morning, membranes were washed with TBST and then probed with the HRP-linked goat anti-rabbit IgG secondary antibody (ProteinTech, SA00001-2) diluted 1:5000 in TBST for 90 minutes at room temperature. Following incubation, the secondary antibody was

removed, the membrane was rinsed with TBST, and then the blots were developed and imaged following the protocol outlined in Section 4.2.5.

GloSensor assay. HEK293T cells were seeded at cell density of 50k cells/well in a poly-D-lysine pre-treated white, 96-well plate in 100 µL DMEM + 10% FBS. Cells were co-transfected overnight with either pTriEx-Glosensor or pCS2-Glosensor (50 ng) and the indicated TEVp expression construct (50 ng) using Lipofectamine 2000 following the protocol outlined in Section 4.2.3. The following morning, the transfection media (150 µL) was carefully removed so as to not disturb the adherent cells and replaced with fresh 10% DMEM + 10% FBS. Cells were incubated an additional 24 hours. Following incubation, the plate was removed from the incubator and luminescence was measured using the Bright Luciferase Assay system (Promega, E2610). BrightGlo reagent (40 µL) was added to each well of plated cells (total volume in the well after addition 140 µL), and luminescence was measured on the Tecan M1000 platereader.

mRNA synthesis. Synthetic mRNAs expressing TEVp, TEVp-HA, TEVp-mCherry, TEVp-P2A-mCherry, Glosensor, and TEVa-GFP were prepared using the mMessage mMachine Sp6 *in vitro* transcription kit (ThermoScientific AM1340), purified by PCIA extraction and ethanol precipitation, and analyzed by agarose gel electrophoresis as outlined in Section 4.1.9.

***In vitro* translation of mRNA constructs.** Translation of mRNA constructs was performed using a nuclease-treated rabbit reticulocyte lysate *in vitro* translation system (Promega L4960). Translation reactions of the indicated mRNA constructs (1 µg) were assembled following the manufacturer's protocol and incubated at 30 ºC for 90 minutes. For western blot analysis, an aliquot of the translation reaction (10 µL) was mixed with 4X Laemlli buffer (40 µL) and boiled at 95 ºC for 10 minutes. Extra translation reaction and lysates were stored at –20 ºC. Lysates (20

μL) were resolved on a 10% SDS-PAGE gel topped with a 4% stacking gel. Analysis of protein expression by western blotting was performed following the protocol outlined in Section 4.2.5.

TEVa-GFP sensor activation in cells. HEK293T cells (50-80k cells/well) were seeded in a poly-D lysine treated, black 96-well plate in 100 μL DMEM + 10% FBS. The following day, cells were transiently transfected with either pmKate-2-C-TEVa-GFP, pCS2-TEVa-GFP, pT-TEVa-GFP-IRES-mLumin, or pCS2-TEVa-GFP-IRES-mLumin (100 ng) alone or co-transfected with the indicated TEVp expression construct (100 ng) overnight using Lipofectamine 2000 following the protocol outlined in Section 4.2.3. The following morning, the transfection media (150 μL) was carefully removed so as to not disturb the adherent cells and replaced with fresh 10% DMEM + 10% FBS. Cells were incubated an additional 24 hours. Prior to imaging, media was removed and replaced with DMEM containing no phenol red indicator (100 μL, GE SH3028401). Images were acquired using FITC and dsRed filter sets.

General live cell fluorescence imaging. For imaging experiments, cells were seeded into a black, 96-well plate at a cell density of ranging from 40-80k cells/well. Cells transfected with fluorescence protein reporters were imaged using the Tokai Hit incubated stage (Inu) on the Zeiss Axio Observer Z1 using the LD-Plan-Neoflaur 20X objective and either a FITC (chroma filter 49002, ex. ET 470/40 nm, em. ET 525/50 nm) or dsRed/Cy3 (43HE, Ex. BP 550/25 nm, em. 605/70 nm) filter set. Image processing was completed using Slidebook 4.0 (3i) and FIJI (National Institutes of Health) software.

1.5.2.5.3 Zebrafish Protocols

Zebrafish aquaculture, breeding, and embryo microinjection were performed following the protocols outlined in Sections 4.4.1, 4.4.2, and 4.4.3 respectively. Embryos from the natural mating of wild-type adult AB* zebrafish were collected and used for all injections.

Embryo microinjection solution preparation. All mRNA solutions were prepared such that the desired injection amount was delivered following a 2 nL injection (i.e., 200 pg mRNA injection solution contained 100 pg/nL mRNA). Synthetic mRNAs expressing various TEVp constructs, GloSensor, or TEVa-GFP were injected into the yolk sac of 1- to 4-cell stage zebrafish embryos. EZ Cut recombinant TEVp was either diluted from a 100 ng/µL (for 15 pg injection) or directly from the commercial stock (1 mg/mL, for 1 ng injection). Phenol red was added to injection solutions to a final concentration of 0.05% and used as a tracer dye for injection.

Preparation of embryo lysates for western blot analysis. At 24 hpf, mRNA injected embryos were pooled into batches of 100 and manually dechorionated using forceps. Embryos were deyolked on ice in embryo deyolking buffer (900 mL E3 water mixed with 100 mL 10X protease inhibitor cocktail, 10X stock prepped by mixing 1 tablet cOmplete, Mini, EDTA-free protease inhibitor cocktail, Sigma 11836170001 in 1 mL E3 water) by vigorous pipetting with a P1000 tip until the solution was milky white in color. Embryos were centrifuged at max speed at 4 ºC for 10 minutes, resulting in a relatively big, light brown pellet. Supernatant was discarded. The pellet was washed with deyolking buffer (500 µL) on ice and centrifuged again. The supernatant was discarded. The pellet was resuspended in lysis buffer (~ 2 µL per embryo, 20 mM Tris, 150 mM NaCl, 1 mM EDTA, 1 mM EGTA, 1% Triton X-100) supplemented with protease inhibitor cocktail (diluted from 10X stock) by pipetting and the deyolked embryos were lysed on

ice by vigorous pipetting with a P200 pipette tip (minimum 15 times) and protein concentration in the lysate was determined following the protocol outlined in Section 4.4.6. Embryo lysates were analyzed by western blot following the protocol outlined in Section 4.2.5. *Note: in the course of this work, a more efficient lysis protocol was optimized (see Section 4.4.6) and is the preferred lysis protocol for analyzing embryo lysates by western blot.*

GloSensor activation in embryo lysates. Embryos injected with GloSensor and TEVp mRNA constructs were developed to 24 hpf. Embryos (n = 15) were pooled into three groups of 5 and lysed following the protocol in Section 4.4.5. Lysates were pipetted into a white, 96-well plate and mixed with BrightGlo reagent (10 μL). Luminescence was measured on the Tecan M1000 plate reader.

TEVa-GFP sensor activation in embryos. Fluorescence activation of TEVa-GFP injected embryos was followed by fluorescence imaging on the Leica MZ205FA fluorescent stereoscope following the protocol outlined in Section 4.4.4. At the indicated time point embryos were grouped, and images were captured using PLANAPO 1.6X objective lens and the zoom set to 7.85X magnification. Imaging parameters were set using the Leica software as follows: brightfield- transmitted light intensity set to 1953 using a 5 ms exposure time and the gain set to 2. Fluorescent images were captured using the GFP filter sets with the illuminated light intensity set to 100 using a 1 second exposure time and the gain set to 2.

1.6 Small Molecule-Responsive cMOs

While photocaged cyclic MOs offer advantages such as high spatial and temporal resolution, they are not ideal for studies of gene expression within deep tissues or non-transparent

organisms. Small molecule triggers represent an innovative regulatory approach. Though numerous small molecules have been used to chemically control protein function,[141-143] very few examples of small molecule-triggered oligonucleotides exist. Current chemical control strategies have been limited to regulating the function of aptamers, riboswitches, and G-quadruplexes.[144-146] These approaches are not generally applicable to other nucleic acid-based tools and often require genetic encoding of the response element to interrogate a biological process, so they are limited to regulating exogenous transgenes and not endogenous genes. Further, application of these tools in animal models remains to be seen.

Herein, we report the first chemically activated MO. Small molecules have enormous potential as conditional triggers as they are minimally invasive and can be applied with high temporal resolution. Furthermore, they do not require irradiation equipment and they can easily be applied to large numbers of embryos in parallel. Various biorthogonal small molecule pairs have proven useful as probes, enabling studies into biological processes without perturbing the endogenous system.[147-149] Based on their biorthogonality and history of use in vivo,[149] we selected the azide/phosphine pair to generate a cMO linker that is cleaved through a Staudinger reduction-induced self-immolation.

1.6.1 Design and Synthesis of a Phosphine-Triggered cMO

The linker is based on a *p*-azidobenzyl motif which, following exposure to a phosphine trigger, will undergo a self-immolative cleavage via a Staudinger reduction. The cyclic *para*-azidobenzyl cMO is reduced generating a *p*-aminobenzyl intermediate following exposure to a phosphine trigger. This intermediate then collapses, undergoing a 1,6-elimination and subsequent decarboxylation to cleave the carbamate linkage. The resulting iminoquinone methide intermediate

is then quenched with water.[150-152] Once cleaved, the linear MO is active, allowing for hybridization to its target mRNA and silencing of gene expression (Figure 1-31). We placed the azido group in the 6-position rather than the 4-position, as 1,6-eliminations occur nearly twice as quickly as 1,4-eliminations,[152, 153] and we expected reduced steric hindrance for the phosphine. In designing the linker, we utilized a carbamate leaving group, as it is stable to physiological conditions and well-established for self-immolation.[152, 154] Furthermore, the benzylic position of the linker was substituted as this has shown to accelerate self-immolation by stabilizing the partial positive charge that develops during elimination.[152] These design considerations are supported by recent comparisons of azidobenzyl carbamates as phosphine-removable protecting groups in biological settings.[155, 156] Aside from the substituted *p*-azidobenzyl carbamate core, we functionalized the linker with *N*-hydroxysuccinimide (NHS) ester and chloroacetamide handles for cyclization of MOs modified at the termini with the proper amino- and thiol-handles.

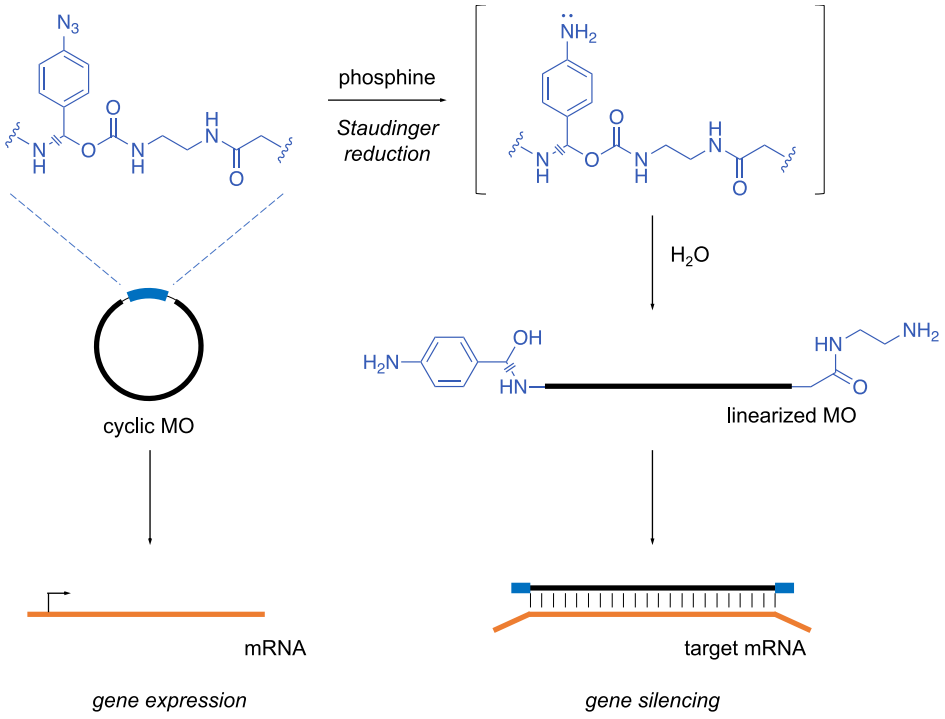

Figure 1-31: Small molecule activation of the *p*-azidobenzyl caged cMO
Following exposure to a phosphine trigger, the *p*-azidobenzyl linker undergoes a Staudinger reduction, forming a *p*-aminobenzyl intermediate. The linker then rapidly self-cleaves via a 1,6-elimination and subsequent decarboxylation to generate the active, linearized MO which can then hybridize to target mRNAs and silence gene expression.

The linker was synthesized by former undergraduate Deiters lab member, Bradley Lukasak, in 10 steps from commercially available 4-aminoacetophenone (**42**) and the scheme is presented in Figure 1-32. Diazotization and azide substitution of **42** yielded the aryl azide **43**.[156] Bromination of **43** provided the α-bromoketone **44**,[157] which was then transformed into the corresponding primary amine **45** utilizing hexamine in a Delépine reaction. The primary amine was then reacted with methyl adipoyl chloride to form the amide **46**.[64] Treatment with sodium borohydride reduced the ketone, affording alcohol **47**, which was conjugated to ethylenediamine after activation with 1,1-carbonyldiimidazole (CDI), and was subsequently capped with 2-chloroacetyl chloride to form the chloroacetamide **48**.[66] Saponification of the methyl ester **48** with aqueous lithium hydroxide afforded the corresponding carboxylic acid **49**, which was activated to

the NHS-ester using *O*-(*N*-succinimidyl)-*N,N,N',N'*-tetramethyluronium tetrafluoroborate (TSTU) to provide the final linker **50**.

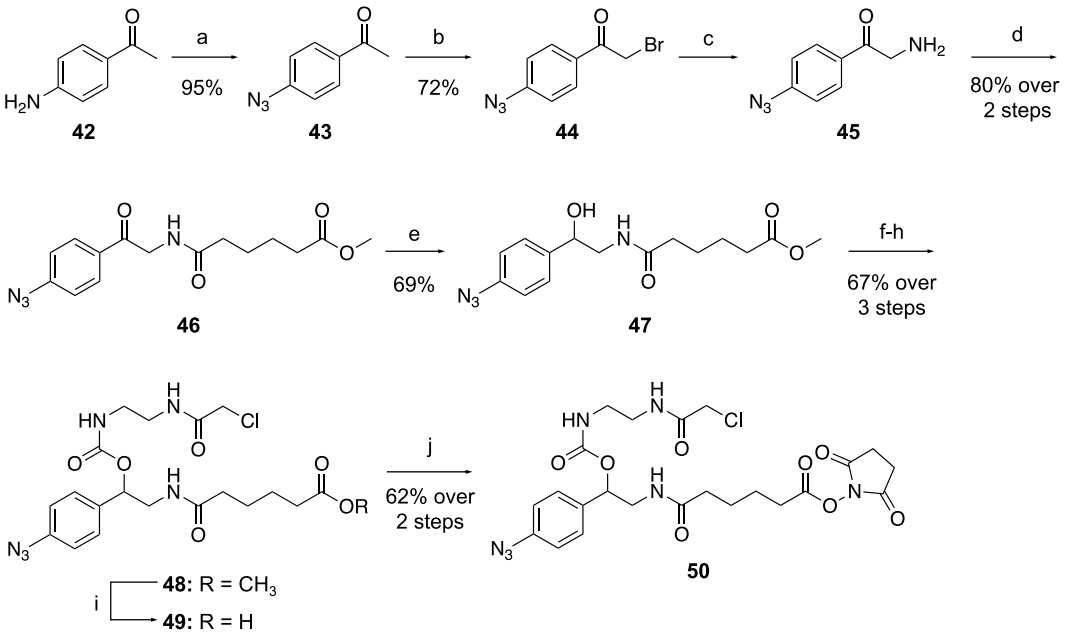

Figure 1-32: Synthesis of p-azidobenzyl cMO linker 50
Reagents and conditions: a) $NaNO_2$, H_2SO_4, NaN_3, 95%; b) Br_2, DCM, 72%; c) hexamine, DCM; d) methyl adipoyl chloride, DIPEA, DCM, 80% over 2 steps; e) sodium borohydride, methanol, 69%; f) CDI, DCM; g) ethylenediamine, DCM; h) 2-chloroacetyl chloride, TEA, DCM, 67% over 3 steps; i) aq. LiOH, THF; j) TSTU, TEA, ACN, 62% over 2 steps. Linker **50** was synthesized by former undergraduate lab member, Bradley Lukasak.

The linker **50** was then used to prepare a *p*-azidobenzyl-caged cMO targeting the T-box transcription factor *no tail a* (*ntla*, 5'-GACTTGAGGCAGACATATTTCCGAT-3', anti-start codon underlined). As mentioned previously, the *ntla* MO (**27**) was purchased (GeneTools) with 5'-amine and 3'-disulfide modifications to allow for bioconjugation to the small molecule linker. In previously reported macrocyclization protocols, the amine was first reacted with the NHS ester prior to thiol reduction and subsequent cyclization via an intramolecular thioether formation.[66, 67] However, to avoid premature reduction of the *p*-azidobenzyl linker, the reduction step must be performed first. As such, the linear *ntla* MO was first incubated with resin-immobilized tris(2-

carboxyethyl)phosphine (TCEP) to reduce the 3'-disulfide to the free thiol, generating reduced *ntla* MO **51**. The reduced MO **51** was then reacted with excess linker **50** to generate the *p*-azidobenzyl *ntla* cMO **53** (Figure 1-33A). Analysis of reaction progression by MALDI-TOF MS revealed that the NHS-ester moiety of **50** first reacts with the primary amine on the MO forming an amide linkage to the 5'-termini to form intermediate **52** (Figure 1-33B-D). The conjugated product then undergoes a spontaneous, intramolecular cyclization through reaction of the free 3'-thiol on the MO with the chloroacetamide moiety on the linker to generate the desired cMO macrocycle **53**. Undesired, linear MO reaction species were removed from the reaction mixture using iodoacetyl- and NHS-functionalized resins and purification by high-performance liquid chromatography (HPLC) (representative chromatogram presented in Figure 1-33E). Further, a doubly conjugated product (**54**) was detected via MALDI-MS analysis, and while this linear species cannot be removed with either of the functionalized resins, this linear species could be removed through HPLC purification (Figure 1-33E).

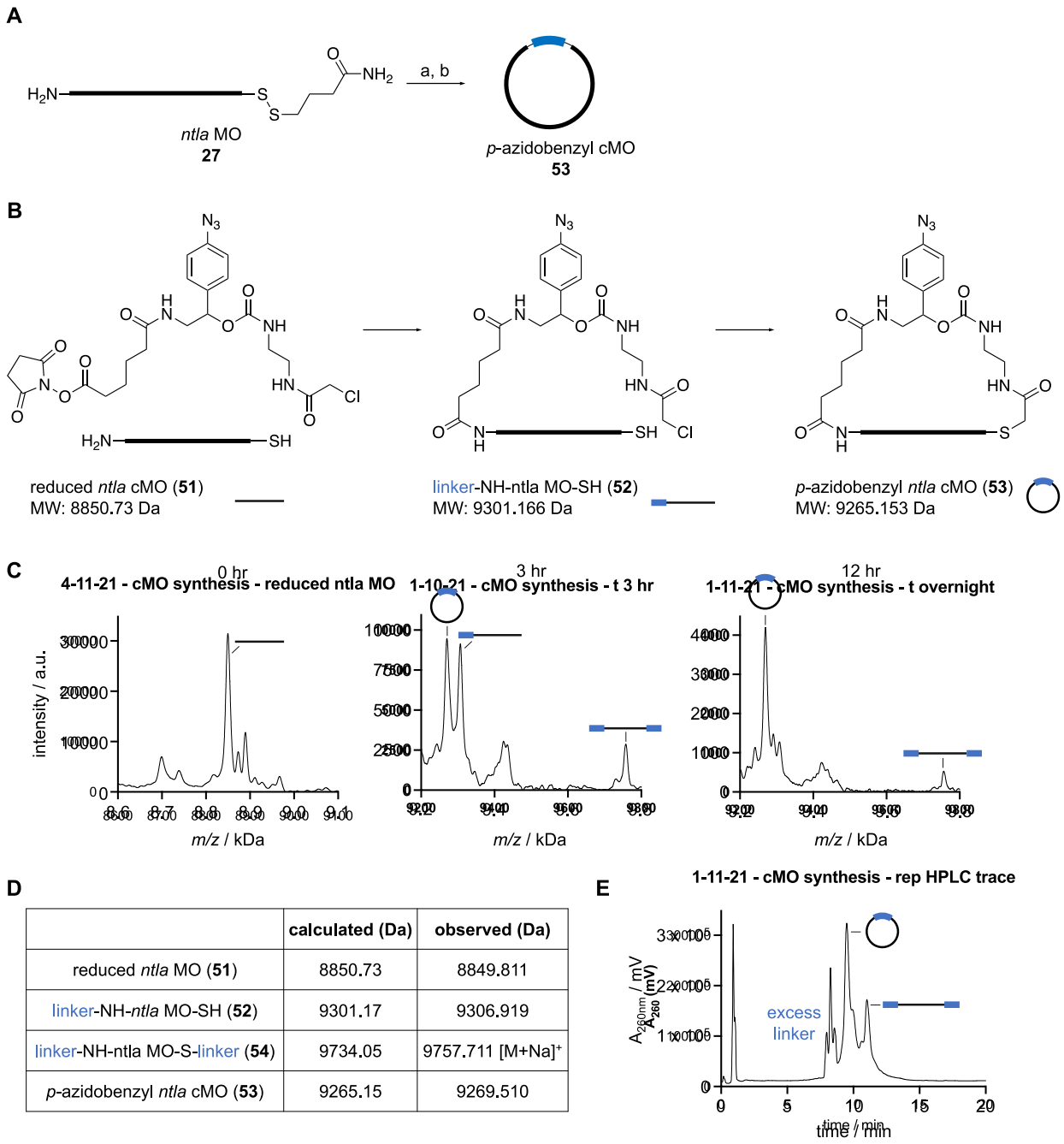

	calculated (Da)	observed (Da)
reduced *ntla* MO (**51**)	8850.73	8849.811
linker-NH-*ntla* MO-SH (**52**)	9301.17	9306.919
linker-NH-ntla MO-S-linker (**54**)	9734.05	9757.711 $[M+Na]^+$
p-azidobenzyl *ntla* cMO (**53**)	9265.15	9269.510

Figure 1-33: Synthesis of *p*-azidobenzyl *ntla* cMO 53
A) General synthetic scheme of *p*-azidobenzyl *ntla* cMO. Reagents and conditions: a) Resin-immobilized TCEP, Tris-HCl buffer pH 8; b) **50**, Tris-HCl buffer pH 8. B) Reaction of macrocyclization step of synthesis. The NHS-ester of the linker initially reacts with the 5'-amine terminus of the MO followed by spontaneous reaction with the free 3'-thiol to generate the macrocyclic product **53**. C) MALDI-TOF MS specta of crude reaction mixture a 0, 3, and 12 hours. C) MALDI-TOF MS masses of key reaction species indicated in panel C. E) Representative HPLC chromatogram of the crude MO cyclization reaction.

1.6.2 Evaluation of Chemical Decaging with *p*-Azido-caged Rhodamine Sensor

We first sought to evaluate phosphine-triggered decaging using a model fluorescence-based system. We designed and synthesized a dextran-conjugated caged Q-rhodamine sensor **55b**. We chose Q-rhodamine as the fluorescent core due to its excellent photostability, high extinction coefficient (>80,000 M^{-1} cm^{-1}),[158] quantum yield of almost 1,[159] and the ability to utilize the near total loss of fluorescence upon amino group acylation for our caging approach.[160] We installed two *p*-azidobenzyl carbamates, which upon exposure to a phosphine undergo a Staudinger reduction-mediated self-immolation as previously described, thus generating the free fluorophore **56** (Figure 1-34A). Sensor **55a/b** was synthesized by fellow Deiters lab member, Joshua Wesalo.

With the sensor **55a** in hand, a small panel of phosphines were screened for fluorescence activation of the sensor (Figure 1-34B). Based on previous reports,[155, 161, 162] 2-(diphenylphosphino)benzamide (**57**, also referred to as 2DPBM) was selected, as it has repeatedly demonstrated superior activation kinetics. Further, it is relatively stable to oxidation, soluble up to 100 μM in water, and nontoxic, making it practical for use in biological experiments. These properties all stem from the *ortho*-amido group, which enhances solubility and improves hydrolysis kinetics via a neighboring group effect.[162] The corresponding carboxylic acid, 2-(diphenylphosphino)benzoic acid (**58**, 2DPBA), which has enhanced solubility in addition to the same set of desirable properties, was evaluated alongside 2DPBM. In an effort to enhance the neighboring group effect by increasing electron density at the amide with minimal perturbation to the P(III) center, a methoxy group was installed at the 4- and 6- positions (**59**, 4-OMe-2DPBM and **60**, 6-OMe-2DPBM, respectively). These phosphines were synthesized by fellow lab member, Joshua Wesalo. Lastly, 4-(diphenylphosphino)benzoic acid (**61**, 4DPBA) and 4-(diphenylphosphino)benzamide (**62**, 4DPBM) were evaluated as controls that are unable to exhibit

the neighboring group effect. Overall, 2DPBM showed the best activation kinetics, decaging the sensor rapidly ($t_{½}$ ~ 11 min) compared to other phosphines tested at the same concentration (50 μM) (Figure 1-34C). Data presented in Figure 1-34C was collected by fellow lab member, Joshua Wesalo.

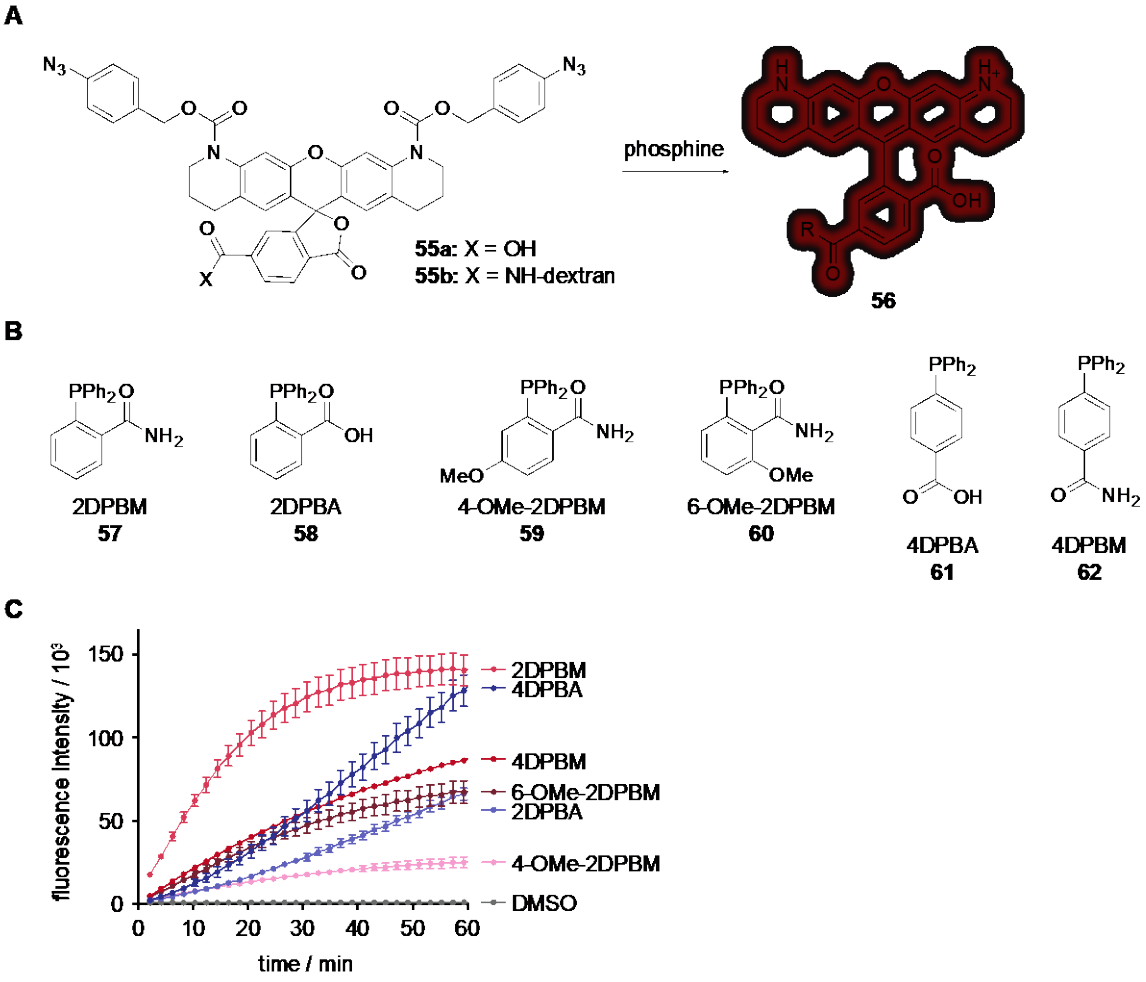

Figure 1-34: Activation of p-azidobenzyl caged rhodamine sensor 55a *in vitro*
A) Q-rhodamine is caged with p-azidobenzyl carbamates. Following exposure to phosphine, fluorescence is activated via a Staudinger reduction-induced decaging. Rhodamine sensor **55a** was synthesized by fellow lab member, Joshua Wesalo. B) Structures and names of phosphine panel. Phosphines **59** and **60** were synthesized by Joshua Wesalo. C) Fluorescence activation of the sensor (5 μM) was monitored over time following incubation with the various phosphines (50 μM) at 29 ºC. Error bars represent standard deviations from the average of three independent experiments. Data in panel C was generated by Joshua Wesalo.

For testing of our chemical decaging strategy in zebrafish embryos, the rhodamine sensor was conjugated to an amine-modified dextran polymer via NHS-activation of the carboxylate functionality on the pendant aryl ring, generating **55b**. Dextran-conjugated fluorophores have a long history of use in zebrafish embryos[163-167] as they are nontoxic, hydrophilic,[168] and prevent diffusion out of the blastomeres.[165, 169]

2DPBM (**57**) was chosen as the phosphine trigger as it demonstrated the fastest kinetics in our initial screen and has been previously been used for Staudinger reductions in mammalian cells.[156, 161] Generally, phosphines are susceptible to oxidation and while the half-life of 2DPBM (**57**) under aquaculture conditions is ~ 200 min (Figure 1-35), we anticipate the rate of phosphine oxidation to be accelerated within a metabolically active zebrafish embryo. The half-life of 2DPBM (**57**) was determined by fellow lab member, Joshua Wesalo.

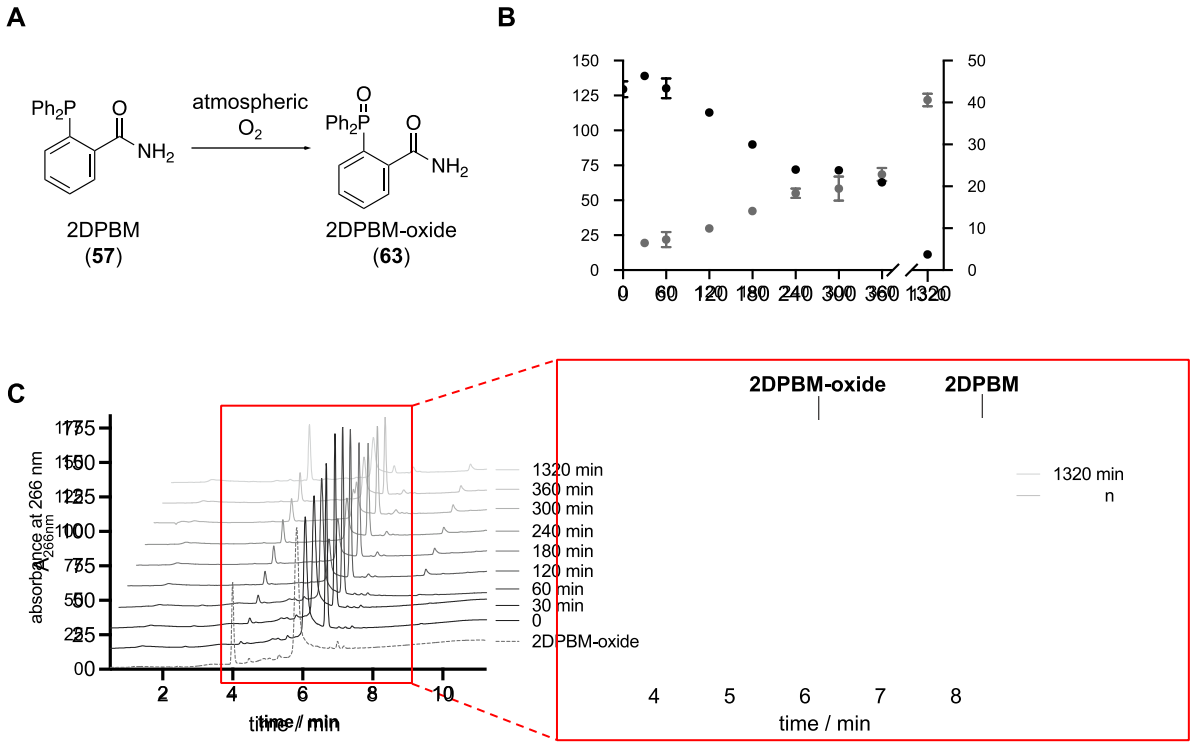

Figure 1-35: Determination of 2DPBM half-life under aquaculture conditions

A) Representative reaction scheme of 2DPBM oxidation by atmospheric oxygen. B) 2DPBM was incubated under zebrafish aquaculture conditions (29 ºC) and oxidation was monitored over time by HPLC. The corresponding peak heights of 2DPBM **57** and 2DPBM-oxide **63** were quantified and plotted to determine the compound half-life (~ 200 min). C) Representative HPLC chromatograms of 2DPBM oxidation under aquaculture conditions. Data was generated by Joshua Wesalo.

To ensure the integrity and availability of the phosphine trigger, treated embryos were soaked in E3 water supplemented with 2DPBM (**57**) and the media was refreshed once after the initial treatment. Previous reports demonstrate rapid diffusion of small molecules into zebrafish embryos, suggesting this method as a quick and efficient means of compound delivery.[170] Furthermore, pulsed phosphine dosing has been demonstrated as a more effective regimen than single dosing in the release of azido-modified pro-drugs in mammalian cell culture.[151] Accordingly, no toxicity was observed in zebrafish embryos treated with 2DPBM (**57**, 100 µM), for varying durations of phosphine exposure (Figure 1-36).

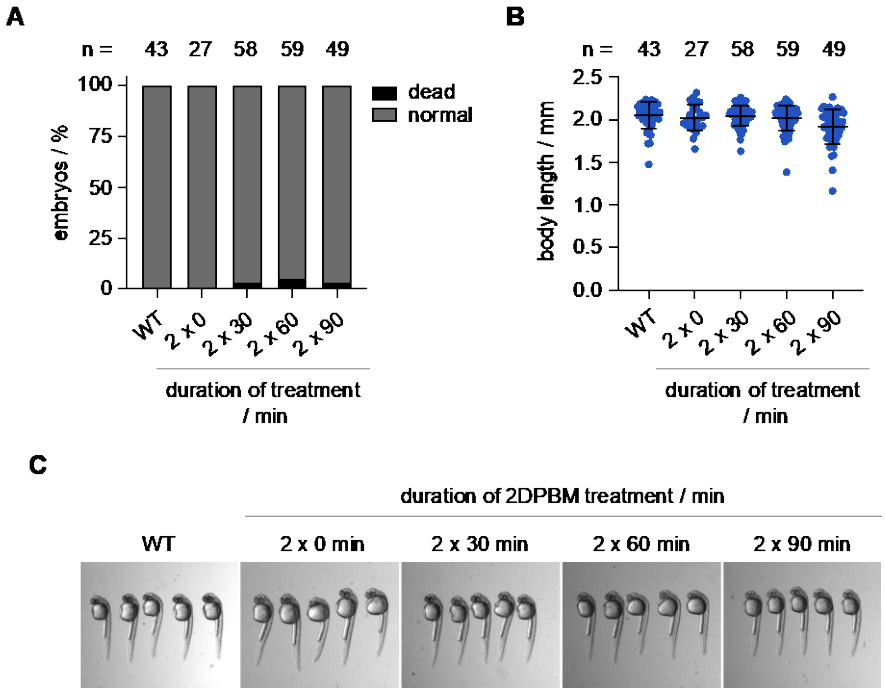

Figure 1-36: Evaluation of 2DPBM toxicity *in vivo*
Toxicity analysis (A), body length quantification (B) and representative images (C) of 24 hpf zebrafish embryos that were soaked in 2DPBM (**57**, 100 µM). Embryos were soaked in E3 water supplemented with 2DPBM beginning at ~

2 hpf. Embryos were soaked for the indicated duration of time before treatment was refreshed and then were incubated for an equivalent length of time. Following treatment, embryos were transferred to E3 water and incubated until 24 hpf for analysis.

Zebrafish embryos at the 1-cell stage were microinjected in the yolk with sensor **55b**, and fluorescence activation was monitored over the first 8 hours of embryonic development (Figure 1-37A-B). Reagents microinjected into the yolk sac prior to the 8-cell stage are globally distributed to the developing embryo via cytoplasmic bridging between the yolk and the dividing cells.[165] At 2 hours post fertilization (hpf), the injected zebrafish embryos were transferred to E3 water supplemented with 2DPBM (**57**, 100 μM) and were incubated at 29 ºC for the indicated amount of time (30, 60, or 90 min). The treatment water was refreshed with fresh 2DPBM-supplemented water and embryos were soaked for an equivalent amount of time. At the conclusion of the second incubation, embryos were transferred into phosphine-free E3 water. Fluorescence activation of the sensor was observed within 30 minutes of 2DPBM (**57**) exposure, suggesting efficient delivery through embryo soaking (Figure 1-37C). Furthermore, no fluorescence increase was detected in injected embryos in the absence of 2DPBM (**57**). These results indicate that the *p*-azidobenzyl carbamate is stable to the developing zebrafish embryo environment, despite previous reports speculating aromatic azides are susceptible to metabolic reduction *in vivo*.[171] Together, these results demonstrate that 2DPBM (**57**) permeates through the chorion into the embryo and validates quick Staudinger reduction-mediated decaging *in vivo*.

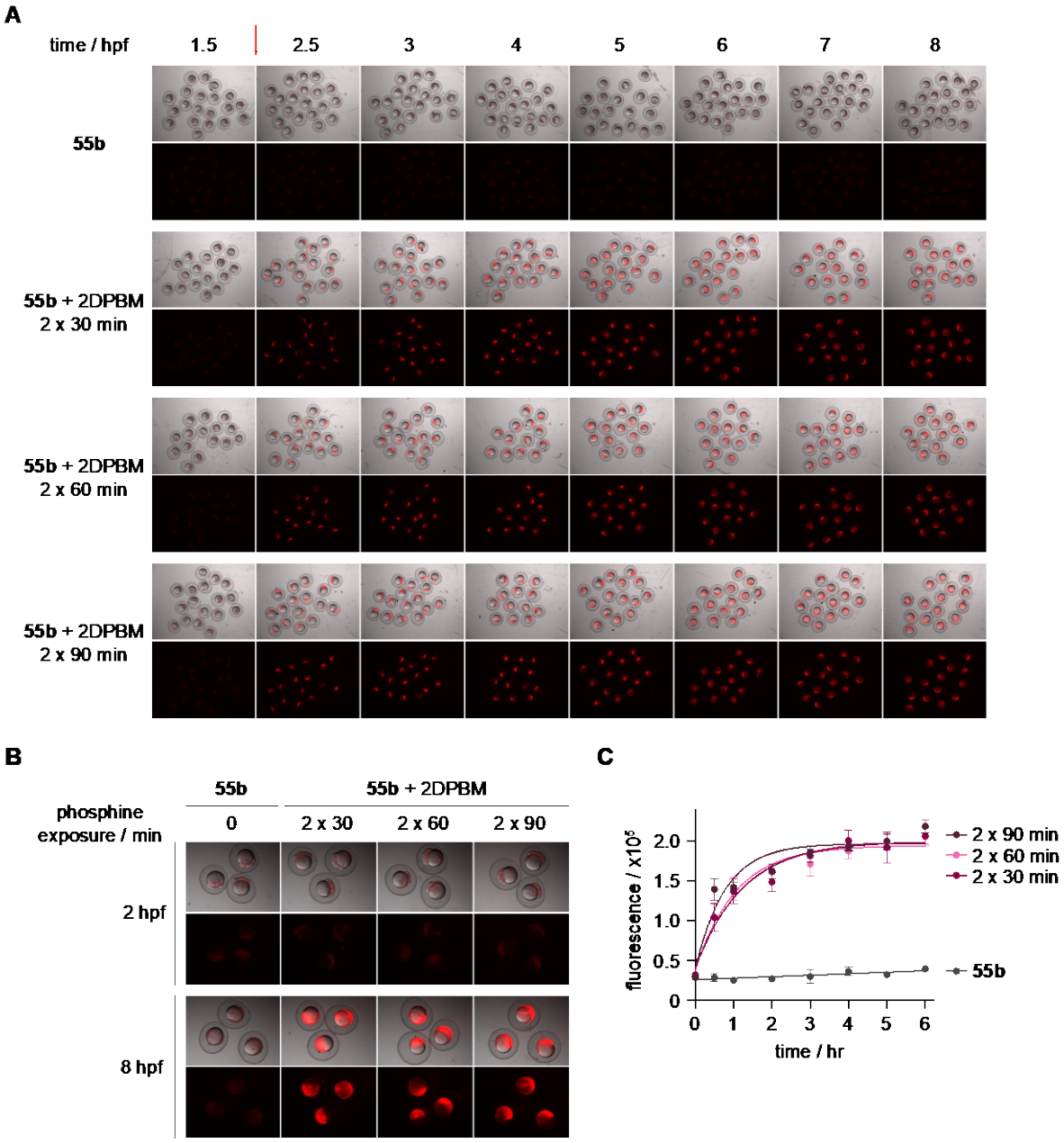

Figure 1-37: Fluorescence activation of *in vivo*

A) Micrographs of zebrafish embryos injected with the caged rhodamine sensor **55b** and soaked in E3 water supplemented with either DMSO (0.2%) or 2DPBM (100 μM). Embryos were subject to pulsed treatment for the indicated duration of time. Fluorescence activation was imaged up to 8 hpf. B) Zoomed in micrographs of select embryos per each condition before phosphine treatment (2 hpf) and 6 hours post-treatment (8 hpf). C) Quantification of rhodamine fluorescence (n = 5 embryos/condition) demonstrates efficient activation of **55b** following 2DPBM treatment and supports the micrograph findings. Error bars represent standard deviations from the average of 5 embryos.

1.6.3 Evaluation of Small Molecule-Triggered cMO Activation

Having validated chemical activation of the *p*-azidobenzyl-caged fluorescent sensor, we next sought to evaluate small molecule-triggered activation of MO function using the *p*-azidobenzyl *ntla* cMO **53**. As mentioned previously, *ntla* encodes the zebrafish ortholog of Brachyury, a T-box transcription factor required for axial mesoderm development.[112, 113, 172] We first analyzed phosphine-triggered linearization of our *p*-azidobenzyl *ntla* cMO *in vitro* (Figure 1-38). The cMO was diluted to a final concentration of 6 μM (so as to mimic the conditions utilized for zebrafish studies)[10] and incubated in the presence of DMSO or 2DPBM (**57**) at 29 ºC. Cleavage of the cMO was assessed by MALDI-TOF mass spectrometry (Figure 1-38B-C). Gratifyingly, in the presence of 2DPBM full linearization of the *p*-azidobenzyl *ntla* cMO was observed as indicated by the detection of the masses consistent with the cleaved iminoquinone methide intermediate **64** and the quenched product **65**. The detection of these linearized products suggests that the self-immolative mechanism of linker cleavage proceeds via the anticipated Staudinger reduction-induced 1,6-elimination discussed previously (Figure 1-31). Furthermore, no linearized MO products are detected when the cMO is treated with vehicle (DMSO) alone, suggesting that the cMO is stable and linearization is chemoselectively induced through a phosphine-mediated azide reduction.

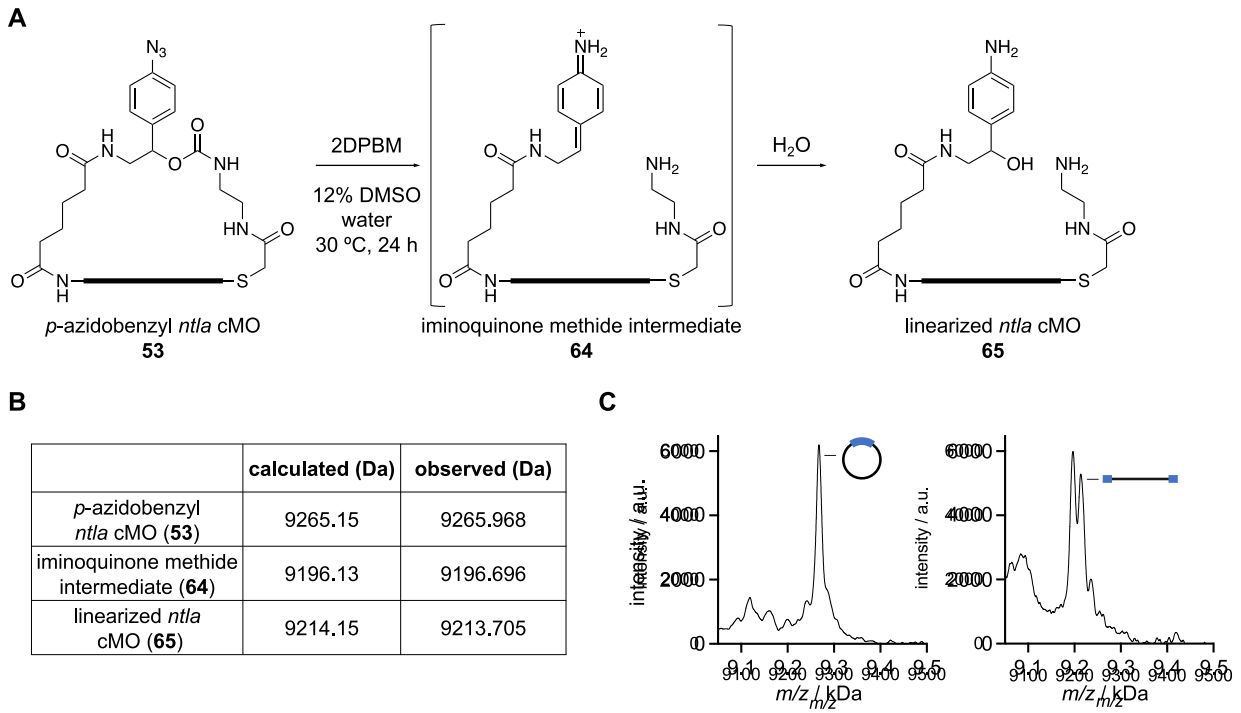

	calculated (Da)	observed (Da)
p-azidobenzyl *ntla* cMO (**53**)	9265.15	9265.968
iminoquinone methide intermediate (**64**)	9196.13	9196.696
linearized *ntla* cMO (**65**)	9214.15	9213.705

Figure 1-38: Linearization of *p*-azidobenzyl *ntla* cMO *in vitro*
A) The structure of the *p*-azidobenzyl caged *ntla* cMO **53**. Upon exposure to the phosphine trigger, the azide is reduced to the corresponding amine via the Staudinger reduction. The linker then undergoes self-immolation through a 1,6-elimination and subsequent decarboxylation, generating an iminoquinone methide intermediate **64**, which is immediately quenched with water to form the linearized product **65**. B) Cleavage of the *p*-azidobenzyl *ntla* cMO **53** by 2DPBM **57** was monitored by MALDI-TOF mass spectrometry. C) MALDI-TOF mass spectrum of the *p*-azidobenzyl *ntla* cMO following 24 h incubation with DMSO (left) and 2DPBM (right).

We next sought to determine if phosphine-triggered linearization would also rescue MO silencing function. The ability of photocaged cMOs to bind to their target sequences following irradiation has previously been exclusively evaluated with biophysical assays including melt temperature measurements, fluorescence activation of molecular beacons, and gel shift assays.[66, 68, 76] However, these assays solely measure target hybridization and do not directly reflect how a cyclic, and subsequently linearized, MO will function within the context of mRNA translation. Thus, we adopted a lysate-based translation system to screen phosphine-triggered MO function *in vitro*.[57, 173] A luciferase reporter construct was generated in which the *ntla* MO binding sequence (ntlaBS) was cloned directly upstream of and in frame with the firefly luciferase coding sequence

(ntlaBS-Fluc). To generate pCS2-ntlaBS-Fluc, we first generated pCS2-Fluc. The coding sequence for Fluc was amplified from pGL3 (Promega) using P29 and P30 and cloned into the BamHI and XhoI sites of the pCS2+ backbone. Then, the consensus binding sequence targeted by the *ntla* MO was cloned upstream of Fluc via PCR amplification of pCS2-Fluc using primers P31 and P32 (which contain overhangs with ntlaBS) and assembled using Gibson assembly. For use as an expression control, the coding sequence of Renilla luciferase (Rluc) was PCR amplified using P33 and P34 and ligated into the BamHI and EcoRI restriction sites of the pCS2+ backbone. For application in the lysate-based expression system, synthetic mRNAs expressing ntlaBS-Fluc and Rluc were prepared by linearizing the corresponding plasmids (pCS2-ntlaBS-Fluc and pCS2-Rluc, respectively) and performing an *in vitro* transcription reaction.

In the presence of a linear *ntla* MO, the expression of the corresponding ntlaBS-Fluc mRNA is repressed due to sequence-specific hybridization of the MO to the target mRNA, blocking the translational machinery from accessing the start codon (Figure 1-39A). We observed a dose-dependent inhibition of luciferase expression with increasing concentration of linear *ntla* MO, and nearly full silencing at 2 μM (Figure 1-39B). When treated at the same concentration, the cyclic *p*-azidobenzyl *ntla* cMO exhibited no significant reduction in luciferase expression, indicating that target binding and silencing activity is impeded by the cMO curvature. Further, the reticulocyte lysate is supplemented with thiol-based reducing agents, dithiothreitol and cysteine, further supporting the stability of the *p*-azidobenzyl carbamate to the endogenous reducing environment. It is only after activation with 2DPBM that nearly full silencing of luciferase expression, identical to that observed with the linear *ntla* MO, is observed (Figure 1-39C). These results indicate that the developed cMO provides an excellent small molecule ON to OFF switch of gene function, based on a Staudinger reduction.

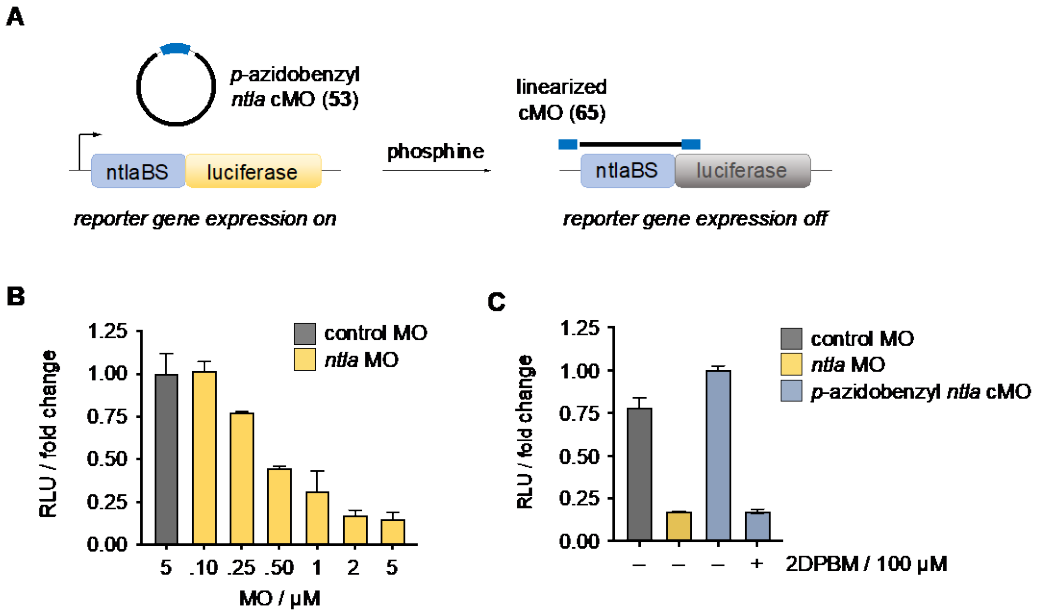

Figure 1-39: Small molecule-triggered activation of MO function *in vitro*
A) In the presence of the cyclic *p*-azidobenzyl *ntla* cMO **53**, luciferase is expressed as cyclization impedes target binding and masks antisense activity. Treatment with phosphine induces cMO cleavage, generating the active, linearized MO which represses luciferase expression. B) Titration of linear *ntla* MO induces dose-dependent silencing of Fluc expression. C) Nearly complete silencing of Fluc expression is observed following 2DPBM-mediated activation of the cyclic *p*-azidobenzyl *ntla* cMO **53**, while no effect on reporter expression is observed with cMO alone. Data represents the means ± standard deviation from at least three independent experiments.

Having established efficient, conditional control of ntlaBS-driven reporter gene expression *in vitro*, we next investigated the ability of our cyclic *p*-azidobenzyl *ntla* cMO **53** to regulate endogenous *ntla* expression in zebrafish embryos using small molecule control. Silencing of *ntla* expression during the early stages of embryo development induces distinct morphological defects including a loss of notochord cells, posterior truncation, and U-shaped somites, which are evident by 24 hours post-fertilization (hpf) (Figure 1-40A).[112, 113] Zebrafish embryos were microinjected with either a negative control MO, a linear *ntla* MO, or our *p*-azidobenzyl *ntla* cMO. As mentioned previously, reagents microinjected into the yolk sac prior to the 8-cell stage are globally distributed to the developing embryo via cytoplasmic bridging between the yolk and the dividing cells.[165] As previous reports with photocaged cMOs report some phenotype in the absence of conditional trigger (~ 15-25%),[66-69] cMOs must be carefully dosed so as to avoid this background activity. In

our hands, an obvious trend between the concentration of the injection solution and background activity of the *p*-azidobenzyl *ntla* cMO reagent was evident (Figure 1-40B). We hypothesize that injection of more concentrated solutions of cMO increases the effective intracellular concentration of the cMO relative to the target transcript prior to the onset of gene (in this case, *ntla*) expression.[174] While background activity can result from other factors inherent to the MO sequence (G/C content) or cMO curvature, the concentration of the injection solution must be carefully determined to minimize background silencing activity in the embryo environment.

To evaluate small molecule-triggered cMO activation *in vivo*, zebrafish embryos were microinjected with 100 pg (2 nL, 50 pg/nL MO) of either a negative control MO, a linear *ntla* MO, or our *p*-azidobenzyl *ntla* cMO. At 3 hpf, embryos were transferred to E3 water supplemented with either DMSO (0.2%) or 2DPBM (100 μM) and soaked following the treatment regimen that we identified as highly efficient in Figure 1-37: two 90-minute incubations. Following treatment, embryos were transferred to E3 water and incubated until 24 hpf, at which point they were analyzed for the *ntla* loss-of-function phenotype (Figure 1-40C). Since, the hallmark indicator of the *ntla* morphant phenotype includes loss of posterior tissue, phenotypic strength was scored based on quantification of shortened embryo body length (Figure 1-40D). Embryos injected with the cyclic *p*-azidobenzyl *ntla* cMO **53** and exposed to DMSO exhibited minimal phenotypic changes. These results are consistent with our luciferase reporter assay (Figure 1-39), indicating that the curvature induced through macrocyclization with our *p*-azidobenzyl linker is sufficient to block MO activity *in vivo*. The cMO remains functionally inert until treatment with 2DPBM, as evidenced by 82% of cMO-injected embryos exhibiting a strong, *ntla* morphant phenotype after treatment with the small molecule phosphine trigger. Furthermore, wild-type zebrafish embryos treated with 2DPBM at the same concentration and duration exhibit no obvious toxicity or

developmental defects (Figure 1-36), supporting that the phenotypic result can be specifically attributed to MO-induced gene silencing and establishing the Staudinger reduction as a potentially broadly applicable conditional control mechanism for biological processes in the zebrafish model.

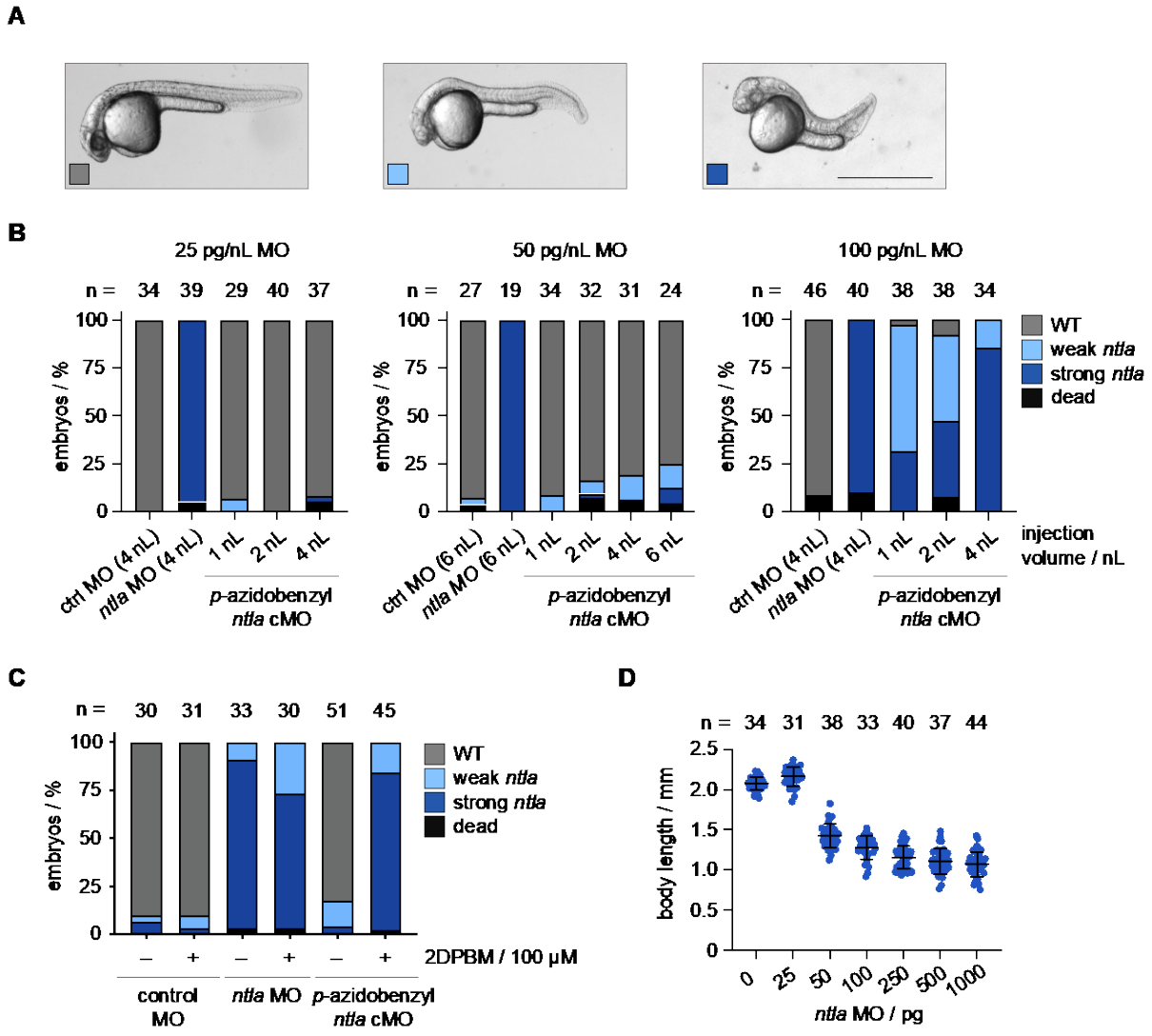

Figure 1-40: Small molecule-triggered activation of *p*-azidobenzyl *ntla* cMO *in vivo*
A) Representative images of *ntla* morphant phenotypes in zebrafish embryos at 24 hpf. Scale bar equals 1 mm. B) Phenotypic analysis of embryos injected with cMO solutions varying in concentration. C) Phenotypic scoring of embryos injected with the indicated morpholino reagent and soaked in E3 water supplemented with DMSO (0.2%) or 2DPBM (**57**, 100 µM). D) Body length quantification of zebrafish embryos at 24 hpf injected at the 1-cell stage with increasing amounts of linear *ntla* MO.

To demonstrate the robustness of our approach, we synthesized a second *p*-azidobenzyl cMO targeting *spadetail* (*spt*). *Spt* is a T-box transcription factor that acts downstream of *ntla* and is a key player in directing mesodermal cell fates during trunk development.[172, 175-177] While *spt* morphants exhibit relatively normal tail development, they lack somites in the trunk and tail. Additionally, the trunk and mesodermal progenitor cells in *spt* null embryos are mislocalized and form a mass of cells at the end of the tail, which serves as the predominant indicator of the *spt* phenotype (Figure 1-41A).[178, 179]

Zebrafish embryos were injected with the cyclic *p*-azidobenzyl *spt* cMO (**66**) and soaked in E3 water supplemented with 2DPBM (**57**, 100 μM) or DMSO (negative control) following the same treatment regimen as established for *ntla* silencing. At 24 hpf, embryos were scored for a loss-of-function *spt* phenotype (Figure 1-41B). Zebrafish embryos injected with the cMO and soaked with vehicle (0.2% DMSO) demonstrate minimal phenotypic response (16%), consistent with that observed following injection of the cyclic *p*-azidobenzyl *ntla* cMO. Following soaking with phosphine trigger, MO-mediated *spt* silencing is efficiently rescued as evidenced by the majority of embryos exhibiting strong *spt* morphant phenotype (84%), comparable to that observed in embryos injected with the linear *spt* MO. Taken together, these results validate that bioorthogonal small molecules, such as azides and phosphines, can be effectively engineered into molecular switches to regulate gene expression in live animals.

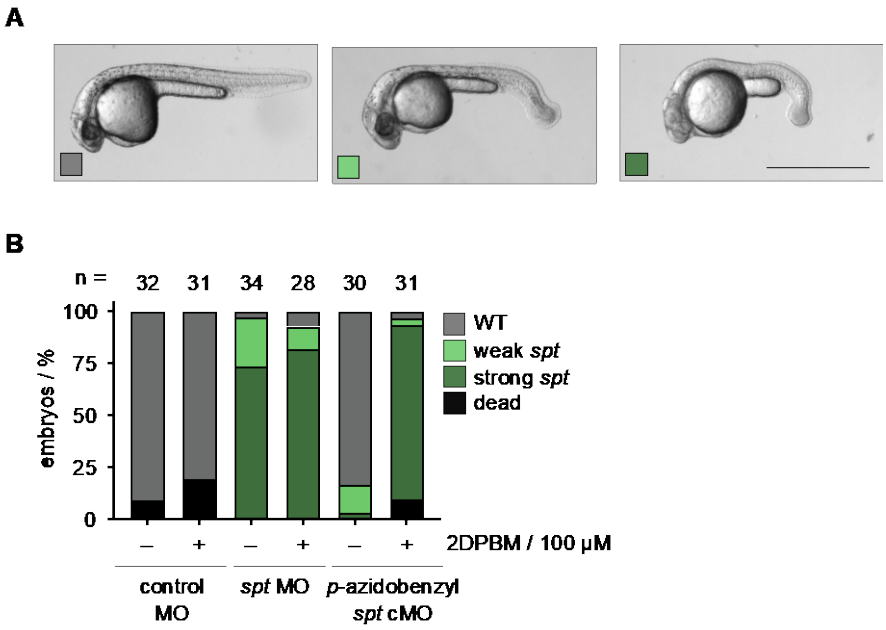

Figure 1-41: Small molecule-triggered activation of *p*-azidobenzyl *spt* cMO *in vivo*
A) Representative images of *spt* morphant phenortpes in zebrafish embryos at 24 hpf. B) Phenotypic scoring of zebrafish embryos injected with the indicated morpholino reagents and either soaked in E3 water supplemented with DMSO (0.2%) or 2DPBM (100 µM). Scale bar equals 1 mm.

1.6.4 Summary and Outlook

In summary, we have successfully demonstrated the first example of a chemically controlled oligonucleotide-based tool to regulate gene function *in vitro* and *in vivo*. By exploiting the biorthogonality of the Staudinger reduction, we designed and synthesized a *p*-azidobenzyl linker that can undergo self-cleavage following exposure to a phosphine trigger. The use of a Staudinger reduction as an effective and rapid chemical decaging strategy was established through the successful, phosphine-triggered activation of a rhodamine-based fluorescent sensor. Furthermore, the caged fluorophore demonstrated stability of aryl azide-based caging groups in an aquatic embryo. Based on these results, we then demonstrated efficient rescue of MO silencing following small molecule exposure, as evidenced by silencing of reporter gene expression in a

lysate translation system. Finally, the functionality and robustness of our modular approach for controlling endogenous gene expression with *p*-azidobenzyl cMOs was validated through small molecule-triggered silencing of two separate, developmentally relevant genes in zebrafish embryos.

The strategy disclosed herein complements the current suite of optically- and enzymatically- triggered antisense agents, and introduces, for the first time, small molecule control of nucleic acid function. The phosphine trigger induces rapid cMO activation with precise temporal resolution and enables user-controlled gene silencing in deep and opaque tissues, overcoming some of the limitations of optochemical and optogenetic approaches. Additionally, this strategy can be easily applied to other nucleic acid-based technologies, as chemical modifications are readily introduced into oligonucleotides. We anticipate that small molecule-activated cMOs will nicely complement current cyclic cMO strategies and can be used in combination with other methods to independently control the expression of a single gene within synchronous multigene networks.

1.6.5 Materials and Methods

1.6.5.1 Synthetic Protocols

General chemical methods. All reagents were purchased from commercial suppliers and used without further purification. All reactions were performed in flame dried glassware and stirred magnetically. Flash chromatography was performed using an ISCO CombiFlash RF (Teledyne) with normal phase silica gel cartridges. NMR spectra were recorded on Bruker Ultrasheild 300 MHz, 400 MHz, or 500 MHz spectrometers. Analytical LC-MS data were collected on a Shimadzu LCMS-2020 and a Thermoscientific Q-Exactive Orbitrap. High

resolution mass spectrometry was performed by the University of Pittsburgh facilities. All morpholino compounds were co-spotted with sinapic acid matrix (10 mg/mL in 1:1 water/acetonitrile containing 0.1% trifluoroacetic acid) on a Bruker Daltonics MSP 96 target ground steel BC MALDI plate (Cat. No. 8280799) and analyzed on a Bruker Daltonics UltrafleXtreme MALDI TOF-mass spectrometer (linear positive mode).

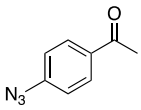

4-Azidoacetophenone (43). Compound **43** was synthesized by former lab member Bradley Lukasak following a previously reported protocol. Spectral data matched previous literature reports.[156]

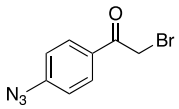

1-(4-Azidophenyl)-2-bromoethanone (44). Compound **44** was synthesized by former lab member Bradley Lukasak following a previously reported protocol. Spectral data matched previous literature reports.[157]

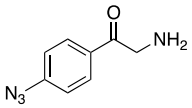

2-Amino-1-(4-azidophenyl)ethanone (45). Hexamethylenetetramine (416 mg, 2.97 mmol) was added to a solution of **44** (509 mg, 2.12 mmol) in dichloromethane (5 mL). The reaction mixture was stirred at room temperature until an insoluble white salt was formed (~90 min). The mixture was filtered and the resulting white solid was washed sequentially with dichloromethane (25 mL) and diethyl ether (25 mL). The solid was dissolved in a mixture of ethanol (4.5 mL) and concentrated HCl (0.75 mL) and was stirred at room temperature until the formation of a white

solid (~40 min). The suspension was stirred at room temperature for an additional hour. The reaction mixture was then vacuum filtered, and the resulting white solid was washed sequentially with dichloromethane (25 mL) and diethyl ether (25 mL). The crude solid was dried and used without further purification. ^{1}H NMR (400 MHz, d6-DMSO) δ 8.36 (br s, 2H), 8.04 (d, J = 8.4 Hz, 2H), 7.30 (d, J = 8.8 Hz, 2H), 4.57 (d, J = 5.2 Hz, 2H). ^{13}C NMR (400 MHz, DMSO-d6) δ 191.5, 145.6, 130.3, 119.5, 44.6. HRMS-ESI m/z calculated for $C_8H_8N_4O$ $[M+H]^+$ 177.07709, observed 177.07790.

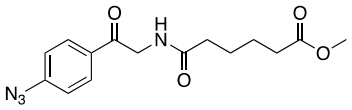

Methyl 6-((2-(4-azidophenyl)-2-oxoethyl)amino)-6-oxohexanoate (46). Compound **45** (451 mg, 2.12 mmol) was dissolved in dichloromethane (20 mL). DIPEA (953 µL, 5.51 mmol) was added to the solution and the mixture was cooled to 0 ºC on ice. Methyl adipoyl chloride (432 uL, 2.54 mmol) was dissolved in dichloromethane (2 mL) and added dropwise to the solution while stirring at 0 ºC. This solution was gradually warmed to room temperature while stirring overnight. The reaction mixture was concentrated under reduced pressure, redissolved in ethyl acetate (25 mL) and washed with saturated $NaHCO_3$ (50 mL). The aqueous layer was extracted with ethyl acetate (3 x 40 mL). The organic layers were combined, washed with brine (50 mL), dried with anhydrous Na_2SO_4 (~10 g), filtered over a cotton plug, and concentrated under reduced pressure. The product was purified by flash column chromatography on SiO_2 eluting with 50% ethyl acetate in hexanes to yield **46** (538 mg, 80% over two steps) as a white solid. ^{1}H NMR (400 MHz, CDCl3) δ 7.97 (d, J = 8.4 Hz, 2H), 7.11 (d, J = 8.8 Hz, 2H), 6.57 (br s, 1H), 4.72 (d, J = 4.4 Hz, 2H), 3.66 (s, 3H), 2.33 (m, 4H), 1.69 (m, 4H). ^{13}C NMR (400 MHz, CDCl3) δ 192.9, 174.0, 172.9, 146.2, 131.1, 130.1, 119.5, 51.7, 46.4, 36.2, 33.8, 25.2, 24.6. HRMS-ESI m/z calculated for $C_{15}H_{18}N_4O_4$ $[M+Na]^+$ 341.12220, observed 341.12320.

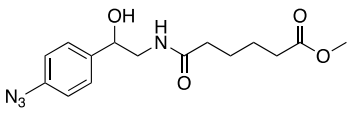

Methyl 6-((2-(4-azidophenyl)-2-hydroxyethyl)amino)-6-oxohexanoate (47). Sodium borohydride (5 mg, 0.12 mmol) was weighed into a flame dried flask. Compound **46** (77 mg, 0.24 mmol) was dissolved in anhydrous methanol (4.8 mL), cooled to 0 ºC in an ice bath, and added to the reaction vessel under a nitrogen atmosphere. The reaction was stirred at 0 ºC for 10 minutes and then gradually warmed to room temperature. The reaction was monitored by TLC running in 80% ethyl acetate in hexanes. Following complete disappearance of starting material after ~45 minutes, the reaction mixture was quenched with water (10 mL). The product was extracted using ethyl acetate (3 x 15 mL). The organic layers were combined, was washed with brine (25 mL), dried with anhydrous Na_2SO_4 (~10 g), filtered over cotton, and concentrated under reduced pressure. The crude product was purified by flash column chromatography on SiO_2 eluting with 80% ethyl acetate in hexanes to yield **47** (53.2 mg, 69%) as an off-white foamy solid. ^{1}H NMR (400 MHz, CDCl3) δ 7.33 (d, J = 8.4 Hz, 2H), 6.99 (d, J = 8.4 Hz, 2H), 6.21 (br s, 1H), 4.81 (dd, J = 2.8 Hz, 7.6 Hz, 1H), 3.65 (s, 3H), 3.64-3.61 (m, 1H), 3.26-3.32 (m, 1H), 2.31 (m, 2H), 2.20 (m, 2H), 1.62 (m, 4H). ^{13}C NMR (500 MHz, CDCl3) δ 174.4, 174.2, 139.6, 138.7, 127.4, 119.2, 73.2, 51.8, 47.7, 36.1, 33.7, 25.1, 24.3. HRMS-ESI m/z calculated for $C_{15}H_{20}N_4O_4$ $[M+H]^+$ 321.15573, observed 321.15508.

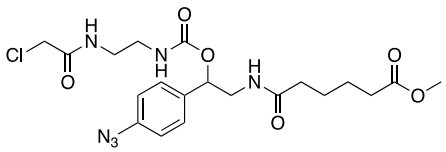

Methyl 9-(4-azidophenyl)-1-chloro-2,7,12-trioxo-8-oxa-3,6,11-triazaheptadecan-17-oate (48). Compound **47** (55 mg, 0.170 mmol) was dissolved in dichloromethane (1 mL) and added to 1,1'-carbonyldiimidazole (69 mg, 0.425 mmol) dissolved in anhydrous dichloromethane (700

μL). The reaction was stirred under a nitrogen atmosphere at room temperature and monitored by TLC with 90% ethyl acetate in hexanes until full disappearance of starting material was observed (~2 hours). The reaction mixture was then diluted with dichloromethane (15 mL), washed twice with water (2 x 20 mL), dried over anhydrous $MgSO_4$ (~5 g), filtered over cotton, and concentrated under reduced pressure to yield the crude imidazole carbamate as a yellow gum. The imidazole carbamate was dissolved in anhydrous dichloromethane (750 μL) and the solution was cooled to 0 °C in an ice bath. Ethylenediamine (20 μL, 0.3 mmol) was added dropwise, and the reaction mixture gradually warmed to room temperature over 1 hour. The solvent was removed under reduced pressure and the crude amine (colorless oil) was dried under high vacuum for 3 hours. Without further purification, the crude material was dissolved in dichloromethane (1.7 mL) and DIPEA (180 μL, 1.02 mmol) and cooled to 0 °C in an ice bath. 2-Chloroacetyl chloride (40 μL, 0.51 mmol) dissolved in dichloromethane (1.3 mL) was added to the solution, dropwise and slowly. The mixture was allowed to stir at room temperature for 20 minutes. The reaction mixture was quenched through the addition of 5% saturated aq. $NaHCO_3$ (15 mL) and extracted with ethyl acetate (3 x 20 mL). The organic layers were combined, dried over anhydrous Na_2SO_4 (~10 g), filtered over cotton, and concentrated under reduced pressure. The crude residue was purified by flash column chromatography on SiO_2 eluting with chloroform/acetone in a stepwise gradient from 1:0 to 1:1 to yield **48** (55 mg, 67%) as an off-white foamy solid. ^{1}H NMR (400 MHz, CDCl3) δ 7.31 (d, J = 8.4 Hz, 2H), 7.21 (br s, 1H), 7.01 (d, J = 8.4 Hz, 2H), 5.97 (br s, 1H), 5.76 (m, 1H), 5.45 (br s, 1H), 4.02 (s, 2H), 3.83-3.88 (m, 1H), 3.67 (s, 3H), 3.51-3.55 (m, 1H), 3.39-3.44 (m, 3H), 3.24-3.27 (m, 1H), 2.34 (s, 2H), 2.18 (d, J = 4 Hz, 2H), 1.63 (br s, 5H). ^{13}C NMR (400 MHz, CDCl3) δ 174.3, 173.1, 167.2, 156.3, 140.3, 134.8, 127.9, 119.4, 74.8, 51.8, 44.3, 42.7, 41.1, 40.2,

36.3, 33.8, 25.2, 24.4. HRMS-ESI m/z calculated for $C_{20}H_{27}ClN_6O_6$ $[M+H]^+$ 483.17534, observed 483.17560.

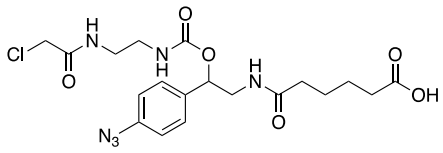

9-(4-Azidophenyl)-1-chloro-2,7,12-trioxo-8-oxa-3,6,11-triazaheptadecan-17-oic acid (49). Compound **48** (20 mg, 41 μmol) was dissolved in tetrahydrofuran (700 μL), and the solution was cooled to 0 °C in an ice bath. An aqueous solution of lithium hydroxide (0.5 M, 500 μL) was slowly added to the reaction mixture while stirring at room temperature. The reaction mixture was stirred for 2 hours, after which the pH of the reaction was adjusted to pH 3 with 1M HCl. The reaction was diluted to 10 mL with water and was then extracted with ethyl acetate (3 x 15 mL). The organic layers were combined, dried over anhydrous Na_2SO_4 (~5 g), filtered over cotton, and concentrated under reduced pressure to yield the pure carboxylic acid as a beige solid (20.2 mg) in quantitative yield. The carboxylic acid was used in the next step without further purification. ^{1}H NMR (400 MHz, DMSO-d6) δ 12.15 (br s, 1H), 8.21 (t, J = 5.2 Hz, 1H), 7.92 (t, J = 5.6 Hz, 1H), 7.32 (d, J = 8.4 Hz, 2H), 7.27 (t, J = 5.6 Hz, 1H), 7.10 (d, J = 8 Hz, 2H), 5.57 (t, J = 6.8 Hz, 1H), 4.25 (s, 1H), 4.02 (s, 2H), 3.33-3.36 (m, 4H), 3.10-3.13 (m, 3H), 3.00-3.03 (m, 2H), 2.14-2.17 (m, 2H), 2.01-2.04 (m, 2H), 1.41 (br s, 4H). ^{13}C NMR (400 MHz, DMSO-d6) δ 174.3, 172.1, 166.1, 155.5, 138.8, 136.3, 128.0, 119.0, 73.1, 43.5, 42.6, 41.6, 34.9, 33.6, 24.7, 24.0. HRMS-ESI m/z calculated for $C_{19}H_{25}ClN_6O_6$ $[M+H]^+$ 468.15241, observed 469.16187.

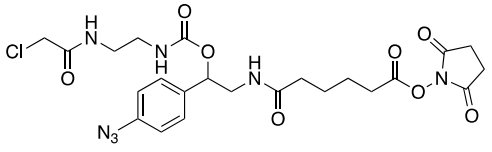

2,5-Dioxopyrrolidin-1-yl-9-(4-azidophenyl)-1-chloro-2,7,12-trioxo-8-oxa-3,6,11-triazaheptadecan-17-oate (50). In a flame-dried vial, **49** (20.2 mg, 43 μmol) was dissolved in dry acetonitrile (700 μL) followed by the addition of triethylamine (15 μL, 0.108 mmol). The reaction was cooled to 0 ºC in an ice bath for 10 minutes under a nitrogen atmosphere. TSTU (19.3 mg, 64 μmol) was added to the reaction and the reaction was stirred at 0 ºC for 30 minutes. The reaction was removed from the ice bath and gradually warmed to room temperature, while stirring, for 2.5 hours. Following complete disappearance of the starting material on TLC (running in 4% methanol in dichloromethane), the solvent was evaporated under reduced pressure and the residue was redissolved in dichloromethane (~500 μL). The crude material was purified by flash column chromatography on SiO_2 eluting with 4% methanol in dichloromethane to yield **50** as a white foamy solid (15.1 mg, 62% over 2 steps). ^{1}H NMR (400 MHz, CDCl3) δ 7.31 (d, J = 8 Hz, 2H), 7.16 (br s, 1H), 7.01 (d, J = 8.4 Hz, 2H), 6.12 (m, 1H), 5.74 (m, 1H), 5.38 (m, 1H), 4.00 (d, 2H), 3.81 (m, 1H), 3.47 (m, 4H), 3.25 (m, 1H), 2.84 (br s, 3H), 2.80 (s, 1H), 2.63 (m, 2H), 2.22 (m, 2H), 1.75 (m, 4H). ^{13}C NMR (400 MHz, CDCl3) δ 172.9, 169.5, 168.7, 167.2, 156.4, 140.2, 134.8, 127.9, 119.4, 74.7, 44.4, 42.7, 40.9, 40.2, 38.9, 35.9, 30.8, 25.8, 24.8, 24.1. HRMS-ESI m/z calculated for $C_{23}H_{28}ClN_7O_8$ [M+H]+ 565.16879, observed 566.17851.

Synthesis of *p*-azidobenzyl cyclic cMOs. The cyclic *ntla* and *spt* cMOs bearing a *p*-azidophenyl cleavable linker were synthesized using a 25-base MO oligomer with 5'-amine and 3'-disulfide modifications purchased from GeneTools, LLC. Sequences can be found in Table 1-4. Concentrations of all MO and cMO solutions were determined by taking the average of three measurements of the MO solution diluted in 0.1 N HCl (1:10 or 1:20) and measuring absorbance at 265 nm on an ND-1000 NanoDrop spectrophotometer following the recommended protocol from GeneTools (see Section 4.3.2).

Table 1-4: List of morpholinos and sequences
Terminal modifications are specified. The disulfide amide is for sulfhydryl linkage. The anti-start codon is indicated in **bold**.

Morpholino	Sequence (5' to 3')
control (**67**)	CCTCTTACCTCAGTTACAATTTAT
no tail a (*ntla*) (**27**)	amine-GACTTGAGGCAGA**CAT**ATTTCCGAT-disulfide amide
spadetail (*spt*) (**68**)	amine-CTCTGATAGCCTG**CAT**TATTTAGCC-disulfide amide

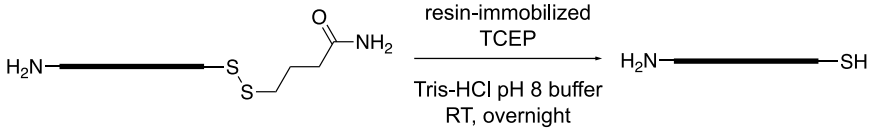

Reduced, linear *ntla* MO (51). Resin immobilized TCEP (400 µL) (Pierce Biotechnology, Inc.) was washed with 0.1 M Tris-HCl buffer pH 8 (3 x 400 µL) in a centrifuge filter tube. The 25-base MO oligomer (*ntla* **27** or *spt* **68**) (100 µL, 1 mM) was dissolved in 0.1 M Tris-HCl buffer pH 8 (400 µL) and added to the immobilized TCEP. The reaction mixture was shaken at room temperature overnight. The crude MO was collected by centrifugation at 1500 rpm for 1 minute. The gel slurry was washed with Tris-HCl buffer pH 8 (100 µL) and the filtrates were combined. The reduced MO was purified on a Shimadzu LC20AD HPLC (5-60% acetonitrile in 0.1M TEAA buffer, 20 minute gradient) on a ACE Excel 3 Oligo Beta Test HPLC column (100 x 4.6 mm, serial no. A252326) using a 1 mL/min flow rate. The MO was monitored via absorbance at 260 nm on a SP-20AD UV/Vis detector and eluted as one broad peak at ~ 9-11 minutes. The purified, reduced MO product was analyzed by MALDI-TOF mass spectrometry co-spotted with a sinapic acid matrix (2:1 matrix/analyte), calculated: 8851.719 Da, observed: 8851.853 Da according to the protocol outlined in Section 4.3.3). The purified MO fractions were pooled and lyophilized to dryness.

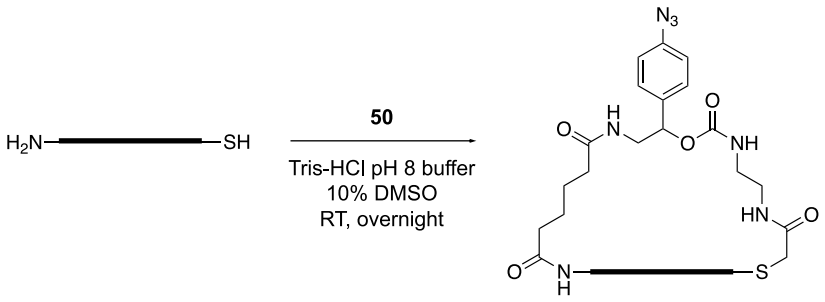

Cyclic *p*-azidobenzyl cMO (*ntla* 53, *spt* 66). The purified, reduced MO **51** was resuspended in water (110 µL) and diluted to a final concentration of 65 µM in 0.05 M Tris-HCl pH 8 buffer (1.2 mL). To this, the *p*-azidobenzyl linker **50** (5.9 µL from a 50 mM stock in DMSO) was diluted to 2 mM in DMSO (134.1 µL). The linker solution in DMSO (140 µL, 2 mM) was added to the MO solution (total volume 1.4 mL), and the reaction was briefly vortexed and incubated at room temperature overnight. The cyclization was monitored by MALDI-TOF MS (co-spotting with sinapic acid matrix and water until dry) until complete cyclization was observed: calculated 9266.141 Da, observed 9265.460 Da. The cyclized cMO was purified on a Shimadzu LC20AD HPLC under the same conditions mentioned above (see protocol in Section 4.3.4). A representative chromatogram is shown in Figure 1-33D. The collected fractions were combined and lyophilized to dryness.

The dry *p*-azidobenzyl cMO (*ntla* **53**, *spt* **66**) was resuspended in 100 µL water. To remove any unreacted amine-modified linear MO, the cMO was further purified with NHS-activated agarose (Thermo Scientific P126196). Dry NHS-activated agarose (20 mg) was suspended in PBS (400 µL) in a spin cup filter (Thermo Scientific PI69702). The swollen resin was centrifuged (5000 rpm, 1 minute) and the swelling buffer was discarded. The cMO solution was diluted 1:1 with PBS (200 µL total volume) and added to the NHS-agarose resin. The tube was inverted slowly to mix and then incubated at room temperature for 30 minutes per the manufacturer's recommended protocol. Following incubation, the tube was centrifuged (5000 rpm, 1 min) and the flow-through

was collected. The resin was rinsed with PBS (100 µL), and the flow-through was combined with that from the first spin. The combined elutions were purified on a Shimadzu LC-20AD HPLC using the same conditions mentioned previously (see protocol in Section 4.3.4). The collected fractions were combined and lyophilized to dryness.

To remove any unreacted, thiol-modified linear MO, the cMO was purified with SulfoLink Coupling Resin (Thermo Scientific PI20401). Resin slurry (100 µL) was pipetted into a spin cup filter and rinsed with the manufacturer's recommended coupling buffer (50 mM Tris, 5 mM EDTA-Na pH 8.5) twice (400 µL/rinse). Following each rinse, the spin cup filter was centrifuged (1000 rpm, 1 minute) and the flow-through was discarded. The dry cMO was resuspended in water (50 µL) and diluted 1:1 with the coupling buffer (100 µL total volume). The cMO solution was directly added to the resin, and rocked end-over-end at room temperature for 20 minutes, and then allowed to settle on the benchtop for 30 minutes per the manufacturer's protocol. Following incubation, the cMO solution was collected by centrifugation (5000 rpm, 2 minutes). The resin was rinsed once with coupling buffer (100 µL) and centrifuged again (10,000 rpm, 2 minutes) to ensure all cMO was collected. The flow-through was combined and the cMO was purified on a Shimadzu LC20-AD HPLC using the same conditions as mentioned previously (see Section 4.3.4). The collected HPLC fractions were combined and the cMO was lyophilized to dryness.

The purified, dry cMO was resuspended in water (25 µL) and the concentration was determined on a ND-1000 NanoDrop spectrophotometer following the recommended protocol from GeneTools (1:10 dilution in 0.1 N HCl, 265 nm, constant = 34) according to the protocol outlined in Section 4.3.2.[180] A typical concentration was ~150-200 ng/µL and the MO was aliquoted (1-3 µL per aliquot), and stored at –20 ºC.

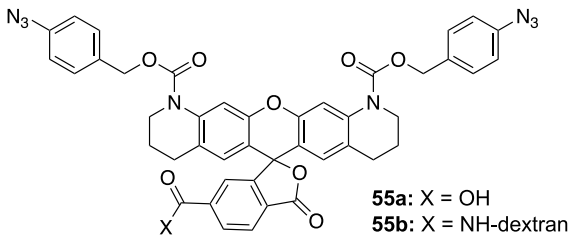

Caged Q-rhodamine sensor (55a, dextran-conjugated 55b). Compound **55a/b** was synthesized and fully characterized by fellow lab member Joshua Wesalo.

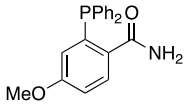

2-(Diphenylphosphenyl)-4-methoxybenzamide (59, 4-OMe-2DPBM). Compound **59** was synthesized and fully characterized by fellow lab member Joshua Wesalo in 3 steps from commercially available 2-amino-4-methoxybenzoic acid.

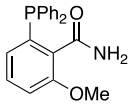

2-(Diphenylphosphenyl)-6-methoxybenzamide (60, 6-OMe-2DPBM). Compound **60** was synthesized and fully characterized by fellow lab member Joshua Wesalo in 3 steps from commercially available 2-amino-6-methoxybenzoic acid.

1.6.5.2 Biochemical Protocols

***p*-Azidobenzyl *ntla* cMO linearization.** Control MO (**67**) and *p*-azidobenzyl *ntla* cMO (**53**, 3.6 μL, 10 μM) were mixed with either DMSO (0.72 μL) or 2DPBM (0.72 μL, 500 μM in DMSO, 10 eq) and water (1.8 μL) to a final volume of 6.1 μL. Samples were incubated at 30 ºC. Aliquots (3 μL) of the reaction were removed at either 90 minutes or 24 hours and co-spotted on the MALDI plate with sinapic acid matrix until a dry, crystallized spot was obtained for analysis. Due to the presence of DMSO in the samples, the matrix to sample ratios were often higher (> 3:1)

and water also had to be co-spotted in order aid in co-evaporation of DMSO to obtain a dry, crystallized sample for analysis. The reaction was analyzed on via MALDI in linear positive mode (see Section 4.3.3) using an average of 10 shots per spot and 100% laser power. The data and the representative MALDI-TOF mass spectrum are presented in Figure 1-38.

Cloning of DNA constructs. Top10 calcium competent cells were used for all cloning. See Table 1-5 for a list of all primers used. The Firefly luciferase coding sequence was PCR amplified from pGL3 (Promega, E1751) with P29 and P30 using DreamTaq polymerase (ThermoFisher) following the protocol outlined in Section 4.1.1. PCR products were purified following the protocol outlined in Section. pCS2+ and the PCR insert were restriction digested (see Section 4.1.2) with BamHI and XhoI (NEB) to generate the respective backbone and insert fragments. Equimolar amounts of backbone and Fluc were ligated overnight with T4 DNA Ligase (NEB) according to the procedure in Section 4.1.3 to generate pCS2-Fluc. The construct was confirmed by Sanger sequencing performed by Genewiz using their "SP6" and "M13-48REV" sequencing primers.

The pCS2-ntlaBS-Fluc was generated from pCS2-Fluc using Gibson isothermal assembly (see Section 4.1.4). The ntlaBS sequence was added to Fluc through PCR amplification with P31 and P32 using DreamTaq (Section 4.1.1). The PCR amplicon was treated with Dpn1 prior to Gibson isothermal assembly (see Section 4.1.4).[181] The 1-fragment Gibson assembly reaction was set up using 100 ng of the PCR amplicon following the previously reported protocol.[181] The reaction was incubated at 50 ºC for 1 hour and then transformed into Top10 competent cells. The construct was confirmed by Sanger sequencing at Genewiz using P35 and the available "M13-48REV" reverse sequencing primer.

To generate pCS2-Rluc, the *Renilla* luciferase coding sequence was PCR amplified from pRL-TK (Promega, E2241) with P33 and P34 using Phusion Polymerase following the protocol outlined in Section 4.1.1. pCS2+ and the purified insert was restriction digested with BamHI and EcoRI (NEB) following the procedure outlined in section 4.1.2. The Rluc amplicon was ligated into the backbone using T4 DNA ligase following the protocol outlined in Section 4.1.3. The construct was verified by Sanger sequencing at Genewiz using P35 and their "M13-48REV" sequencing primer.

Table 1-5: List of primers used to generate DNA constructs
Restriction sites are indicated in **bold**.

Primer	Sequence (5' → 3')
P29	TCTTTTTGCA**GGATCC**ATGGAAGACGCCAAAAACATAAAG
P30	TCACTATAGT**TCTAGA**TCATTACACGGCGATCTTTCCG
P31	ATCGGAAATATGTCTGCCTCAAGTCCCGGCAGCGGCGAAGACGCCAAAA ACA
P32	GCCGCTGCCGGGACTTGAGGCAGACATATTTCCGATGGATCCTGCAAAAA GAA
P33	ATGC**GGATCC**ATGACTTCGAAAGTTTATGA
P34	ACGT**GAATTC**TTATTGTTCATTTTTGAGAACTC
P35	CATTCTGCCTGGGGACGTC

mRNA synthesis. pCS2-ntlaBS-Fluc and pCS2-Rluc plasmids were linearized with NotI-HF (NEB). The digested constructs were electrophoresed on a 0.8% agarose gel and gel extracted following the protocol outlined in section 4.1.8. Linear DNA (1 μg) was transcribed into mRNA using the mMessage mMachine *in vitro* transcription kit (ThermoFisher AM1340) following the manufacturer's protocol. The mRNA synthesis and purification is outlined in Section 4.1.9. The mRNA was diluted to a working concentration of ~ 1000 ng/μL aliquoted and stored as 3 μL aliquots at –20 ºC.

Inhibition of ntlaBS-Fluc translation *in vitro*. *In vitro* translation reactions were prepared using the Rabbit Reticulocyte Lysate Translation System, Nuclease-Treated (Promega, L4960) following a modified version of the manufacturer's protocol. A lysate master mix containing all the necessary kit components and Rluc mRNA (20 ng/reaction) was prepared on ice. Translation reactions were prepared by mixing 28 µL of lysate master mix, ntlaBS-Fluc mRNA (1 µg), and morpholino (7 µL). The translation reaction was aliquoted into three 10 µL reactions for biological replicates. The reactions were incubated at 30 ºC for 90 minutes. Following incubation, a 2.5 µL aliquot of each reaction was removed and pipetted into a white, opaque-bottom, 96-well plate (Greiner 07-000-138). Luminescence was measured on a TECAN M1000 plate reader using a Dual Luciferase Reporter Assay Kit (Promega E1980). Luciferase Assay Reagent (LAR, 40 µL) was added to the well, incubated for 10 seconds, and then firefly luminescence signal was measured. Then, Stop-and-Glo reagent (S&G, 40 µL) was added to the same well and renilla luciferase signal was measured. Luminescence signal was measured using a 1 second integration time.

For the linear *ntla* MO dose response, the linear *ntla* MO was diluted from a 1 mM stock to generate stocks of 50, 10, and 1 µM in water, which were then diluted to 3.75 µL in water to attain final concentrations of 1-5 µM (diluted from 50 µM MO stock), 250-500 nM (diluted from 10 µM MO stock), and 100 nM (diluted from 1 µM MO stock) in the final translation reactions (20 µL final volume), respectively (see Figure 1-39B). A master mix containing all components for the translation reaction was prepared on ice and linear scaled down (35 µL to 20 µL) following the manufacturer's protocol (to conserve lysate). The master mix (16.8 µL) was mixed with the MO solution (3.75 µL) on ice and then incubated at 30 ºC for 90 minutes. Then, luminescence was measured as specified above.

For cMO cleavage experiments, all MO solutions were diluted in water to a final concentration of 10 μM. Where indicated, 2DPBM (from a 50 mM DMSO stock) was added to the MO solution and diluted to a final concentration of 100 μM. In the negative control reactions, the corresponding volume of DMSO was added. The final volume of DMSO or 2DPBM and MO solution was 7 μL. The morpholino solutions were incubated at 30 ºC for 90 minutes. Following incubation, the morpholino solutions were added to a translation master mix (prepared as specified above, 28 μL) translation reactions to attain a final MO concentration of 2 μM (see Figure 1-39C). The reactions were incubated at 30 ºC for 90 minutes and then luminescence was measured as specified above.

1.6.5.3 Zebrafish Protocols

Zebrafish aquaculture and husbandry was maintained following that outlined in section 4.4.1. All zebrafish breeding and microinjections were performed following the protocol specified in sections 4.4.2 and 4.4.3, respectively.

Phosphine treatment. E3 water supplemented with 2DPBM (**57**) was prepared by diluting 2DPBM from a 50 mM stock in DMSO to a final concentration of 100 μM in E3 water. E3 water supplemented with DMSO was prepared by diluting the corresponding volume of DMSO in E3 water. For soaking treatment, all E3 water was removed from plated zebrafish embryos and immediately replaced with the indicated treatment solutions. Embryos were soaked in treatment solutions for either 30, 60, or 90 minutes at 29 ºC, at which point the treatment solution was refreshed, and embryos were incubated for an additional 30, 60, or 90 minutes, respectively, at 29 ºC. Following incubation, all treatment solution was removed and replaced with E3 water containing 0.1% methylene blue.

Phosphine-mediated activation of sensor 55b *in vivo*. At ~ 2 hours post-injection, embryos injected with **55b** were pooled and plated (n = 15-20/plate) in separate, 35 mm petri dishes in E3 water (2.5 mL, no methylene blue). At the indicated time point, E3 water was removed, and embryos were soaked in E3 water supplemented with either DMSO (0.2%) or 2DPBM (100 μM) following the treatment regimen specified above (2.5 mL/plate). In between time points, embryos were incubated at 29 ºC. Following treatment incubation, media was removed and replaced with E3 water containing 0.1% methylene blue. Fluorescence was monitored through imaging at the indicated time points (0.5, 1, 2, 3, 4, 5, 6 hr) with a Leica M205 FA microscope with an mCherry filter set (ex. 560/40 nm, em. 630/75 nm) and the bright field channel following the procedure outlined in Section 4.4.4. Grouped images of pooled embryos were captured using the PLANAPO 0.63x objective at 25X zoom and representative images of 3 randomly selected embryos within the group were captured using the PLANAPO 1.6x objective at 25X zoom. Imaging parameters were as follows: grouped images – (a) brightfield – 40 ms exposure, gain 1.5, (b) mCherry – 1000 ms exposure, gain 3.0; Representative images: (a) brightfield – 40 ms exposure, gain 1.5, (b) mCherry – 300 ms exposure, gain 3.0. Images were exported as .jpeg files from the Leica software.

Fluorescence intensity quantification was performed in FIJI following previous reports.[182] First, images were converted to 16-bit grayscale images and since the FIJI software autothresholds brightness, the brightness of each image was adjusted such that it was identical for each time point. Using the freehand selection tool, the total fluorescence intensity (integrated density) of 5 randomly selected embryos was measured by drawing around the selected, individual embryos. Then, the mean intensity of the background (mean gray value) was measured by drawing a region outside (dark, non-fluorescent) of the embryo. The corrected total fluorescence intensity of each

embryo was calculated using the following equation: corrected total fluorescence = integrated density – (area of the embryo x mean gray value of background). The corrected total fluorescence intensity of the 5 randomly selected embryos was averaged. The error is represented as the standard deviation of the corrected fluorescence intensity values of the 5 measured embryos.

Phosphine-mediated cMO activation. At ~ 2 hpf, morpholino injected embryos were seeded into a 12-well plate (n = 20-40 embryos/well). At ~ 3 hpf, E3 water was removed and replaced with E3 water supplemented with DMSO (0.2%) or 2DPBM (**57**, 100 μM). Embryos were soaked following the treatment regimen outlined above (2 x 90 min, 2 mL media/well). Following incubation, the treatment solution was removed and replaced with E3 water containing 0.1% methylene blue. Embryos were incubated at 29 ºC until 24 hpf for phenotypic analysis.

Phenotypic analysis. All embryos were manually dechorionated at 24 hpf using forceps. Embryos were anesthetized in tricaine (16 mg/mL, 6.1 μM) in E3 water. Embryos were imaged on a Leica MZ16 microscope equipped with a QImaging Retiga 1300 camera. Images were captured using the QCapture imaging software. Bright field images were captured using the 0.11X zoom (entire grouped images), 2.0X zoom (representative images of 5 embryos), or 2.5X zoom (for single embryo images) with exposure times of 40 ms (see Section 4.4.4).

For scoring of *ntla* morphant phenotypes, the body length of each embryo was measured using the straight-line tool in FIJI. Embryo body lengths were scored such that the average length of control MO-injected embryos was set to 1 and the average length of *ntla* MO-injected embryos was set to 0. Parameters for phenotypic scoring were established using the standard deviation of the body lengths for each control group: “normal (wild-type phenotype)” = 0.6 – 1 , “weak *ntla*” phenotype = 0.26 – 0.59, “strong *ntla*” phenotype = 0 – 0.25. *Spt* morphant phenotypes were scored based on visual inspection of injected embryos at the 24 hpf. Specifically, the extent of tail

curvature and size and appearance of the cell mass at the tip of the tail were closely analyzed. Embryos were classified as "weak *spt*" if mild tail curvature and blunting of the tail tip was observed. Embryos were classified as "strong *spt*" if strong tail curvature and an obvious cell mass was observed at the tip of the tail.

2.0 Development of Small Molecule Allosteric Inhibitors of Sulfotransferases

2.1 Introduction to Sulfotransferases

The metabolic system is a living system's main line of defense against foreign and hazardous substances, such as synthetic drugs and environmental toxins, which have the potential to compromise homeostatic pathways.[183] Metabolism serves as the major clearance pathway for roughly 75% of xenobiotics through activation, deactivation, and detoxification of their corresponding small molecule metabolites.[184, 185] This process involves various enzymes responsible for functionalization (phase I) and conjugation (phase II) of metabolites to facilitate excretion from the body via the urine or bile.[186] Phase I metabolizing enzymes include cytochrome P450s (CYPs), monoamine oxidases (MAOs), and flavin containing monooxygenases (FMOs) which either introduce or unmask polar functionalities onto molecules through oxidation, reduction, and hydrolysis reactions.[187] Phase II enzymes recognize and react with functional groups introduced or exposed during phase I, producing glucuronidated, sulfonated, and/or methylated metabolites which can readily be excreted.[188] Sulfotransferases (SULTs) are a family of phase II metabolizing enzymes that catalyze the transfer of a sulfuryl group (SO_3^-) from a donor molecule, 3'-phosphoadenosine-5'-phosphosulfate (PAPS), to a nucleophilic acceptor moiety present on a substrate molecule (Figure 2-1).

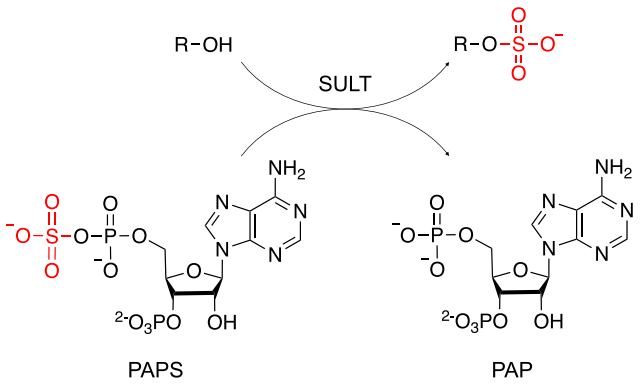

Figure 2-1: Reaction scheme of SULT-mediated sulfuryl transfer
General reaction scheme of SULT-mediated sulfonation of a substrate alcohol by the co-factor PAPS.

There are two classes of SULT enzymes, the cytosolic SULTs and the membrane-associated SULTs.[189] Membrane-associated SULTs are mostly localized to the Golgi apparatus and catalyze sulfuryl transfer onto large biomolecules such as polysaccharides and tyrosyl residues in proteins and peptides. Also classified by cellular localization, the human cytosolic sulfotransferases are a small, highly homologous 13-member family that catalyze sulfonation of drugs, hormones, neurotransmitters, and steroids. These enzymes were initially thought to solely play a role in metabolism and detoxification pathways, but further research uncovered their role as key players in a diverse array of cellular events.[189] Sulfonation contributes to regulatory pathways by altering substrate affinity for target proteins and receptors,[190] and controlling substrate half-life by increasing plasma solubility thereby facilitating compound excretion.[191]

There are five distinct families of SULT enzymes in mammals: SULT1, SULT2, SULT3, SULT4 and SULT5. Of these families, only SULT-1, -2, and -4 have been identified in humans and are expressed in various areas of the body including the liver, gastrointestinal tract, brain, and skin.[192] SULTs possess two distinct binding pockets necessary for catalysis – a co-factor (PAPS) binding pocket and a substrate binding pocket. While the overall SULT structure – including the co-factor binding pocket – is highly conserved, a large degree of structural variation occurs in the

substrate binding sites. Structural studies have shown that high flexibility within these sites contributes to substrate overlap observed amongst SULT enzymes, which has made it difficult to assess substrate-dependent regulatory patterns. However, these studies have also identified key non-conserved residues that confer substrate preference in individual isoforms.[193, 194] Similarly, mutagenesis studies have identified the critical residues in respective isoforms responsible for dictating preference of substrate binding, such that when point mutations are introduced, the critical interactions are disrupted, resulting in reduced substrate affinity and altered catalytic properties.[195]

Substrate preference is also influenced by the cellular role of the enzyme. For example, SULT1A3 is the major enzyme involved in the metabolism of monoamine neurotransmitters such as dopamine. While SULT1A1 can also recognize dopamine as a substrate, it preferentially sulfonates simple phenolic compounds.[195] More recently, reports have suggested that substrate specificity can be dictated by sites other than the designated substrate binding site.[196, 197] It has been demonstrated that SULT substrate specificity can be mediated through a 30-residue flap located over the active site. Upon PAPS binding, this active site "cap" isomerizes between an open and closed form, with equilibrium favoring a closed cap conformation, restricting access of substrates to catalytic residues based on size.

The universal sulfo-donor molecule for SULT enzymes is PAPS, which is synthesized from adenosine triphosphate (ATP) via a two-step enzymatic process catalyzed by ATP sulfurylase and APS kinase, respectively, in the cytosol of eukaryotes. PAPS is utilized by the cytosolic SULT enzymes to sulfonate xenobiotics and other small endogenous compounds, thereby facilitating excretion from the body. The PAPS binding region of SULT enzymes is highly conserved at the amino acid level and contains three structural features essential for PAPS binding: (i) the 5'-

phsphosulfate binding loop (PSB loop), (ii) the 3'-phosphosulfate loop (PB loop), and (iii) the SLH3 motif. A conserved GxxGxxK motif next to the PB loop has been shown to be critical for PAPS binding through mutagenesis studies.[189] Mutation of any one of these residues resulted in an increase in K_m towards PAPS, and mutation of all three residues rendered an inactive enzyme.[198]

The mechanism of sulfuryl transfer occurs between two substrates, the co-factor PAPS and the acceptor substrate – specific to each SULT enzyme. Following catalysis, the enzyme releases two products, the sulfurylated acceptor and 3'-phosphoadenosine (PAP). The complete elucidation of the kinetic mechanism of SULT2A1 has been determined through isotope trapping experiments with the isoform's primary substrate, dehydroepiandrosterone (DHEA).[199] It was shown that sulfuryl transfer by SULT2A1 occurs via a random sequential mechanism under rapid equilibrium thereby establishing that the order of substrate binding is not relevant to catalysis. Due to the high degree of homology amongst the human cytosolic SULT family, this general mechanism is assumed to be conserved among other members. There are three, known conserved active site residues that contribute to this catalytic mechanism: His108, Lys48, and Lys107. When a substrate enters the active site it is deprotonated by the conserved catalytic base, His108,[200] generating a negative charge on the acceptor nucleophile which is stabilized by the nearby, conserved Lys107. The acceptor molecule attacks the sulfur atom of PAPS and sulfuryl transfer is facilitated through coordination of Lys48 with the leaving group oxygen atom (Figure 2-2). Site directed mutagenesis of the active site lysine residues to anything other than arginine renders the enzyme inactive.[201] This catalytic mechanism is considered consistent for all SULTs that utilize PAPS as a co-factor.

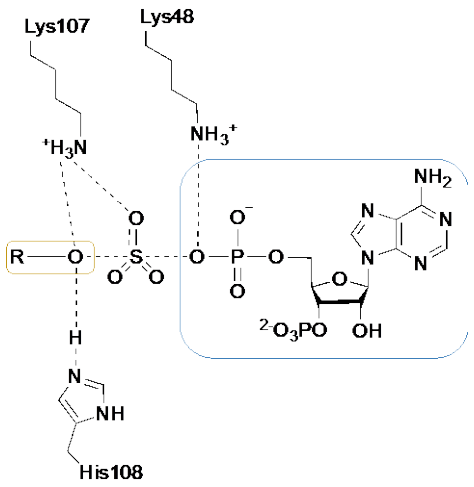

Figure 2-2: Transition state of SULT-mediated sulfonation
Sulfuryl transfer mediated by SULT1E1 from PAPS (blue) to substrate (yellow) occurs through an in-line SN2-like nucleophilic attack mediated by conserved active site residues as deduced by previous structural studies.

2.2 Role of Sulfotransferases in Disease

The human cytosolic SULT enzymes were at one time believed to serve solely as key players in detoxification for the human metabolome. Over time it was learned that these enzymes, due to their wide tissue distribution, regulate complex, disease-relevant cellular processes in virtually every area in the body. The SULT families have been shown to play key roles in hormone regulation and bioactivation of xenobiotics such as hydroxylated aryl- and cyclic amines that when sulfonated form reactive electrophiles that can elicit both carcinogenic and mutagenic effects.[202] Further, aberrant activity of SULT enzymes has been linked to disorders such as Parkinson's,[203] cystic fibrosis,[204] and heart disease,[205] as well as various other disease-relevant processes such as neurodegeneration,[206] tumorigenesis,[207] and viral entry into cells.[208] Not surprisingly, disease relevance has been shown to be isoform-dependent. For example, SULT1A1 is dramatically upregulated in various cancers,[209, 210] and is speculated to enable cell survival through inactivation of chemotherapeutics, however, there are no current metabolically stable therapeutics available.

SULT1A3 shows a strong preference for the sulfonation of catecholamines, such as neurotransmitters, over the other human SULT isoforms. Sulfonation prevents catecholamines from binding their receptors[211] and enhances their transport properties[212, 213] which decreases their terminal half-lives.[214] Deficiencies in neurotransmitters can lead to major neurological diseases such as Parkinson's,[203, 215] depression,[216] and schizophrenia.[217, 218] In the case of major depression, treatment typically involves antidepressants such as selective serotonin reuptake or monoamine oxidase inhibitors (SSRIs and MAOIs, respectively),[219] which increase synaptic levels of serotonin. SSRIs prevent the recycling of serotonin but must be carefully dosed so as to prevent a harmful serotonin overload. Treatment with MAOIs prevents the monoamine oxidase-mediated inactivation of tyramine, found in many foods, which elicits a serotonin cascade[220] that can lead to a fatal hypertensive crisis.[221] Individually, these treatment approaches are not effective in 40% of patients, but are shown to be more effective when taken in combination.[222-224] This lack of efficacy, specifically in the case of MAOIs could potentially be caused by the enhanced activity of sulfotransferases, namely SULT1A3, in response to the loss of MAO activity – a process referred to as metabolic compensation. This hypothesis is supported by analysis of human brain micro-dialysates, which revealed that approximately 80% of serotonin is sulfonated.[225] These findings suggest that isoform specific inhibition of not only SULT1A3, but all SULT isoforms, could produce novel, therapeutically meaningful alternatives that should be explored.

2.3 Approaches to Sulfotransferase Inhibition

To further understand SULT-related implications in disease progression and carcinogenesis, the functional role these enzymes play in drug and xenobiotic metabolism must

first be understood. Both the regulation and inhibition of SULT enzymes are recognized as the least studied areas of SULT biology. Several reports show evidence supporting transcriptional regulation of some cytosolic SULTs through nuclear receptor activation by xenobiotics and their corresponding metabolites,[226, 227] steroids,[228, 229] and glucocorticoids[230] in rodent models. The regulatory patterns observed did not entirely mirror the regulation of human cytosolic sulfotransferases,[231, 232] as several of the same induction, repression, and gender-specific expression patterns were not consistent between species. Recently, it has been shown that PAPS can allosterically regulate SULT1A1 turnover through binding, causing conformational changes in the active site cap. This suggests that SULTs can be regulated in a tissue-specific manner dependent on the local concentration of PAPS.[233]

Both the high structural homology amongst SULTs and their broad, overlapping substrate specificity, have made understanding the contribution of an individual isoform to a specific pathogenic implication difficult. Structural analysis of the individual SULT isoforms has been useful for gaining insight into the substrate preferences and mechanistic details of these enzymes. Recent efforts, however, have been directed towards the development of selective small molecule inhibitors to validate the role of a particular SULT or SULT family in disease progression, with the potential for further progression into potent therapeutics. In this manner, there have been several approaches to SULT inhibition. However, a lack of affinity, specificity, and cross-reactivity with other nucleotide-based group-transfer enzymes, such as the kinases, have been observed and have deemed selective SULT inhibition a great challenge.

2.3.1 Adenosine and PAPS-based SULT Inhibitors

One of the first approaches in generating SULT inhibitors was to design structure scaffolds resembling the nucleotide donor molecule, PAPS, with the hopes to outcompete co-factor binding to the active site, thereby blocking sulfuryl transfer onto substrate molecules. Initial strategies for inhibitor discovery included high throughput screens of derivatized purine analogs to try to identify a hit compound that could be optimized for isoform-specific targeting.[234-236]

Serving as essential conjugation enzymes in cells, kinases and sulfotransferases contain several similarities in the active site structures, as both enzymes transfer their corresponding groups (phosphate and sulfate, respectively) from an adenosine-based co-factor. Taking advantage of these similarities, Bertozzi[234] screened a library of inhibitors initially directed for kinase inhibition as potential inhibitors against bacterial carbohydrate sulfotransferase, NodH. Screening identified two compounds, **69** and **70** that could competitively inhibit NodH effectively in the low nano-molar range (Figure 2-3). Unfortunately, as expected, these compounds also inhibited both p38/MAP kinase and cyclin dependent kinase (CDK) at comparable effective concentrations, thereby limiting their capacity in SULT targeted inhibition.

A similar approach was undertaken by the Schultz lab,[235] involving screening purine and pyrimidine analog libraries against beta arylsulfotransferase (β-AST-IV), a common sulfotransferase primarily involved in the detoxification of xenobiotics. They developed a fluorescence assay in which, 4-methylumbelliferylsulfate (4-MUS) was utilized as a sulfate donor molecule. In the presence of β-AST-IV, sulfonation of substrate, PAP, occurs generating PAPS and fluorescent 4-methylumbelliferone (λ_{ex} 360 nm, λ_{em} 449 nm). One compound **71** was identified as a hit in this assay, demonstrating high affinity for β-AST-IV (K_i = 96 nM) and

moderate inhibition against SULT1A1 (K_i = 770 nM) when screened against other SULT enzymes (Figure 2-3). The inhibition model of **71** displayed competitive inhibition against substrate, and not PAPS, suggesting this compound was competing for the aryl binding site of β-AST-IV and not the anticipated PAPS binding site.

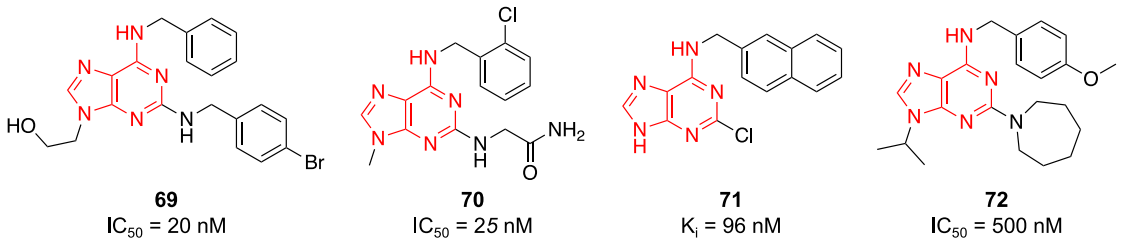

Figure 2-3: Adenine-based SULT inhibitors
Derivatized adenine analogs and their corresponding inhibitory constants against sulfotransferases.

Using a modified two-step approach, Bertozzi[236] screened a library of purine analogs against the estrogen sulfotransferase (SULT1E1 or EST) for both enzyme binding and inhibition. Binding was analyzed using an immobilized enzyme mass spectrometry (IEMS) assay and enzyme inhibition was then determined through a radiolabel transfer thin layer chromatography (TLC) assay. Compound binding was evaluated by relative peak intensities prior to and post-incubation of the small molecule library with immobilized SULT1E1. Compounds that exhibited reduced peak intensity were assumed to bind the enzyme and were subsequently tested for inhibition of SULT1E1. In this inhibition assay, ^{35}S-labeled PAPS was incubated with SULT1E1, SULT substrate, and the potential inhibitor compound. Radiolabel transfer reactions were monitored by TLC and phosphor-imaging to observe if ^{35}S was transferred to substrate. If no radiolabeled substrate was observed, it was assumed that the compound performed as an effective inhibitor. Screening resulted in the discovery of **72** (Figure 2-3). While inhibition of SULT1E1 by **72** was

moderate (IC_{50} = 500 nM), this inhibitor exhibited cross-reactivity with CDKs. Several other compounds demonstrated enzyme inhibition at concentrations too high for therapeutic application.

2.3.2 Bisubstrate SULT Inhibitors

Another approach to SULT inhibition sought to overcome the aforementioned selectivity issues by generating bisubstrate structures that contained moieties targeting both the PAPS and substrate binding pockets in an effort to increase specificity for a particular SULT isoform or subfamily. Improving inhibitor selectivity involved exploiting small differences within the substrate binding site. Furthermore, inhibitors capable of simultaneously engaging both the substrate and co-factor binding sites were expected to be more potent due to the enhanced binding energy and entropic advantage of pre-positioning of the substrate in proximity to its respective binding site. This bisubstrate approach has proven successful in the inhibition of other group transfer enzymes such as kinases[237, 238] and glycosyltransferases[239] *in vitro*.

Utilizing this methodology, Bertozzi[240] focused efforts towards developing bisubstrate inhibitors to target SULT1E1. Potential inhibitors were readily synthesized by reacting aminooxynucleosides with various drug-like, hydrophobic aldehydes generating an oxime linkage between the two targeting moieties. This high-throughput synthetic method generated 67 potential inhibitors which were subsequently screened for SULT binding and inhibition through the same two-step approach mentioned previously.[236] This screen identified four compounds (Figure 2-4A, **73**-**76**) that exhibited more than 80% inhibition of SULT1E1. It was suggested that due to the structural diversity among the strongest inhibitors that these compounds were able to bind disparate regions of the enzyme that would be difficult to rationally predict through traditional

methods. However, Bertozzi did not test these compounds for selectivity against other SULT isoforms.

In an effort to further dial in selectivity for SULT1E1, Bertozzi[241] later narrowed her focus to substrates primarily exclusive to the SULT1E1 isoform, such as estrone. Utilizing bisubstrate mimicry, the Bertozzi group synthesized a bisubstrate inhibitor targeting SULT1E1 by conjugating estrone to a PAP derivative via a phosphoanhydride linker (Figure 2-4B, **77**). When inhibitory behavior was analyzed, this compound displayed competitive inhibition against PAPS (K_i = 2.9 nM) and noncompetitive behavior towards the substrate, estrone (K_i = 4 nM) suggesting this compound was unable to contact both binding sites, possibly restricted by the phosphoanhydride linker length as well as conformational restraints.

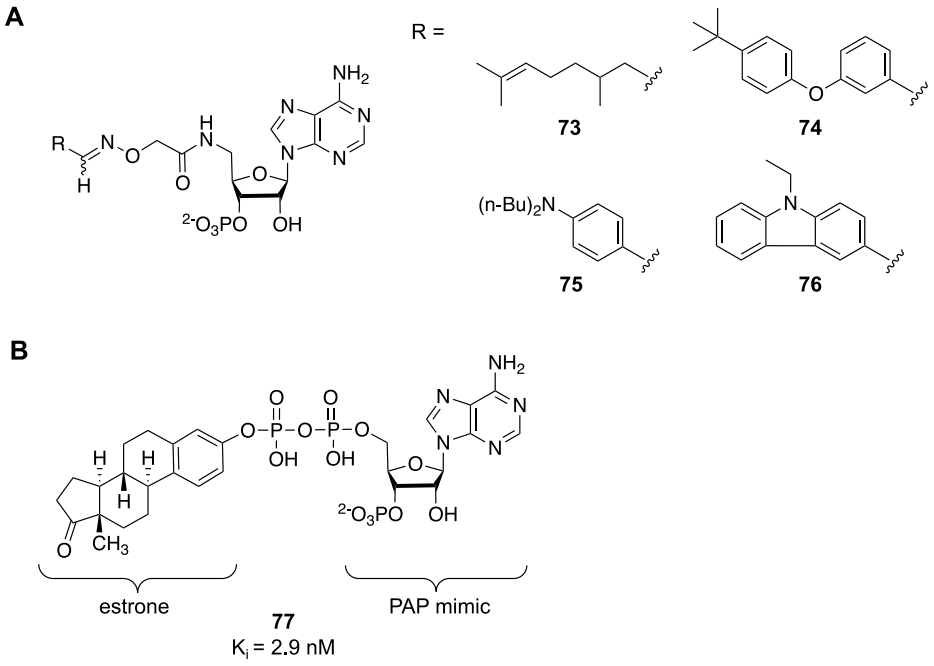

Figure 2-4: Bisubstrate inhibitors of SULT1E1
A) Structures of aminooxynucleoside-linked inhibitors identified in a high-throughput screen for inhibition against SULT1E1. B) Strategic design of a bisubstrate SULT1E1 inhibitor linking the SULT1E1 substrate, estrone, to a co-factor mimetic via a phosphoanhydrided linker.

The most potent bisubstrate inhibitors to date were generated by the Wong lab.[242] Adenine and derivatives thereof were coupled to various substituted benzoic acids and screened to determine the optimal, most potent inhibitory pairs. Once selected, these compounds underwent additional optimization, varying both linker composition and length to maximize inhibitory activity. Compounds **78**, **79**, and **80** displayed inhibition of β-AST-IV in the low nano-molar range, exhibiting the best inhibition of any bisubstrate inhibitors developed to date (Figure 2-5). However, these compounds were not tested for selectivity against other sulfotransferases. Additionally, while very potent *in vitro*, these compounds were not and have not been tested for their potency and selectivity in a cellular environment since their initial publication.

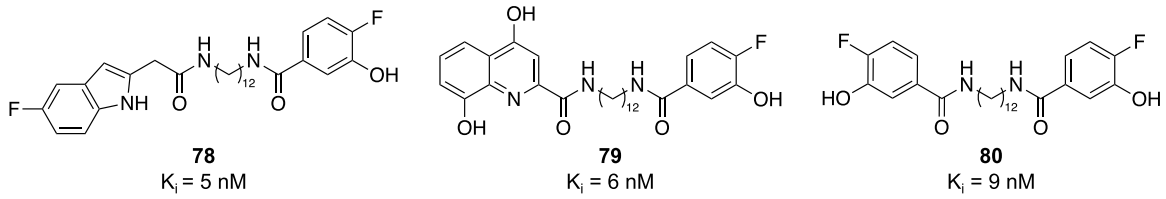

Figure 2-5: Bisubstrate inhibitors of β-AST-IV

2.4 Allosteric Inhibition of Sulfotransferase Enzymes

Efforts in studying allosteric regulation of SULT activity has centered around two of the most well-studied and structurally homologous isoforms, SULT1A1 and SULT1A3. Prior to 2015, the allosteric inhibition of SULTs was suggested to occur with a wide range of compounds such as polychlorinated biphenyls,[243] non-steroidal anti-inflammatory drugs (NSAIDs),[244] and naturally occurring polyphenols, also referred to as catechins.[245] However, none of these reports sought to discover why or how this inhibition occurs. One of the first studies highlighting the isoform-

specific allosteric inhibition of SULT enzymes was conducted by Coughtrie and colleagues, who were able to demonstrate isoform selective inhibition of SULT1A1 by epigallocatechin gallate (Figure 2-6A, **81,** also known as EGCG),[245] which is not a natural substrate for this isoform. Having exhibited uncompetitive inhibition against PAPS, it was suggested that **81** was inhibiting at a site other than the PAPS binding site. Further studies revealed that the affinity of **81** increases when the enzyme is already bound to PAPS.[246] In the presence of enzyme alone **81** exhibits a dissociation constant (K_D) of 820 nM. However, when bound to either the enzyme-PAPS complex or to the enzyme-PAPS-*para*-nitrophenol (pNP, a model acceptor substrate) ternary complex, the affinity of **EGCG** for SULT1A1 increases 21-fold (38 nM and 35 nM, respectively).[246]

Follow-up structure activity relationship (SAR) studies of **81** with SULT1A1 revealed that **81** binds to the edge of the active site cap when PAPS is bound to the enzyme (Figure 2-6B).[247] When the gallic acid moiety is removed, producing (–)-gallocatechin (**82**), this compound is a non-specific inhibitor of numerous SULTs (K_i = 700 nM). However, when gallic acid moiety is present, the K_i decreases 20-fold (K_i ~35 nM) and **81** becomes isoform selective for SULT1A1. Structural analysis revealed that the (–)-gallocatechin portion of **81** embeds into enzyme side chains and is oriented to interact with unique features of the active site cap. This finding suggests that the gallic acid moiety is what confers the observed SULT1A1 isoform specificity (Figure 2-6C). The interaction between **81** and the active site cap dictates the inhibition observed as the enzyme is trapped in its cap-closed conformation, preventing PAP release and reducing enzyme turnover.[248] The site elucidated in these reports has since been denoted the "catechin site", as it binds catechin compounds, and is present in a number of human cytosolic SULTs.[247] In addition to the catechin site, SULTs are also known to contain a second, separate allosteric site that binds non-steroidal anti-inflammatory (NSAID) compounds, dubbed the "NSAID site."[244, 246] Taken together, these

reports were the first to both shed light on allosteric regulation of SULT1A1, and, perhaps most importantly, to provide mechanistic information on isoform selective allosteric regulation, which has been a long-time goal of SULT biology.

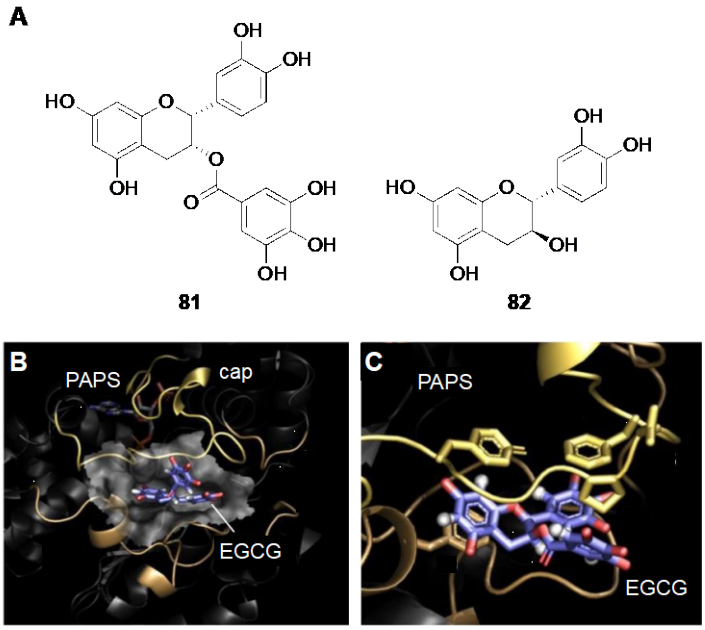

Figure 2-6: Allosteric inhibition of SULT1A1 by (–)-epigallocatechin gallate
A) Structure of (–)-epigallocatechin gallate (**81,** EGCG) and (–)-gallocatechin (**81**). B) EGCG (**81**) bound to SULT1A1 at the edge of the active site cap. C) The gallic acid moiety of EGCG makes interactions with residues in the active site cap that confer isoform specificity. Adapted with permission from Cook *et. al.*, *Proc Natl Acad Sci*, **2016**, 113, 14312.[247]

Allosteric inhibition has also recently been demonstrated in SULT1A3 with endogenous tetrahydrobiopterin (THB, **83**), an intermediate of monoamine neurotransmitter synthesis (Figure 2-7A).[249] Ligand **83** is involved in the oxidative cleavage of aromatic aminohydroxylases, the rate-limiting step of neurotransmitter biosynthesis. Monoamine neurotransmitters, such as dopamine, are the primary class of substrates for sulfonation by SULT1A3. THB has been shown to allosterically inhibit SULT1A3 at its allosteric catechin site with high affinity (K_i = 23 nM), and excellent isoform selectivity for SULT1A3 (Figure 2-7B-C). Allosteric inhibition by this

compound suggests that nature has established a feedback mechanism in which the metabolizing enzyme (SULT1A3) is inhibited due to the accumulation of a biosynthetic intermediate of the substrate that is metabolized.

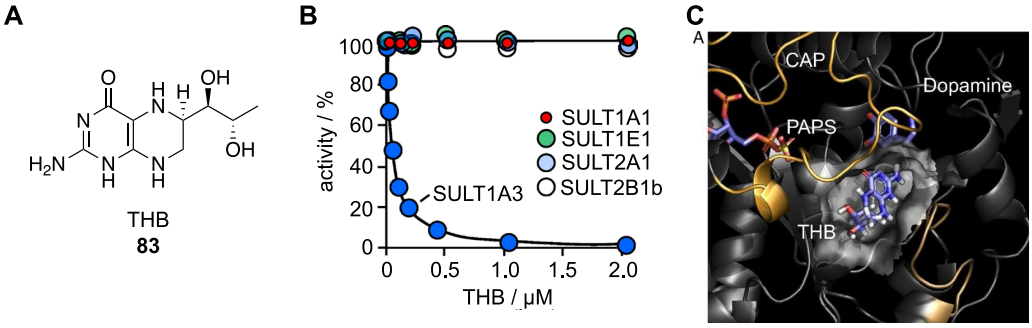

Figure 2-7: Allosteric inhibition of SULT1A3 by tetrahydrobiopterin
A) Structure of tetrahydrobiopterin (**83**, THB). B) THB demonstrates dose-dependent, isoform specific inhibition of SULT1A3 and no activity against any of the other prominent SULT isoforms. C) THB binds to the allosteric SULT1A3 catechin site. Adapted with permission from Cook *et. al., Proc Natl Acad Sci*, **2017**, 114, E5317.[249]

The isoform selectivity achieved with these compounds provides a novel approach into studying and treating diseases linked to the atypical activity of these metabolizing enzymes. Unlike previous attempts to achieve SULT inhibition by targeting the variable substrate-binding and conserved PAPS-binding sites, regulation by targeting allosteric sites shows the most promise for isoform selective inhibition. Similarly, allosteric inhibition of kinases has shown much success in eliciting highly selective and potent inhibition. For example, various allosteric inhibitors targeting MEK1/2 have shown much promise in phase I and phase II clinical trials, including FDA-approval of trametinib for treatment of metastatic melanoma.[250] Achievements in the allosteric inhibition of MEK1/2 have sparked further exploration in identifying and developing inhibitors of other kinase allosteric sites. Additionally, these successes have demonstrated that selectively targeting highly homologous families of group transfer enzymes is within reach. Until recently, there have been no reports of synthetic small molecules targeting SULT allosteric sites. However, such discoveries

would provide a largely unexplored method for studying the disease relevance of individual SULT isoforms.

2.5 Discovery of Isoform Selective Allosteric Inhibitors of SULT1A3

The material presented in Section 2.5 was reprinted in part with permission from **Darrah, K.**; Wang, T.; Cook, I.; Cacace, M.; Deiters, A.; Leyh, T. S., *J. Biol. Chem.,* **2019**, *294(7)*, 2293.[251]

2.5.1 Computational Design of Synthetic Allosteric SULT Inhibitors

The SULT field has been hampered by a lack of access to isoform specific inhibitors. Without such inhibitors, it is difficult to convincingly demonstrate the causality between a SULT activity and an elicited cellular response. For reasons unclear, genetic silencing mechanisms have not been used to comprehensively study SULT function. Rather, SULT studies have largely involved correlating up- or down- regulation of a SULT isoform with a particular pathology or behavior.[252, 253] Successful isoform-specific inhibitors would allow us to observe and/or control individual SULT activity. Until now, only a handful of studies have been aimed at identifying allosteric inhibitors of sulfotransferases, nearly all of which have been discovered serendipitously through screening studies.[243]

SULT1A1 and SULT1A3 are two of the most well-studied enzymes in SULT biology. Due to their highly homologous structures, allosteric inhibitors targeting these isoforms will provide valuable insight into their therapeutic potential. Further, selective inhibitors will establish guidelines to generate inhibitors of other SULT isoforms. In collaboration with the Leyh lab

(Albert Einstein College of Medicine), structures of potential small molecule allosteric inhibitors targeting the SULT catechin site were generated. This catechin site is found exclusively in 8 members of the SULT1 family, including SULT1A1 and SULT1A3. Further, it is mechanistically well defined (based on studies with **81** and **83**) and unique to each of the 8 isoforms that possess it, thus making it a good target for isozyme specific binding and inhibition. Extensive computational screening and docking studies were performed by our collaborators using AutoGrow 3.0 – a computationally-intensive virtual screening algorithm that evolves compound libraries to optimize drug-like characteristics and target affinities. The AutoGrow code was altered by our collaborators to enable docking with GOLD, rather than AutoDock, due to its enhanced side-chain flexibility and ability to accurately predict the affinities of SULT ligands.[254, 255] Analysis with this program determined the optimal core scaffold to be 6-(1H-1,2,3-triazol-4-yl)quinoline (Figure 2-8). The predicted affinity of the modeled inhibitor scaffold for SULT1A3 (K_D = 0.42 μM) was nearly identical to that of (–)-gallocatechin (**82**, K_D = 0.73 μM). Positions of R-group substitution were optimized through computational analysis, and the potential inhibitor candidates were modeled against the catechin sites of SULT1A3 and SULT1A1. Further analyzed by visual inspection, derivatized structures with the optimal core scaffold were produced (**84-88**, Figure 2-8). The predicted affinities and isoform selectivity of these potential catechin site-targeting inhibitors were determined through binding free energy calculations and predicted to be 3-4 orders of magnitude greater than that of any naturally occurring catechin. All computational work was performed by Ian Cook (Leyh lab).

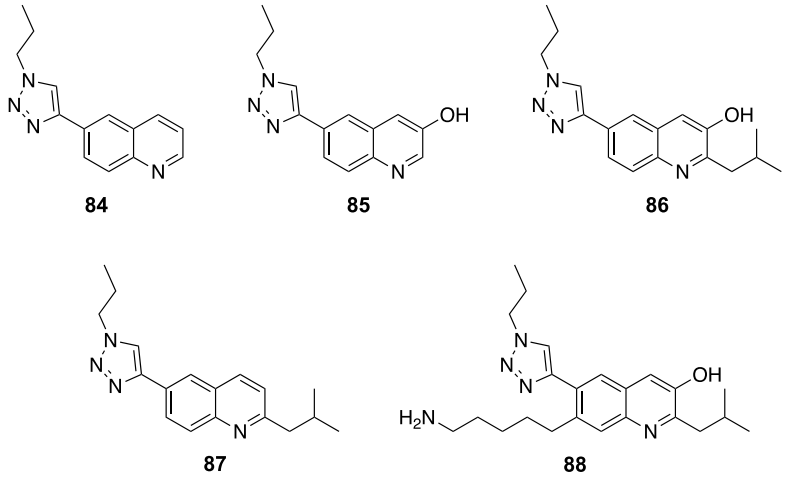

Figure 2-8: Structures of proposed SULT catechin site inhibitors
Structures of potential inhibitors generated through in silico analysis and docking in the SULT1A1 and SULT1A3 catechin sites. Computational analysis was performed by Ian Cook (Leyh lab).

2.5.2 Synthesis and Screening of Predicted Compounds

Of the proposed allosteric inhibitors in Figure 2-8, **84** and **87** were synthesized. Synthesis of **84** was performed using a Sonogashira coupling between commercially available 6-iodoquinoline (**89**) and trimethylsilylacetylene in the presence of trimethylamine, catalytic bis(triphenylphosphine)palladium(II) dichloride and copper(I) iodide in tetrahydrofuran to afford **90** in 96% yield. Subsequent trimethylsilyl deprotection with potassium carbonate in methanol produced the corresponding alkyne **91**. *n*-Propylazide (**92**) was synthesized with commercially available 1-bromopropane and sodium azide in a water-DMSO mixture that is slowly warmed to 50 ºC and stirred until two layers form. The reaction is monitored using ^{1}H NMR by removing aliquots of the top layer containing a mixture of the starting alkyl halide and the product. Once the reaction reached 60-70% conversion, the azide was decanted from the reaction solution and pushed forward crude in a Huisgen 1,3-dipolar cycloaddition with **91** affording **84** in 47% yield over three steps (Figure 2-9).

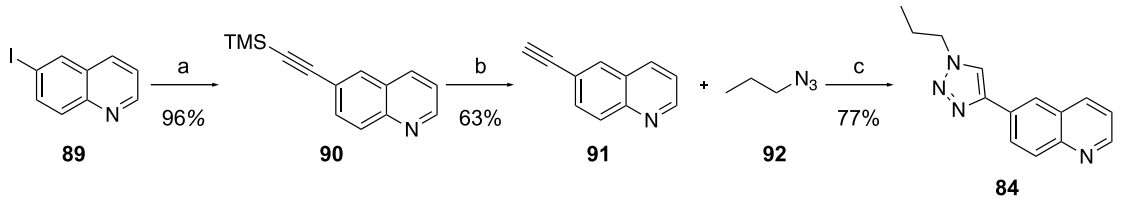

Figure 2-9: Synthetic route to 84
Reagents and conditions: a) trimethylsilylacetylene, $Pd(PPh_3)_2Cl_2$, copper(I) iodide, TEA, THF, 96%; b) K_2CO_3, methanol, 63%; c) copper(II) sulfate pentahydrate, sodium ascorbate, 1:1 THF/H_2O, 77%.

A Friedlander reaction was used to synthesize **87** from 2-amino-5-bromobenzaldehyde (**93**) and 4-methyl-2-pentanone (**94**) through a modified version of a previously reported protocol[256] to exclusively produce the 2-monosubstituted regioisomer **95**. A Sonogashira coupling[257] with trimethylsilylacetylene afforded **96** and subsequent deprotection to produce the alkyne **97**. The [3+2] cycloaddition reaction of **97** with *n*-propyl azide (**92**) was performed under similar conditions reported in the synthesis of **84** to produce **87** in 38% yield over four steps (Figure 2-10).

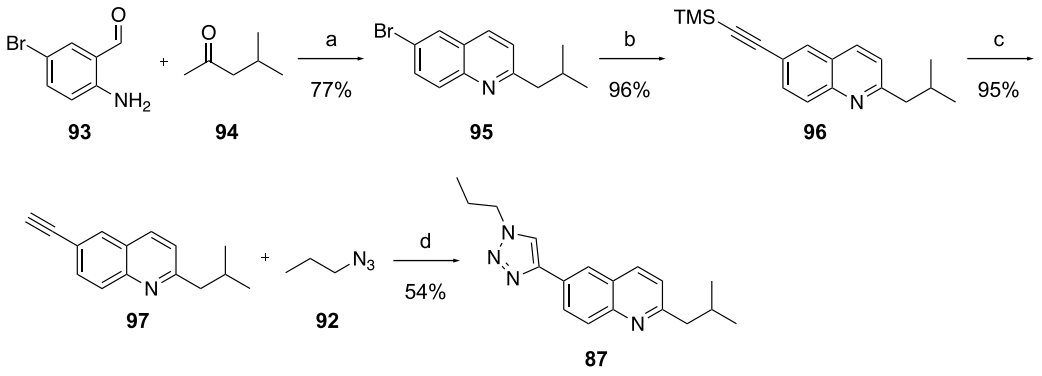

Figure 2-10: Synthetic route to 87
Reagents and conditions: a) pyrrolidine, H_2SO_4, EtOH, 77%; b) trimethylsilylacetylene, $Pd(PPh_3)_2Cl_2$, triphenylphosphine, copper(I) iodide, TEA, THF, 96%; c) K_2CO_3, methanol, 95%; d) copper(II) sulfate pentahydrate, sodium ascorbate, 1:1 THF/H_2O, 54%.

Both **84** and **87** were tested by the Leyh lab for *in vitro* inhibition of SULT1A1 and SULT1A3 through initial rate inhibition studies. Inhibition constants (K_i) were obtained using 1-

hydroxypyrene (1-HP) as an acceptor substrate for both SULT enzymes. 1-HP is an ideal substrate for assaying SULT inhibition due to its excellent kinetic parameters with both SULTs under study.[249] Upon sulfonation 1-HP exhibits a stable, strong shift in emission wavelength from 387 nm to 375 nm.[258] All initial rate experiments were performed by Ian Cook and Ting Wang (Leyh lab). Both predicted compounds **84** and **87** lacked specificity and potency as potential allosteric SULT inhibitors. Although **84** showed modest inhibition of both isoforms (SULT1A1 K_i = 4.7 μM, SULT1A3 K_i = 3.1 μM), its inherent promiscuity discredited its potential as an isoform specific allosteric inhibitor for either enzyme. The predicted inhibition constants for this compound were in the lower nano-molar range (K_i = 4 nM for SULT1A3 and K_i = 400 nM for SULT1A1). Inhibition of both enzymes with **87** was not observed at 10 μM treatment, indicating that it was not valid candidate for allosteric inhibition.

In attempts to understand inconsistencies between predicted results and experimental observations, the triazole substitution at C-6 of the quinoline scaffold was replaced with an amide bond to produce **98** and **99**. Both compounds were analyzed in computational binding studies to estimate binding affinities and isoform specificity for SULT1A1 and SULT1A3. Compound **99** was predicted to bind SULT1A3 with high affinity (K_D = 0.75 nM) and to be 200-fold more selective for SULT1A3 over SULT1A1. Compound **98** was anticipated to be moderately SULT1A3 selective (predicted K_D = 28 nM), however the difference in the predicted binding affinity for SULT1A1 (K_D = 110 nM) was not substantial enough to anticipate this compound as a highly isoform selective compound.

Compound **98** was synthesized in 2 steps starting from commercially available methyl quinolone 6-carboxylate (**100**). Saponification of the methyl ester afforded **101** in 43% yield. Using standard peptide coupling conditions, **101** was reacted with *n*-butylamine in the presence of

N,N-diisopropylethylamine (DIPEA) and 1[bis(dimethylamino)methylene]-1H-1,2,3-triazolo[4,5-b]pyridinium-3-oxide hexafluorophosphate (HATU) in dimethylformamide to produce **98** (Figure 2-11).

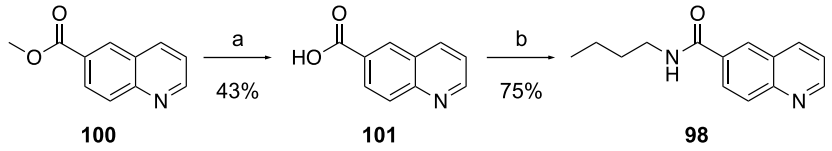

Figure 2-11: Synthetic route to 98
Reagents and conditions: a) 1M LiOH, methanol, 43%; b) n-butylamine, HATU, DIPEA, DMF, 75%.

Synthesis of **99** occurred via a nitro reduction of methyl 3-formyl-4-nitrobenzoate (**102**) with hydrogen and 10% palladium on carbon to yield the corresponding amine **103**. The same regioselective Friedlander quinoline synthesis conditions were used to react **103** with 4-methyl-2-pentanone (**94**) to produce **104**. The amide was synthesized from **104** using a methyl ester deprotection and subsequent peptide coupling reaction to yield **99** in 42% yield over the final two steps (Figure 2-12).

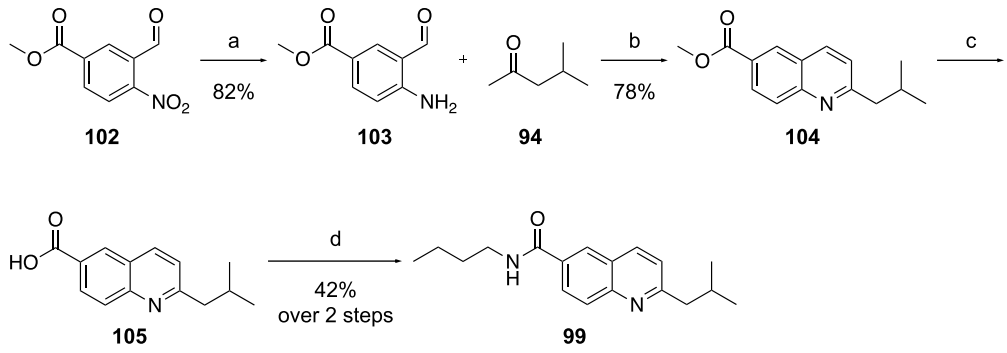

Figure 2-12: Synthetic route to 99
Reagents and conditions: a) hydrogen, 10% palladium on carbon, methanol, 82%; b) pyrrolidine, H_2SO_4, EtOH, 78%; c) 1M LiOH, methanol; d) n-butylamine, HATU, DIPEA, 42% over 2 steps.

When tested in initial rate inhibition studies, neither compound showed significantly improved SULT inhibition compared to that of **84** and **87**. Compound **98** exhibited no inhibition of either isoform up to treatment concentrations of 10 μM. Compound **99** showed 3.9-fold isoform specificity for SULT1A3 over SULT1A1 (SULT1A1 K_i = 5.1 μM, SULT1A3 K_i = 1.3 μM) when compared to **84** (1.5-fold SULT1A3 isoform specificity), it was not significant enough to avoid cross reactivity with SULT1A1 in a cellular environment.

With minimal success of the computationally predicted compounds as SULT inhibitors, synthetic intermediates were tested in initial rate inhibition studies (Figure 2-14A). Compounds **95** and **104** were synthetic intermediates from routes described above. Intermediates **106** and **107** were isolated from attempts in the preparation of **97** through alkyne installation at C-6 through a Corey-Fuchs reaction. Methyl ester reduction of **104** followed by oxidation to the aldehyde **107** was synthesized as reported previously (Figure 2-14B).[259]

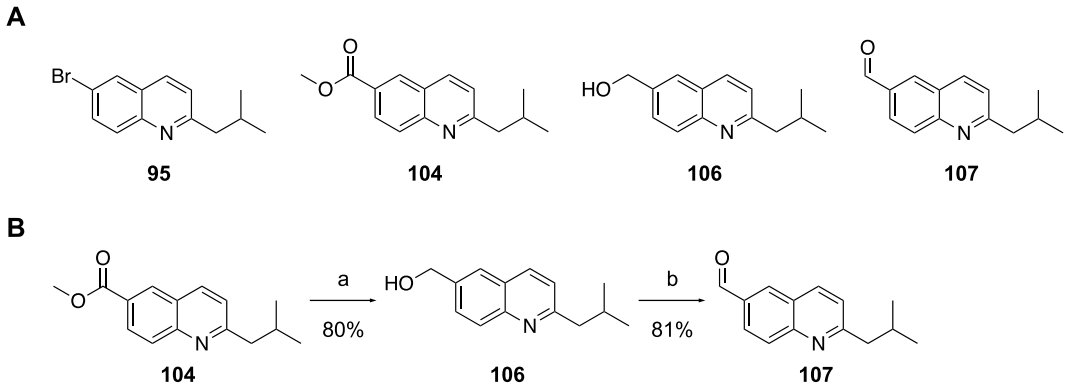

Figure 2-13: Synthetic intermediates evaluated for allosteric SULT1A3 inhibition
A) Structures of intermediates evaluated in initial rate inhibition studies *in vitro*. B) Synthetic routes to intermediates **106** and **107**. Reagents and conditions: a) DIBAL-H, THF, 80%; b) Dess-Martin periodinane, DCM, 81%.

Gratifyingly, initial rate studies of the synthetic intermediates revealed **106** as both a high affinity and highly selective inhibitor of SULT1A3.[251] No inhibition of either isoform was observed at 10 μM treatment with **95**, **104**, or **107**. Compound **106** inhibited SULT1A3 at 34 nM

treatment and displayed an increased 203-fold specificity for SULT1A3 over SULT1A1, rendering this an extremely potent, isoform specific inhibitor. However, the assay used for these studies does not indicate the mechanism of inhibition and therefore, allosteric inhibition could not be confirmed through this assay alone. At saturating inhibitor concentrations, the enzyme turnover is reduced to nearly half (54%) of the uninhibited enzyme (Figure 2-15), indicating that the enzyme can still function partially in the presence of inhibitor.

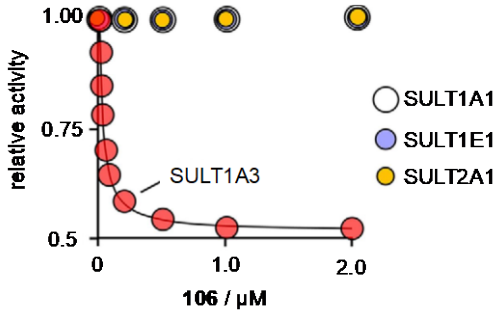

Figure 2-14: Evaluation of isoform-selectivity of inhibitor 106
The initial rates of SULT-mediated sulfonation of 1-HP are plotted as a function of inhibitior concentration normalized to [**106**] = 0 µM. Figure adapted from Darrah et. al., *J. Biol. Chem.*, **2019**, 294, 2293.[251]

2.5.3 Biological Evaluation and Characterization of SULT Inhibition by 106

To better understand how **106** was inhibiting SULT1A3, structural analogs were synthesized and tested in inhibition studies and binding assays (Figure 2-16A). Because several C-6 modified analogs were tested, SAR studies were more focused around substitution at C-2. Additional analogs (**108-113**) were synthesized using Friedlander conditions to react **103** with various ketones (**94, 114-116**) to produce several aliphatic substitutions at the C-2 position (**108, 109, 111-113**) (Figure 2-16B). Lithium aluminum hydride (LAH) reduction of commercially available methyl quinoline 6-carboxylate (**100**) afforded **108** in 85% yield. A Friedlander reaction of **103** and 5-methylhexan-2-one (**116**) produced compound **119** as the major product (63%) and

120 as the minor 2,3-disubstituted product (26%). These ester intermediates were subsequently reduced with lithium aluminum hydride to form the corresponding C-2 alcohol, **112** and **113**, respectively. To understand how the primary alcohol at C-6 contributes to binding and inhibition, an additional analog (**110**) was synthesized containing a methoxy group in place of the primary alcohol. This compound was synthesized from **106** and thionyl chloride in dichloromethane to produce the primary alkyl chloride **121** which then underwent an S_N2 reaction with sodium methoxide in methanol to generate **110** (Figure 2-16C).

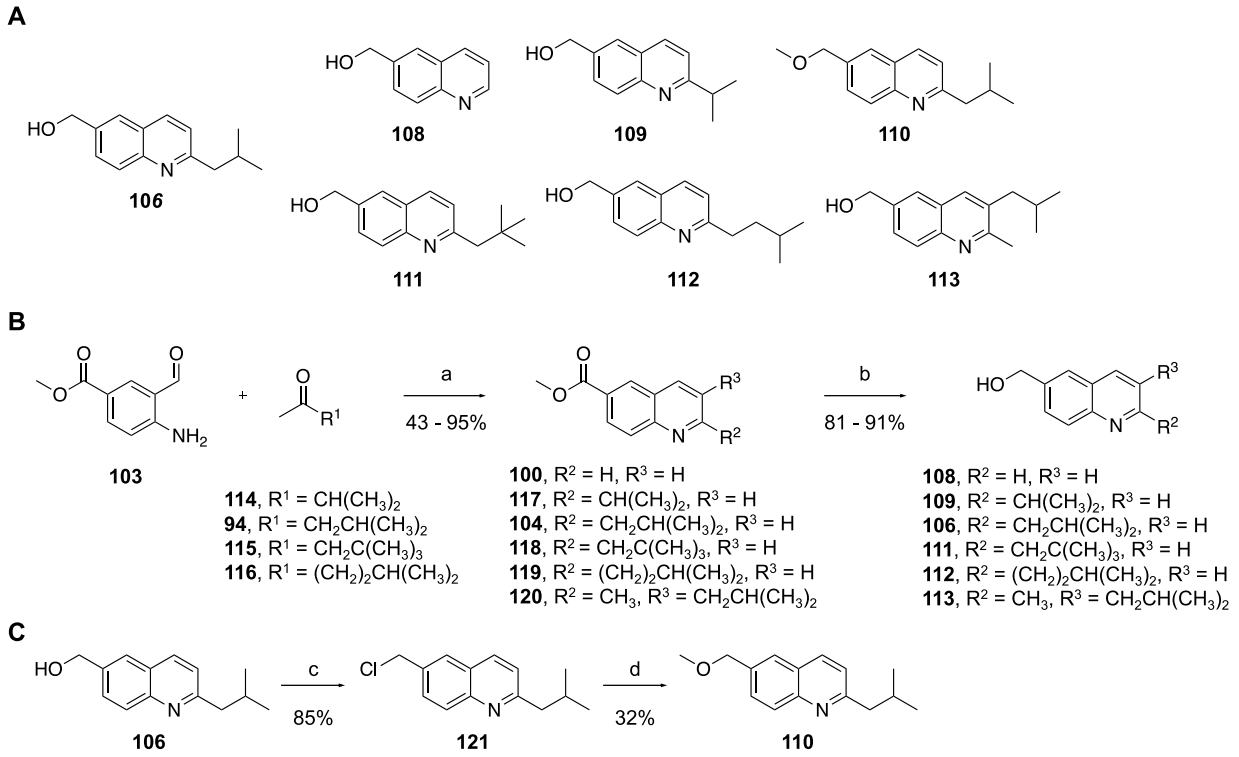

Figure 2-15: Structure-activity studies and synthesis of 106 analogs
A) Structures of C-6 modified analogs for structure-activity studies of **106**. B) Synthetic routes to structural analogs **108**-**113**. Reagents and conditions: a) pyrrolidine, H_2SO_4, EtOH, 43-95%; b) lithium aluminum hydride, THF, 81-91%. C) Synthetic route to structural analog **110**. Reagents and conditions: c) thionyl chloride, DCM, 85%; d) sodium methoxide, methanol, 32%.

When all of these analogs were tested in initial rate inhibition studies by the Leyh lab, only **113** and **110** displayed inhibition towards SULT1A3 at 10 μM treatment. The lack of inhibitory

activity was particularly surprising due to the structural similarities between the analogs and the parent compound. Identified as a less potent inhibitor of SULT1A3 than **106**, **113** demonstrated a measured K_i of 7.5 (± 0.5) μM. At saturating treatment concentrations, **113** reduced enzyme turnover to 17% of the uninhibited enzyme. Unfortunately, **113** had an almost identical effect on SULT1A1, reducing enzyme turnover to 20% at a similar affinity (K_i = 7.7 ± 0.3 μM). From the SAR study, it was determined that the isobutyl chain at the C-2 position of the quinoline scaffold was absolutely critical for isoform specificity, as deviation from this group completely abolished both inhibitor activity and specificity. Although isobutyl substitution at C-3 is tolerated in **113**, this change in R-group substitution on the ring compromised both SULT1A3 isoform specificity and overall potency of the inhibitor. Demonstrating a similar result, **110** exhibited 90% inhibition of both SULT1A1 and SULT1A3 at saturating concentrations. The spectacular inhibition was overshadowed by poor, almost equivalent affinity for both enzymes (K_i = 5.7 μM for SULT1A1, K_i = 6.1 μM for SULT1A3).

Substitution of the alcohol for a methoxy group (**110**) increased the efficacy of the inhibitor, but compromised isoform specificity. In attempts to rationalize isoform selectivity of **106** for SULT1A3, our collaborator (Ian Cook, Leyh Lab) determined the structure of **106** bound to SULT1A3 through a spin labeling NMR strategy developed by the Leyh lab.[247] A total of six spin labeled SULT1A3 mutants were constructed. Spin labels were strategically placed such that virtually the entire surface of the enzyme was within a detectable distance (25 Å) of a spin label, coating the enzyme surface in a paramagnetic field. Spin label mutants were generated via mutagenesis of selected residues to cysteine (Cys) and subsequent covalent labeling with 3-maleimido-PROXYL (3-MP) or its diamagnetic homolog N-cyclohexylmaleimide (CM). Initial rate and inhibition parameters were conducted to validate that spin labeling does not compromise

the ligand binding or catalytic activity of the enzyme. The design, mutagenesis, expression, and characterization of spin labeled SULT1A3 mutants was conducted by Ting Wang and Ian Cook.

When a ligand binds to the mutant protein, the resulting paramagnetic effects are detected through ligand exchange between the enzyme and solvent. From this interaction, the ligand position can be triangulated by measuring the distance from the spin labeled residue to reveal an initial position of binding on the enzyme. The magnitude of the paramagnetic effects is distance dependent; the closer a ligand binds to a spin label, the stronger the effect and vice versa. Using these general distances, the structure was refined using docking programs to determine the site and orientation of ligand binding. All docking and MD simulation work was conducted by Ian Cook.

From refinement of the NMR analysis, a protein model of 106 bound to SULT1A3 was developed (Figure 2-17). It was determined that 106 was not binding to either of the known, intended allosteric sites of SULT1A3 – catechin and NSAID – but surprisingly, was binding to the active site cap. While the active site cap has been reported to cause SULT inhibition due to binding of compounds at other known allosteric sites,[248, 249] this is the first report demonstrating direct compound binding to the active site cap that results in SULT inhibition, suggesting the active site cap is a novel allosteric site present on SULT enzymes.

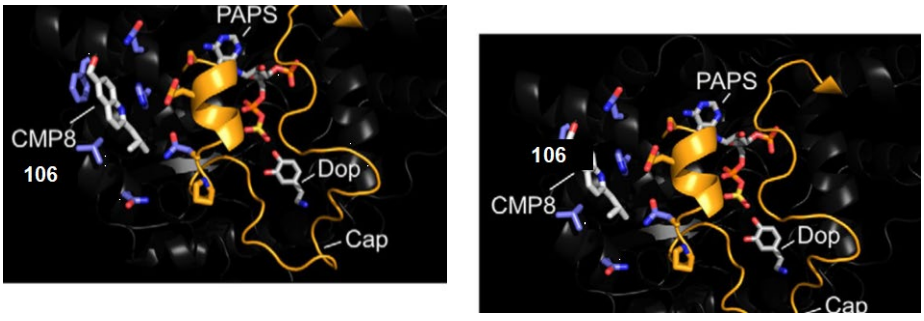

Figure 2-16: Docking of 106 in the SULT1A3 active site cap
Protein model of **106** (gray) docked into SULT1A3 (black) near active site cap (orange) at a distance (left image). Key residue interactions between inhibitor and active site cap are indicated (right). Figure adapted from *Darrah et. al*., *J. Biol. Chem.*, **2019**, 294, 2293.[251]

Based on modeling analysis, several residues in this pocket interact with **106** and stabilize binding at all positions in the compound, indicating that every functionality is both critical to SULT1A3 binding and essential for isoform specificity as demonstrated in the **106**-analog SAR study. SULT1A3 mutants were generated by Ting Wang to confirm these interactions and orientation of **106** in the cap binding site (Table 2-1). All mutants were evaluated with 1-HP as an acceptor substrate to confirm that the mutations did not significantly alter inherent kinetic parameters. H-bonding interactions between the side chain amino group of Q225 are in proximity to the H-bond accepting alcohol at C-6 of **106**. The quinoline ring system is perfectly centered between F222 and H226 which facilitate and stabilize binding through pi-stacking interactions. When F222A and H226A mutations are introduced, both pi-stacking stabilization interactions are lost, resulting in a decreased affinity of **106** for SULT1A3. These residues also contribute to isoform specificity as the corresponding residues in SULT1E1 and SULT2A1 are not aromatic and do not provide this stabilization,[260-262] therefore, cannot bind **106**. Also shown in proximity to the aliphatic chain of **106** are N71 and N235. Introduction of an N71H point mutation, the naturally occurring residue in SULT1A1, resulted in complete loss of inhibitor binding, suggesting this residue is also critical to isoform specificity. The bulky histidine residue at this position in SULT1A1 blocks binding of **106** to this site as there is not enough room to accommodate an isobutyl group and thus, no inhibition by **106** is observed. SULT2A1 contains an alanine at this position, but due to lack of both F222 and H226, binding is not stabilized and no inhibition of this isoform with **106** is observed. An L67G mutation changes the K_i and K_D of **106** only slightly, indicating hydrophobic interactions do not significantly contribute to binding, but are present between the isobutyl group and leucine side chain.

Table 2-1: Initial rate parameters of 106 with SULT1A3 mutants
Standard deviations are indicated in parentheses.

mutant	K_i (μM)	Turnover at saturation (%)	K_D (μM)
WT	0.034 (0.003)	51	0.051 (0.004)
F222A/H226A	2.0 (0.2)	53	1.9 (0.2)
L67G	0.18 (0.01)	50	0.22 (0.03)
N71H	ND	ND	ND

Based on the site of binding, it was hypothesized that inhibition by **106** is due to stabilization of the closed conformation of the active site cap, thereby limiting the access of acceptor substrates to the active site and slowing release of the bound nucleotide co-factor. As previously mentioned, the SULT1A3 active site cap is dynamic and can isomerize between a closed and open form upon PAPS binding, with equilibrium favoring the closed conformation.[196, 260, 263] Upon **106** binding to the active site cap, the isobutyl chain disrupts the interaction between N71 and N235, disrupting cap dynamics and stabilizing the closed conformation of SULT1A3, resulting in the observed enzyme inhibition. Although no inhibition was observed for the several analogs of **106**, we sought to determine if these compounds were capable of binding to the enzyme to uncover what contributes to the lack of potency as isoform-specific inhibitors.

Equilibrium binding studies with SULT1A3 were conducted for **106**-analogs, **109** and **112**. Upon ligand binding, there is a detectable change in internal fluorescence of the enzyme. By monitoring fluorescence change (λ_{ex} 290 nm, λ_{em} 340 nm) ligand binding can be determined. Structural analogs, **109** and **112**, were titrated into a reaction solution containing SULT1A3, 1-HP, PAPS, and **106** at saturating concentrations. If either **109** or **112** is capable of binding to the cap site, SULT1A3 activity should be recovered as the non-inhibiting analog will displace **106** from the cap. Not surprisingly, analogs **109** and **112** demonstrated binding to the cap site with comparable affinities (160 nM and 87 nM, respectively) to **106** (45 nM) despite showing no

inhibitory activity (Figure 2-18). The inhibitory activity of **106** is primarily due to the disruption of the N71 and N235 interaction by the isobutyl substituent at the quinoline C-2. When one carbon is removed from this aliphatic chain, generating an isopropyl substituent (**109**), the aliphatic chain is shortened and therefore cannot reach the N-residues in the cap to disrupt the interaction, and inhibit enzyme turnover. When one carbon is added to the chain (**112**), there is increased flexibility in the aliphatic chain such that it can rotate freely outside of the pocket with L67 and thus, exhibits the same result. These results validate that isoform specific inhibition by **106** is very sensitive to length of the aliphatic chain and confirm the isobutyl tail is optimal at the C-2 position. These experiments were performed by Ting Wang (Leyh lab). All together, these results confirm both the binding mode and hypothesized inhibitory profile of **106**.

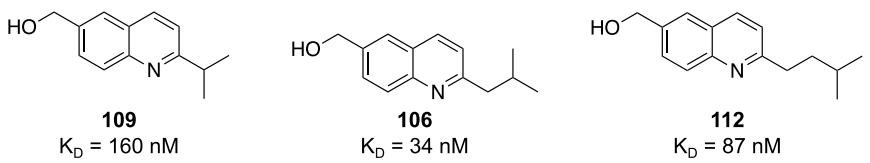

Figure 2-17: SULT1A3 binding affinities of 106 and structural analogs

2.6 Development and Optimization of Second Generation Allosteric SULT1A3 Inhibitors

Having designed the first, synthetic allosteric inhibitor of SULT1A3 that targets a novel allosteric site within SULT1A3, we sought to use our computational approach to refine the structure of hit compound **106** to enhance its overall inhibitory profile. Using **106** as a framework, we developed a set of potential second-generation inhibitor compounds that should bind SULT1A3 tighter, enhance stabilization of the closed cap conformation, and further reduce SULT1A3 turnover – all while preserving isoform-specificity. *In silico* analysis of the allosteric cap binding

site revealed that placement of a terminal carboxamide in the isobutyl tail at the C-2 position on the quinoline scaffold would interfere with the interactions between N71 and N235, residues which are essential to the active site cap dynamics. We hypothesized that a terminal carboxamide at this position will serve as a decoy, firmly locking the cap in a closed conformation, and as a result, reducing enzyme turnover. Our analysis predicted four, synthetically accessible compounds (**121** – **124**) that were anticipated to bind SULT1A3 tighter than **106** (Figure 2-19). Additionally, we expanded our approach beyond quinoline structures to incorporate other heterocyclic core scaffolds such as 1, 2, 3, 4- tetrahydroacridines, 2,6-disubstituted naphthalenes, and 1,8-naphthyridines.

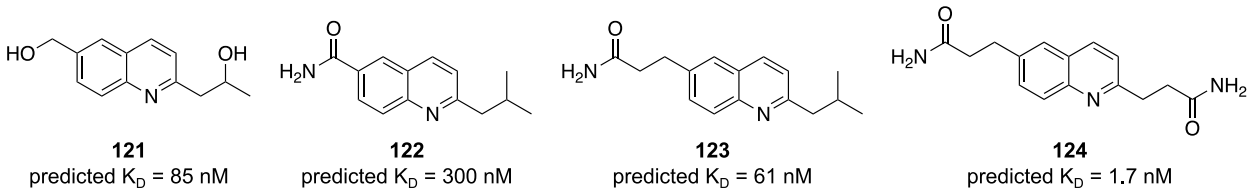

Figure 2-18: Structures of proposed second generation SULT1A3 inhibitors

2.6.1 Synthesis of Second Generation SULT1A3 Inhibitors

Attempts to synthesize compound **121**, followed the same general synthetic scheme previously mentioned. A Friedlander quinoline synthesis of **103** with pentane-2,4-dione yielded the minor 2,3-disubstituted product in 36% yield. The major 2-monosubstituted product was not isolated. Reduction of the minor Friedlander product with $LiAlH_4$ yielded the alcohol **127** in 47% yield (Figure 2-20A). A similar hydroxyl-containing analog was synthesized by fellow lab member, Mary Cacace, using a Friedlander quinoline synthesis with 1-hydroxypropan-2-one. The

di-substituted Friedlander product **130** was the major product, isolated in 59% yield (Figure 2-20B). When tested in initial rate inhibition studies by the Leyh lab, neither compound demonstrated inhibition of either SULT1A1 or SULT1A3 at 30 μM treatment, suggesting this substitution pattern was not suitable for SULT inhibition.

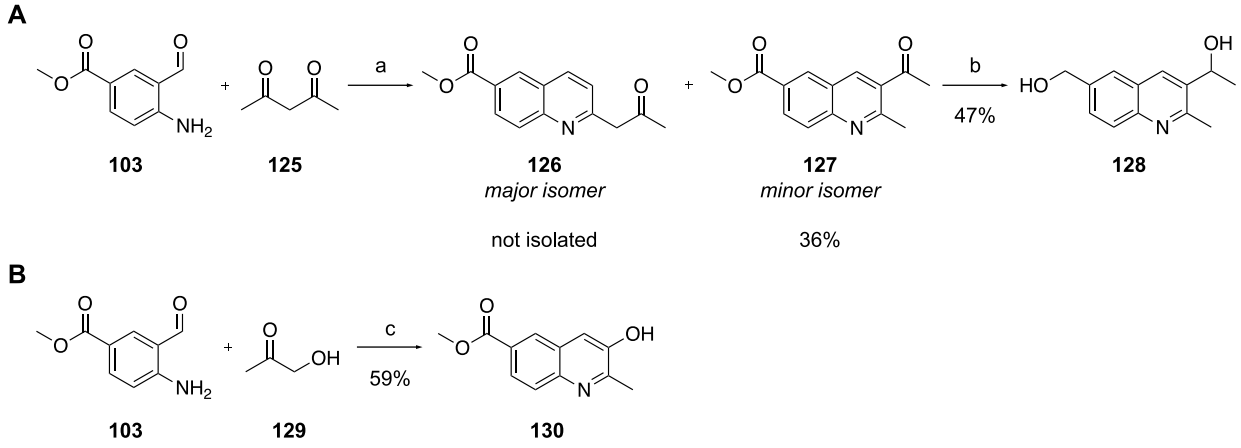

Figure 2-19: Synthetic routes to hydroxyl-containing inhibitors 128 and 130
A) Synthetic route to **128**. Reagents and conditions: a) pyrrolidine, H_2SO_4, EtOH, 36%; b) lithium aluminum hydride, THF, 47%. B) Synthetic route to **130**. Reagents and conditions: c) pyrrolidine, H_2SO_4, EtOH, 59%. Compound **130** was synthesized by Mary Cacace.

Derivatives of **106** containing a carboxamide at the C-6 position (**122-124**) were predicted to bind the SULT1A3 active site cap with high affinity due to stronger H-bonding interactions with Q225. Compound **122** was synthesized from intermediate **105** in the synthesis of **96**. The carboxylic acid **105** was activated as an N-hydroxysuccinimide (NHS) ester using N, N, N', N'-tetramethyl-O-(N-succinimidyl)uranium tetrafluoroborate (TSTU), which was then treated with ammonia to generate carboxamide **122** (Figure 2-21A). A second predicted derivative with a longer aliphatic linker (**123**) was synthesized starting with a Heck cross coupling of aryl-bromide **95** and acrylamide (**131**) to produce **132**. Reduction of the double bond through a palladium catalyzed hydrogenation yielded compound **123** in 96% yield (Figure 2-21B). Compounds **122**

and **123**, as well as intermediate **132**, were tested in initial rate inhibition studies with SULT1A3. Gratifyingly, predicted compounds **122** and **123** exhibited isoform specific SULT1A3 inhibition with inhibitory constants (0.86 μM and 70 nM, respectively) in agreement with their predicted values. Upon treatment at saturating compound concentrations, both compounds demonstrated more than 85% inhibition of SULT1A3 turnover, a stark improvement over that observed with our original compound **106**, thereby validating the predictive model. Additionally, synthetic intermediate **132** was 55-fold more selective for SULT1A3 over SULT1A1, with a measured K_i of 0.11 μM, and reduced enzyme turnover to 58% of that exhibited by the uninhibited enzyme.

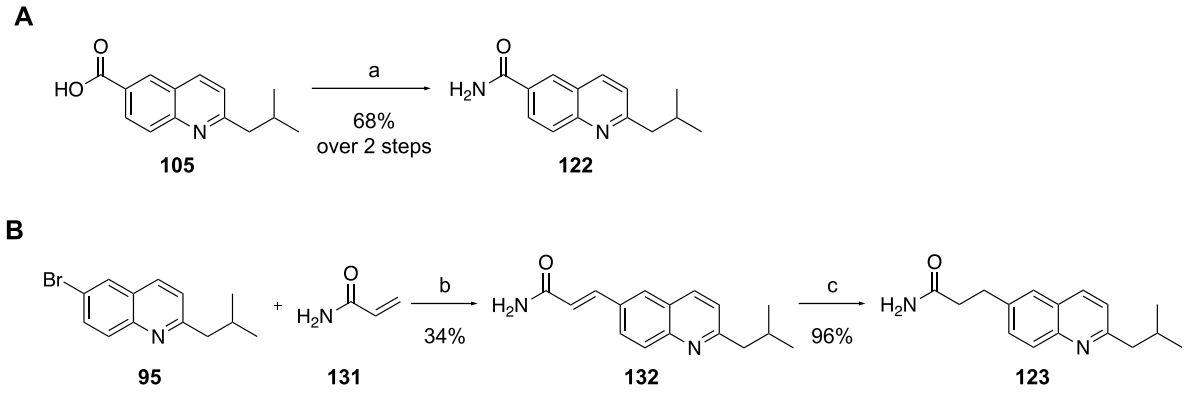

Figure 2-20: Synthetic route to 122 and 123
A) Reagents and conditions: a) (i) TSTU, TEA, acetonitrile, 83%; (ii) ammonia (0.5 M in dioxane), 82%. B) Reagents and conditions: b) palladium(II) acetate, tri(o-tolyl)phosphine, TEA, DMF, 34%; c) hydrogen, palladium(II) hydroxide, methanol, 96%.

While these compounds exhibited significantly improved inhibitory properties, **124** displayed the best predicted SULT1A3 binding affinity of 1.7 nM, therefore synthetic efforts towards this inhibitor were pursued (Figure 2-22A). Synthesis efforts toward **124** began with a Friedlander quinoline synthesis with commercially available 2-amino-5-bromobenzaldehyde (**133**) and ethyl levulinate (**134**). Both the mono- and di-substituted regioisomers, **135** and **136** respectively, were isolated, however the desired 2-monosubstituted **135** was isolated in 17% yield.

A Heck reaction of **135** with ethyl acrylate afforded the di-ester **137**, which was then deprotected under basic conditions to form the di-acid **139**. A peptide coupling with ammonium chloride (NH_4Cl) in the presence of 1-ethyl-3-(3-dimethylaminopropyl)carbodiimide (EDCI) and DIPEA to generate the **124**-precursor **140** failed. To reduce the number of steps and provide a more direct installation of one of the carboxamides, a Heck coupling of **135** with acrylamide was performed and the product isolated in 75% yield. The double bond was reduced through a palladium catalyzed hydrogenation to generate **141** (Figure 2-22B).

With **141** being few synthetic steps remaining to the final compound **124**, conditions for installing the amide at the C-2 position were screened using **135** as a model substrate before moving the syntheses of **141** forward (Figure 2-22C). The ethyl ester **135** was deprotected under basic conditions to produce the terminal carboxylic acid at the C-2 position on the quinoline ring (**142**). Since amide installation via reaction of an NHS-ester with ammonia proved to be reliable, conditions for activating the C-2 carboxylic acid as an NHS-ester were attempted. Synthetic efforts in attaining the NHS ester **143** through reaction with TSTU or 1-ethyl-3-(3-dimethylaminopropyl)carbodiimide (EDCI) and NHS failed. As an alternative route, conversion of the carboxylic acid to the corresponding acyl chloride (**144**) was attempted but also failed (Figure 2-22D). The synthetic difficulties with the NHS activation at the C-2 position coupled with the consistently low-yields (15 – 38% yields) in generating **135** in the Friedlander reaction, proved this route toward generating **124** to be unreliable.

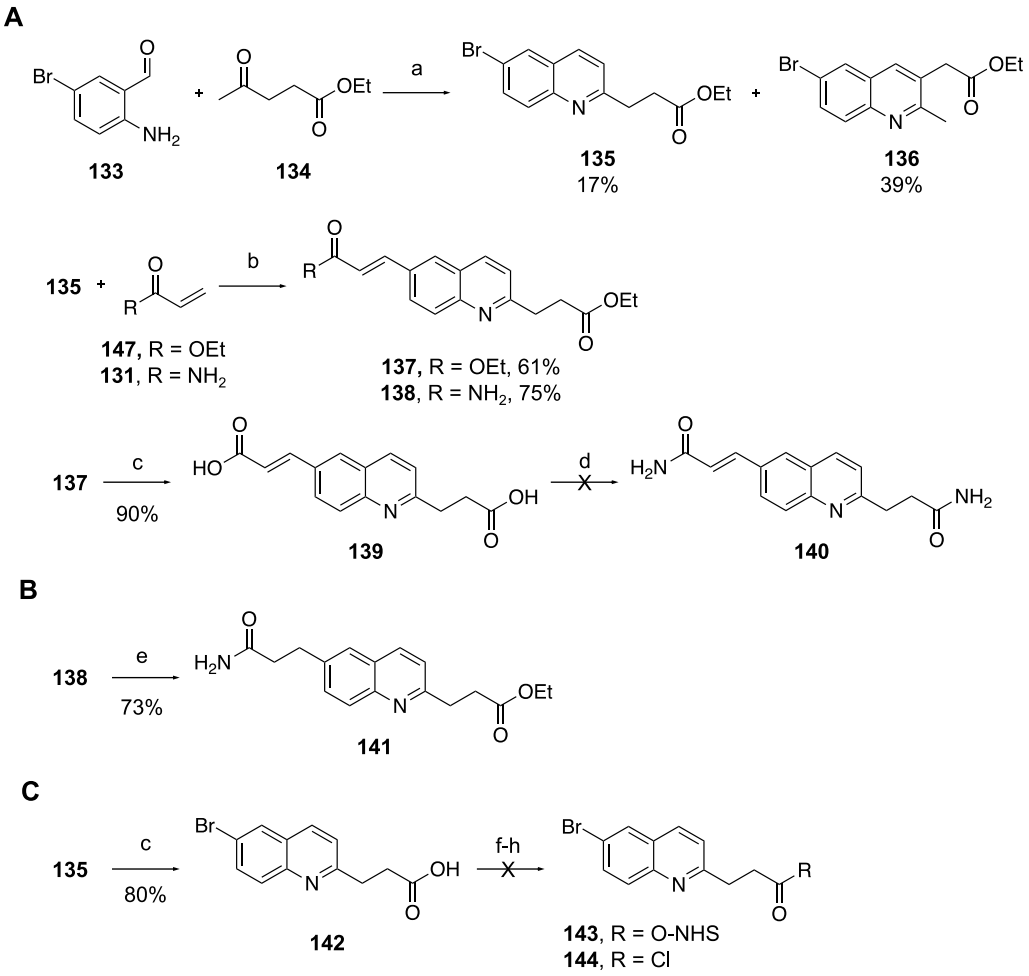

Figure 2-21: Synthetic attempts toward 124
Reagents and conditions: a) pyrrolidine, H_2SO_4, EtOH; b) palladium(II) acetate, tri(o-tolyl)phosphine, TEA, DMF; c) 1M LiOH, THF; d) ammonium chloride, EDCI, DIPEA, DMF; e) hydrogen, palladium(II) hydroxide, methanol; f) TSTU, TEA, acetonitrile; g) NHS, EDCI, THF; h) $SOCl_2$, cat. DMF, DCM.

To reduce the number of transformations, a symmetric synthetic approach was pursued (Figure 2-23). Using commercially available 6-bromo-2-quinolin-2-ol (**145**), the C-2 hydroxyl was converted to the corresponding triflate **146** rapidly and in quantitative yields following a reaction with triflic anhydride. A double Heck reaction with ethyl acrylate (**147**) afforded the di-ester in 19% yield. In hopes to increase the yield by using a more reactive starting material, commercially available quinolin-2,6-diol (**148**) was converted to the corresponding di-triflate **149** and subject to the same microwave-assisted Heck reaction conditions to produce the di-ester **150** in 27% yield.

While this route did slightly improve the yield, this reaction was not reproducible. Additionally, a Heck coupling with either **146** or **149** and acrylamide was attempted but was not successful in generating the di-amide compound.

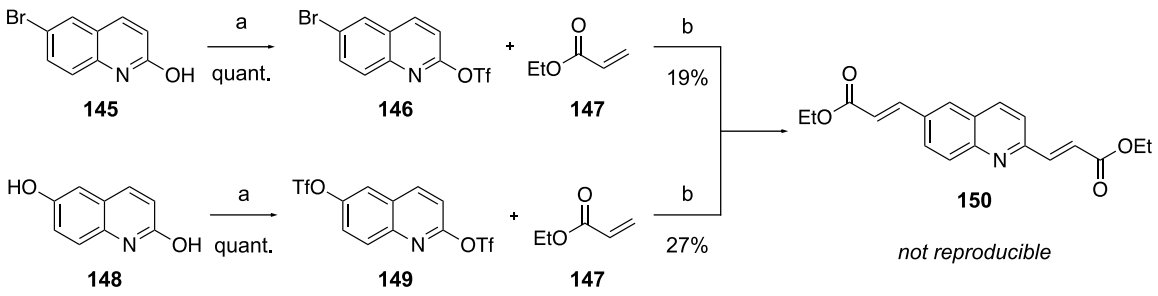

Figure 2-22: Symmetric synthesis approach for generating 124
Reagents and conditions: a) triflic anhydride, pyridine, DCM, quantitative; b) palladium(II) acetate, TBAB, LiCl, K_2CO_3, DMF, μwave, 110 ºC.

Due to our previous success in screening synthetic intermediates, intermediates in the synthesis toward **124** were tested in initial rate inhibition studies (Figure 2-24). The initial rate studies were performed by the Leyh lab. Of the three compounds tested, only compound **141** exhibited isoform specific inhibition of SULT1A3. With an inhibitory constant of 0.33 μM, **141** exhibited 63% inhibition of recombinant SULT1A3 validating the functional group substitution pattern. Based on these results, we hypothesize that the flexibility of the saturated amide at the C-6 position allows **141** to hydrogen bond with Q225 and better stabilize its position when binding to the SULT1A3 active site cap. Additionally, the ester at the C-2 position may only weakly influence the cap dynamics, and therefore result in the observed inhibition. Compounds **135** and **138** did not show any inhibitory activity of either isoform at 10 μM treatment.

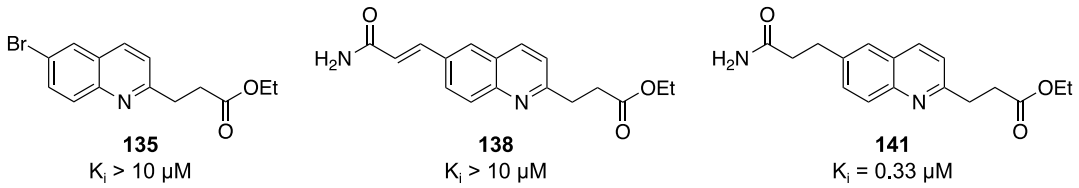

Figure 2-23: Structures and inhibitory constants of synthetic intermediates towards generating 124
Inhibitory constants were determined following initial rate SULT1A3 inhibition studies performed by the Leyh Lab.

To evaluate the contribution of the C-2 ester to inhibitory activity, we synthesized **156**, an analog containing a carboxamide only at the C-6 position (Figure 2-25A). Commercially available 6-bromoquinoline (**151**) was subject to a Heck reaction with **147** to form ester **152**. The ester was deprotected under basic conditions to generate the acid **153**, which was then activated with TSTU to form the corresponding NHS ester (**154**). Treatment with ammonia in dioxane afforded carboxamide **155**. The double bond was reduced using a palladium catalyzed hydrogenation to afford the saturated amide **156**. When tested in initial rate inhibition studies, **156** did not exhibit any activity against either isoform (Figure 2-25B). Synthetic intermediates **153** and **155** were also tested, however only **153** exhibited any SULT1A3 inhibition. Compound **153** behaved as a mild inhibitor of SULT1A3 (K_i = 4.1 µM), demonstrating both slight isoform selectivity over SULT1A1 and 72% inhibition of SULT1A3 at saturating treatment concentrations.

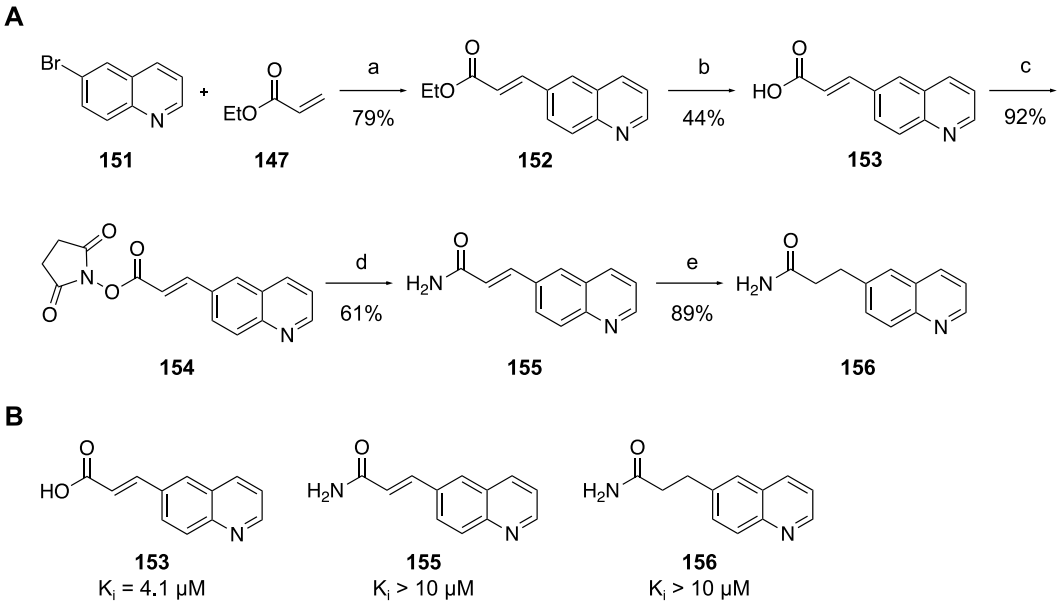

Figure 2-24: Synthesis and initial rate studies of 156
A) Synthetic route to **156**. Reagents and conditions: a) palladium(II) acetate, tri(o-tolyl)phosphine, TEA, DMF, 79%; b) 1M LiOH, THF, 44%; c) TSTU, TEA, acetonitrile, 92%; d) ammonia (0.5 M) in dioxane, 61%; e) hydrogen, palladium(II) hydroxide, methanol, 89%. B) Inhibitory constants were determined following initial rate SULT1A3 inhibition studies performed by the Leyh lab.

2.6.2 Exploration of Other Heterocyclic Core Scaffolds

In addition to exploring the enhanced cap stabilization effects through C-2 and C-6 functionalization, we also opted to explore heterocyclic core scaffolds beyond quinoline-based structures to further optimize our inhibitors. We sought to "tie up" our initial lead compound, **106**, generating a 1, 2, 3, 4-tetrahydroacridine core structure (Figure 2-26). Three of these "closed" structures (**157**-**159**) were analyzed *in silico* for SULT1A3 affinity and the ability to enhance cap stabilization in comparison to **106**. The fully closed **106**-analog, **157**, was predicted to have moderate affinity for SULT1A3 (K_i = 520 nM), to have 6-fold preference for SULT1A3 over SULT1A1, and to demonstrate 51% inhibition of SULT1A3 activity through stabilization of the active site cap. However, when a terminal carboxamide is substituted at the C-7 position on this

scaffold, as in **159**, the compound is predicted to be a high affinity (K_i = 31 nM) and an extremely specific SULT1A3 inhibitor (> 750-fold more selective for SULT1A3 over SULT1A1). Further, this potential inhibitor is predicted to better stabilize the closed conformation of the active site cap and, as a result, inhibit SULT1A3 turnover an additional 30% more than our original lead compound **106**.

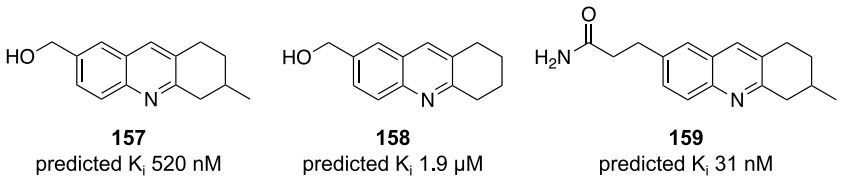

157
predicted K_i 520 nM

158
predicted K_i 1.9 µM

159
predicted K_i 31 nM

Figure 2-25: Structures and predicted inhibitory constants of closed 106-analogs

Due to the promising results from the computational analysis, attempts at the synthesis of these compounds were pursued by fellow lab member, Mary Cacace. In attempts to generate the amide containing **159**, 2-amino-5-bromobenzaldehyde (**133**) and 5-methylcyclohexane-1,3-dione (**160**) underwent a Friedlander reaction following conditions reported previously, generating the methyl substituted 1, 2, 3, 4-tetrahydroacridine scaffold **161**. No regioselectivity issues were encountered due to the symmetry of the starting ketone. A Wolff-Kishner reduction of **161** to generate **162** was successful, however this intermediate was not reactive in the subsequent Heck reaction (Figure 2-27A). Due to the promising results *in vitro* with quinoline structures containing a primary carboxamide at the quinoline C-6 position, a similar derivative (**168**) was synthesized with this heterocyclic scaffold (Figure 2-27B). This compound was synthesized using a Friedlander reaction starting with **103** (analogous to the conditions reported above) to generate intermediate **164**. Through a series of methyl ester deprotection, followed by NHS-activation, **166** was treated with ammonia in dioxane to form the amide **167**. Reduction of the ketone with $LiAlH_4$

afforded the C-1 modified alcohol derivative **168** in 70% yield. This synthesis was completed by fellow lab member, Mary Cacace.

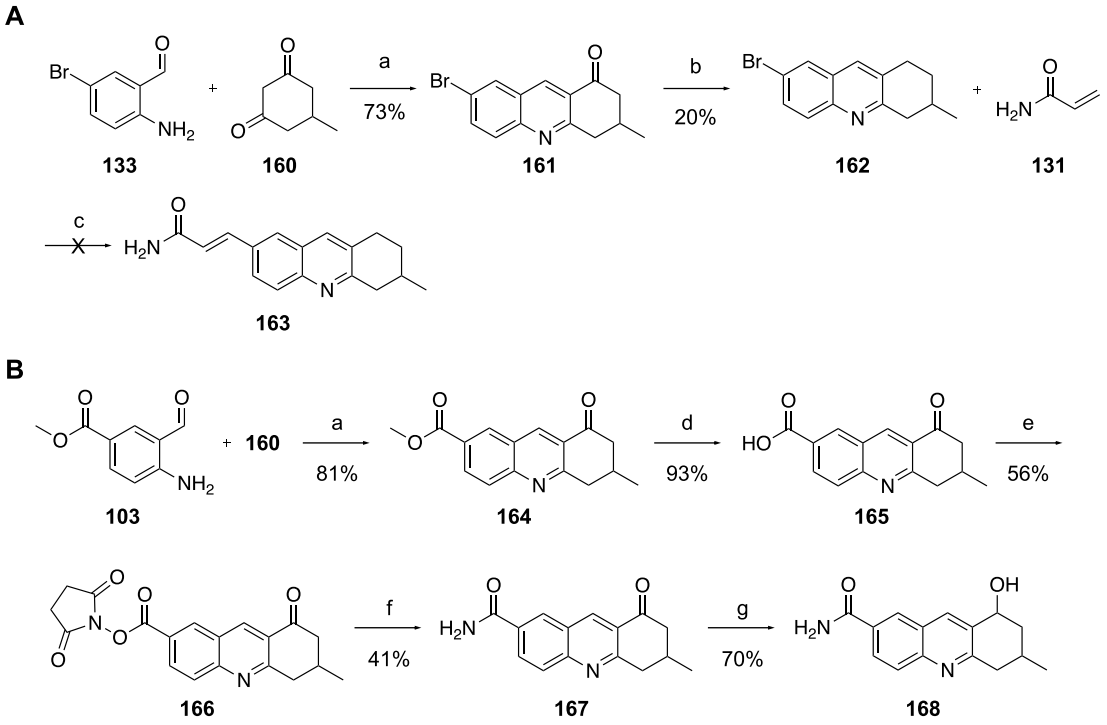

Figure 2-26: Synthetic routes towards "tied-up" inhibitor compounds
A) Attempted synthetic route towards generating predicted compound **159**. Reagents and conditions: a) pyrrolidine, H_2SO_4, EtOH; b) hydrazine, potassium hydroxide, diethylene glycol, 20%; c) palladium(II) acetate, tri(o-tolyl)phosphine, TEA, DMF. B) Synthesis of **168**. Reagents and conditions: d) 1M LiOH, THF, 93%; e) TSTU, TEA, acetonitrile, 56%; f) ammonia (0.5 M) in dioxane, 41%; g) $LiAlH_4$, THF, 70%. Synthesis was completed by fellow lab member, Mary Cacace.

Several synthetic intermediates towards the predicted tri-cyclic compounds were evaluated in initial rate inhibition studies (Figure 2-28). Compounds including **161**, **164**, **165**, **167** and **168** were tested, three of which demonstrated inhibitory activity against SULT1A3. Compound **164** inhibited SULT1A3 turnover 35% at saturating treatment, exhibiting a K_i of 0.66 µM. Both carboxamide-containing intermediates, **167** and **168**, performed much better (K_i = 0.11 µM and 85 nM, respectively), with **167** demonstrating 75% inhibition at saturating treatment. These results

instill optimism that the computational predictions are valid and predicted structures will perform as or better than expected.

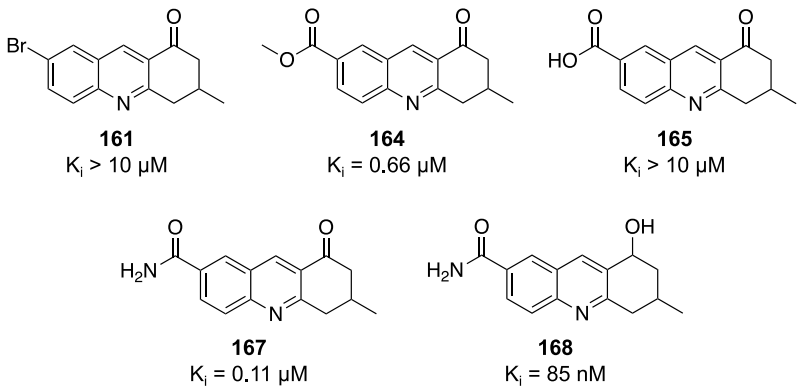

Figure 2-27: Initial rate SULT1A3 inhibition studies of "tied-up" 106-analogs
Inhibitory constants were determined through initial rate inhibition studies performed in the Leyh lab.

Additionally, heterocyclic scaffolds containing one less nitrogen (naphthalene, **169**) and one additional nitrogen (1,8-naphthyridine, **170**-**172**) than a quinoline ring were explored (Figure 2-29). In addition to synthetic accessibility,[256] we hypothesize that scaffolds containing a second nitrogen atom on the ring, forming a 1,8-naphthyridine core structure, will increase solubility and drug-likeness of the current library of SULT1A3 inhibitors. Structures were analyzed *in silico* and most were predicted to be higher affinity SULT1A3 inhibitors, in comparison with the optimal quinoline-based inhibitor **106**.

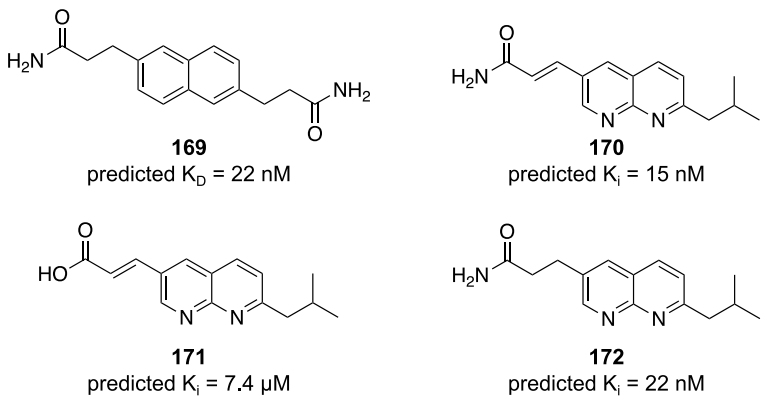

Figure 2-28: Structures and predicted inhibitory properties of core ring-optimized SULT1A3 inhibitors

A symmetric synthesis approach was pursued in hopes of synthesizing the derivatized naphthalene compound **169** (Figure 2-30A). A double Heck cross-coupling reaction with starting with either commercially available 2,6-dibromonaphthalene (**173**) or the corresponding synthesized di-triflate **175** (synthesized following conditions specified previously) and ethyl acrylate generated the 2,6-disubstituted-ethyl ester. The 2,6-dibromonaphthalene starting material consistently yielded the di-ester product in reproducible, high yields and therefore was the preferred substrate for synthesizing **176**. Deprotection of the ester under basic conditions afforded the di-acid **177**, which was very insoluble and difficult to work with. Attempts to synthesize the corresponding amide from di-acid **177** included a peptide coupling with NH_4Cl and EDCI, NHS-activation, and synthesis of the acyl chloride and subsequent treatment with ammonia. Direct ester to amide conversion was attempted following previously reported conditions[264] with catalytic sodium cyanide and ammonia, but was not successful. The di-ester and di-acid intermediates **176** and **177** were evaluated in initial rate inhibition studies *in vitro*, however neither compound displayed inhibitory activity towards either isoform (Figure 2-30B).

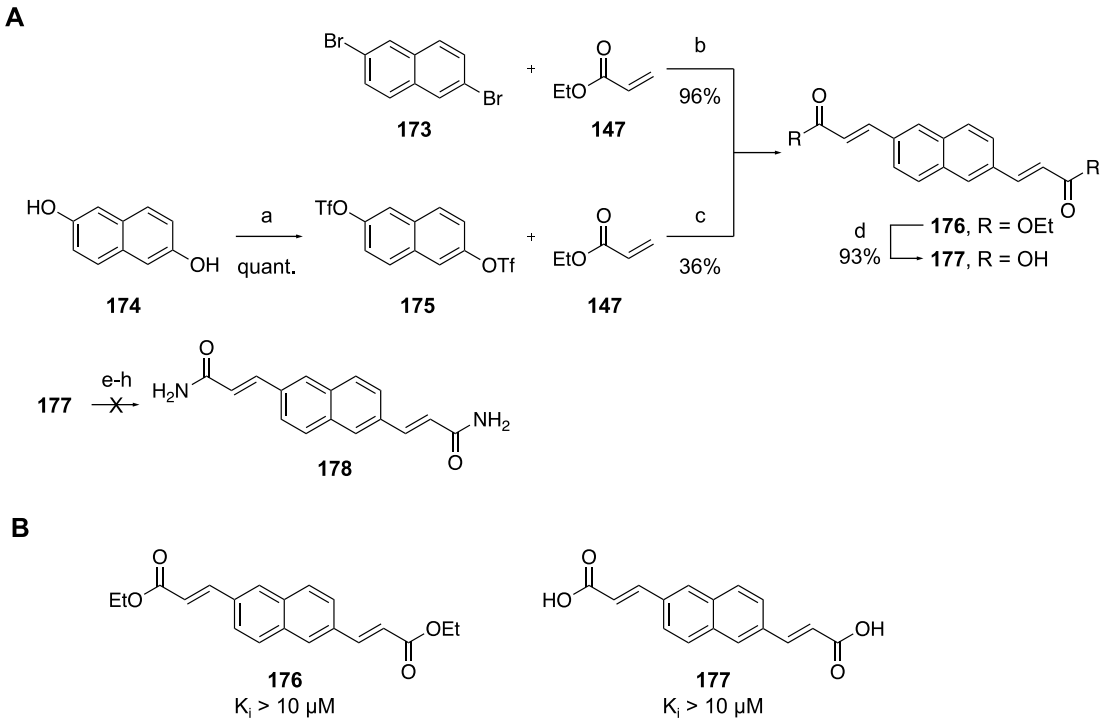

Figure 2-29: Synthetic efforts and initial rate studies of naphthalene-based inhibitor scaffolds
A) Reagents and conditions: a) triflic anhydride, pyridine, DCM; b) palladium(II) acetate, tri(o-tolyl)phosphine, TEA, DMF; c) palladium(II) acetate, tetrabutylammonium chloride, sodium bicarbonate, DMF; d) 1M LiOH, THF; e) ammonium chloride, EDCI, DIPEA, DMF; f) (i) oxalyl chloride, cat. DMF, DCM, (ii) ammonia in dioxane; (g) TSTU, TEA, ACN; h) 20 mol% sodium cyanide, ammonia in methanol. B) Inhibitory constants of naphthalene-based compounds **176** and **177**. Inhibitory constants were determined through initial rate inhibition studies against SULT1A3 performed by the Leyh Lab.

The advantageous properties predicted with the 1,8-naphthyridine heterocyclic core scaffold led to synthetic exploration of naphthyridine derivatives. C-2 monosubstituted naphthyridines can be easily accessed using the same reaction conditions reported previously for regioselective synthesis of C2-monosubstituted quinoline heterocycles.[256] 1, 8-Naphthyridine structures **170**-**172**, containing similar substitution patterns as the best predicted quinoline-based inhibitors, were analyzed *in silico*. Following the trends we have observed in prior computational analyses, the amide-bearing analogs **170** and **172** were predicted to be high affinity (K_i = 15 nM and 22 nM, respectively) and isoform specific SULT1A3 inhibitors (Figure 2-31A). Synthesis of these compounds was pursued by fellow lab member Mary Cacace (Figure 2-31B).

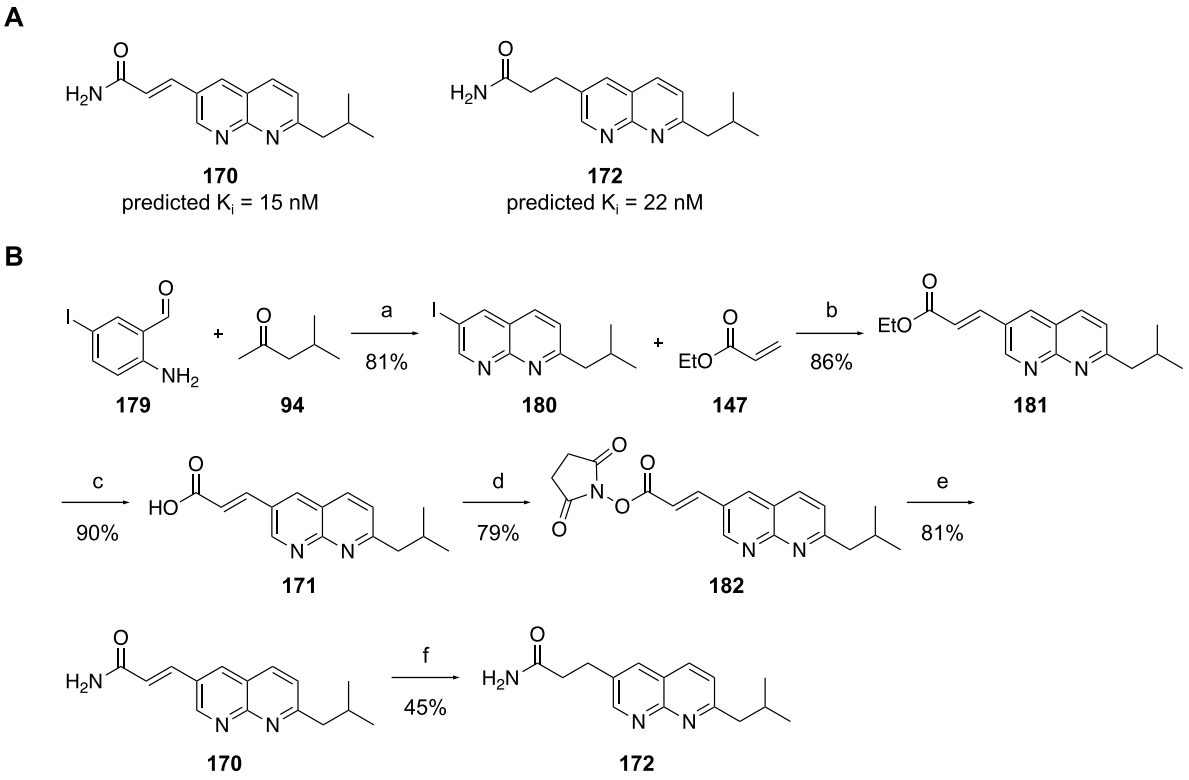

Figure 2-30: Synthetic route to 170 and 172
A) Structures and inhibitory constants of 1,8-naphthyridine-based inhibitors. Inhibitory constants were predicted *in silico* by the Leyh Lab. B) Synthesis of 1,8-naphthyridine-based inhibitor analogs. Reagents and conditions: a) pyrrolidine, H_2SO_4, EtOH, 81%; b) palladium(II) acetate, tri(o-tolyl)phosphine, TEA, DMF, 86%; c) 1M LiOH, THF, 90%; d) TSTU, TEA, acetonitrile, 79%; e) ammonia (0.5 M) in dioxane, 81%; f) hydrogen, palladium(II) hydroxide, methanol, 45%. This synthesis was completed by Mary Cacace.

When evaluated *in vitro* through initial rate inhibition studies (experiments performed by the Leyh lab), all three compounds demonstrated inhibitory activity with SULT1A3 (Figure 2-32). Compound **170** was a moderate, isoform-specific inhibitor of SULT1A3, inhibiting 29% of SULT1A3 turnover with a K_i 3.1 μM. However, when the acid was replaced with a saturated (**172**) or unsaturated (**171**) terminal carboxamide, affinity of the compounds for SULT1A3 increased dramatically, exhibiting inhibitory constants of 17 nM and 11 nM, respectively. Treatment with either amide-containing inhibitor at saturation resulted in nearly complete inhibition (more than

90%) of SUL1A3 catalysis. These inhibitors are a significant improvement over the first-generation inhibitor, **106**, and were carried forward for *in cellulo* and *in vivo* studies.

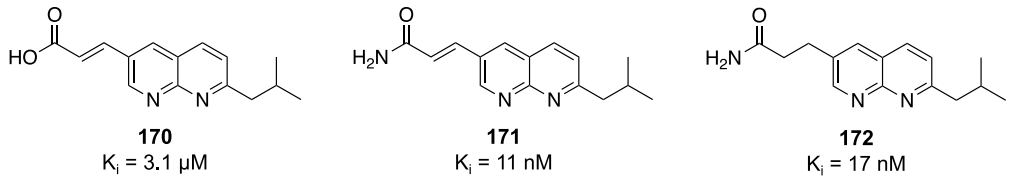

Figure 2-31: Evaluation of 170-172 in initial rate SULT1A3 inhibition studies
Inhibitory constants were determined through initial rate inhibition studies with SULT1A3. Experiments were performed by the Leyh lab.

2.6.3 Biochemical and Biological Evaluation of 123 and 171

The material presented in Section 2.6.3 was reprinted in part with permission from Cook, I.; Cacace, M.; Wang, T.; **Darrah, K.**; Deiters, A.; Leyh, T. S., *J. Biol. Chem.* **2020**, 296, 100094.[265]

Of all the optimized analogs and synthetic intermediates tested, **123** and **171** demonstrated potent, isoform-specific inhibition of SULT1A3 (Figure 2-33A). The affinity and specificity of **123** and **171** were evaluated in initial rate studies against four major SULT isoforms expressed in the brain and the liver – SULT1A1, SULT1E1, and SULT2A1 (Figure 2-33B). As is evident, both compounds bound tightly and exhibited a high degree of specificity. No detectable inhibition of the other SULT isoforms was detectable up to 10 μM following treatment with **123**. While **171** behaved similarly towards SULT1E1 and SULT2A1, this compound demonstrated weak inhibition of SULT1A1 (Ki 3.1 μM). Both compounds are partial inhibitors, and their percent

inhibition values at saturation (83% and 98% for **123** and **171**, respectively) agree well with the predicted values.

To confirm that the optimized inhibitors, **123** and **171**, were binding to the active site cap (as was the case of our initial lead inhibitor **106**), competitive binding studies of **123** and **171** against **106** was demonstrated in an initial rate study in which **106** was titrated against saturating concentrations of the competing, improved inhibitor (Figure 2-33C). The maximal percent inhibition achieved with saturating concentrations of **106** is 54%, a value substantially less than that of **123** or **171** (83 and 98%, respectively). If **106** is capable of competing with and displacing the optimized inhibitors, an alleviation of inhibition that plateaus at 54% should be observed as **106** is titrated into the reaction mixture. These experiments were performed by the Leyh lab. Gratifyingly, this is exactly what is observed, validating that the optimized inhibitors are binding to and inhibiting SULT1A3 via engagement with the active site cap.

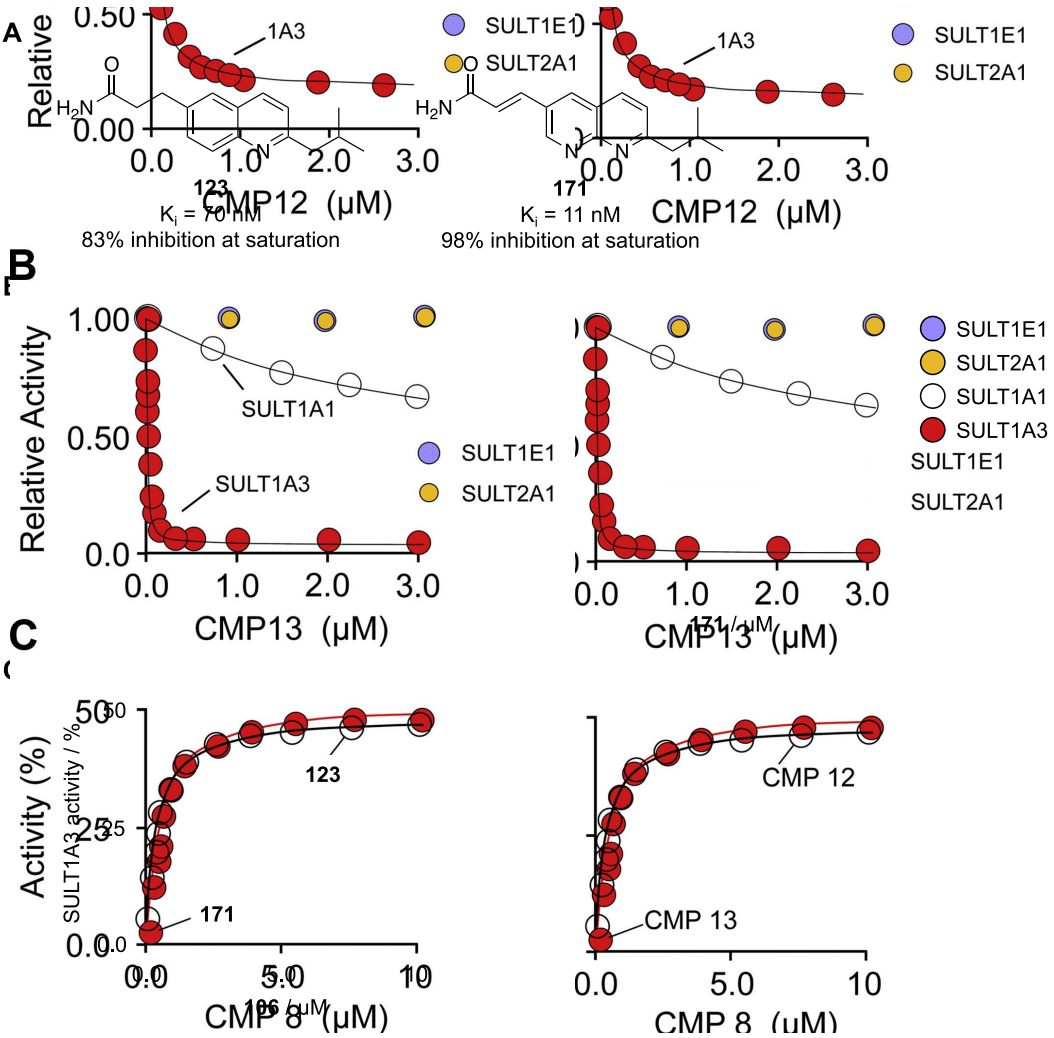

Figure 2-32: Biochemical evaluation of affinity, specificity, and binding site of 123 and 171
A) Structures and *in vitro* SULT1A3 inhibition parameters of optimal allosteric SULT1A3 inhibitors. B) Initial rate inhibition studies of **123** and **171** against SULT1A3 and other prominent SULT isoforms. Initial rates of SULT-catalyzed sulfonation of 1-HP are plotted as a function of inhibitor concentration. C) Competition experiments of **123** and **171** with **106** reveal that the optimized inhibitors inhibit SULT1A3 function at the active site cap. Experiemts presented in panels B and C were performed by the Leyh lab.

To assess the inhibition mechanism of **171**, we next sought to validate that PAP release from the cap-open forms of SULT1A3 is independent of **171**. The rate constants of PAPS binding and release from the cap-open form of SULT1A3 were determined in the presence and absence of saturating inhibitor **171** (Figure 2-34A). Binding was monitored via changes in intrinsic fluorescence associated with ligand binding. As a way to sterically "hold" the active site cap in an open form, we utilized 4-hydroxytamoxifen (Tam). Tam binds at the acceptor pocket and is too

large to bind the cap-closed enzyme; hence, at saturation, it "fastens" the cap open, and permits ligand-binding studies with ligands that would otherwise induce cap closure. In effect, Tam stalls the binding reaction at a point where the ligand has bound but the cap has not yet closed. It should be noted that the affinities of PAP for SULT1A3 (unliganded) and SULT1A3 bound to TAM (liganded) are virtually indistinguishable, suggesting these ligands only interact indirectly through their effects on the cap dynamics.[251, 266]

The binding of **171** to SULT1A3 alone, SULT1A3 bound to PAP (E·PAP, "cap closed"), or SULT1A3 bound to PAP and Tam (E·PAP·Tam, "cap open"), were measured via equilibrium and pre-steady state binding studies. PAP and Tam were used at saturating concentrations (100 and 200 x K_D, respectively). Consistent with cap-stabilizing interactions, **171** binds the cap closed enzyme (E·PAP, K_D = 11 nM) 12-fold more tightly than the cap open form (E·PAP·Tam, K_D = 130 nM). To determine whether **171** and PAP interact in the cap open form, the affinity of **171** for SULT1A3 alone and SULT1A3 "held open" with Tam (E·PAP·Tam) are virtually indistinguishable (130 and 133 nM, respectively), suggesting **171** does not communicate with either ligand in the cap-open complex (Figure 2-34A).

While it was confirmed that **171** does not communicate with PAP in the cap-open complex, we next sought to determine if **171** causes the PAP on- and off-rate constants to vary in fixed ratio, which will occur if **171** stabilizes the cap to the same extent in the presence or absence of nucleotide co-factor. PAP on- and off-rate constants for a series of open and closed complexes were determined using stopped-flow fluorescence (Figure 2-34B). These experiments were performed by the Leyh lab. The pre-steady state data revealed that PAP adds to both the cap open SULT1A3 and inhibitor-bound SULT1A3 with virtually identical on-rate constants, indicating that the cap is open in the inhibitor bound form. The effect of the inhibitor is observed only in the PAP

off-rate constant which decreases 14-fold in the presence of **171** (Figure 2-34C). Furthermore, in the presence of **171** and Tam, which holds SULT1A3 in a cap-open form, PAP release is identical to the rate observed in the absence of inhibitor. These findings support that **171** alone does not detectably close the cap and its binding does not influence the off-rate constant of PAP from the cap-open form.

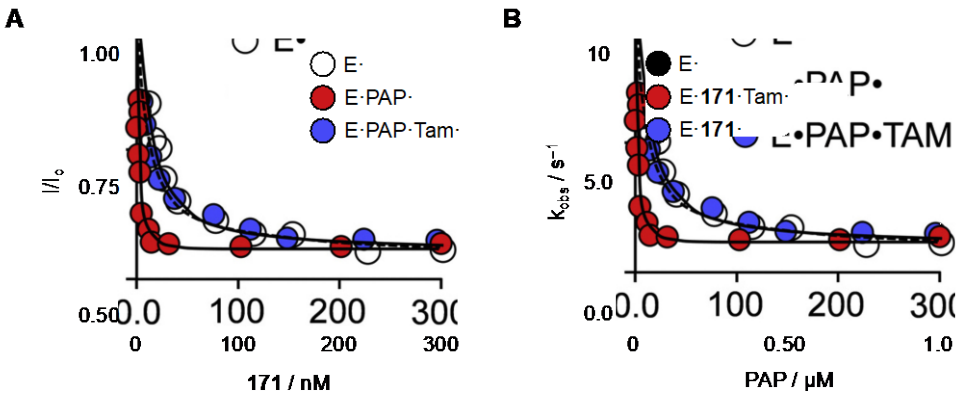

C

complex	k_{on} (μM^{-1} s^{-1})	k_{off} (s^{-1})	K_D (μM)[a]	K_D (μM)[b]
E·	6.9	2.5	0.36	0.32
E·171·	6.6	0.18	0.029	0.031
E·171·Tam·	6.5	2.3	0.35	0.35

Figure 2-33: Biochemical assessment of the mechanism of SULT1A3 inhibition by 171
A) Equilibrium binding studies of **171** to SULT1A3 alone (E·), SULT1A3 bound to PAP (cap closed, E·PAP·), or SULT1A3 bound to PAP and Tam (cap open, E·PAP·Tam·). Binding was monitored via ligand-induced changed in SULT1A3 intrinsic fluorescence (λ_{ex} = 290 nm, λ_{em} = 335 nm). B) Pre-steady state binding of **171** to enzyme in the presence of PAP. PAP binding was measured via stopped-flow fluorescence. C) Kinetic values for PAP binding to the various SULT1A3 complexes. [a]binding constant determined using the k_{on}/k_{off}, [b]binding constant determined by equilibrium binding. These experiments were performed by the Leyh lab.

Since PAP release is slowed in the presence of **171**, we hypothesize that **171** is disrupting the cap dynamics through stabilization of the closed conformation, analogous to that observed with initial lead inhibitor **106**. When docked in the active site cap of SULT1A3 (Figure 2-35), both compounds, **123** and **171**, exhibit similar binding modes to that of the first-generation inhibitor **106**, corroborating the proposed mechanism of inhibition. The pi-stacking interactions between

the aromatic cap residues (F222 and H226) and the core scaffold of each inhibitor confer the high SULT1A3 specificity observed for these inhibitors as these residues are not aromatic in other isoforms and would not allow for this essential interaction. Additionally, stronger H-bonding interactions between the C-6 carboxamide and Q225 help further stabilize the active site cap.

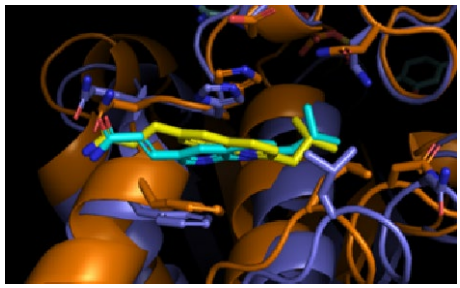

Figure 2-34: Mechanistic validation of SULT1A3 inhibition by 123 and 171
Structures of **123** (yellow, SULT1A3 is orange) and **171** (cyan, SULT1A3 is blue) bound to SULT1A3 active site cap. Structural docking studies and model generated by the Leyh lab (AECOM).

With promising inhibitory profiles in *in vitro* experiments, **123** and **171** were evaluated further in a cellular model. SULT enzymes are ubiquitously expressed at a basal level, and while the abundance of SULTs can vary by tissue, overlapping substrate specificity and compensatory mechanisms make it difficult to assay the activity (or non-activity) of a particular isoform. Therefore, *in cellulo* experiments must be carefully designed such that the response to the compound can be precisely credited back to the functional perturbation of the isoform of interest. To move forward with evaluating potency of optimized hit compounds **123** and **171** *in cellulo*, a stable human mammary epithelial (HME) cell line that overexpresses SULT1A3 was cultured by Ting Wang (Leyh lab). This cell line, which expresses SULT1E1 and does not express endogenous SULT1A3 to a level detectable by western blot, is typically sensitive to dopamine stimulation through activation of downstream signaling pathways.[267, 268] By stably expressing SULT1A3 and

stimulating with dopamine, this sensitivity is perturbed due to metabolism of dopamine by SULT1A3.

HME cells were transfected with plasmid containing the coding region of SULT1A3 or a negative control.[269] The transfectants were grown to near confluence (60-70%) and then harvested. SULT1A3 levels in the cell extract were assessed by measuring SULT1A3 turnover at saturating concentrations of substrate, per one microgram of HME cell extract. The SULT1A3 activity in the $HME^{SULT1A3+}$ transfectants ranged from 1 to 85 times the levels present in the negative control extracts. Furthermore, SULT1A3 levels in SH-SY5Y cells, a known human dopaminergic cell line,[270] and human platelets, where SULT1A3 levels are comparable to those in the central nervous system,[271] are roughly 40 times the levels in the HME negative control extracts. Consequently, a transfectant with extract activity 42 times that of the negative control isolate was selected for further experiments.

To establish conditions for cellular studies, the dopamine concentration and time dependence of dopamine metabolism in the $HME^{SULT1A3+}$ cells were assessed. Following SULT-mediated catalysis, dopamine is metabolized to dopamine-3O-sulfate and dopamine-4O-sulfate metabolites (Figure 2-36A). Cells were cultured to near confluence (60-70%) and treated with exogenous dopamine (100 μM). Following incubation, the media was analyzed by HPLC for the presence of dopamine metabolites such as, dopamine sulfate, 3-methoxytyramine, 3,4-dihydroxyphenylacetic acid, and homovanillic acid, which can be separated by HPLC and detected by measuring absorbance at 280 nm. These experiments were performed by Ian Cook in the Leyh lab. Only dopamine and dopamine sulfate were detected in the cell media, and together, they constituted more than 95% of the exogenous dopamine that was added to the media. Dopamine sulfate formation is linear with time up to 36 hours post-addition (Figure 2-36B). Furthermore, the

concentration of dopamine sulfate in the media at 24 hours post-treatment with exogenous dopamine linearly correlates with the concentration of exogenous dopamine added to the media (Figure 2-36C). The time and dose-dependent response indicates that dopamine uptake, conversion from dopamine-to-dopamine sulfate, and dopamine sulfate export are in a steady state indicating that the system is saturated with dopamine. Therefore, at 100 µM dopamine the system is expected to respond linearly (1:1) with SULT1A3 inhibition.

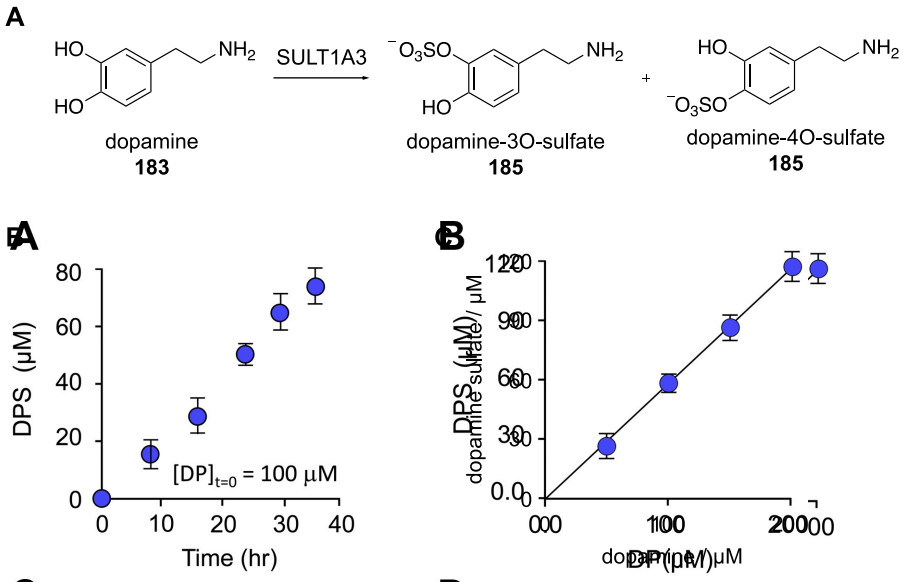

Figure 2-35: Validation of a HME$^{SULT1A3+}$ stable cell line
A) SULT1A3 catalyzed dopamine metabolism generates dopmaine sulfate metabolites **185** and **186**. B) HME$^{SULT1A3+}$ cells were treated with dopamine (100 µM) and the concentration of dopamine sulfate in the media was determined by HPLC analysis of the media at the indicated time point. C) HME$^{SULT1A3+}$ cells were treated with dopamine (0-200 µM). At 24 hours post-treatment, the concentration of dopamine sulfate in the media was determined by HPLC analysis. The amount of dopamine sulfate formed increases with increasing dopamine at initial treatment. These experiments were performed by the Leyh lab.

Having confirmed the activity of SULT1A3 in the stable HME cells and validating a protocol for quantifying dopamine sulfonation over time, the potency of the optimized inhibitors **123** and **171** was tested in cells. Cells were treated with dopamine (100 µM) and either **123** or **171** at varying concentrations (up to 3 µM and 200 nM, respectively). The relative abundance of

dopamine and dopamine sulfate was isolated by HPLC and quantified by OD280 measurements (Figure 2-37A). Upon treatment with inhibitors, **123** demonstrated an inhibitory concentration (IC_{50}) of 260 nM and 84% inhibition at saturation. Gratifyingly, **171** was an extremely effective inhibitor of SULT1A3 exhibiting nearly complete (95%) loss of dopamine sulfate formation with an IC_{50} of 12 nM (Figure 2-37B). These results are consistent with the initial rate studies. The nearly coincident percent inhibition at saturating inhibitor values suggests that the rate of SULT1A3-mediated dopamine metabolism is what limits dopamine sulfate accumulation in the media, and that export of the sulfated metabolite is fast relative to its formation, as has been reported previously.[269, 272, 273] Together, the data presented here validate these compounds as potent, highly selective inhibitors of SULT1A3, and suggest that the flux through the major neurotransmitter sulfonation pathway can be controlled in cell-based studies and perhaps also in an animal model.

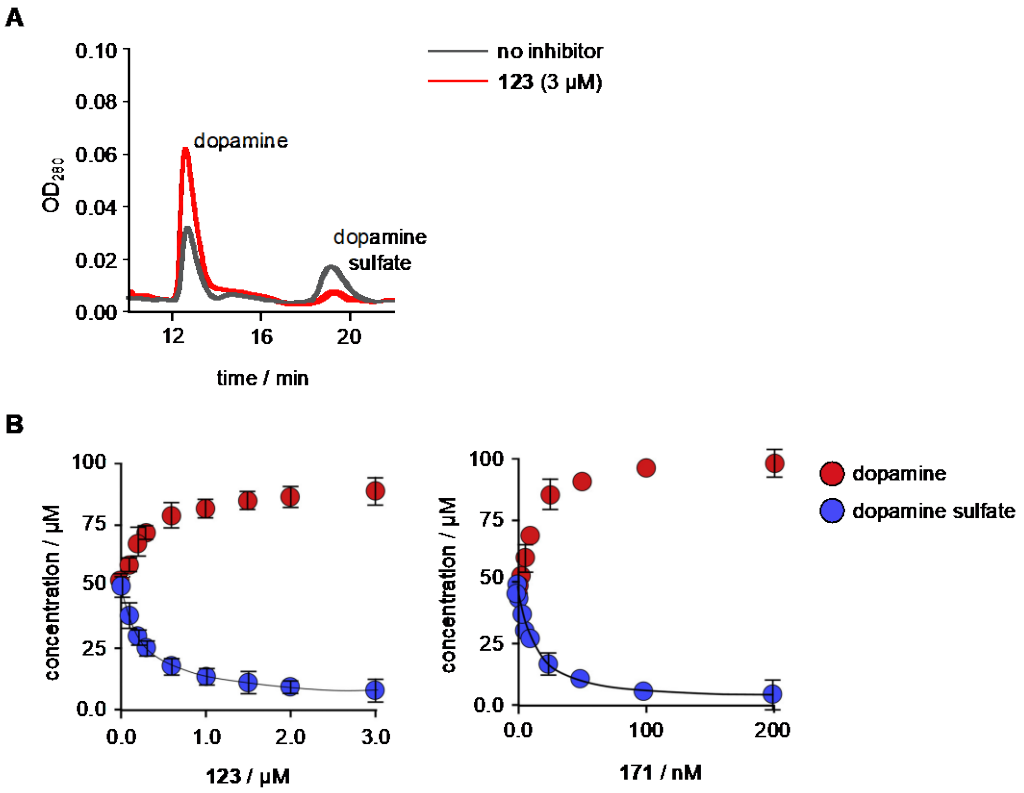

Figure 2-36: Inhibition of endogenous SULT1A3-mediated dopamine metabolism with 123 and 171
A) Sample HPLC chromatogram of the relative abundance of dopamine and dopamine sulfate after 24 hr treatment with exogenous dopamine in the absence (gray) or presence of **123** (red). B) Quantification of dopamine (blue) and dopamine sulfate (red) levels in HME cells upon treatment with **123** (left) or **171** (right). Data was generated by the Leyh lab.

2.7 Summary and Outlook

Through this work, we have successfully designed and synthesized the first small molecule allosteric inhibitors of the sulfotransferase enzyme family. In a collaborative effort with the Leyh lab (Albert Einstein College of Medicine) we have discovered an inhibitor of high affinity and high potency that can regulate SULT1A3 activity in an isoform selective manner. This inhibitor binds to a newly discovered allosteric site on SULT1A3. Compound **106** inhibits SULT1A3 activity at the 30-residue active site cap, disrupting cap dynamics by stabilizing the cap-closed

conformation. This stabilization restricts acceptor substrates from reaching the catalytic residues in the active site for sulfonation and slows nucleotide release from the enzyme. The inhibitor, while highly selective (> 203-fold), partially reduces enzyme turnover to 46% that of the uninhibited enzyme. Using **106** as a framework, we have optimized the inhibitor through computational docking and SAR studies to generate several compounds that bind SULT1A3 tighter and further stabilize the active site cap to reduce SULT1A3 turnover. Compounds **123** and **171** demonstrate more than 90% inhibition of SULT1A3 activity at low nanomolar treatment. These results were validated when compounds were tested in an engineered HME cell line that stably expresses SULT1A3. Following treatment with inhibitors, we observed inhibition of SULT-mediated dopamine metabolism at effective concentrations of 260 nM (**123**) and 12 nM (**171**).

In the next steps, we plan to evaluate the best inhibitors and expand our testing to animal models. SULT1A3 is only expressed in humans and higher primates.[206] SULT1D1 is the isoform expressed in dogs and rodents that is functionally comparable to SULT1A3 as it also sulfonates neurotransmitters. Three of the best inhibitors that were discovered through this work (**123**, **171**, and **172**) were tested for inhibition against both SULT1A3 and SULT1D1 from different species in order to determine the most suitable model for animal studies (Table 2-2). Based on this data, the mouse is the most suitable animal model for future studies as each of our inhibitors demonstrated inhibition of SULT1D1 comparable to that observed of the human SULT1A3. Mice have been previously been engineered such that their SULT1A1/2 enzymes have been knocked out and replaced with human SULT isoforms,[274] suggesting a stable mouse line could also be generated for compound testing.

Table 2-2: Inhibition of SULT1A3 homologues in different species
Data generated by the Leyh lab (AECOM).

	species (SULT isoform)											
compound	human (1A3)		green monkey (1A3)		rhesus macaque (1A3)		dog (1D1)		mouse (1D1)		rat (1D1)	
	K_i (nM)	% inh	K_i (nM)	% inh	K_i (nM)	% inh	K_i (nM)	% inh	K_i (nM)	% inh	K_i (nM)	% inh
123	50	83	170	71	38	97	77	83	79	82	2500	33
171	9.6	97	72	91	12	97	117	81	65	92	270	37
172	17	90	87	72	25	95	52	73	32	91	1100	21

Having determined the mouse as a suitable model, we plan to perform pharmacokinetic and pharmacodynamic studies with our compounds and evaluate those that perform best in pre-clinical mouse models of major depression. Major depression is a common mental health disorder linked to reduced availability of the "feel good" neurotransmitters, dopamine and serotonin.[275] Current therapeutics for major depressive disorder include monoamine oxidase inhibitors (MAOIs) and selective serotonin reuptake inhibitors (SSRIs), which increase the synaptic levels of serotonin.[219] These medications are widely-prescribed, however it is evident that some limitations exist including intolerance, delayed therapeutic onset, and limited effectiveness[276] potentially because only one enzyme class is targeted by each of these drugs.[277, 278] While SULT1A3 is a known metabolic enzyme against serotonin and dopamine, it is not currently a drug target for major depressive disorder. We hypothesize that inhibitors of SULT1A3, whether administered alone or as a co-treatment with current drugs, will increase the bioavailability of these neurotransmitters, hopefully resulting in an enhanced patient response.

Since SULT1A3 is only present in primates, we then plan to extend our clinical evaluation into non-human primates, with the eventual hope of translating our compounds to the bedside for use as a novel therapeutic. The design strategy and workflow implicated here were successfully used in generating the first synthetic, (wo)man-made, isoform-specific inhibitors of the human

cytosolic sulfotransferase family. The work conducted here lays the groundwork for future studies of SULT isoforms and the biological implications of the enzymes, opening the door of discovery to a completely untouched layer of sulfotransferase biology.

2.8 Materials and Methods

General chemical methods. All reactions were performed in flame dried glassware and stirred magnetically. All starting materials were purchased directly from commercial sources and used without further purification. All reactions were monitored by thin layer chromatography (TLC) unless otherwise indicated. ^{1}H and ^{13}C NMR were performed on a Bruker Ultrashield 300MHz, 400MHz, or 500MHz instrument. High resolution mass spectrometry was performed by the University of Pittsburgh facilities.

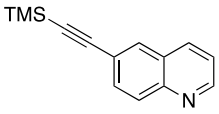

6-((Trimethylsilyl)ethynyl)quinoline (90). This compound was synthesized according to a previously reported protocol. The analytical data matched literature reports.[279]

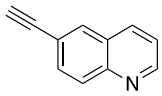

6-Ethynylquinoline (91). 6-Iodoquinoline (100 mg, 0.392 mmol) was dissolved in THF (1 mL) at room temperature while stirring. Bis(triphenylphosphine)palladium(II) dichloride (14 mg, 0.020 mmol) and copper(I) iodide (4 mg, 0.020 mmol), and triethylamine (82 μL, 0.588 mmol) were added sequentially while stirring at room temperature. Trimethylsilylacetylene (82 μL, 0.588

mmol) was added dropwise under nitrogen atmosphere. The reaction stirred at room temperature for 3 hours and turned black. The reaction mixture was concentrated *in vacuo* and dried under high vacuum for several hours. The black residue was carried through crude to the next step. The crude reaction mixture was resuspended in methanol (1 mL) at room temperature. Potassium carbonate (26 mg, 0.185 mmol) was added, and the reaction was stirred at room temperature for 2 hours. After 2 hours, the reaction was diluted in water (5 mL) and dichloromethane (10 mL). The aqueous layer was extracted with dichloromethane (2 x 10 mL). The organic layers were combined, washed with brine (25 mL), dried over Na_2SO_4, filtered over cotton, and concentrated *in vacuo*. The residue was purified by flash chromatography on SiO_2 in 20% ethyl acetate in hexanes to yield a light brown solid (35.7 mg, 60% over two steps). ^{1}H NMR (400 MHz, $CDCl_3$) δ 8.93 (dd, J = 1.6 Hz, 4 Hz, 1H), 8.15 (d, J = 8 Hz, 1H), 8.08 (d, J = 8.8 Hz, 1H), 8.01 (d, J = 1.2 Hz, 1H), 7.77 (dd, J = 2 Hz, 8.8 Hz, 1H), 7.45 (dd, J = 4 Hz, 8 Hz, 1H), 3.2 (s, 1H). ^{13}C NMR (400 MHz, $CDCl_3$) δ 150.7, 147.3, 136.6, 132.8, 132.1, 129.3, 128.1, 121.9, 120.9, 83.1, 78.8. HRMS calcd for $[M+H]^+$ 154.06, observed 154.06509.

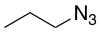

1-Azidopropane (92). Sodium azide (860 mg, 13.2 mmol) was dissolved in water (1 mL) at room temperature. Dimethyl sulfoxide (3 mL) was added to the stirring solution. 1-Bromopropane (1 mL, 11 mmol) was added dropwise to the stirring solution, which was then heated to 50 ºC. The reaction was stirred at 50 ºC for 2 hours before two layers formed, after which the reaction could be followed by 1H NMR. A small aliquot of the top layer (5 drops, ~ 50 µL) from the crude reaction mixture was carefully removed with a syringe and needle. The aliquot was mixed with deuterated chloroform and analyzed on the 400 MHz 1H NMR. This layer contained a mixture of 1-bromopropane and 1-azidopropane. Once 50-60% conversion to product was

observed by 1H-NMR, the rest of the clear, top layer was decanted by pipetting and used without further purification in the subsequent click reaction. ^{1}H NMR (400 MHz, $CDCl_3$) δ 3.06 (t, J = 6.8 Hz, 2H), 1.45 (m, J = 7.2 Hz, 2H), 0.79 (t, J = 7.6 Hz, 3H). While the ^{1}H NMR indicates product formation, compound characterization is incomplete due to missing ^{13}C NMR and HRMS data.

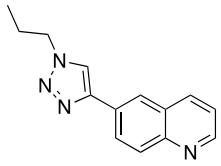

6-(1-Propyl-1*H*-1,2,3-triazol-4-yl)quinoline (84). 6-ethynylquinoline (**91**) (20 mg, 0.131 mmol), copper sulfate pentahydrate (3.27 mg, 0.013 mmol), and sodium ascorbate (5.2 mg, 0.026 mmol) were dissolved in THF (440 µL) and water (440 µL) at room temperature. Crude 1-azidopropane **92** (50 µL, excess) was added dropwise to the reaction mixture at room temperature while stirring. After stirring for 1 hour, the reaction mixture was diluted in ethyl acetate (10 mL) and water (10 mL). The aqueous layer was extracted with ethyl acetate (3x, 10 mL). The organic layers were combined, washed with brine (20 mL), dried over Na_2SO_4, filtered over cotton, and concentrated under reduced pressure. The crude material was purified by flash chromatography on SiO_2 with 2% methanol in dichloromethane to yield **84** as a white solid (28.9 mg, 77%). ^{1}H NMR (400 MHz, $CDCl_3$) δ 8.91 (s, 1H), 8.38 (d, J = 1.2 Hz, 1H), 8.20 (dd, J = 8.4 Hz, 1.2 Hz, 1H), 8.15 (d, J = 8.8 Hz, 1H), 8.11 (dd, J = 8.8 Hz, 1.6 Hz, 1H), 7.89 (s, 1H), 7.42 (dd, J = 8.4 Hz, 4.4 Hz, 1H), 4.41 (t, J = 7.2 Hz, 2H), 2.02 (m, 2H), 1.02 (t, J = 7.2 Hz, 3H). ^{13}C NMR (400 MHz, $CDCl_3$) δ 150.5, 148.0, 147.1, 136.4, 130.0, 128.9, 128.6, 127.5, 124.1, 121.7, 120.0, 52.2, 23.8, 11.1. HRMS calcd for $[M+H]^+$ 239.1298, observed 239.1281.

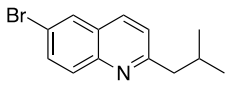

6-Bromo-2-isobutylquinoline (95). 2-Amino-5-bromobenzaldehyde (**93**) (110 mg, 0.500 mmol) was dissolved in ethanol (800 µL) at room temperature. Pyrrolidine (45 µL, 0.550 mmol) and then concentrated sulfuric acid (8 µL, 0.150 mmol) were added to the reaction mixture while stirring. 4-Methyl-2-pentanone (**94**) (69 µL, 0.550 mmol) was added dropwise. After overnight stirring, the reaction was concentrated *in vacuo*. The yellow-brown residue was diluted with ethyl acetate and purified by flash chromatography on silica gel using a gradient of 12% ethyl acetate in hexanes to afford **95** as a yellow solid (117 mg, 76%). ^{1}H NMR (400 MHz, $CDCl_3$) δ 7.96 (d, J = 8.8 Hz, 1H), 7.93 (d, J = 2.4 Hz, 1H), 7.91 (d, J = 8.8 Hz, 1H), 7.74 (dd, J = 8.8 Hz, 2 Hz, 1H), 7.28 (d, J = 8.4 Hz, 1H), 2.83 (d, J = 7.2 Hz, 2H), 2.20 (m, 1H), 0.97 (d, J = 6.8 Hz, 6H). ^{13}C NMR (500 MHz, $CDCl_3$) δ 162.9, 146.7, 135.0, 132.8, 130.9, 129.6, 128.0, 123.0, 119.5, 48.4, 29.5, 22.7. HRMS calcd for $[M+H]^+$ 264.039, observed 264.0398.

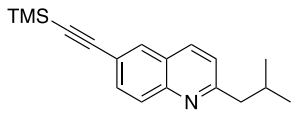

2-Isobutyl-6-((trimethylsilyl)ethynyl)quinoline (96). 6-Bromo-2-isobutyl quinoline (93.8 mg, 0.355 mmol) was diluted in tetrahydrofuran (350 µL). To the solution was added bis(triphenylphosphine)palladium(II) dichloride (12.5 mg, 17.8 µmol) and triphenylphosphine (9.5 mg, 35.5 µmol). Triethylamine (500 µL) was added the reaction mixture dropwise while stirring. The reaction vial was purged with nitrogen gas for 15 minutes, then additional tetrahydrofuran (100 µL) was added (to account for volume lost during venting). Copper(I) iodide (7 mg, 35.5 µmol) was added to the reaction. After a few minutes stirring at room temperature, the reaction mixture underwent a noticeable yellow to orange color change. Trimethylsilylacetylene (100 µL, 0.710 mmol) was then added to the reaction mixture dropwise at room temperature. The reaction mixture turned black after 5 minutes stirring at room temperature. Following addition of

all reagents, the reaction was heated to 50 ºC and stirred overnight. After complete disappearance of starting material was observed by TLC, the reaction mixture was vacuum filtered over a pad of celite. The celite was washed three times with ethyl acetate (15 mL per wash). The crude product was concentrated under reduced pressure and purified on a silica gel column with 1% ethyl acetate in hexanes. The product **96** (96.1 mg) was isolated in 96% yield. ^{1}H NMR (400 MHz, $CDCl_3$) δ 7.93 (d, J = 8.4 Hz, 1H), 7.90 (d, J = 2 Hz, 1H), 7.88 (d, J = 9.2 Hz, 1H), 7.70 (dd, J = 2 Hz, 8.4 Hz, 1H), 7.25 (d, J = 8.4 Hz, 1H), 2.79 (d, J = 7.6 Hz, 2H), 2.17 (m, J = 6.8 Hz, 1H), 0.94 (d, J = 6.4 Hz, 6H). While the ^{1}H NMR indicates product formation, compound characterization is incomplete due to missing ^{13}C NMR and HRMS data.

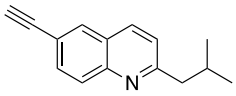

6-Ethylnyl-2-isobutylquinoline (97). 2-Isobutyl-6-((trimethylsilyl)ethynyl)quinoline (**96**, 96.1 mg, 0.341 mmol) was diluted in methanol (1.7 mL). The solution was left to stir at room temperature for 20 minutes, as **96** was not immediately solubilized. Potassium carbonate (23.6 mg, 0.171 mmol) was added at room temperature and the reaction immediately turned bright yellow in color. The reaction was left to stir at room temperature for 3 hours. The crude reaction mixture was concentrated under reduced pressure and dried under vacuum for 4 hours. The crude residue was purified on a silica gel column with 2% ethyl acetate in hexanes yielding 67.9 mg of pure **97** (95%). ^{1}H NMR (400 MHz, $CDCl_3$) δ 8.00 (d, J = 8.8 Hz, 1H), 7.98 (d, J = 8.8 Hz, 1H), 7.95 (d, J = 2 Hz, 1H), 7.72 (dd, J = 2 Hz, 8.8 Hz, 1H), 7.28 (d, J = 8.4 Hz, 1H), 3.160 (s, 1H), 2.84 (d, J = 7.6 Hz, 2H), 2.21 (m, J = 6.8 Hz, 1H), 0.97 (d, J = 6.4 Hz, 6H). ^{13}C NMR (500 MHz, $CDCl_3$) δ 163.5, 147.7, 135.7, 132.3, 131.9, 129.2, 126.4, 122.9, 119.5, 83.6, 48.5, 29.6, 22.6. HRMS calcd for $[M+H]^+$ 209.12, observed 210.12650.

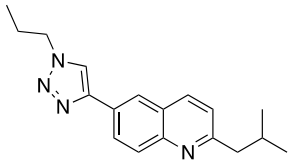

2-Isobutyl-6-(1-propyl-1*H*-1, 2, 3-triazol-4-yl)quinoline (87). 6-ethynyl-2-isobutylquinoline (**97**, 32.7 mg, 0.156 mmol), copper sulfate pentahydrate (4 mg, 0.015 mmol), and sodium ascorbate (6.2 mg, 0.03 mmol) were dissolved in tetrahydrofuran (520 µL) and water (520 µL) at room temperature. Crude 1-azidopropane (**92**) (76% conversion from 1-bromopropane according to 1H-NMR, 100 µL, excess) was added dropwise to the reaction mixture at room temperature while stirring. After stirring for 1 hour, the reaction mixture was diluted in ethyl acetate (10 mL) and water (10 mL). The aqueous layer was extracted with ethyl acetate (3 x 10 mL). The organic layers were combined, washed with brine (20 mL), dried over Na_2SO_4, filtered over cotton, and concentrated under reduced pressure. The crude material was purified by flash chromatography on SiO_2 with 2% methanol in dichloromethane to yield **87** in 54% yield. ^{1}H NMR (400 MHz, $CDCl_3$) δ 8.34 (d, J = 1.6 Hz, 1H), 8.09 (dd, J = 2 Hz, 8.4 Hz, 2H), 8.06 (dd, J = 1.6 Hz, 8.8 Hz, 1H), 7.86 (s, 1H), 4.40 (t, J = 6.8 Hz, 2H), 2.84 (d, J = 7.2 Hz, 2H), 2.22 (m, 1H), 2.01 (m, 2H), 1.00 (m, 9H). ^{13}C NMR (500 MHz, $CDCl_3$) δ 162.6, 147.9, 147.4, 136.3, 129.6, 128.1, 127.4, 127.1, 124.00, 122.7, 119.9, 52.3, 48.5, 29.6, 23.9, 22.7, 11.3. HRMS calcd for $[M+H]^+$ 295.1924, observed 295.1913.

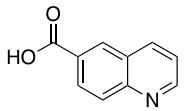

Quinoline-6-carboxylic acid (101). Methyl quinoline 6-carboxylate (50 mg, 0.267 mmol) was diluted in methanol (1 mL). Aqueous lithium hydroxide (1M, 500 µL) was added to the solution dropwise at room temperature. The reaction was left to stir overnight. The next morning, the reaction was adjusted to pH 3-4 with 5M hydrochloric acid the product precipitated out of

solution. The white solid was collected by vacuum filtration (19.3 mg, 42%) and used without further purification. Analytical data matched previous literature reports.[280]

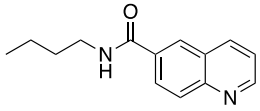

***N*-butylquinoline-6-carboxamide (98).** Quinoline-6-carboxylic acid (16.8 mg, 0.097 mmol) was diluted in dimethylformamide (300 µL) at room temperature. The starting material was not fully solubilized until the addition of diisopropylethylamine (DIPEA, 50 µL, 0.291 mmol). The reaction mixture was cooled to 0 ºC and then (1-[bis(dimethylamino)methylene]-1H-1,2,3-triazolo[4.5-b]pyridinium-3-oxide hexafluorophosphate (HATU, 55.3 mg, 0.145 mmol) was added. Butylamine (12 µL, 0.116 mmol) was added to the reaction dropwise, while stirring at 0 ºC. The reaction was gradually warmed to room temperature overnight. The next morning, the reaction mixture was diluted in ethyl acetate (10 mL) and water (10 mL). The aqueous layer was extracted with ethyl acetate (3 x 10 mL). The organic layers were combined, washed with brine (20 mL), dried over Na_2SO_4, filtered over cotton, and concentrated under reduced pressure. The crude material was purified on a silica gel column with a gradient of 1 to 2% methanol in dichloromethane to yield **98** in 75% yield (16.7 mg). ^{1}H NMR (400 MHz, $CDCl_3$) δ 8.98 (dd, J = 4.4 Hz, 1.6 Hz, 1H), 8.29 (d, J = 2.0 Hz, 1H), 8.24 (d, J = 8.0 Hz, 0.8 Hz, 1H), 8.14 (d, J = 8.8 Hz, 1H), 8.03 (dd, J = 8.8 Hz, 2.0 Hz, 1H), 7.47 (dd, J = 8.0 Hz, 4.0 Hz, 1), 6.31 (br s, 1H), 3.52 (q, J = 7.2 Hz, 2H), 1.65 (m, 2H), 1.45 (m, 2H), 0.98 (t, J = 7.2 Hz, 3H). ^{13}C NMR (500 MHz, $CDCl_3$) δ 167.0, 152.0, 149.4, 137.0, 132.9, 130.0, 127.7, 127.6, 127.2, 122.0, 40.2, 31.9, 20.3, 13.9. HRMS calcd for $[M+H]^+$ 229.1343, observed 229.1340.

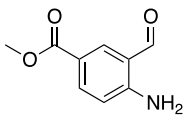

Methyl 4-amino-3-formylbenzoate (103). Methyl 3-formyl-4-nitrobenzoate (200 mg, 0.956 mmol) was dissolved in methanol (8 mL) at room temperature. Palladium on carbon (20 mg, 10% w/w) was added to the reaction mixture while stirring. Hydrogen was bubbled through the reaction, while stirring at room temperature for 2 hours. The reaction mixture was diluted in methanol (8 mL) and vacuum filtered over celite. The filtrate was concentrated *in vacuo*, dried, and purified by flash chromatography on SiO_2 in 20% ethyl acetate in hexanes to yield a light yellow solid (140 mg, 82%). ^{1}H NMR (400 MHz, $CDCl_3$) δ 9.90 (s, 1H), 8.25 (d, J = 2 Hz, 1H), 7.95 (dd, J = 2, 8.8 Hz, 1H), 6.65 (d, J = 8.8 Hz, 1H), 3.89 (s, 3H). ^{13}C NMR (400 MHz, $CDCl_3$) δ 193.8, 166.3, 153.11, 138.8, 136.0, 118.4, 118.0, 115.9, 52.0. HRMS calcd for $[M+H]^+$ 180.06, observed 180.06537.

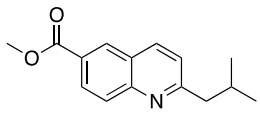

Methyl 2-isobutylquinoline-6-carboxylate (104). The synthetic protocol for this compound was adapted from a previously reported protocol.[256] Methyl 4-amino-3-formylbenzoate (25 mg, 0.140 mmol) was diluted in ethanol (300 µL) at room temperature. Pyrrolidine (13 µL, 0.154 mmol) and then concentrated sulfuric acid (2 µL, 0.007 mmol) were added to the reaction mixture while stirring. 4-Methyl-2-pentanone (20 µL, 0.154 mmol) was added dropwise. After overnight stirring, the reaction was concentrated and dried. The resulting dark orange oil was diluted with DCM and purified by flash chromatography on SiO_2 in 20% ethyl acetate in hexanes to yield a yellow oil (26.5 mg, 78%). ^{1}H NMR (400 MHz, $CDCl_3$) δ 8.54 (d, J = 1.6 Hz, 1H), 8.26 (dd, J = 7.2 Hz, 1.6 Hz, 1H), 8.14 (d, J = 6.4 Hz, 1H), 8.06 (d, J = 6.8, 1H), 7.32 (d, J = 6.8 Hz, 1H), 3.98 (s, 3H), 2.86 (d, J = 6 Hz, 2H), 2.23 (m, 1H), 0.98 (d, J = 5.6 Hz, 6H). ^{13}C NMR (500

MHz, $CDCl_3$) δ 167.0, 165.0, 150.0, 137.2, 130.8, 129.3, 129.0, 127.3, 126.0, 123.0, 52.5, 48.6, 29.5, 22.7. HRMS calcd for $[M+H]^+$ 244.13, observed 244.13409.

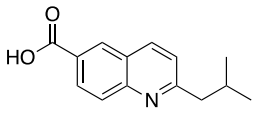

2-Isobutylquinoline-6-carboxylic acid (105). Methyl 2-isobutylquinoline-6-carboxylate (23.1 mg, 0.095 mmol) was diluted in methanol (1 mL) at room temperature. A 1M solution of lithium hydroxide (300 µL, 0.3 mmol) was added to the solution stirring at room temperature. After stirring for 2 hours, the reaction was acidified to pH 4 with 5 M hydrochloric acid upon which a white precipitate formed. The reaction mixture was diluted in ethyl acetate (5 mL). The aqueous layer was extracted with EtOAc (3 x 5 mL). The organic extracts were combined, washed with brine (15 mL), dried over Na_2SO_4, filtered over cotton, and concentrated *in vacuo*. The crude white solid was carried forward without further purification. ^{1}H NMR (400 MHz, $CDCl_3$) δ 13.14 (br s, 1H), 8.61 (d, J = 1.6 Hz, 1H), 8.44 (d, J = 8.4 Hz, 1H), 8.16 (dd, J = 2 Hz, 8.8 Hz, 1H), 7.99 (d, J = 8.8 Hz, 1H), 7.49 (d, J = 8.4 Hz, 1H), 2.81 (d, J = 7.2 Hz, 2H), 2.19 (m, 1H), 0.91 (d, J = 6.8 Hz, 6H). ^{13}C NMR (400 MHz, $CDCl_3$) δ 167.1, 164.2, 149.1, 137.4, 130.6, 128.8, 128.7, 127.8, 125.7, 122.9, 47.4, 28.5, 22.4. HRMS calcd for $[M+H]^+$ 230.11, observed 230.11784.

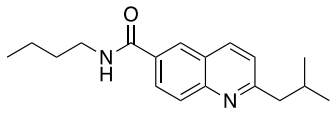

***N*-butyl-2-isobutylquinoline-6-carboxylate (99).** The crude carboxylic acid **105** (0.095 mmol) was dissolved in DMF (500 µL) and cooled to 0 ºC. Diisopropylethylamine (75 µL, 0.431 mmol), and butylamine (17 µL, 0.172 mmol) were added sequentially while stirring at 0 ºC. HATU (81 mg, 0.215 mmol) was added, and the reaction was stirred at 0 ºC for 10 minutes, before warming to RT. After overnight stirring the reaction was diluted with ethyl acetate and worked

up with water. The aqueous layer was extracted with ethyl acetate (3 x 10 mL). The organic layers were combined, washed with brine (20 mL), dried over Na_2SO_4, filtered over cotton, and concentrate *in vacuo*. The crude mixture was resuspended in dichloromethane (~ 500 µL) and purified by flash chromatography on SiO_2 with 40% ethyl acetate in hexanes to yield **99** as a light brown solid (17.2 mg, 42% over two steps). ^{1}H NMR (400 MHz, $CDCl_3$) δ 8.26 (d, J = 2 Hz, 1H), 8.12 (d, J = 8.4 Hz, 1H), 8.07 (d, J = 8.8 Hz, 1H), 7.99 (dd, J = 8.8 Hz, 2 Hz, 1H), 7.32 (d, J = 8.4 Hz, 1H), 6.28 (br s, 1H), 3.51 (m, 2H), 2.86 (d, J = 7.2 Hz, 2H), 2.23 (m, 1H), 1.65 (m, 2H), 1.45 (m, 2H), 0.98 (m, 9H). ^{13}C NMR (400 MHz, $CDCl_3$) δ 166.9, 164.2, 131.8, 129.3, 127.3, 126.8, 126.1, 122.9, 48.4, 40.0, 31.8, 29.4, 22.6, 20.2, 13.8. HRMS calcd for $[M+H]^+$ 285.1889, observed 285.1977.

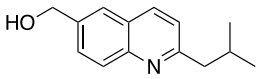

(2-Isobutylquinolin-6-yl)methanol (106). Methyl 2-isobutylquinoline-6-carboxylate (22.8 mg, 0.094 mmol) was diluted in tetrhydrofuran (500 µL) and cooled to –80 ºC in an acetone/dry ice bath. Diisobutylaluminum hydride (DIBAL-H) was added dropwise at –80 ºC and stirring under nitrogen atmosphere. The reaction was stirred for 20 minutes at –80 ºC and then warmed to 0 ºC and stirred for 4 hours. The reaction was quenched and worked up following a previously reported literature procedure.[259] The residue was purified by flash chromatography on SiO_2 in 2% methanol in dichloromethane to yield **106** as an off-white solid (16.2 mg, 80%). ^{1}H NMR (400 MHz, $CDCl_3$) δ 8.03 (dd, J = 8.4 Hz, 0.8 Hz, 2H), 7.76 (s, 1H), 7.66 (dd, J = 8.8 Hz, 1.6 Hz, 1H), 7.28 (d, J = 1.6 Hz, 1H), 4.89 (s, 2H), 2.85 (d, 7.6 Hz, 2H), 2.21 (m, 1H), 0.98 (d, J = 6.4 Hz, 3H). ^{13}C NMR (500 MHz, $CDCl_3$) δ 162.2, 147.4, 138.7, 136.2, 128.9, 128.7, 126.7, 124.9, 122.3, 64.8, 48.2, 29.6, 22.6. HRMS calcd for $[M+H]^+$ 216.139, observed 216.1392.

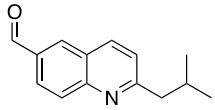

2-Isobutylquinoline-6-carbaldehyde (107). This compound was synthesized following a modified version of a literature reported protocol.[281] (2-Isobutylquinolin-6-yl)methanol (**106**, 97.8 mg, 0.454 mmol) was diluted in water-saturated dichloromethane (1.5 mL) and was stirred at room temperature for 15 minutes. Dess-Martin periodinane (450 mg, 0.95 mmol) was added portion-wise over 15 minutes (3 x 150 mg). After final addition, diethyl ether (1.5 mL) and a solution of sodium thiosulfate (1.3 g, 5 mmol) in an 80% saturated sodium bicarbonate buffer (1.5 mL) was added to the reaction mixture. The reaction was stirred at room temperature for 45 minutes. The reaction was worked up according to the literature protocol. The crude residue was purified on a silica gel column eluting with 10% ethyl acetate in hexanes to provide 78.9 mg **107** (81% yield). ^{1}H NMR (400 MHz, $CDCl_3$) δ 10.16 (s, 1H), 8.30 (d, J = 1.2 Hz, 1H), 8.20 (d, J = 8.4 Hz, 1H), 8.16 (dd, J = 8.8 Hz, 1.6 Hz, 1H), 8.12 (d, J = 8.8 Hz, 1H), 7.37 (d, J = 8.4 Hz, 1H), 2.88 (d, J = 7.2 Hz, 2H), 2.24 (m, 1H), 0.98 (d, J = 6.4 Hz, 6H). ^{13}C NMR (500 MHz, $CDCl_3$) δ 191.6, 165.7, 150.8, 137.3, 133.8, 133.4, 130.3, 126.8, 126.2, 123.3, 48.6, 29.5, 22.6. HRMS calcd for $[M+H]^+$ 214.1234, observed 214.1226.

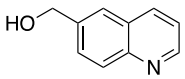

Quinolin-6-ylmethanol (108). Methyl quinoline 6-carboxylate (25 mg, 0.134 mmol) was dissolved in anhydrous tetrahydrofuran (670 µL) and cooled on ice to 0 ºC. Lithium aluminum hydride (LAH, 6.1 mg, 0.161 mmol) was added slowly. The reaction stirred at 0 ºC until complete disappearance of starting material was observed on a TLC (run in 2% methanol in dichloromethane). The reaction was quenched with 10% tetrahydrofuran in water (670 µL) and stirred at 0 ºC for 10 minutes. The reaction was diluted with water and extracted with ethyl acetate.

The aqueous layer was extracted with ethyl acetate (3 x 10 mL). The organic layers were combined, washed with brine (20 mL), dried over Na_2SO_4, filtered over cotton, and concentrated under reduced pressure. The crude mixture was resuspended in dichloromethane (~500 µL) and purified by flash chromatography on SiO_2 with 4% methanol in dichloromethane to yield 20.4 mg of **108** (85% yield). ^{1}H NMR (400 MHz, $CDCl_3$) δ 8.88 (dd, J = 4 Hz, 1.6 Hz, 1H), 8.14 (dd, J = 8.4 Hz, 0.8 Hz, 1H), 8.08 (d, J = 8.8 Hz, 1H), 7.81 (s, 1H), 7.70 (dd, J = 8.8 Hz, 2 Hz, 1H), 7.40 (dd, J = 8.4 Hz, 4.4 Hz, 1H), 4.91 (s, 2H), 2.39 (br s, 1H). ^{13}C NMR (500 MHz, CDCl3) δ 150.3, 147.8, 139.7, 136.2, 129.6, 128.9, 128.2, 121.4, 64.8. HRMS calcd for $[M+H]^+$ 160.0764, observed 160.0732.

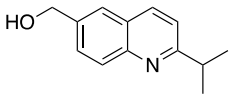

(2-Isopropylquinolin-6-yl)methanol (109). Methyl 2-isopropylquinoline-6-carboxylate (11.1 mg, 0.048 mmol) was diluted in tetrahydrofuran (400 µL) at room temperature under N_2 and then cooled to -80 ºC in a dry ice/isopropanol bath. Lithium aluminum hydride (5.5 mg, 0.145 mmol) was added at – 80 ºC. The reaction was stirred at – 80 ºC for 10 minutes and was then slowly warmed to 0 ºC. After 2 hours stirring at 0 ºC, the reaction was quenched with 10% THF in water (5 mL) at 0 ºC. The reaction stirred at 0 ºC for 10 minutes, and then was diluted with ethyl acetate. The aqueous layer was extracted with ethyl acetate (3 x 5 mL). Organic layers were combined, washed with brine (15 mL), dried with Na_2SO_4, filtered over cotton, and concentrated *in vacuo*. The residue was purified by flash chromatography on SiO_2 with 4% methanol in dichloromethane to yield **109** as an off-white solid (7.8 mg, 81%). ^{1}H NMR (400MHz, $CDCl_3$) δ 8.05 (d, J = 8.4 Hz, 1H), 8.01 (d, J = 8.4 Hz, 1H), 7.73 (s, 1H), 7.64 (dd, J = 8.8 Hz, 2 Hz, 1H), 7.34 (d, J = 8.4 Hz, 1H), 4.87 (s, 2H), 3.25 (m, 1H), 1.38 (d, J = 6.8 Hz, 6H). ^{13}C NMR (500 MHz,

$CDCl_3$) δ 167.8, 147.4, 138.5, 136.5, 129.3, 128.6, 126.9, 125.0, 119.5, 65.1, 37.4, 22.7. HRMS calcd for $[M+H]^+$ 202.1234, observed 202.1213.

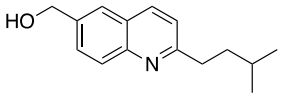

(2-Isopentylquinolin-6-yl)methanol (112). Methyl 2-isopentylquinoline-6-carboxylate (18 mg, 0.070 mmol) was diluted in tetrahydrofuran (370 µL) at room temperature under nitrogen gas and then cooled to –80 ºC in a dry ice/isopropanol bath. Lithium aluminum hydride (6.8 mg, 0.179 mmol) was added at –80 ºC. The reaction was stirred at –80 ºC for 10 minutes and was then warmed to 0 ºC. After 2 hours stirring at 0 ºC, the reaction was quenched with 10% tetrahydrofuran in water (5 mL). The reaction was stirred at 0 ºC for 10 minutes and diluted with ethyl acetate (5 mL). The aqueous layer was extracted with ethyl acetate (3 x 5 mL). Organic layers were combined, washed with brine (15 mL), dried with Na_2SO_4, filtered over cotton, and concentrated *in vacuo*. The residue was purified by flash chromatography on SiO_2 with 4% methanol in dichloromethane to yield **112** as an off-white solid (15.3 mg, 91%). ^{1}H NMR (400 MHz, $CDCl_3$) δ 7.72 (d, J = 8.4 Hz, 1H), 7.77 (s, 1H), 7.71 (s, 1H), 7.59 (dd, J = 2 Hz, 8.8 Hz, 1H), 4.86 (s, 2H), 2.71 (s, 3H), 2.63 (d, J = 7.2 Hz, 2H), 1.96 (m, 1H), 0.97 (d, J = 6.4 Hz, 6H). ^{13}C NMR (500 MHz, $CDCl_3$) δ 158.9, 146.2, 138.4, 135.9, 133.8, 128.7, 127.9, 127.2, 124.6, 65.2, 42.4, 28.8, 23.4, 22.6. HRMS calcd for $[M+H]^+$ 230.1547, observed 230.1529.

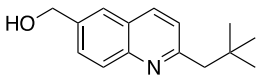

(2-Neopentylquinolin-6-yl)methanol (111). Methyl 2-neopentylquinoline-6-carboxylate (**118**, 22.2 mg, 0.086 mmol) was diluted in anhydrous tetrahydrofuran at room temperature. The solution was cooled to –80 ºC in a dry ice/isopropanol bath and then lithium aluminum hydride (4 mg, 0.104 mmol) was added. The reaction was left to stir for 30 minutes at –80 ºC and then

gradually warmed to 0 ºC. After 2 hours stirring at 0 ºC, the reaction was quenched with 10% tetrahydrofuran in water (5 mL). The quenched reaction solution was diluted with water and extracted with ethyl acetate. The aqueous layer was extracted with ethyl acetate (3 x 10 mL). The organic layers were combined, washed with brine (20 mL), dried over Na_2SO_4, filtered over cotton, and concentrated under reduced pressure. The crude mixture was resuspended in dichloromethane (~500 µL) and purified by flash chromatography on SiO_2 with 2% methanol in dichloromethane to yield 16.7 mg of **111** (84% yield). ^{1}H NMR (400 MHz, $CDCl_3$) δ 8.05 (d, J = 9.2 Hz, 1H), 8.03 (d, J = 8.8 Hz, 1H), 7.77 (d, J = 0.8 Hz, 1H), 7.66 (dd, J = 8.8 Hz, 2.0 Hz, 1H), 7.27 (d, J = 8.0 Hz, 1H), 4.88 (s, 2H), 2.88 (s, 2H), 1.01 (s, 9H). ^{13}C NMR (500 MHz, $CDCl_3$) δ 161.1, 147.6, 138.4, 135.3, 129.6, 128.5, 126.6, 125.0, 123.7, 65.2, 52.7, 32.7, 29.9. HRMS calcd for $[M+H]^+$ 230.155, observed 230.1540.

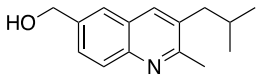

(3-Isobutyl-2-methylquinolin-6-yl)methanol (113). Methyl 3-isobutyl-2-methylquinoline-6-carboxylate (**120**, 7.2 mg, 0.028 mmol) was diluted in tetrahydrofuran (400 µL) at room temperature under a nitrogen atmosphere and then cooled to –80 ºC in a dry ice/isopropanol bath. Lithium aluminum hydride (3.2 mg, 0.084 mmol) was added at –80 ºC. The reaction was stirred at –80 ºC for 10 minutes and was then warmed to 0 ºC. After 2 hours stirring at 0 ºC, the reaction was quenched with 10% tetrahydrofuran in water (3 mL). The reaction was stirred at 0 ºC for 10 minutes and diluted with ethyl acetate (5 mL). The aqueous layer was extracted with ethyl acetate (3 x 5 mL). Organic layers were combined, washed with brine (15 mL), dried with Na_2SO_4, filtered over cotton, and concentrated *in vacuo*. The residue was purified by flash chromatography on SiO_2 with 4% methanol on dichloromethane to yield **113** as an off-white solid (5.4 mg, 84%). ^{1}H NMR (500 MHz, $CDCl_3$) δ 8.00 (d, J = 8.5 Hz, 1H), 7.98 (d, J = 8.5

Hz, 1H), 7.713 (s, 1H), 7.62 (dd, J = 8.5 Hz, 1.5 Hz, 1H), 7.27 (d, J = 8.0 Hz, 1H), 4.85 (s, 2H), 2.94 (t, J = 7.5 Hz, 2H), 1.67 (m, 3H), 0.96 (d, J = 6.5 Hz, 6H). ^{13}C NMR (500 MHz, $CDCl_3$) δ 163.3, 147.4, 138.6, 136.3, 129.0, 128.7, 126.6, 124.93, 121.6, 64.9, 39.2, 37.3, 28.3, 22.6. HRMS calcd for $[M+H]^+$ 230.1547, observed 230.1544.

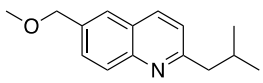

2-Isobutyl-6-(methoxymethyl)quinoline (110). 6-(Chloromethyl)-2-isobutylquinoline (**121**, 28.6 mg, 0.122 mmol) was dissolved in methanol (2 mL) at room temperature while stirring. Sodium methoxide (14 mg, 0.244 mmol) was added and the reaction was heated to reflux (60 ºC). After 24 hours stirring at reflux, sodium methoxide (14 mg) was added. After refluxing an additional 24 hours, the reaction was diluted in water and extracted with ethyl acetate (3 x 5 mL). The organic layers were combined, washed with brine (15 mL), dried over Na_2SO_4, filtered over cotton, and concentrated *in vacuo*. The crude material was purified by flash chromatography on SiO_2 with 15% ethyl acetate in hexanes to yield **110** as a white solid (8.9 mg, 32%). ^{1}H NMR (400 MHz, $CDCl_3$) δ 8.03 (d, J = 2.4 Hz, 8.8 Hz, 2H), 7.73 (s, 1H), 7.64 (dd, J = 2 Hz, 8.8 Hz, 1H), 7.26 (d, J = 8.4 Hz, 1H), 4.62 (s, 2H), 3.44 (s, 3H), 2.84 (d, J = 7.6 Hz, 2H), 2.21 (m, 1H), 0.97 (d, J = 6.8Hz, 6H). ^{13}C NMR (400 MHz, $CDCl_3$) δ 162.4, 147.4, 136.0, 135.77, 129.2, 126.6, 126.0, 122.4, 74.5, 58.4, 48.4, 29.6, 22.7. HRMS calcd for $[M+H]^+$ 230.158, observed 230.1543.

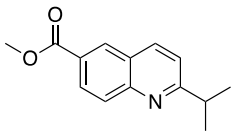

Methyl 2-isopropylquinoline-6-carboxylate (117). The synthetic protocol for this compound was adapted from a previously reported protocol.[256] Methyl 4-amino-3-formylbenzoate (**103**, 20 mg, 0.112 mmol) was diluted in ethanol (500 µL) at room temperature. Pyrrolidine (11

μL, 0.134 mmol) and then concentrated sulfuric acid (2 μL, 0.038 mmol) were added to the reaction mixture while stirring. 3-Methyl-2-butanone (15 μL, 0.134 mmol) was added dropwise. After overnight stirring, the reaction was concentrated and dried. The resulting dark orange oil was diluted with dichloromethane and purified by flash chromatography on SiO_2 in 10% ethyl acetate in hexanes to yield a clear oil (11.1 mg, 43%). ^{1}H NMR (400 MHz, $CDCl_3$) δ 8.53 (d, J = 1.6 Hz, 1H), 8.25 (dd, J = 2 Hz, 8.8 Hz, 1H), 8.16 (d, J = 8.4 Hz, 1H), 8.06 (d, J = 8.8Hz, 1H), 7.39 (d, J = 8.4 Hz, 1H), 3.98 (s, 3H), 3.27 (m, 1H), 1.40 (d, J = 6.8 Hz, 6H). ^{13}C NMR (400 MHz, $CDCl_3$) δ 170.2, 166.9, 138.2, 130.8, 129.3, 127.6, 126.2, 120.3, 52.5, 37.3, 29.8, 22.5. HRMS calcd for $[M+H]^+$ 230.11, observed 230.11810.

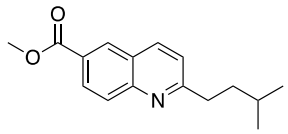

Methyl 2-isopentylquinoline-6-carboxylate (119). The synthetic protocol for this compound was adapted from a previously reported protocol.[256] Methyl 4-amino-3-formylbenzoate (**103**, 20 mg, 0.112 mmol) was diluted in ethanol (700 μL) at room temperature. Pyrrolidine (11 μL, 0.134 mmol) and then concentrated sulfuric acid (2 μL, 0.038 mmol) were added to the reaction mixture while stirring. 5-Methyl-2-hexanone (**116**, 19 μL, 0.134 mmol) was added dropwise. After overnight stirring, the reaction was concentrated and dried under high vacuum. The resulting dark orange oil was diluted with dichloromethane and purified by flash chromatography on SiO_2 in 5% ethyl acetate in hexanes to yield a clear oil (18.2 mg, 63%). ^{1}H NMR (400 MHz, $CDCl_3$) δ 8.54 (d, J = 1.6 Hz, 1H), 8.26 (dd, J = 1.6 Hz, 8.8 Hz, 1H), 8.15 (d, J = 8.4 Hz, 1H), 8.06 (d, J = 8.8 Hz, 1H), 7.36 (d, J = 8.4 Hz, 1H), 3.98 (s, 3H), 2.99 (m, 2H), 1.69 (m, 3H), 0.99 (d, J = 6.4 Hz, 6H). ^{13}C NMR (400 MHz, $CDCl_3$) δ 166.81, 165.9, 149.4, 137.9,

130.8, 129.3, 128.9, 127.5, 126.0, 122.3, 52.5, 39.0, 37.3, 28.3, 22.6. HRMS calcd for $[M+H]^+$ 258.14, observed 258.14999.

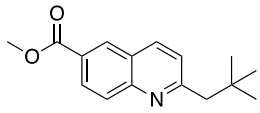

Methyl 2-neopentylquinoline-6-carboxylate (118). The synthetic protocol for this compound was adapted from a previously reported protocol.[256] Methyl 4-amino-3-formylbenzoate (16.3 mg, 0.091 mmol) was diluted in ethanol (500 µL) at room temperature. Pyrrolidine (9 µL, 0.109 mmol) and then concentrated sulfuric acid (2 µL, 0.038 mmol) were added to the reaction mixture while stirring. 4,4-Dimethylpentan-2-one (**115**, 16 µL, 0.109 mmol) was added dropwise. After overnight stirring, an additional equivalent of **115** (13 µL, 0.091 mmol) and pyrrolidine (7.5 µL, 0.091 mmol) was added to the reaction mixture to push the reaction to completion. The reaction was stirred at room temperature for an additional 4 hours and then concentrated under reduced pressure and dried under vacuum. The resulting dark orange oil was diluted with dichloromethane (~ 500 µL) and purified by flash chromatography on SiO_2 in 20% ethyl acetate in hexanes to yield 22.2 mg of **118** (95%). ^{1}H NMR (400 MHz, $CDCl_3$) δ 8.55 (d, J = 2 Hz, 1H), 8.26 (dd, J = 2 Hz, 8.8 Hz, 1H), 8.13 (d, J = 8.4 Hz, 1H), 8.08 (d, J = 8.8 Hz, 1H), 3.98 (s, 3H), 2.903 (s, 2H), 1.02 (s, 9H). HRMS calcd for $[M+H]^+$ 257.14, observed 258.14866. While the ^{1}H NMR and HRMS indicate product formation, compound characterization is incomplete due to missing ^{13}C NMR data.

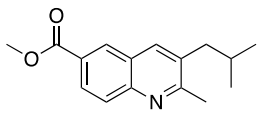

Methyl 3-isobutyl-2-methylquinoline-6-carboxylate (120). The synthetic protocol for this compound was adapted from a previously reported protocol.[256] Methyl 4-amino-3-

formylbenzoate (**103**, 20 mg, 0.112 mmol) was diluted in ethanol (700 µL) at room temperature. Pyrrolidine (11 µL, 0.134 mmol) and then concentrated sulfuric acid (2 µL, 0.038 mmol) were added to the reaction mixture while stirring. 5-Methyl-2-hexanone (**116**, 19 µL, 0.134 mmol) was added dropwise. After overnight stirring, the reaction was concentrated *in vacuo* and dried. The resulting dark orange oil was diluted with dichloromethane and purified by flash chromatography on SiO_2 in 5% ethyl acetate in hexanes to yield a clear oil (8.0 mg, 26%). ^{1}H NMR (400 MHz, $CDCl_3$) δ 8.51 (d, J = 2 Hz, 1H), 8.21 (dd, J = 2 Hz, 8.8 Hz, 1H), 8.01 (d, J = 8.4 Hz, 1H), 7.88 (s, 1H), 3.98 (s, 3H), 2.75 (s, 3H), 2.66 (d, J = 7.2 Hz, 2H), 1.98 (m, 1H), 0.99 (d, J = 6.8 Hz, 6H). ^{13}C NMR (400 MHz, $CDCl_3$) δ 166.7, 161.2, 138.1, 134.8, 130.3, 129.1, 128.0, 127.6, 126.5, 52.6, 42.1, 28.8, 22.6. HRMS calcd for $[M+H]^+$ 258.14, observed 258.15109.

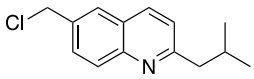

6-(Chloromethyl)-2-isobutylquinoline (121). Compound **106** (18 mg, 0.084 mmol) was diluted in dichloromethane (500 µL) and cooled to 0 ºC. Thionyl chloride (9 µL, 0.125 mmol) was added dropwise at 0 ºC. The reaction mixture was gradually warmed to room temperature while stirring for 3 hours. The reaction was concentrated *in vacuo* and purified by flash chromatography on SiO_2 in 15% ethyl acetate in hexanes to yield a light yellow oil (14.8 mg, 75%). ^{1}H NMR (400 MHz, $CDCl_3$) δ 8.06 (d, J = 8.4 Hz, 1H), 8.04 (d, J = 8.4 Hz, 1H), 7.77 (s, 1H), 7.70 (dd, J = 1.6 Hz, 8.8 Hz, 1H), 7.29 (d, J = 8.4 Hz, 1H), 4.75 (s, 2H), 2.85 (d, J = 7.2 Hz, 2H), 2.21 (m, 1H), 0.97 (d, J = 6.8 Hz, 6H). ^{13}C NMR (400 MHz, $CDCl_3$) δ 163.1, 147.7, 136.2, 134.9, 129.9, 129.7, 127.2, 126.6, 122.7, 48.3, 46.2, 29.6, 22.7. HRMS calcd for $[M+H]^+$ 234.10, observed 234.10524.

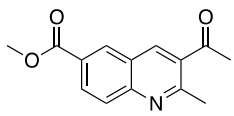

Methyl 2-(2-oxopropyl)quinoline-6-carboxylate (127). Methyl 4-amino-3-formylbenzoate (**103**, 50 mg, 0.279 mmol) was diluted in ethanol (400 µL). Pyrrolidine (28 µL, 0.335 mmol) and then concentrated sulfuric acid (4.5 µL, 0.084 mmol) were added to the reaction mixture while stirring. 2,4-Pentanedione (**125**, 34.2 µL, 0.335 mmol) was added dropwise. After overnight stirring, an additional 1.2 equivalent of **125** (34.2 µL, 0.335 mmol) and pyrrolidine (28 µL, 0.335 mmol) was added the reaction mixture to push the reaction to completion. After the reaction was stirred at room temperature for an additional 8 hours, the mixture was concentrated under reduced pressure and dried under vacuum. The resulting dark orange oil was diluted with dichloromethane (~ 500 µL) and purified by flash chromatography on SiO_2 in 15% ethyl acetate in hexanes to yield a light yellow solid (23.7 mg, 32%). ^{1}H NMR (400 MHz, $CDCl_3$) δ 8.60 (d, J = 1.6 Hz, 1H), 8.54 (s, 1H), 8.35 (dd, J = 1.6 Hz, 8.8 Hz, 1H), 8.04 (d, J = 8.8 Hz, 1H), 3.98 (s, 3H), 2.91 (s, 3H), 2.71 (s, 3H). While the ^{1}H NMR indicates product formation, compound characterization is incomplete due to missing ^{13}C NMR and HRMS data.

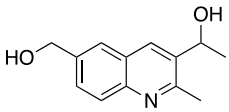

1-(6-hydroxymethyl)-2-methylquinolin-3-yl)ethan-1-ol (128). Methyl 3-acetyl-2-methylquinoline-6-carboxylate (23.7 mg, 0.097 mmol) was diluted in tetrahydrofuran (970 µL) at room temperature under nitrogen and then cooled to –80 ºC in a dry ice/isopropanol bath. Lithium aluminum hydride (5 mg, 0.117 mmol) was added at –80 ºC. The reaction was stirred at –80 ºC for 10 minutes and was then warmed to 0 ºC. After 1 hour stirring at 0 ºC, the reaction was quenched with 10% tetrahydrofuran in water (3 mL). The reaction was stirred at 0 ºC for 10 minutes and diluted with dichloromethane (5 mL). The aqueous layer was extracted with dichloromethane (3 x 10 mL). Organic layers were combined, washed with brine (25 mL), dried

with Na_2SO_4, filtered over cotton, and concentrated *in vacuo*. The residue was purified by flash chromatography on SiO_2 to yield 10 mg **128** (47% yield). ^{1}H NMR (400 MHz, $CDCl_3$) δ 8.07 (s, 1H), 7.86 (d, J = 8.4 Hz, 1H), 7.55 (d, J = 8.8 Hz, 2H), 5.16 (q, J = 6 Hz, 1H), 4.81 (s, 2H), 2.66 (s, 3H), 1.51 (d, J = 6.4 Hz). While the ^{1}H NMR indicates product formation, compound characterization is incomplete due to missing ^{13}C NMR and HRMS data.

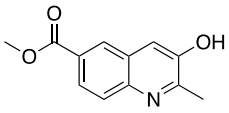

Methyl 3-hydroxy-2-methylquinoline-6-carboxylate (130). Methyl-4-amino-formylbenzoate (89 mg, 0.494 mmol) was dissolved in ethanol (1 mL) at room temperature. Pyrrolidine (49 µL, 0.593 mmol) and concentrated sulfuric acid (8 µL, 0.148 mmol) were added sequentially. 1-Hydroxypropan-2-one (**129**, 42 µL, 0.593 mmol) was added last and the reaction stirred at 50 ºC for two and a half hours before it was concentrated *in vacuo*. The resulting solid was redissolved in ethyl acetate (~ 500 µL) and purified by flash chromatography on silica gel using 30% ethyl acetate in hexanes to afford a beige solid (63 mg, 59%). ^{1}H NMR (400 MHz, d6-DMSO) δ 8.46 (d, J = 1.6 Hz, 1H), 7.94 (dd, J = 2, 8.8 Hz, 1H), 7.89 (d, J = 8.4 Hz, 1H), 7.58 (s, 1H), 3.89 (s, 3H) 2.55 (s, 3H). ^{13}C NMR (400 MHz, DMSO) δ 166.0, 154.8, 154.8, 150.4, 150.2, 128.9, 127.8, 127.4, 126.8, 125.1, 52.2, 20.0. HRMS calcd for $[M+H]^+$ 217.07, observed 218.08098.

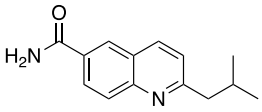

2-Isobutylquinoline-6-carboxamide (122). 2-Isobutylquinoline-6-carboxylic acid (**105**, 46 mg, 0.201 mmol) was dissolved in acetonitrile (2 mL) and cooled to 0 ºC while stirring. Triethylamine (71 µL, 0.508 mmol) was added dropwise at 0 ºC. TSTU (67 mg, 0.223 mmol) was

added to the reaction at 0 ºC, and the reaction was left to stir at 0 ºC for 10 min. The reaction warmed to room temperature over an hour. The reaction was concentrated *in vacuo* and the crude material was used without further purification. The crude material was dissolved in a 0.5M ammonia solution in dioxane (6 mL, excess) added dropwise to the solution at 0 ºC. Upon complete addition of ammonia in dioxane, the reaction was stirred at 0 ºC for 2 minutes, and then removed from the ice bath and allowed to warm to room temperature. The reaction was stirred at room temperature for 4 hours and then concentrated *in vacuo*. The crude solid was dried under high vacuum and purified by flash chromatography on SiO_2 eluting with 3% methanol in dichloromethane to yield **122** as a white solid (31 mg, 68% over two steps). ^{1}H NMR (400 MHz, $CDCl_3$) δ 8.37 (d, J = 1.2 Hz, 1H), 8.18 (dd, J = 2.8 Hz, 8.4 Hz, 2H), 8.10 (d, J = 8.4 Hz, 1H), 7.36 (d, J = 8.4 Hz, 1H), 6.50 (br s, 1H), 6.04 (br s, 1H), 2.91 (d, J = 7.6 Hz, 2H), 2.24 (m, 1H), 0.98 (d, J = 6.4 Hz, 6H). ^{13}C NMR (400 MHz, $CDCl_3$) δ 168.7, 164.4, 138.2, 128.4, 126.2, 123.2, 47.8, 29.7, 22.7. HRMS calcd for $[M+H]^+$ 229.13, observed 229.13394.

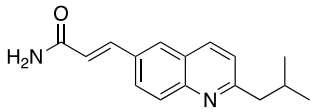

(*E*)-3-(2-isobutylquinolin-6-yl)acrylamide (132). 6-Bromo-2-isobutylquinoline (116 mg, 0.439 mmol) was dissolved in dimethylformamide (2 mL) at room temperature before palladium(II) acetate (9.8 mg, 0.044 mmol) and tri(o-tolyl)phosphine (54 mg, 0.176 mmol) were added sequentially. Triethylamine (620 µL, 4.39 mmol) and acrylamide (93 mg, 1.31 mmol) were added, and the reaction stirred at 80 ºC overnight. The reaction was cooled to room temperature and diluted with ethyl acetate (15 mL) and water (30 mL). The aqueous layer was extracted with ethyl acetate (3 x 15 mL). The organic layers were combined, washed with brine (30 mL), dried over anhydrous Na_2SO_4, filtered, and concentrated *in vacuo*. The brown oil was redissolved in

dichloromethane (~ 500 μL) and purified by flash chromatography on silica gel using 2.5% methanol in dichloromethane to yield an off-white solid (104 mg, 87%). ^{1}H NMR (400 MHz, $CDCl_3$) δ 8.07 (d, J = 8.4 Hz, 1H), 8.04 (d, J = 9.2 Hz, 1H), 7.88 (m, 2H), 7.84 (d, J = 15.6 Hz, 1H), 7.31 (d, J = 5.2 Hz, 1H), 6.59 (d, J = 15.6 Hz, 2H), 5.59 (br s, 2H), 2.86 (d, J = 7.2 Hz, 2H), 2.22 (m, 1H), 0.98 (d, J = 6.8 Hz, 6H). ^{13}C NMR (400 MHz, $CDCl_3$) δ 167.4, 163.5, 142.1, 136.3, 131.8, 129.7, 129.0, 127.0, 126.7, 122.8, 119.9, 48.3, 29.5, 22.6. HRMS calcd for $[M+H]^+$ 254.14, observed 255.14889.

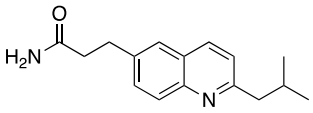

3-(2-isobutylquinolin-6-yl)propanamide (123). (*E*)-(2-Isobutylquinolin-6-yl)acrylamide (50 mg, 0.197 mmol) was dissolved in methanol (8 mL) and the reaction mixture was cooled to 0 ºC. Palladium hydroxide (6 mg, 0.039 mmol) was added to the reaction mixture while stirring. Hydrogen was bubbled through the reaction using a balloon as it stirred to room temperature over two hours. The reaction mixture was filtered over celite, concentrated *in vacuo*, and purified by flash chromatography on silica gel using 5% methanol in dichloromethane to afford a light yellow solid (48 mg, 96%). ^{1}H NMR (400 MHz, $CDCl_3$) δ 8.00 (d, J = 8.0 Hz, 1H), 7.99 (d, J = 8.4 Hz, 1H), 7.60 (br s, 1H), 7.56 (dd, J = 2.0 Hz, 1.6 Hz, 1H), 7.24 (s, 1H), 3.17 (t, J = 7.6 Hz, 2H) 2.84 (d, J = 7.2 Hz, 2H) 2.64 (t, J = 7.6 Hz, 2H), 2.19 (m, 1H), 0.97 (d, J = 6.4 Hz, 6H). ^{13}C NMR (400 MHz, $CDCl_3$) δ 173.9, 161.8, 146.8, 138.1, 135.6, 130.3, 129.0, 126.7, 126.2, 122.2, 48.2, 37.2, 31.2, 29.5, 22.5. HRMS calcd for $[M+H]^+$ 256.35, observed 257.16512.

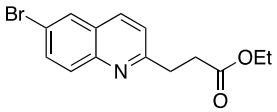

Ethyl 3-(6-bromoquinolin-2-yl)propanoate (135). The synthetic protocol for this compound was adapted from a previously reported protocol.[256] 2-Amino-5-bromobenzaldehyde (**133**, 350 mg, 1.74 mmol) was dissolved in ethanol (2.5 mL) at room temperature. Pyrrolidine (156 µL, 1.91 mmol) and concentrated sulfuric acid (15.2 µL, 0.5 mmol) were added sequentially at room temperature. Ethyl levulinate (**134**, 271 µL, 1.91 mmol) was added dropwise at room temperature and the reaction stirred overnight. The reaction mixture was concentrated *in vacuo* and the resulting dark orange oil was dried on high vacuum. The crude reaction was resuspended in dichloromethane and purified by flash chromatography on SiO_2 with a gradient of 5-20% ethyl acetate in hexanes to yield a light yellow solid (203.7 mg, 38%). ^{1}H NMR (500 MHz, $CDCl_3$) δ 7.96 (d, J = 8 Hz, 1H), 7.93 (d, J = 2 Hz, 1H), 7.87 (d, J = 9 Hz, 1H), 7.73 (dd, J = 2.5 Hz, 9 Hz, 1H), 7.33 (d, J = 8.5 Hz, 1H), 4.14 (q, J = 7.5 Hz, 2H), 3.28 (t, J = 7 Hz, 2H), 2.91 (t, J = 7 Hz, 2H), 1.23 (t, J = 7 Hz). ^{13}C NMR (400 MHz, $CDCl_3$) δ 173.2, 161.1, 146.6, 135.3, 132.9, 130.8, 129.7, 128.1, 122.5, 119.7, 60.6, 33.6, 33.0, 14.4. HRMS calcd for $[M+H]^+$ 308.02, observed 308.03134.

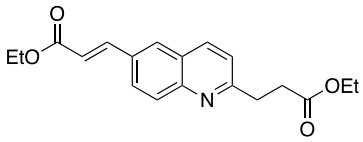

Ethyl (*E*)-3-(2-(3-ethoxy-3-oxopropyl)quinolin-6-yl)acrylate (137). Palladium acetate (1 mg, 0.032 mmol) and tri(o-tolyl)phosphine (4 mg, 0.013 mmol) were dissolved in dimethylformamide (150 µL) in a flame-dried glass vial. Ethyl 3-(6-bromoquinolin-2-yl)propanoate (**135**, 10 mg, 0.032 mmol) was diluted in dimethylformamide (25 µL) and added to the reaction mixture. Triethylamine (45 µL, 0.32 mmol) and then ethyl acrylate (**147**, 10.6 µL, 0.097 mmol) were added to the reaction mixture while stirring at room temperature. The reaction was then heated to 80 ºC in an oil bath, and then stirred at 80 ºC for 1 hour. Following complete

disappearance of starting material by TLC, the reaction was removed from heat, cooled to room temperature, and then diluted with ethyl acetate (10 mL) and water (50 mL). The aqueous layer was extracted with ethyl acetate (3 x 20 mL). The organic layers were combined, washed with water (30 mL), then brine (30 mL), dried over anhydrous Na_2SO_4, filtered over a cotton plug, and concentrated under reduced pressure. The crude residue was purified by flash chromatography on SiO_2 eluting with 20% ethyl acetate in hexanes to yield 6.3 mg of **137** (61%). ^{1}H NMR (400 MHz, $CDCl_3$) δ 8.06 (d, J = 8.4 Hz, 1H), 7.99 (d, J = 9.2 Hz, 1H), 7.86 (m, 2H), 7.35 (d, J = 8.4 Hz, 1H), 6.54 (d, J = 15.6 Hz, 1H), 4.29 (q, J = 7.2 Hz, 2H), 4.14 (q, J = 7.2 Hz, 2H), 3.30 (t, J = 7.2 Hz, 2H), 2.92 (t, J = 7.6 Hz, 2H), 1.36 (t, J = 7.2 Hz, 3H), 1.24 (t, J = 6.8 Hz, 3H). ^{13}C NMR (400 MHz, $CDCl_3$) δ 173.1, 167.0, 161.9, 148.8, 143.9, 136.7, 132.2, 129.8, 129.1, 127.4, 126.9, 122.5, 119.3, 60.7, 60.6, 33.7, 33.1, 29.8, 14.5, 14.4. While the ^{1}H and ^{13}C NMR data indicates product formation, compound characterization is incomplete due to missing HRMS data.

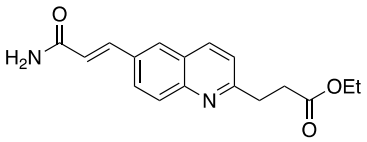

Ethyl (*E*)-3-(6-(3-amino-3-oxoprop-1-en-1-yl)quinolin-2-yl)propanoate (138). Ethyl 3-(6-bromoquinolin-2-yl)propanoate (175 mg, 0.567 mmol) was dissolved in dimethylformamide (2.2 mL). Palladium(II) acetate (12.7 mg, 0.057 mmol), tri(o-tolyl)phosphine (69 mg, 0.227 mmol), and trimethylamine (800 µL, 5.67 mmol) were added sequentially at room temperature under nitrogen atmosphere. Acrylamide (**131**, 121 mg, 1.70 mmol) was added last and the reaction was heated to 80 ºC for 5 hours. The reaction was cooled to room temperature and diluted with ethyl acetate (10 mL) and water (25 mL). The aqueous layer was extracted with ethyl acetate (5 x 10 mL). The organic layers were combined, washed with water (25 mL) and then brine (25 mL), dried over Na_2SO_4, filtered over cotton, and concentrated *in vacuo*. The dark brown solid was

redissolved in dichloromethane (~ 500 μL) and purified on a silica gel column by flash chromatography in 3% methanol in dichloromethane to yield a beige solid (162 mg, 95%). ^{1}H NMR (400 MHz, $CDCl_3$) δ 8.02 (d, J = 8.4 Hz, 1H), 7.96 (d, J = 9.2 Hz, 1H), 7.81 (m, 2H), 7.78 (d, J = 15.6 Hz, 1H), 7.32 (d, J = 8.4 Hz, 1H), 6.57 (d, J = 15.6 Hz, 1H), 5.91 (br s, 2H), 4.13 (q, J = 7.2 Hz, 2H), 3.29 (t, J = 7.2 Hz, 2H), 2.91 (t, J = 7.2 Hz, 2H), 1.23 (t, J = 7.2 Hz, 3H). ^{13}C NMR (400 MHz, $CDCl_3$) δ 173.2, 167.8, 161.7, 148.7, 141.9, 136.7, 132.2, 129.8, 129.0, 127.2, 127.0, 122.4, 120.5, 60.6, 33.7, 33.1, 14.4. HRMS calcd for $[M+H]^+$ 299.13, observed 299.14049.

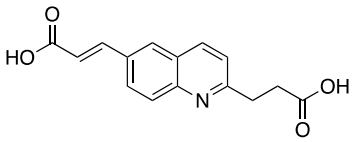

(*E*)-3-(2-(2-carboxyethyl)quinolin-6-yl)acrylic acid (139). Ethyl (*E*)-3-(2-(3-ethoxy-3-oxopropyl)quinolin-6-yl)acrylate (**137**, 35.5 mg, 0.108 mmol) was diluted in tetrahydrofuran (870 μL). Aqueous lithium hydroxide (1 M, 435 μL) was added dropwise to the reaction mixture and the reaction was stirred at room temperature for 5 hours. The reaction was adjusted to pH 3 with 5 M hydrochloric acid and diluted with water (15 mL) and ethyl acetate (15 mL). The aqueous layer was extracted three times with ethyl acetate (10 mL). The organic layers were combined, washed with brine (25 mL), dried over Na_2SO_4, filtered over cotton, and concentrated under reduced pressure to yield the pure product (26.4 mg) in 90% yield. ^{1}H NMR (400 MHz, d6-DMSO) δ 12.32 (br s, 2H), 8.26 (d, J = 8.4 Hz, 1H), 8.20 (s, 1H), 8.07 (dd, J = 1.6 Hz, 8.8 Hz, 1H), 7.90 (d, J = 8.8 Hz, 1H), 7.77 (d, J = 16 Hz, 1H), 7.49 (d, J = 8.4 Hz, 1H), 6.67 (d, J = 16 Hz, 1H), 3.17 (t, J = 7.2 Hz, 2H), 2.80 (t, J = 7.2 Hz, 2H). ^{13}C NMR (400 MHz, $CDCl_3$) δ 173.9, 167.5, 162.0, 147.9, 143.2, 136.6, 131.7, 129.2, 129.0, 127.7, 126.5, 122.5, 120.1, 32.9. 32.1. While the ^{1}H and ^{13}C NMR data indicates product formation, compound characterization is incomplete due to missing HRMS data.

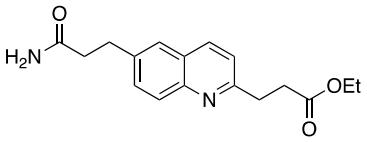

Ethyl 3-(6-(3-amino-3-oxopropyl)quinolin-2-yl)propanoate (141). Ethyl (*E*)-3-(6-(3-amino-3-oxoprop-1-ene-1-yl)quinolin-2-yl)propanoate (46 mg, 0.153 mmol) was dissolved in methanol (3 mL) and cooled to 0 ºC in an ice bath. Palladium(II) hydroxide (4.5 mg, 20% [w/w]) was added to the reaction mixture while stirring. Hydrogen was bubbled through the reaction, and the reaction was gradually warmed to room temperature. Hydrogen was bubbled through the reaction for 5 hours while stirring. The reaction mixture was diluted in methanol (8 mL) and vacuum filtered over a pad of celite. The filtrate was concentrated *in vacuo*, dried, and purified by flash chromatography on SiO_2 in 4% methanol in dichloromethane to yield **141** as a white solid (33.4 mg, 73%). ^{1}H NMR (400 MHz, $CDCl_3$) δ 8.10 (dd, J = 3.2 Hz, 8.4 Hz, 2H), 7.63 (s, 1H), 7.58 (dd, J = 2 Hz, 8.8 Hz, 1H), 7.37 (d, J = 8.4 Hz, 1H), 5.85 (br s, 1H), 5.62 (br s, 1H), 4.10 (q, J = 7.2 Hz, 2H), 3.35 (t, J = 7.2 Hz, 2H), 3.12 (t, J = 7.6 Hz, 2H), 2.93 (t, J = 7.2 Hz, 2H), 2.61 (t, J = 8 Hz, 2H), 1.21(t, J = 7.2 Hz, 3H). ^{13}C NMR (400 MHz, $CDCl_3$) δ 174.2, 172.9, 159.7, 144.7, 139.7, 138.0, 131.8, 127.3, 127.1, 126.5, 122.0, 60.7, 37.1, 33.4, 32.5, 31.3, 14.3. HRMS calc for $[M+H]^+$ 301.158, observed 301.15620.

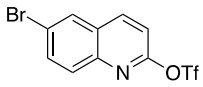

6-Bromoquinolin-2-yl trifluoromethanesulfonate (146). 6-Bromoquinolin-2-ol (**145**, 50 mg, 0.223 mmol) was dissolved in dichloromethane (2.24 mL). Pyridine (110 µL, 1.338 mmol) was added dropwise and the reaction was cooled to 0 ºC on ice for 15 minutes. Trifluoromethane sulfonic anhydride (150 µL, 0.892 mmol) was added dropwise at 0 ºC and the reaction was stirred at 0 ºC for 1 hour. The reaction mixture was diluted with ethyl acetate (25 mL). The organic layer

was washed with 0.1 M aqueous hydrochloric acid (25 mL). The organic layer was dried over Na_2SO_4, filtered over cotton, and concentrated *in vacuo*, to yield pure **146** as a light brown solid (75.8 mg, 95%). ^{1}H NMR (400 MHz, $CDCl_3$) δ 8.27 (d, J = 8.8 Hz, 1H), 8.06 (d, J = 2 Hz, 1H), 7.92 (d, J = 9.2 Hz, 1H), 7.87 (dd, J = 2 Hz, 9.2 Hz, 1H), 7.27 (d, J = 8.8 Hz, 1H). While the ^{1}H NMR data indicates product formation, compound characterization is incomplete due to missing ^{13}C NMR and HRMS data.

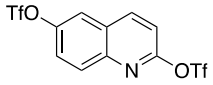

Quinoline-2,6-diyl bis(trifluoromethanesulfonate) (149). Quinoline-2,6-diol (**148**, 107 mg, 0.664 mmol) was dissolved in dichloromethane (6.2 mL). Pyridine (600 µL, 7.43 mmol) was added dropwise and the reaction was cooled to 0 ºC on ice for 15 minutes. Trifluoromethane sulfonic anhydride (840 µL, 4.95 mmol) was added dropwise at 0 ºC and the reaction was stirred at 0 ºC for 30 minutes. The reaction mixture was diluted with dichloromethane (50 mL). The organic layer was washed with 0.1 M hydrochloric acid (50 mL). The organic layer was dried over Na_2SO_4, filtered over cotton, and concentrated *in vacuo*, to yield pure **149** as a light brown solid (267.6 mg, 89%). ^{1}H NMR (400 MHz, $CDCl_3$) δ 8.4 (d, J = 8.8 Hz, 1H), 8.16 (d, J = 9.2 Hz, 1H), 7.85 (d, J = 2.4 Hz, 1H), 7.70 (dd, J = 2.8 Hz, 9.2 Hz, 1H), 7.36 (d, J = 8.8 Hz, 1H). 19F NMR (400 MHz, $CDCl_3$) δ -72.58, -72.82. ^{13}C NMR (400 MHz, $CDCl_3$) δ 154.7, 147.9, 144.9, 142.1, 131.9, 127.9, 125.1, 120.5, 120.4, 119.4, 117.3, 117.2, 115.1. While the NMR data indicates product formation, compound characterization is incomplete due to missing HRMS data.

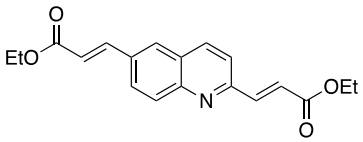

Diethyl 3,3'-(quinoline-2,6-diyl)(2*E*,2'*E*)-diacrylate (150). Quinoline-2,6-diyl bis(trifluoromethanesulfonate) (**149**, 50 mg, 0.118 mmol) was mixed with palladium acetate (21.2 mg, 0.094 mmol), tetrabutylammonium bromide (152 mg, 0.472 mmol), potassium carbonate (196 mg, 1.42 mmol), and dimethylformamide (3 mL) in a glass microwave vial equipped with a stir bar. Ethyl acrylate (50.2 µL, 0.472 mmol) was added last and the reaction mixture was briefly swirled by hand to mix. The microwave vial was capped and then placed in a CEM Discover microwave synthesizer. The reaction vial was heated to 100 ºC for 20 mins, and power was held constant between 20 – 30 watts. Following microwave irradiation, the glass microwave vial was rinsed with ethyl acetate (10 mL). Rinses were combined and then mixed with water (100 mL). The aqueous layer was extracted with ethyl acetate three times (20 mL). The organic layers were combined, washed with brine (50 mL), dried over Na_2SO_4, filtered over cotton, and then concentrated under reduced pressure. The crude residue was resuspended in dichloromethane (~ 750 µL) and purified by flash chromatography on SiO_2 in 2% methanol in chloroform to yield **150** (9.5 mg) in 27% yield. ^{1}H NMR (400 MHz, $CDCl_3$) δ 8.2 (d, J = 8.4 Hz, 1H), 8.13 (d, J = 8.8 Hz, 1H), 7.91 (m, 3H), 7.82 (d, J = 16 Hz, 1H), 7.64 (d, J = 8.4 Hz, 1H), 7.02 (d, J = 16 Hz, 1H), 6.58 (d, J = 16 Hz, 1H), 4.29 (m, 4H), 1.36 (t, J = 7.2 Hz). While the ^{1}H NMR data indicates product formation, compound characterization is incomplete due to missing ^{13}C NMR and HRMS data.

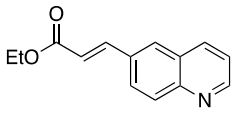

Ethyl (*E*)-3-(quinolin-6-yl)acrylate (152). 6-Iodoquinoline (200 mg, 0.784 mmol) was diluted in dimethylformamide (1 mL). Palladium acetate (35 mg, 0.157 mmol), tri(o-tolyl)phosphine (95 mg, 0.314 mmol), and trimethylamine (219 µL, 1.57 mmol) were added sequentially under nitrogen atmosphere. Ethyl acrylate (100 µL, 1.18 mmol) was added dropwise

to the reaction mixture. The reaction mixture was heated to 80 ºC and stirred for 2 hours. The reaction was cooled to room temperature and diluted with ethyl acetate (4 mL) worked up in water (50 mL). The aqueous layer was extracted with ethyl acetate (3 x 10 mL). The organic layers were combined, washed with brine (30 mL), dried over Na_2SO_4, filtered over cotton, and concentrated under reduced pressure. The crude solid was redissolved in dichloromethane (~ 750 µL) and purified by flash chromatography on SiO_2 with 15% ethyl acetate in hexanes to yield a light yellow solid (134 mg, 75%). ^{1}H NMR (400 MHz, $CDCl_3$) δ 8.90 (d, J = 2.8 Hz, 1H), 8.14 (d, J = 8 Hz, 1H), 8.07 (d, J = 9.2 Hz, 1H), 7.88 (m, 2H), 7.82 (d, J = 16 Hz, 1H), 7.41 (dd, J = 4 Hz, 8.4 Hz, 1H), 6.55 (d, J = 16 Hz, 1H), 4.28 (q, J = 7.2 Hz, 2H), 1.34 (t, J = 7.2 Hz, 3H). ^{13}C NMR (400 MHz, $CDCl_3$) δ 166.8, 151.3, 149.0, 143.6, 136.5, 132.7, 130.3, 129.2, 128.3, 127.3, 121.9, 119.7, 60.7, 14.3. HRMS calcd for $[M+H]^+$ 228.09, observed 228.10211.

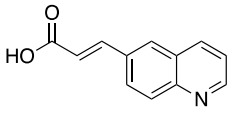

(*E*)-3-(quinolin-6-yl)acrylic acid (153). Ethyl (*E*)-3-(quinolin-6-yl)acrylate (**152**, 343 mg, 1.51 mmol) was diluted in tetrahydrofuran (2 mL) and stirred at room temperature. A 1 M solution of lithium hydroxide (3.3 mL) was added dropwise and the reaction was stirred for 2 hours. After stirring at room temperature for two hours, the crude reaction mixture was pH adjusted to pH = 1 with 5 M hydrochloric acid, upon which a white precipitate formed. The reaction mixture was vacuum filtered and the filtered solid was rinsed with water (25 mL). The white solid (269 mg, 90%) was collected and used without further purification. ^{1}H NMR (400 MHz, d6-DMSO) δ 12.54 (br s, 1H), 8.92 (d, J = 2.4 Hz, 1H), 8.38 (d, J = 8.4 Hz, 1H), 8.26 (s, 1H), 8.13 (d, J = 8.8 Hz, 1H), 8.01 (d, J = 8.8 Hz, 1H), 7.76 (d, J = 16 Hz, 1H), 7.57 (dd, J = 4 Hz, 8 Hz, 1H), 6.71 (d, J = 16

Hz). ^{13}C NMR (300 MHz, d6-DMSO) δ 167.4, 151.4, 148.3, 142.9, 136.5, 132.4, 129.5, 129.4, 127.9, 127.7, 122.10, 120.8. HRMS calcd for $[M+H]^+$ 200.21, observed 200.07036.

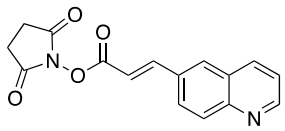

2, 5-Dioxopyrrolidin-1-yl (*E*)-3-(quinolin-6-yl)acrylate (154). (E)-3-(quinolin-6-yl)acrylic acid (**153**, 30 mg, 0.151 mmol) was dissolved in acetonitrile (1.5 mL). Triethylamine (53 µL, 0.378 mmol) was added dropwise at room temperature while stirring. The reaction was cooled to 0 ºC on ice for 15 minutes prior to the addition of N, N, N', N'-tetramethyl-O-(N-succinimidyl)uranium tetrafluoroborate (TSTU, 67.7 mg, 0.225 mmol). The reaction was gradually warmed from 0 ºC to room temperature overnight. The next morning, the reaction was concentrated under reduced pressure and dried under vacuum. The resulting residue was redissolved in dichloromethane (500 µL) and purified on a silica gel column by flash chromatography in 2% methanol in dichloromethane to yield 41 mg **154** (92% yield). ^{1}H NMR (300 MHz, $CDCl_3$) δ 8.97 (d, J = 4.2 Hz, 1H), 8.20 (d, J = 8.4 Hz, 1H), 8.14 (d, J = 8.7 Hz, 1H), 8.10 (d, J = 16.2 Hz, 1H), 7.97 (s, 1H), 7.93 (dd, J = 8.7 Hz, 1H), 7.46 (dd, J = 4.2 Hz, 8.1 Hz, 1H), 6.73 (d, J = 16.2 Hz, 1H), 2.90 (s, 4H). While the ^{1}H NMR data indicates product formation, compound characterization is incomplete due to missing ^{13}C NMR and HRMS data.

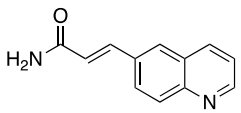

(E)-3-(quinolin-6-yl)acrylamide (155). 2, 5-Dioxopyrrolidin-1-yl (*E*)-3-(quinolin-6-yl)acrylate (**154**, 20 mg, 0.067 mmol) was dissolved in a solution of 0.5 M ammonia in dioxane (1.5 mL) and stirred at room temperature for 30 minutes. The reaction mixture was concentrated under reduced pressure and then dried under vacuum. The crude residue was resuspended in

dichloromethane (500 µL) and purified via flash chromatography on a silica gel column using 5% methanol in dichloromethane to yield **155** in 61% yield (8.3 mg). ^{1}H NMR (300 MHz, d6-DMSO) δ 8.90 (dd, J = 1.5 Hz, 4.2 Hz, 1H), 8.38 (dd, J = 1.2 Hz, 8.4 Hz, 1H), 8.12 (d, J = 1.5 Hz, 1H), 8.04 (d, J = 9 Hz, 1H), 7.96 (dd, J = 1.8 Hz, 8.7 Hz, 1H), 7.56 (m, 3H), 7.18 (s, 1H), 6.76 (d, J = 15.9 Hz, 1H). While the ^{1}H NMR data indicates product formation, compound characterization is incomplete due to missing ^{13}C NMR and HRMS data.

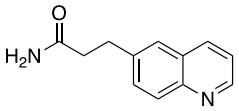

3-(quinolin-6-yl)propanamide (156). (E)-3-(quinolin-6-yl)acrylamide (**155**, 20 mg, 0.101 mmol) was diluted in methanol (1 mL). Palladium hydroxide (4 mg, 20 mol %) was carefully added and the walls of the reaction vial were rinsed with methanol (1 mL). Hydrogen was bubbled through the reaction, while stirring at room temperature for 30 minutes. The reaction mixture was diluted in methanol (10 mL) and vacuum filtered over celite. The filtrate was concentrated *in vacuo*, dried, and purified by flash chromatography on SiO_2 with 4% methanol in dichloromethane to yield **156** (17.9 mg) in 89% yield. ^{1}H NMR (400 MHz, $CDCl_3$) δ 8.86 (dd, J = 1.6 Hz, 4.4 Hz, 1H), 8.14 (d, J = 8 Hz, 1H), 8.08 (d, J = 8.4 Hz, 1H), 7.66 (s, 1H), 7.60 (d, J = 8.4 Hz, 1H), 7.40 (dd, J = 4 Hz, 7.6 Hz, 1H), 5.37 (br s, 2H), 3.18 (t, J = 7.2 Hz, 2H), 2.64 (t, J = 7.6 Hz, 2H). While the ^{1}H NMR data indicates product formation, compound characterization is incomplete due to missing ^{13}C NMR and HRMS data.

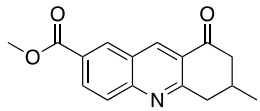

Methyl 6-methyl-8-oxo-5, 6, 7, 8-tetrahydroacridine-2-carboxylate (164). The synthetic protocol for compound **164** was adapted from a previously reported protocol.[256] Methyl

4-amino-3-formylbenzoate (**103**, 100 mg, 0.558 mmol) was diluted in ethanol (1 mL) at room temperature. Pyrrolidine (50 µL, 0.614 mmol) and concentrated sulfuric acid (9 µL, 0.167 mmol) were added sequentially at room temperature. The reaction was heated to 50 ºC. Once at temperature, 5-methylcyclohexane-1,3-dione (77mg, 0.614 mmol) was added. The reaction was stirred at 50 ºC for 5 hours before being concentrated *in vacuo*. The resulting light brown oil was resuspended in dichloromethane and purified by flash chromatography on SiO_2 in 20% ethyl acetate in hexanes to yield **164** as a white solid (121.7 mg, 81%). ^{1}H NMR (400 MHz, $CDCl_3$) δ 8.93 (s, 1H), 8.70 (d, J = 1.6 Hz, 1H), 8.39 (d, J = 1.6 Hz, 8.8 Hz, 1H), 8.10 (d, J = 8.8 Hz, 1H), 4.01 (s, 1H), 3.43 (dd, J = 3.6 Hz, 15.2 Hz, 1H), 3.03 (dd, J = 10.8 Hz, 16.8 Hz, 1H), 2.91 (m, 1H), 2.51 (m, 2H), 1.25 (d, J = 6.4 Hz, 3H). ^{13}C NMR (400 MHz, $CDCl_3$) δ 166.2, 163.7, 138.1, 132.8, 131.7, 129.0, 128.4, 126.4, 126.0, 52.6, 47.0, 41.8, 28.9, 21.3. HRMS calcd for $[M+H]^+$ 270.11, observed 270.11295.

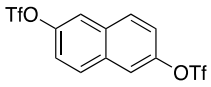

Naphthalene-2,6-diyl bis(trifluoromethanesulfonate) (175). Naphthalene-2,6-diol (**174**, 25 mg, 0.156 mmol) was dissolved in dichloromethane (1.56 mL). Pyridine (75 µL, 0.936 mmol) was added dropwise and the reaction was cooled to 0 ºC on ice for 15 minutes. Trifluoromethane sulfonic anhydride (102 µL, 0.624 mmol) was added dropwise at 0 ºC and the reaction was stirred at 0 ºC for 30 minutes. The reaction mixture was diluted with ethyl acetate (15 mL). The organic layer was washed with 0.1 M hydrochloric acid (25 mL). The organic layer was dried over Na_2SO_4, filtered over cotton, and concentrated *in vacuo*, to yield pure **175** (64.6 mg) as a brown solid in quantitative yield. ^{1}H NMR (400 MHz, d6-DMSO) δ 8.33 (d, J = 9.2 Hz, 2H), 7.78 (dd, J = 2.4 Hz, 8.8 Hz, 1H). ^{13}C NMR (400 MHz, $CDCl_3$) δ 148.0, 132.5, 131.0, 121.7, 119.6. ^{19}F NMR (400

MHz, $CDCl_3$) δ -72.67. While the NMR data indicates product formation, compound characterization is incomplete due to missing HRMS data.

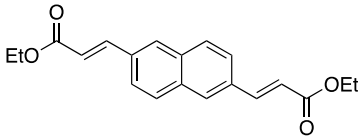

Diethyl 3,3'-(naphthalene-2,6-diyl)(2E,2'E)-diacrylate (176). 2,6-Dibromonaphthalene (**173**, 20 mg, 0.070 mmol) was mixed with palladium acetate (0.2 mg, 7 μmol) and tri(o-tolyl)phosphine (17 mg, 56 μmol) in dimethylformamide (280 μL). Triethylamine (195 μL, 1.4 mmol) was added to the reaction mixture at room temperature. Ethyl acrylate (46 μL, 0.42 mmol) was added dropwise and then the reaction was heated to 100 ºC in an oil bath and stirred overnight. The next morning, the reaction was diluted in ethyl acetate (10 mL). Water (100 mL) was added to the crude reaction mixture and the aqueous layer was extracted with ethyl acetate (20 mL) three times. The organic layers were combined, washed with brine (50 mL), dried over Na_2SO_4, filtered over cotton, and concentrated under reduced pressure. The crude residue was resuspended in dichloromethane (500 μL) and purified by flash chromatography on a silica gel column with 8% ethyl acetate in hexanes. Compound **176** (23 mg) was isolated in 92% yield. ^{1}H NMR (400 MHz, $CDCl_3$) δ 7.89 (s, 1H), 7.84 (d, J = 1.6 Hz, 1H), 7.81 (d, J = 9.6 Hz, 1H), 6.54 (d, J = 16 Hz, 1H), 4.29 (q, J = 7.2 Hz, 2H), 1.36 (t, J = 7.2 Hz, 3H). ^{13}C NMR (400 MHz, $CDCl_3$) δ 167.0, 144.3, 134.2, 133.3, 129.5, 129.3, 124.6, 119.3, 60.7, 14.5. While the NMR data indicates product formation, compound characterization is incomplete due to missing HRMS data.

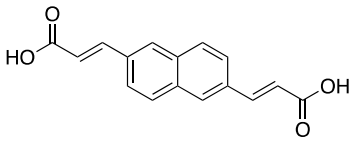

(2E,2'E)-3,3'-(naphthalene-2,6-diyl)diacrylic acid (177). Diethyl 3,3'-(naphthalene-2,6-diyl)(2E,2'E)-diacrylate (**176**, 20 mg, 0.061 mmol) was dissolved in tetrahydrofuran (260 μL). A 1 M solution of lithium hydroxide (130 μL) was added dropwise, and the reaction was stirred at room temperature for 24 hours. The crude reaction mixture was added to a 1 M solution of hydrochloric acid (10 mL) and continued stirring at room temperature for 2 hours, producing a white precipitate. The reaction was centrifuged at 1000 rpm at room temperature for 10 minutes. The acidic aqueous solvent was decanted by pipetting and discarded. The white solid product **177** was dried under vacuum overnight. The product was isolated in 93% yield (19.8 mg) and was used without further purification. ^{1}H NMR (400 MHz, $CDCl_3$) δ 12.49 (br s, 1H), 8.203 (s, 1H), 7.95 (d, J = 8.4 Hz, 1H), 7.91 (d, J = 8.4 Hz, 1H), 7.73 (d, J = 16 Hz, 1H), 6.68 (d, J = 16 Hz, 1H). ^{13}C NMR (400 MHz, d6-DMSO) δ 167.5, 143.6, 133.6, 133.0, 129.3, 129.1, 124.9, 120.2. While the NMR data indicates product formation, compound characterization is incomplete due to missing HRMS data.

3.0 Conditional Control of Protein Degradation

3.1 Introduction to the Ubiquitin-Proteasome System

Post-translational modification of proteins serves as one of the fastest, most fundamental response mechanisms that guides cellular decisions in combating any environmental changes or physiological stimuli that disrupts cellular homeostasis. In particular, modification of proteins with ubiquitin, a highly conserved, small 76 amino acid protein, through a process known as "ubiquitination" has been implicated in various cellular processes including cell cycle progression, signal transduction, endocytosis, and most prominently, proteolytic degradation.[282, 283] Due its diverse role in several, distinct cellular pathways, protein ubiquitination must be carefully regulated such that the cellular machinery can easily differentiate between a ubiquitinated protein that is marked for signal transduction versus one that is tagged for elimination.[284]

Protein ubiquitination is governed by the ubiquitin-proteasome system (UPS), which is the main cellular pathway responsible for modulating protein degradation with strict spatial and temporal control.[282, 283, 285] The ubiquitin-proteasome system has remained an central area of interest in biological research, and its discovery was awarded the 2004 Nobel Prize in chemistry to scientists Avram Hershko, Aaron Ciechanover, and Irwin Rose.[285] Protein degradation is initiated through covalent conjugation of ubiquitin onto the substrate protein via a stepwise enzymatic cascade involving ubiquitin activation, conjugation, and ligation (Figure 3-1). First, the catalytic cysteine of an E1 activating enzyme catalyzes thioester formation with the C-terminal glycine of ubiquitin through an ATP-dependent acyl substitution reaction, forming the activated E1-ubiquitin intermediate. Next, the activated ubiquitin undergoes a transthiolation reaction

resulting in transfer of the activated ubiquitin from the E1 to the E2 conjugating enzyme. Then, the active ubiquitin-E2 complex is recognized by an E3 ubiquitin ligase which facilitates transfer of the ubiquitin from the E2 onto the substrate protein. E3 ubiquitin ligases are divided into three separate families and are classified by the mechanism of which they facilitate ubiquitin transfer.[286, 287] The RING E3 ubiquitin ligases primarily serve as scaffolding proteins which bring E2 enzymes in close proximity to the substrate protein, and ubiquitin is transferred directly from the E2 enzyme onto the substrate protein. In contrast, the HECT family of E3 ubiquitin ligases, ubiquitin is transferred from the E2 enzyme onto the catalytic cysteine of the HECT E3 ligases, forming a thioester intermediate, prior to ligation on the substrate protein. The third, and smallest, class of E3 ligases, the Ring-Between-Ring (RBR) family, facilitate ubiquitin transfer via a hybrid mechanism, combining characteristics of both RING and HECT E3 ligases. RBR E3 ligases engage the ubiqutin-E2 complex but subsequently forms an E3-ubiquitin intermediate prior to modification of the substrate protein.[288]

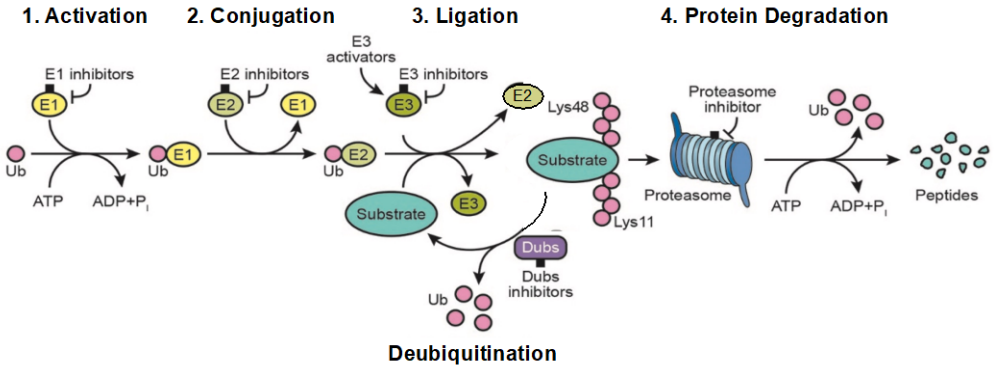

Figure 3-1: Schematic of protein ubiquitination and proteasomal degradation
Figure was adapted from Huang *et. al.*, *Cell Research*, **2016**, 26, 484.[289]

The conjugation of a single ubiquitin forms what are referred to as "mono-ubiquitinated" proteins, which play key roles in chromatin regulation, protein sorting, and protein trafficking.[284]

However, the addition of multiple ubiquitin moieties ("poly-ubiquitination") can occur either through (a) the direct transfer of an oligomeric ubiquitin chain from pre-constructed on the E2 or E3 enzyme onto the substrate protein or (b) through step-wise addition of ubiquitin onto the mono-ubiquitinated protein forming a growing ubiquitin chain.[290] Ubiquitin contains seven lysine residues (K6, K11, K27, K29, K33, K48, and K63) and the branching and topology of the linked chain is indicative of the biological outcome.[291-293] While the molecular mechanisms that dictate lysine selection and ubiquitin chain composition are not completely understood, it is recognized that higher order structural features within the E2 and E3 enzymes significantly contribute to a protein's ubiquitin fate.[294] In some cases, mono- vs polyubiquitination is dictated entirely by the E2 enzyme due to compatibility of the key catalytic residues on the E2 enzyme with proximal lysine residues on the substrate protein. By coordinating with the same substrate protein-loaded E3 complex, one E2 may induce mono-ubiquitination, while a separate E2 enzyme may continue sequential ubiquitination of the growing chain.[294-296] Alternatively, some E2/E3 pairs may regulate initial mono-ubiquitination while another E2/E3 pair is responsible for poly-ubiquitination.[297] However, in other cases the same E2/E3 pair is solely responsible for mono- and poly-ubiquitination of the substrate protein.[294] In the case of protein degradation, polyubiquitination consisting of K11, K48, or K11/K48-mixed branch chains is the primary signal which is recognized and induces proteolytic degradation through the 26S proteasome, while K63-linked chains signal lysosomal degradation pathways.[292, 298]

3.2 Proteolysis Targeting Chimeras (PROTACs)

Proteolysis targeting chimeras, also known as "PROTACs", are a chemical protein knockdown strategy pioneered by Craig Crews (Yale University).[299-305] The PROTAC approach to inducible protein degradation utilizes a heterobifunctional compound which brings a target protein of interest in proximity to an endogenous E3 ubiquitin ligase through recruitment by their respective ligands. This results in the formation of a ternary complex, which facilitates ubiquitin transfer onto the surface lysine residues of the protein of interest (POI), leading to subsequent proteasome-mediated degradation (Figure 3-2). Following target degradation, the PROTAC is left unscathed and can undergo multiple rounds of protein degradation, allowing these agents to act in a catalytic fashion. PROTAC technology has been successfully applied in the degradation of numerous key protein targets in disease states including, but not limited to, cancer, viral infection, immune disorders, and neurodegenerative diseases.[306-312]

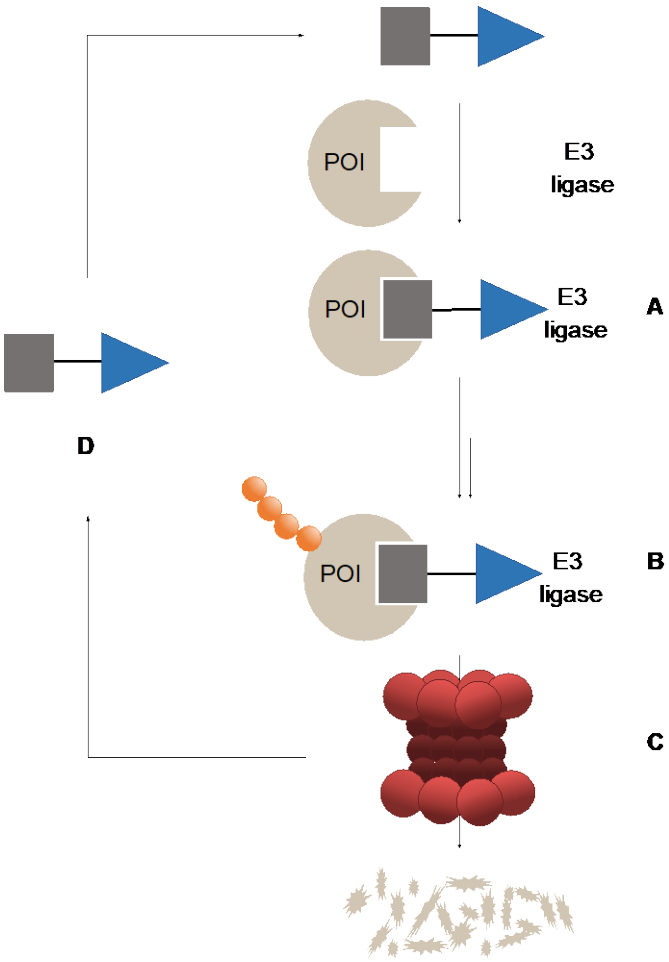

Figure 3-2: Schematic of PROTAC-mediated protein degradation
The heterobifunctional PROTAC recruits the protein of interest (POI) and the E3 ligase bringing them into proximity (A), resulting ubiquitination of the POI (B), and subsequent proteasomal degradation (C). The PROTAC is regenerated and can undergo multiple rounds of protein degradation (D).

Traditionally, therapeutic targeting of proteins has depended on small molecule agonists or inhibitors to modulate of protein function. By taking advantage of deep grooves and ligandable pockets within the protein surface, this "occupancy-driven" model of inhibition relies on high affinity drugs to bind the protein target and elicit a therapeutic effect. Typically, the fraction of the drug bound directly correlates with the affinity to the target and as a result, the therapeutic outcome. However, applications of traditional small molecule pharmacology towards targeting "druggable" proteins has only been accessible to 20% of the proteome.[313] The development of the

PROTAC inducible degradation strategy is currently shifting a paradigm in drug discovery,[314, 315] as compound activity does not rely solely on affinity to its target, but rather the ability to elicit a biological event (i.e., ubiquitination). PROTACs proceed through an "event-driven" model in which the ability of a PROTAC degrader relies on the transient assembly of a productive E3 ligase-PROTAC-POI ternary complex. Further, potent PROTAC-mediated degradation has been observed with ligands that exhibit modest to weak (>10 μM) affinity to the POI, suggesting sufficient ternary complex formation dictates productive ubiquitination and proteasomal degradation.[316-318] Additionally, PROTAC technology has opened doors towards degrading notoriously "difficult-to-drug" proteins including those which lack enzymatic function, such as scaffolding proteins,[319] large multicomponent protein complexes,[320] and more recently, transcription factors.[321, 322]

The first PROTAC was reported 20 years ago targeting the angiogenic methionine aminopeptidase-2 (MetAP-2). The PROTAC design consisted of covalent MetAP-2 inhibitor, ovacilin, tethered to a recruiter phosphodecapeptide for the Skp1-cullin-$F^{\beta TRCP}$ E3 ubiquitin ligase complex.[323] While this report primarily served as a proof-of-concept for inducible protein degradation, the first generation PROTACs suffered from poor cell permeability and low potency requiring extensive optimization to advance as viable chemical tools and potential therapeutics. Efforts to increase cell permeability were successful through the development and discovery of small molecule E3 ubiquitin ligase ligands (Figure 3-3). The utilization of small molecule ligands revolutionized PROTAC technology. The incorporation of small molecule ligands conferred favorable properties to PROTAC compounds such as increased drug-likeness, metabolic stability, and target affinity which led to dramatic improvements in degradation efficiency towards a number of targets including the androgen receptor,[324] BCR-Abl,[325] bromodomain-containing protein 4

(BRD4),[326, 327] MetAP-2,[328] estrogen related receptor α (ERRα),[316] and the aryl hydrocarbon receptor (AHR).[329] Despite that more than 600 E3 ubiquitin ligase proteins exist, ligands recruiting the Von-Hippel Lindau (VHL, **183**) and cereblon (CRBN, **184-186**) E3 ligases are the most utilized in PROTAC technologies.[330-333]

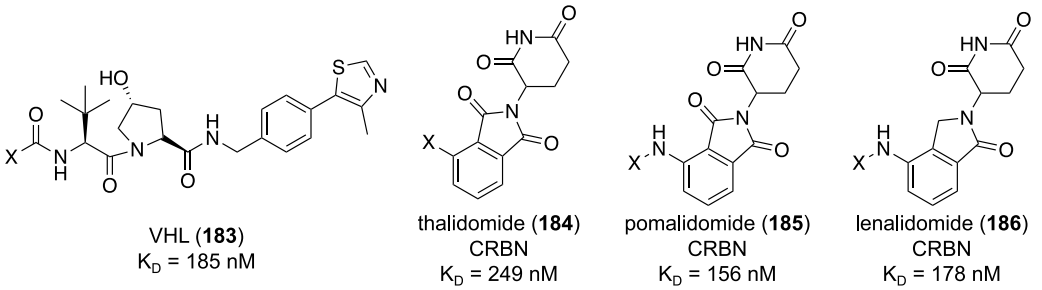

Figure 3-3: Structures of commonly used E3 ubiquitin ligase ligands in PROTAC technology
Structures of E3 ubiquitin ligase ligands (**183-186**) and their affinities towards their respective E3 ligase protein targets. X indicates point of attachment to the PROTAC molecule.

In just the past three years, the PROTAC field has practically exploded, with the number of reports nearly doubling over the course of 2019 into 2020 (Figure 3-4A). The PROTAC field is has picked up a lot of momentum recently with major advances in degrading novel protein targets and the creation of a PROTAC-tracking database (PROTAC-DB) which lists more than 1600 publicly disclosed PROTAC degraders that act on more than 100 protein targets.[334, 335] One exciting avenue for PROTACs has been translation of the degrader compounds into the clinic. In the start of building a PROTAC degrading empire, Crews' founded Arvinas (New Haven, CT) in 2013 and currently has two degraders ARV-110 (**187**) and ARV-471 (**188**) (Figure 3-4B) undergoing phase II and phase I clinical trials, respectively. ARV-110 targets the androgen receptor and has demonstrated 70-90% degradation in patients, while maintaining shown satisfactory safety and tolerability in phase I trials. It is currently being evaluated with in a molecularly-defined patient population in phase II clinical trials (NCT03888612).[336] ARV-471 is

an oral-targeting estrogen receptor (ER) degrader that is currently being assessed as a treatment in patients with locally advanced or metastatic ER positive/HER2 negative breast cancer in phase I clinical trials.[337] In addition to these exciting advances, nearly 15 additional degraders expected to begin clinical evaluation before the end of the year (Table 3-1).[335]

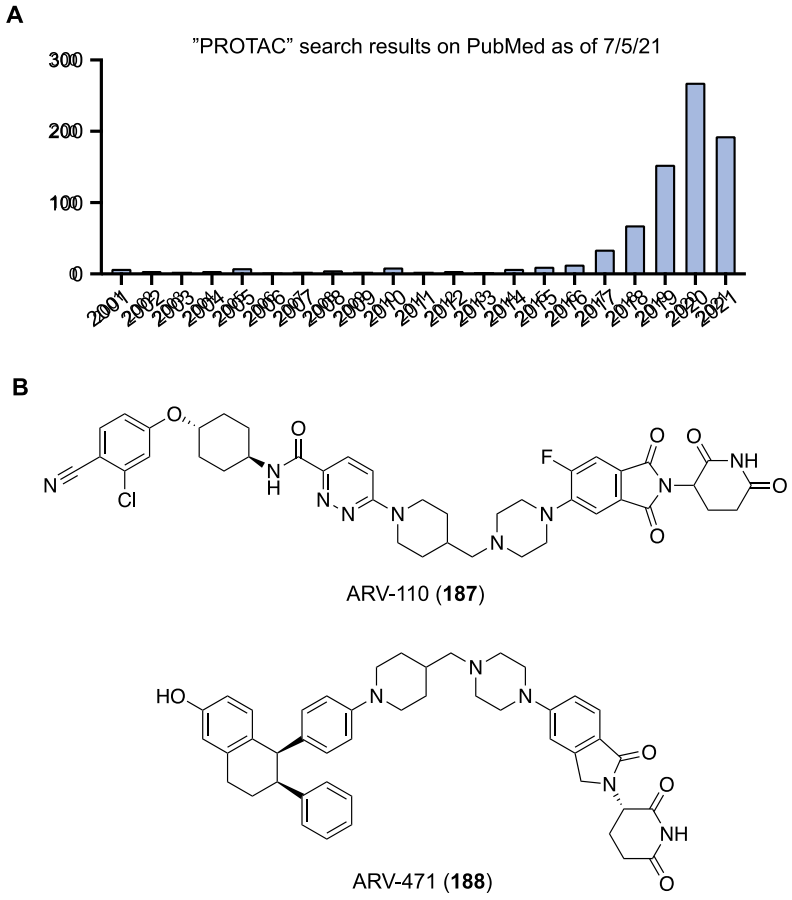

Figure 3-4: Growth of PROTAC field in publications and clinical translation
A) PubMed search results for "PROTACs" as of July 5, 2021. The number of PROTAC-related publications per year has exponentially increased since 2018 and is on track to continue rising in 2021. B) Structures of PROTACs **187** and **188** (reported by Arvinas) currently undergoing evaluation in clinical trials.

The astonishing success of PROTAC technology has opened the door in the creating an entire field devoted to targeted protein degradation technologies. In addition to the start of clinical evaluation of these compounds, numerous research campaigns and commercial development

programs have been implemented in industry settings ranging from biotechnology start-ups, analogous to Crews' Arvinas, to major pharmaceutical companies including Pfizer,[338] AstraZeneca,[339] Boehringer Ingelheim,[340] and GlaxoSmithKline,[341, 342] among others. Advancement of PROTACs themselves is centered around exploring the biophysical characteristics of ternary complex formation using mathematical modeling and computational methods to aid in structure-guided design to expedite successful PROTAC discovery.[339, 343-346] Additionally, efforts to aid in elucidating the structural and mechanistic characteristics to expand the arsenal of available E3 ubiquitin ligase ligands beyond the "old reliable" VHL and CRBN remain a major focus in growing the PROTAC field.[347, 348] Finally, the hijacking of other cellular degradation pathways including the endolysosomal and macroautophagic degradation pathways using lysosome-targeting chimeras (LYTACs)[349-351] and macroautophagic autophagic degradation targeting chimeras (MADTACs),[352-354] respectively, has been successful in degrading extracellular protein targets as well as larger biomolecular structures including organelles. As the PROTAC field continues to flourish, compounds of this type will continue to push the boundaries of what is considered a "druggable protein."[355, 356] Furthermore, applications of this technology to force other enzymatic activity[357] including phosphorylation,[358] dephosphorylation,[359] deubiquitination,[360] nuclease degradation[361] are coming to light and will certainly dramatically transform the current perspective of small molecule modulation of protein function in the years to come.

Table 3-1: Select PROTAC degraders currently undergoing or approaching clinical evaluation
Table adapted from A. Mullard, *Nat. Rev. Drug. Discov.*, **2021**, 20(4), 247.[335]

Drug	Sponsor	Properties	Lead indication	Status
Heterobifunctional degraders				
ARV-110	Arvinas	Androgen receptor degrader	Prostate cancer	Phase II
ARV-471	Arvinas	Oestrogen receptor degrader	Breast cancer	Phase II
ARV-766	Arvinas	Androgen receptor degrader	Prostate cancer	Phase I in 2021
AR-LDD	Bristol Myers Squibb	Androgen receptor degrader	Prostate Cancer	Phase I
DT2216	Dialectic	BCL-XL degrader	Liquid and solid cancers	Phase I
KT-474	Kymera/Sanofi	IRAK4 degrader	Autoimmune disorders	Phase I
KT-413	Kymera	IRAK4 degrader	MYD88-mutant DLBCL	Phase I in 2H2021
KT-333	Kymera	STAT3 degrader	Liquid and solid tumors	Phase I in 2H2021
NX-2127	Nurix	BTK degrader	B cell malignancies	Phase I
NX-5948	Nurix	BTK degrader	B cell malignancies and autoimmune disorders	Phase I in 2H2021
CG001419	Cullgen	TRK degrader	Cancer and other diseases	IND in 2021
CFT8634	C4 Therapeutics	BRD9 degrader	Synovial sarcoma	IND in 2H2021
FHD-609	Foghorn	BRD9 degrader	Synovial Sarcoma	IND in 1H2021

3.3 Optical Control of Targeted Protein Degradation

The material in Section 3.3 was reprinted in part from Naro, Y.; **Darrah, K.**; Deiters A. *J. Am. Chem. Soc.*, **2020**, 142(5), 2193-2197.[362]

While PROTACs have demonstrated robust protein degradation both *in vitro* and *in vivo*, a lack of external control over their function remains a limitation to their application as both chemical tools and therapeutics. Potential toxicity from systemic degradation of proteins in healthy cells, as well as diseased cells, is a critical concern.[363] For example, one study of mice treated with a BRD4 degrader, ARV-771, exhibited noticeable deterioration of skin health, hunching of the spine, lethargy, and decreased mobility as a result of treatment.[364] In addition, undesirable ligase-

mediated off-target effects pose a significant risk and are not yet well understood.[365] Achieving conditional control of PROTAC function may provide the ability to tightly regulate PROTAC activity, leading to an improved therapeutic index, reduced off-target effects, and a highly targetable therapy. To achieve this goal, we sought to develop a broadly applicable approach to controlling PROTAC activity using light (Figure 3-5). Light is an excellent external control element for biological processes, since it acts non-invasively, rapidly, and with spatiotemporal precision.[366] Herein, we report the development of photocaged E3 ligase ligands for both the VHL and CRBN E3 ubiquitin ligases. By utilizing a general photocaging strategy, this approach is applicable to all PROTACs utilizing the VHL or CRBN E3 ligands to induce proteasomal degradation.

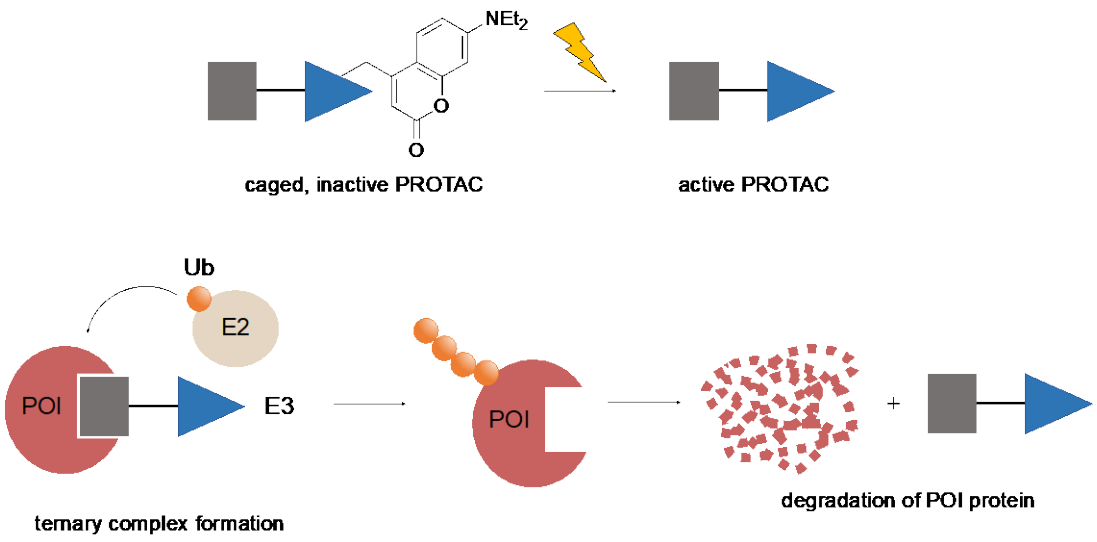

Figure 3-5: Design of optically controlled PROTAC degraders
Placement of a caging group on the E3 ligase ligand (blue triangle) prevents ternary complex formation between the E3 ubiquitin ligase (E3) and the protein of interest (POI). Treatment with light removes the caging group, enabling ternary complex formation, resulting in ubiquitin (Ub, orange circle) transfer and subsequent proteasomal degradation.

3.3.1 Synthesis and Application of a Photocaged VHL Ligand

To develop a caged VHL ligand, we first determined the optimal location for placement of the light-cleavable caging group onto the VHL ligand by analyzing a crystal structure of the protein-ligand complex (PDB: 4W9C). We observed that the hydroxyproline moiety is buried into the binding cleft and is also involved in two hydrogen bond interactions with Ser111 and His115 (Figure 3-6A). This hydrogen bond network has been established as critical for VHL recognition of its endogenous protein target, the oxygen-sensitive hypoxia-inducible factor protein, HIF1-α.[367-369] Furthermore, it has been shown that inversion of the stereochemistry at the hydroxyl group abolishes all PROTAC activity.[316, 370] Taken together, we hypothesized that placement of a bulky caging group on the hydroxyl moiety would render the caged ligand unable to bind VHL until removal of the caging group via light irradiation. To test this hypothesis, we synthesized the VHL-based ERRα PROTAC **189** that targets estrogen related receptor α (ERRα),[316] an orphan nuclear hormone receptor involved in cellular metabolism and with implications in cancer initiation and progression.[371]

As a photolabile caging group, we installed a diethylamino coumarin (DEACM) at the hydroxyl group via a carbonate linkage to yield the caged ERRα PROTAC **190**. The DEACM caging group enables activation by photolysis with ≤405 nm light and release of acidic functional groups with a pK_a below 5.[372] The ERRα PROTAC **189** was synthesized following previous reports.[316] The coumarin caging group was synthesized via allylic oxidation of commercially available 7-diethylamino-4-methyl coumarin (**191**) to generate the corresponding aldehyde. The aldehyde was reduced with sodium borohydride to generate the primary alcohol intermediate **192** which was then activated as a chloroformate using diphosgene. Direct reaction of the activated coumarin **192** with ERRα PROTAC **189** generated the photocaged ERRα PROTAC **190**. Synthesis

of the caged ERRα PROTAC **190** was performed by former lab member Dr. Yuta Naro (Deiters Lab) and the synthetic scheme can be found in Figure 3-6B.

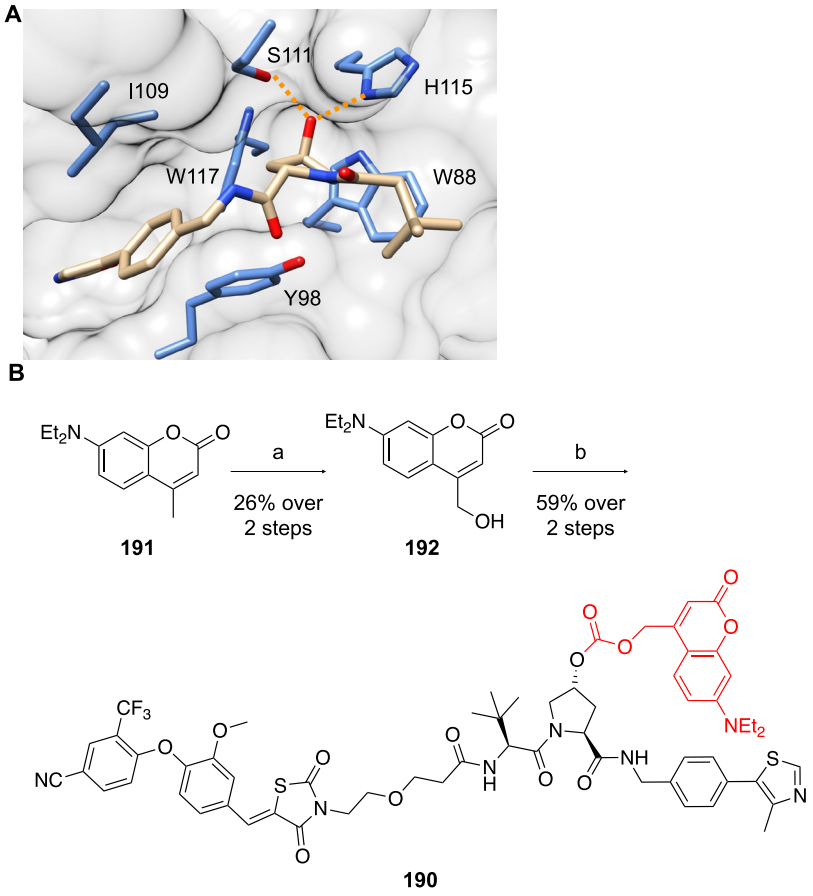

Figure 3-6: Design and synthesis of a photocaged VHL ligand
A) Crystal structure analysis of the VHL ligand bound to the VHL protein (PDB: 4W9C) identifies the hydroxyl group on hydroxyproline as critical for the ligand-protein interaction, evidenced by key hydrogen bond interactions (orange dashed line). B) Synthetic route to caged ERRα PROTAC **190**. Reagents and conditions: a) (i) SeO_2, dioxane, (ii) $NaBH_4$, methanol, 26% over 2 steps; b) disphosgene, DIPEA, DCM, (ii) **189**, DIPEA, DMAP, DCM. ERRα PROTAC **189** and caged ERRα PROTAC **190** were synthesized by former lab member Dr. Yuta Naro.

With caged ERRα PROTAC **190** in hand, we performed a UV exposure time course and monitored PROTAC decaging by HPLC (Figure 3-7). Starting material and products were confirmed by mass spectrometry. Upon increasing exposure to UV light, nearly full conversion of caged ERRα PROTAC **190** to the native, non-caged ERRα PROTAC **189** was observed following just 3 minutes of UV irradiation. Furthermore, the release of the coumarin caging group fragment

was detected and confirmed by LCMS indicating the decaging reaction occurs via the anticipated pathway. These results indicate rapid and efficient decaging of the VHL ligand.

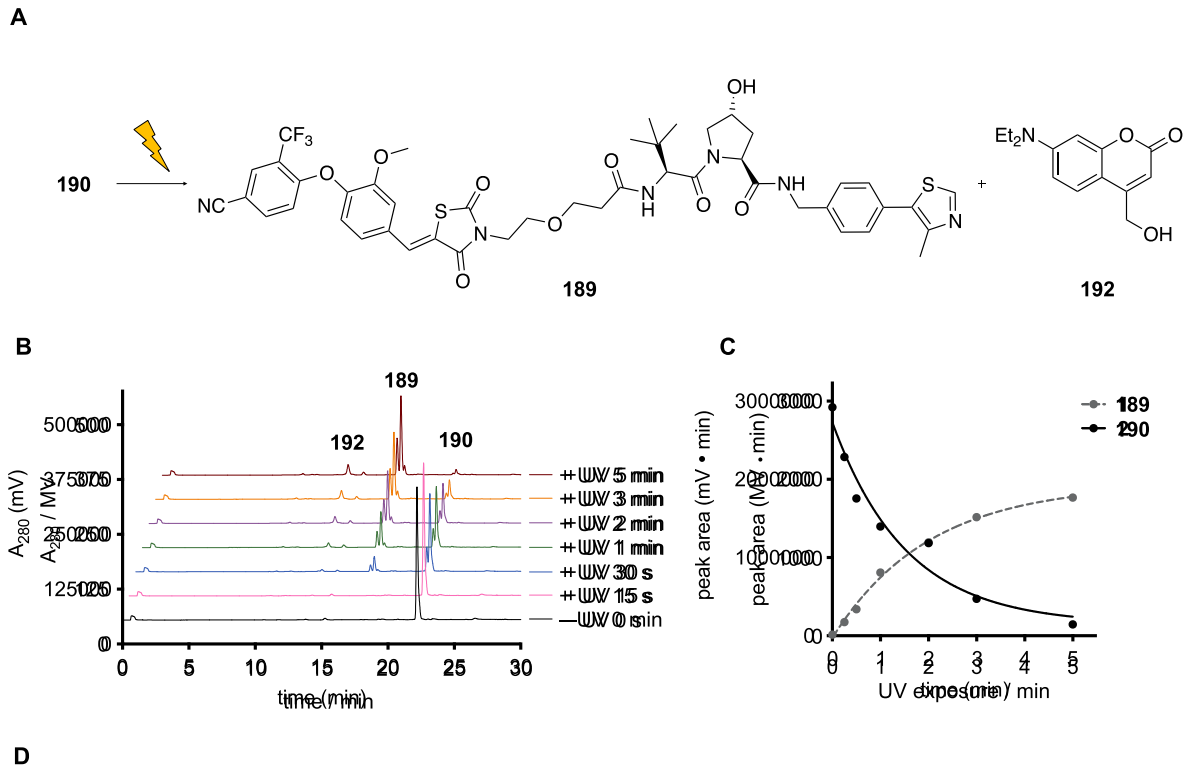

compound	chemical formula	expected mass (Da)	observed mass (Da)
189	$C_{46}H_{47}F_3N_6O_9S_2$	948.28	949.40 $[M+H]^+$
190	$C_{61}H_{62}F_3N_7O_{13}S_2$	1221.38	1222.90 $[M+H]^+$
192	$C_{15}H_{19}NO_3$	261.14	262.05 $[M+H]^+$

Figure 3-7: Photolysis of DEACM-caged ERRα PROTAC 190
A) Reaction scheme of the photolysis of DEACM-caged ERRα PROTAC **190** to form active ERRα PROTAC **189** and the released coumarin caging group fragment **192**. B) HPLC chromatograms of DEACM-caged ERRα PROTAC **190** decaging upon irradiation with UV light. Release of the caging group fragment **192** is also detected.C) In the presence of UV light, there is conversion of **190** to the active ERRα PROTAC **189**. D) Peaks indicating compounds **189**, **190**, and **192** were collected and analyzed by ESI-MS.

To test the ability of the DEACM caging group to block ERRα degradation, MCF-7 cells were treated with DMSO, **189**, or **190** followed by presence or absence of UV irradiation (365 nm, 180 s) (Figure 3-8). After an 8 h incubation, ERRα levels were determined via western blot. As expected, treatment with PROTAC **189** resulted in a significant reduction in ERRα protein relative to DMSO control, matching literature reported results.[316] Gratifyingly, treatment with the

DEACM-caged ERRα PROTAC **190** at twice the concentration of **189** led to no reductions in ERRα protein levels in the absence of UV light. This confirms that the caged compound is completely inactive with regard to E3 ligase recruitment, and that the incorporation of the caging group allows for increased dosing concentrations without any observed activity. In contrast, cells treated with **190** and subjected to UV irradiation exhibited comparable reductions in ERRα protein to that of cells treated with **189**, demonstrating triggering of degradation activity following photolysis of the DEACM caging group.

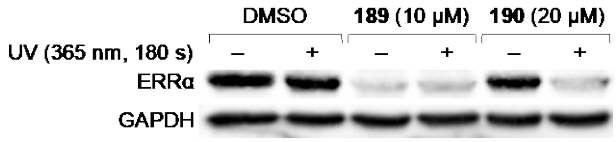

Figure 3-8: Photocontrol of ERRα degradation with 190
Western blot analysis of ERRα protein levels from MCF-7 cells treated with DMSO, **189**, or **190** and either kept in the dark (–UV) or irradiated with UV light (+UV). Western blot performed by former lab member Dr. Yuta Naro.

To confirm that the ERRα degradation observed by the decaged PROTAC (**190** + UV) is the result of E3 ligase-mediated ubiquitination and proteasomal degradation, MCF-7 cells were pre-treated with inhibitors and degradation in these pre-incubated cells was evaluated. To validate E3 ligase mediated ubiquitination, MCF-7 cells were pre-treated with MLN4924. VHL is a type of cullin-RING E3 ligase, which must first be neddylated in order to be active. MLN4924 inhibits the neddylation-activating enzyme, thereby preventing cullin-RING E3 ligase activity.[373] Following pre-treatment with MLN4924 (3 μM), degradation by both the non-caged ERRα PROTAC **189** and decaged ERRα PROTAC (**190** + UV) was inhibited, suggesting the degradation that is observed relies on cullin-RING E3 ligase activity (Figure 3-9A). To validate that the degradation observed is a result of proteasomal activity, MCF-7 cells were pre-treated with reported proteasome inhibitor MG132 (10 μM). Gratifyingly, degradation activity of both the non-caged ERRα PROTAC **189** and decaged ERRα PROTAC **190** was blocked, thereby validating that

degradation proceeds via a proteasome-dependent mechanism (Figure 3-9B). Furthermore, MCF-7 cells treated with the coumarin caging group fragment that is released upon photolysis **192** exhibited no effects on ERRα levels, demonstrating that the observed degradation is entirely mediated by the active PROTAC that is generated via decaging (Figure 3-9C).

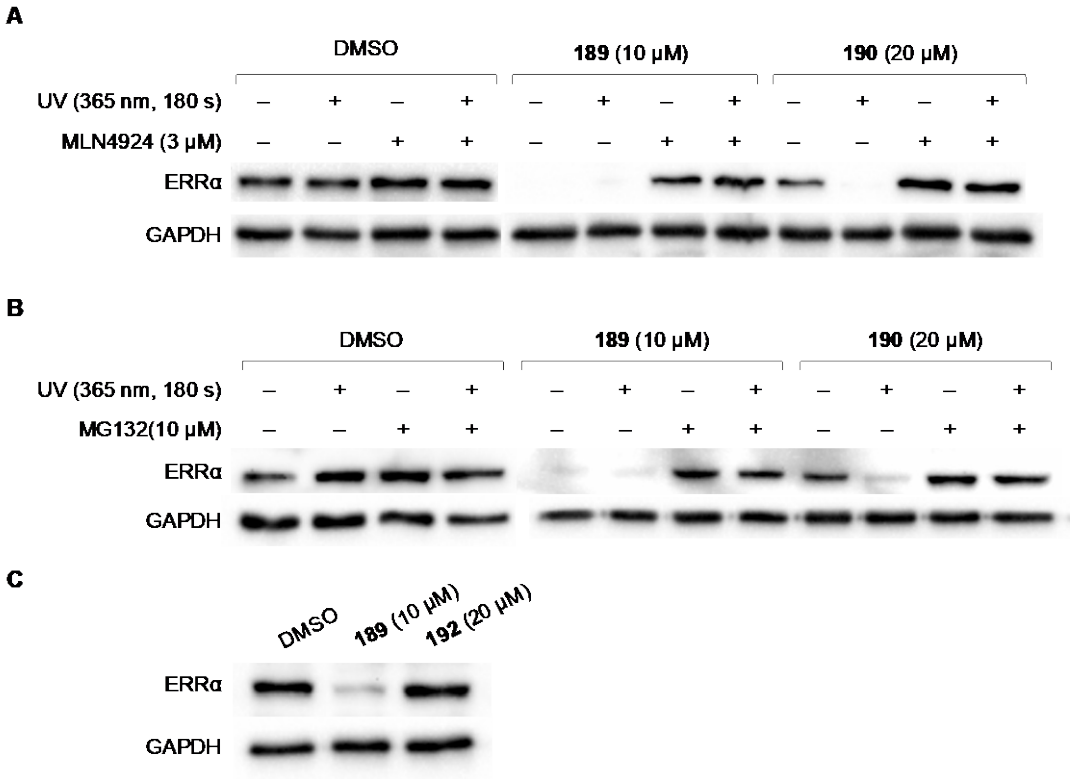

Figure 3-9: Degradation mechanism of ERRα PROTACs
A) Degradation by ERRα PROTACs **189** and **190** is rescued when cells are pre-treated with the neddylation inhibitor MLN4924, validating degradation by PROTACs is dependent on cullin RING E3 ligase activity. B) In the presence of the proteasome inhibitor MG132, degradation of ERRα by the PROTACs is inhibited, suggesting the observed degradation is mediated by the proteasomal machinery. C) Western blot analysis of ERRα protein levels in MCF-7 cells following treatment with coumarin caging group fragment **192**.

In MCF-7 cells, ERRα acts as an antagonist to estrogen receptor α (ERα) by directly competing for binding to their shared consensus palindromic DNA response element (ERRE/ERE).[374] Structural studies have identified that ERRα is constitutively active and is not regulated by traditional estrogen receptor ligands,[375] but rather is regulated by protein co-regulators.[376] While the caged ERRα PROTAC **190** is capable of binding ERRα, binding alone is

not capable of abolishing ERRα-mediated repression. Transcriptional repression by ERRα has been shown to be alleviated through siRNA knockdown.[377] Taking advantage of this mechanism, degradation of ERRα with PROTAC technology would be capable of activating ERα-mediated transcription in MCF-7 cells (Figure 3-10A). To this end, a luciferase reporter containing the ERRE/ERE response element placed upstream of a firefly luciferase gene was transfected into MCF-7 cells, followed by treatment with DMSO, **189**, or **190** in the presence or absence of UV light treatment. Cells treated with **189** demonstrated a 10-fold increase in luciferase signal, indicative of a loss in ERRα-mediated repression following degradation of ERRα (Figure 3-10B). Treatment with the caged ERRα PROTAC **190** at concentrations 5-fold higher than **189** showed no significant increase in luciferase signal in the absence of light, supporting that ERRα ligand binding alone is incapable of inhibiting ERRα repression. However, following treatment with light (405 nm, 30 s), we observed rescue in luciferase expression to levels similar to that observed following treatment with **189**. Experiment was performed by former lab member Dr. Yuta Naro. Taken together, these results demonstrate the ability to control VHL-based PROTAC-mediated protein degradation in cells using both 365 nm and 405 nm light.

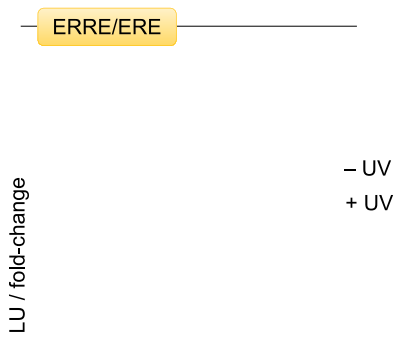

Figure 3-10: Evaluation of the functional implications of conditionally controlled ERRα degradation
A) ERRα represses luciferase expression by occupying the shared ERRE/ERE consensus sequence preventing ERα transactivation. Upon treatment with UV light, the caging group is removed resulting in degradation of ERRα and activation of luciferase expression by ERα. B) MCF-7 cells transfected with 3xERRE/ERE-luc reporter were treated with DMSO, **189**, or **190**, and either kept in the dark or irradiated with UV light. Relative luciferase units (RLU) represent firefly luciferase signal normalized to Renilla luciferase control signal. Data represents the means ± standard deviations from at least three independent experiments. Statistical significance was determined using an unpaired t test; *P< 0.05, **P < 0.001. Data was generated by former lab member Dr. Yuta Naro.

3.3.2 Synthesis and Application of a Photocaged CRBN Ligand

With the goal of expanding this technology to encompass CRBN-based PROTACs as well, we next turned our attention to developing a photocaged CRBN ligand. Crystal structure analysis of the thalidomide-CRBN protein complex depicts the imide moiety on the glutarimide ring to be buried into the hydrophobic binding pocket and involved in a hydrogen bond interaction with the peptide backbone of His380 (Figure 3-11). We again speculated that installation of a caging group would disrupt a crucial hydrogen-bonding network in addition to introducing a significant amount

of steric bulk which could not be accommodated by the binding pocket. This speculation was supported by a previous report which showed that methylation of the imide nitrogen abolished degradation activity of a CRBN-based PROTAC.[378] Thus, we synthesized the known CRBN-based BRD4 PROTAC **193**, which is capable of targeting and degrading bromodomain-containing protein 4 (BRD4).[379] Using chemistry previously established by our lab,[74, 380] we successfully installed a 6-nitropiperonyloxymethyl (NPOM) group onto the glutarimide nitrogen to generate the caged BRD4 PROTAC **194**. The NPOM group was chosen for its stability under aqueous conditions, as the relatively high acidity of imide nitrogens (pK_a = 14) compared to aliphatic amines (pK_a = 30 - 40) has previously proven problematic.[380, 381] The NPOM caging group undergoes efficient photolysis by treatment with 365 nm light and has been employed as a photocaging group in numerous biological applications.[382]

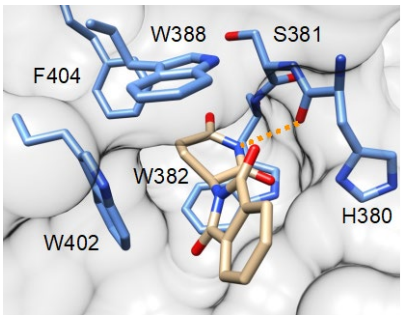

Figure 3-11: Design rationale of a photocaged CRBN ligand
Crystal structure analysis of the CRBN ligand bound to the CRBN E3 ubiquitin ligase (PDB: 4CI1) identifies the imide moiety buried into the hydrophobic binding pocket, while also forming a hydrogen bond interaction with the backbone of His380 (orange dashed line).

The known CRBN-based BRD4 PROTAC was synthesized following the previously reported protocol.[379] The *tert*-butyl ester of the commercially available BRD4 targeting ligand, (+)-JQ1 (**195**) was hydrolyzed with formic acid to form the corresponding carboxylic acid **196**. The CRBN E3 ligase ligand was synthesized via a condensation reaction between commercially

available 3-hydroxyphthalic anhydride (**197**) and 3-aminopiperidine-2,6-dione (**198**) following the literature reported protocol to form thalidomide derivative **199**.[383] Functionalization of the phenolic hydroxyl was achieved through initial reaction with *tert*-butyl chloroacetate followed by ester deprotection with trifluoroacetic acid to form the corresponding carboxylic acid (**200**). The crude carboxylic acid was directly coupled to commercially available Boc-amido-PEG2-amino using 6-chloro-benzotriazole-1-yloxy-tris-pyrrolidinophosphonium hexafluorophosphate (PyClock) to yield the linker functionalized CRBN ligand **201**. Synthesis and installation of the NPOM-caging group onto **201** was performed by former lab member Dr. Yuta Naro following the synthetic route outlined in Figure 3-12. After the caging group was installed, Boc-functionalized **201** was deprotected under acidic conditions to form the free amine which was subsequently coupled to **196** to yield the NPOM-caged BRD4 PROTAC **194**.

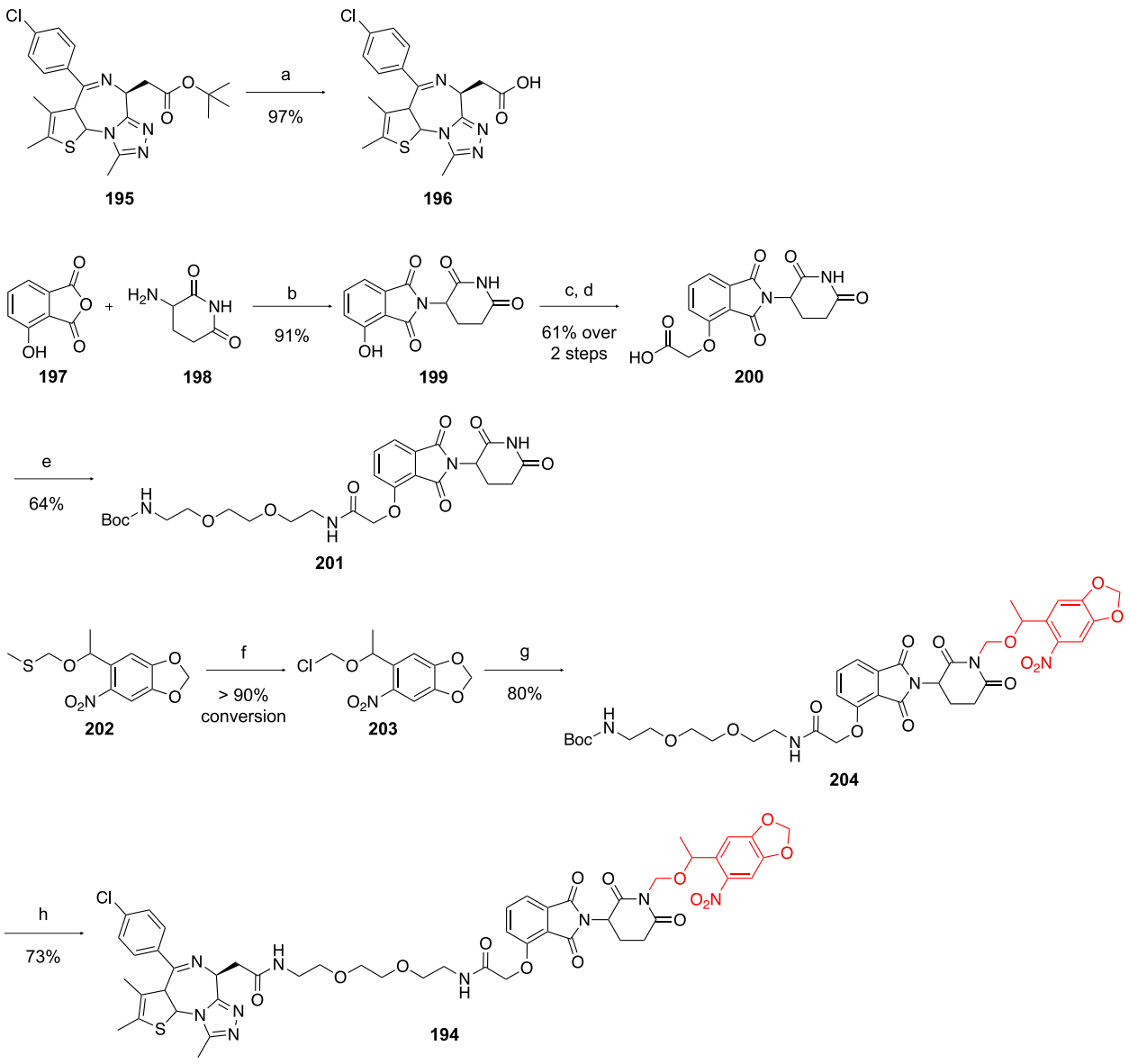

Figure 3-12: Synthesis of caged NPOM-caged BRD4 PROTAC 194
Reagents and conditions: a) formic acid, 97%; b) pyridine, 91%; c) *tert*-butyl chloroacetate, K_2CO_3, DMF; d) 1:1 TFA/DCM, 61% over 2 steps; e) Boc-amido-PEG2-amine, PyClock, DIPEA, DMF, 64%; f) sulfuryl chloride, DMF; g) **201**, DBU, DMF; h) (i) 1:1 TFA/DCM, (ii) **196**, HATU, DIPEA, DCM, 73%.

With photocaged BRD4 PROTAC **194** in hand, we next tested light-activation through a UV exposure time course and monitored product formation by HPLC, followed by confirmation through mass spectrometry (Figure 3-13). We observed clean formation of the non-caged BRD4

PROTAC **193** and the corresponding nitrosoketone caging group product **205** after a 1 minute irradiation, suggesting efficient release of the native CRBN ligand upon photolysis.

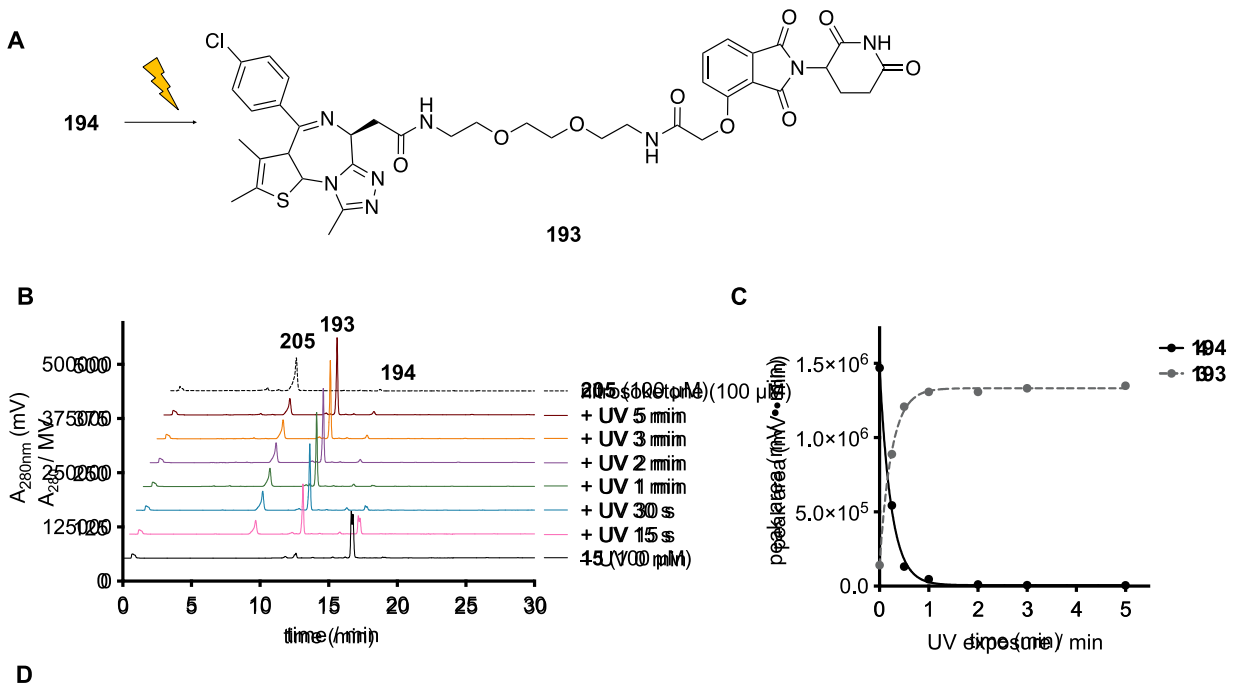

compound	chemical formula	expected mass (Da)	observed mass (Da)
193	$C_{40}H_{43}ClN_8O_9S$	846.26	845.30 $[M+H]^+$
194	$C_{50}H_{52}ClN_9O_{14}S$	1069.30	1070.45 $[M+H]^+$

Figure 3-13: Photolysis of the NPOM-caged BRD4 PROTAC 194
A) Reaction scheme of the photolysis of the NPOM-caged BRD4 PROTAC **194** to form the active BRD4 PROTAC **193** and the release nitrosoketone decaging product **205**. B) HPLC chromatograms of NPOM-caged BRD4 PROTAC **194** decaging. C) Upon UV irradiation, there is clean conversion of **194** to the active, non-caged BRD4 PROTAC **193**. Release of the nitrosoketone caging group fragment **205** formed upon photolysis is also detected. The nitrosoketone was generated independently through photolysis of the corresponding alcohol, confirmed by 1H NMR[384] and LCMS, and used as a standard for HPLC analysis. D) Peaks corresponding to **193** and **194** were collected and analyzed by ESI-MS.

With the caged PROTAC **194** in hand, we tested the ability to optically control CRBN-mediated degradation of BRD4 in cells. Treatment of HEK293T cells with the BRD4 PROTAC **193** resulted in significant degradation of BRD4 within 5 h, as evidenced by western blot. Treatment with caged PROTAC **194** in the absence of light resulted in no degradation of BRD4,

confirming that installation of the NPOM caging is capable of blocking E3 ligase recruitment. However, following irradiation with UV light (365 nm, 180 s), we observed activation of the PROTAC and subsequent degradation of BRD4 by western blot (Figure 3-14).

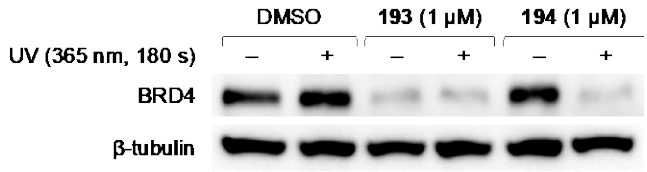

Figure 3-14: Photocontrol of BRD4 degrdation with 194
Western blot analysis of BRD4 protein levels in HEK293T cells treated with DMSO, **193**, or **194** and then either kept in the dark (– UV) or irradiated with UV light (+ UV). Western blot performed by Dr. Yuta Naro.

To confirm that the BRD4 degradation observed by the decaged PROTAC (**194** + UV) is the result of E3 ligase-mediated ubiquitination and proteasomal degradation, HEK293T cells were pre-treated with E3 ligase and proteasome inhibitors and degradation was assessed by western blot. To validate E3 ligase mediated ubiquitination, HEK293T cells were pre-treated with neddylation inhibitor MLN4924 (3 μM). The CRBN E3 ligase is also a cullin RING E3 ligase, and therefore activation by neddylation should be inhibited through MLN4924 treatment. Following inhibitor pre-treatment, degradation by both the non-caged BRD4 PROTAC **193** and decaged BRD4 PROTAC (**194** + UV) was abrogated, suggesting the observed degradation relies on cullin RING E3 ligase activity (Figure 3-15A). To validate that the degradation observed is a result of proteasomal activity, HEK293T cells were pre-treated with MG132 (10 μM) and, gratifyingly, degradation activity of both the non-caged BRD4 PROTAC **193** and decaged BRD4 PROTAC (**194** + UV) was inhibited, thereby validating that degradation proceeds via a proteasome-dependent mechanism (Figure 3-15B). Furthermore, HEK293T cells treated with the nitrosoketone caging group fragment that is released upon photolysis (**205**) exhibited no effects on BRD4 levels,

demonstrating that the observed degradation is entirely mediated by the active, non-caged PROTAC that is generated upon photolysis (Figure 3-15C).

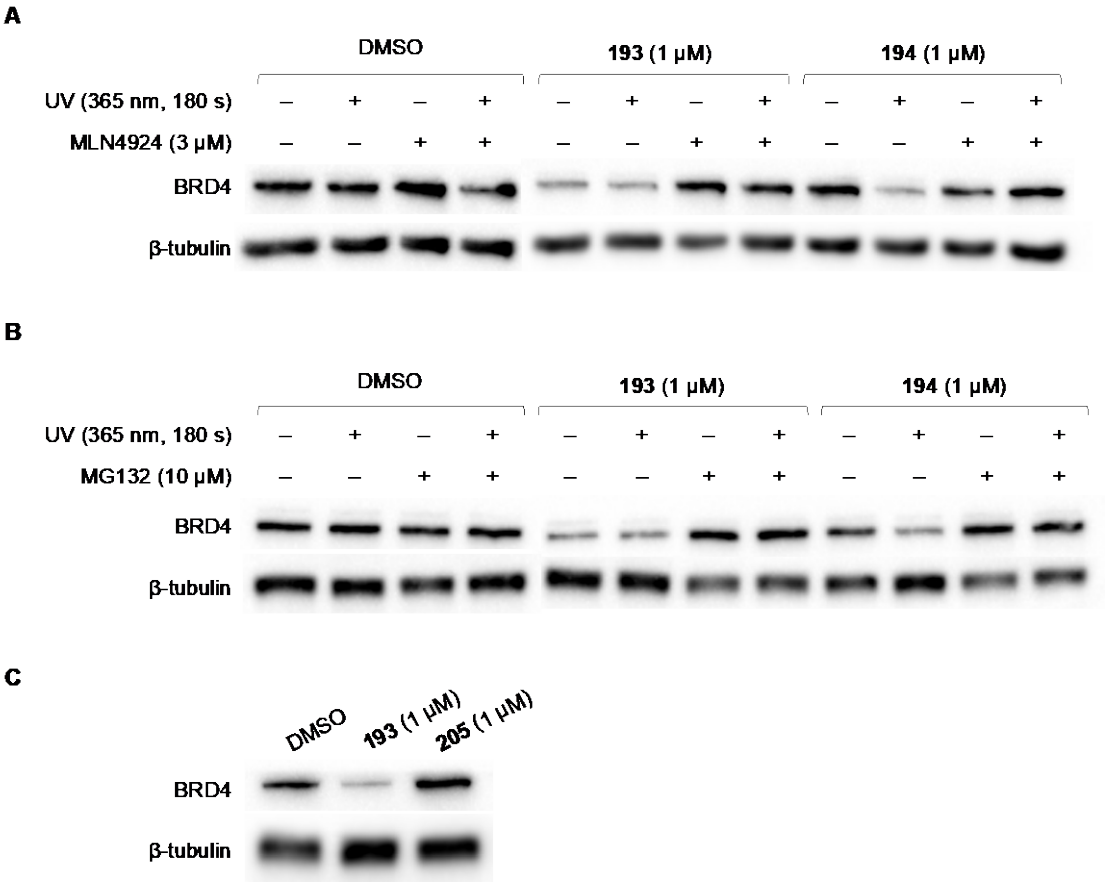

Figure 3-15: Degradation mechanism of BRD4 PROTACs
A) In the presence of MLN4924, degradation of BRD4 is inhibited validating that the observed degradation is dependent on E3 ligase activity. B) Degradationo of BRD4 by PROTACs **193** and **194** is rescued when cells are pre-treated with proteasome inhibitor MG132, validating that BRD4 degradation is mediated by the cellular proteasomal machinery. C) Western blot analysis of BRD4 protein in HEK293T cells following treatment with nitrosoketone caging group fragment **205**. The caging group fragment exhibits no effect on BRD4 protein levels.

Furthermore, we demonstrate temporal control over BRD4 degradation using **194** to optically trigger rapid degradation of a GFP-BRD4 fusion expressed in HEK293T cells (Figure 3-16). Upon treatment with **193**, nearly full degradation of GFP is observed after a 4 hour incubation, regardless of light exposure. In cells treated with NPOM-caged BRD4 PROTAC **194**,

degradation of GFP is observed only after brief UV irradiation (365 nm, 180 s), demonstrating that with our optically controlled degraders we can temporally control induced degradation of the target protein. Together, these results successfully demonstrate the ability to conditionally control protein degradation in cells using a CRBN ligand-based PROTAC reagent.

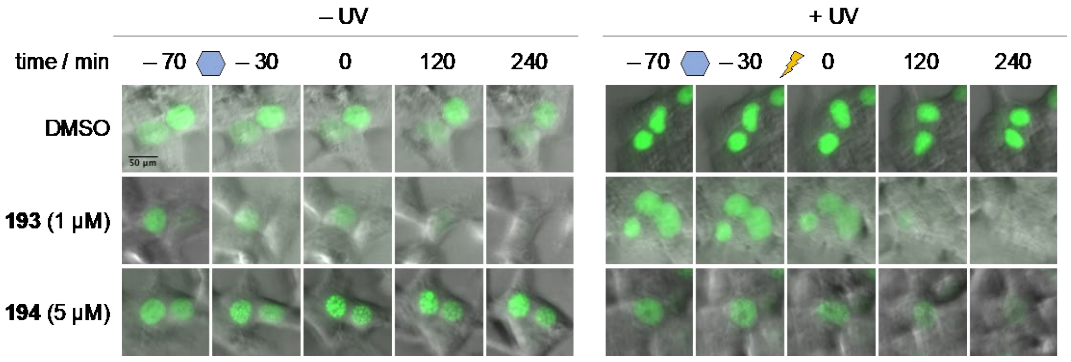

Figure 3-16: Temporally controlled degradation of GFP-BRD4 with 194
HEK293T cells transfected with GFP-BRD4 were incubated with either DMSO, **193**, or **194** for 1 hour. Following incubation, cells were either kept in the dark or irradiated with UV light. GFP levels were monitored via fluorescence imaging over 4 hours post irradiation.

In order to demonstrate optical control of the functional consequences of BRD4 degradation, we next investigated the therapeutic response elicited following photoactivation of PROTACs in a cellular model. It has previously been reported that PROTAC-induced degradation of BRD4 is on the order of 10- to 500-fold more potent at inhibiting cell proliferation than treatment with a traditional BRD4 inhibitor, JQ1, in castration-resistant prostate cancer cell lines.[364] Taking advantage of the marked increase in efficacy observed for BRD4 degradation agents, we treated 22Rv1 cells, a castration-resistant prostate cancer cell line, with **193** and **194** in the presence and absence of light. Treatment with **193** for 72 hours resulted in a 51% reduction in cell viability, while cells treated with caged PROTAC **194** in the absence of light showed no significant reductions in cell viability, demonstrating that BRD4 degradation likely governs the

therapeutic response observed with BRD4 PROTAC **193**. As expected, removal of the caging group through light exposure (365 nm, 180 s) rescued therapeutic efficacy leading to a 39% decrease in cell viability (Figure 3-17A). Data was generated by former lab member Dr. Yuta Naro. To confirm the mechanism of cell death, we also monitored caspase-3/7 activation as an indicator of apoptosis. Treatment of 22Rv1 cells with **193** resulted in a nearly 3-fold increase in caspase-3/7 activity, while treatment with the caged PROTAC **194** in the absence of light had no significant effect. Further, no increase in caspase activity was observed following treatment with BRD4 inhibitor, (+)-JQ1 (**195)**, suggesting inhibition is not sufficient to elicit the therapeutic response. Following irradiation with UV light, caspase-3/7 activity was rescued to levels similar to that observed with PROTAC **193** (Figure 3-17B). Taken together, these results demonstrate that optical control of PROTAC activity is a feasible approach to controlling the therapeutic effects of PROTACs.

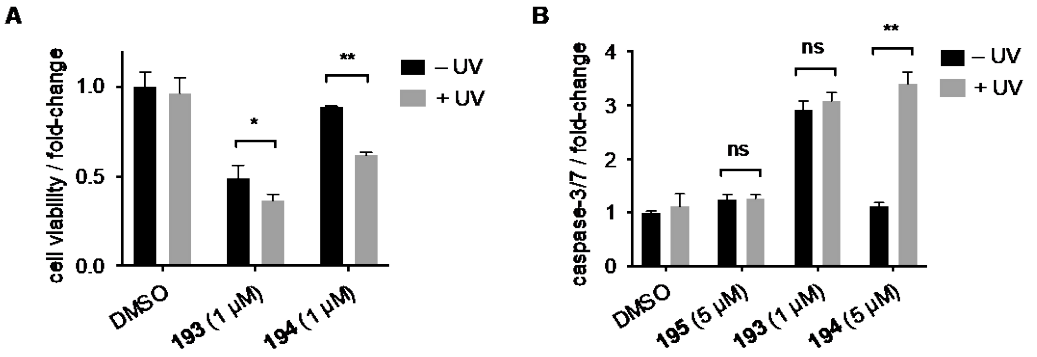

Figure 3-17: Optical control of the therapeutic effects of BRD4 degradation
A) 22Rv1 cells were treated with DMSO, **193**, or **194** in the presence (+ UV) or absence (– UV) of UV light. Cells were incubated 72 hours before determining cell viability using a CellTiterGlo assay. Treatment was normalized to the DMSO control. Data in panel A was generated by former lab member, Dr. Yuta Naro. B) 22Rv1 cells were treated with DMSO, BRD4 ligand **195**, **193**, or **194** in the presence of absence of UV light. Cells were incubated for 24 hours before determining caspase-3/7 activity using a CaspaseGlos-3/7 assay. Statistical significance was determined using an unpaird t test; ns $P>0.05$, *$P<0.05$, **$P<0.001$.

3.3.3 Summary

In summary, we have successfully developed two approaches to optically control PROTAC function through the strategic installation of photocaging groups onto E3 ligase ligands recruiting VHL and CRBN. Introduction of the caging groups completely abolishes the degradation activity of the PROTACs until treatment with light unmasks the E3 ubiquitin ligase ligands returning them to their native states. We demonstrated robust photoactivation of protein degradation in cells and showed that photocontrol of degradation can also function as an effective approach to conditionally control the therapeutic response to treatment. These approaches afford enhanced control over biological processes and has far reaching implications for the development of highly targeted therapies based on precision drug activity profiles. Continued efforts are being made to improve the spectral properties of these reagents with the hopes of shifting absorption into the near IR region for enhanced tissue penetration.

The desire to advance PROTACs by equipping them with external control elements for their advancement as chemical biology tools and potential precision therapeutics has been acknowledged in the optical control field.[385-387] During the preparation of our manuscript and immediately follow publication, several other optical control strategies were reported. In addition to our E3 ligand photocaging strategy with the NPOM and DEACM photocaging groups, the 4,5-dimethoxy-2-nitrobenzyl (DMNB) photocaging group has also been utilized for photocontrolling PROTAC-mediated degradation. Xue and colleagues installed the DMNB-caging group within the CRBN E3 ligase and also the targeting ligand (JQ1) to generate two photocontrolled PROTACs targeting BRD4.[388] Additionally, the Gray Lab (Dana Farber Cancer Institute) and the Tate Lab (Imperial College London) also utilized the DMNB caging group for caging of CRBN- and VHL E3 ubiquitin ligase ligands in PROTACs degrading BRD2 and BRD4 proteins.[389, 390] A second

popular optical control strategy included the incorporation of azobenzene photoswitches within the linker region of the PROTAC-molecule. Although linker composition is a critical design consideration in PROTAC development, successful degradation of BCR-Abl, BRD2, and FKBP12 has been demonstrated with azobenzene-modified PROTACs.[391-393] Furthermore, using their "PHOTAC" strategy, the Trauner lab (NYU) demonstrated reversible OFF to ON to OFF control over BRD2 degradation in cells. The ability to regulate degradation with spatiotemporal resolution will be a key advantage as PROTACs continue to advance and are evaluated in the clinic.

3.3.4 Materials and Methods

3.3.4.1 Synthetic Methods

General chemical methods. All reagents were purchased from commercial suppliers and used without further purification. Flash chromatography was performed using an ISCO CombiFlash RF with normal-phase silica gel cartridges. NMR spectra were recorded on Bruker spectrometers. Analytical LCMS data were collected on a Shimadzu LCMS-2020 and a ThermoScientific Q-Exactive Orbitrap. The purity of final compounds was determined to be > 95% by HPLC analysis on a Shimadzu LC-20AD monitored at 280 nm.

Synthesis of ERRα PROTACs 189 and 190. Synthesis of non-caged ERRα PROTAC **189** and DEACM-caged ERRα PROTAC **190** was conducted by Dr. Yuta Naro following previously published procedures and the analytical data matched literature reports.[316, 394]

Synthesis of BRD4 PROTACs 193 and 194. Synthesis of non-caged BRD4 PROTAC **193** and NPOM-caged BRD4 PROTAC **194** was conducted by Dr. Yuta Naro following previously published procedures and the analytical data matched literature reports.[379, 380, 395]

3.3.4.2 Biological Protocols

Cell culture. Experiments performed using MCF-7 (ATCC) and HEK293T cells (ATCC) were cultured in Dulbecco's Modified Eagle Medium (DMEM, Gibco). Experiments performed using 22Rv1 cells (ATCC) were cultured in Roswell Park Memorial Institute 1640 medium (RPMI-1640, ATCC 30-2001). All media was supplemented with 10% (v/v) Fetal Bovine Serum (FBS, Sigma-Aldrich) and 5% (v/v) penicillin/streptomycin (VWR) and maintained at 37 ºC in a 5% CO2 atmosphere. Cell lines were used within passages 1-35 and all cell lines are tested for mycoplasma contamination (Genlantis MY01100) every 3 months.

Western blot. Cells were seeded into a 12-well plate at a density of 150,000 cells/well (1 mL/well). Following overnight incubation, cells were treated with either DMSO (0.1% [v/v]) or compounds (0.1% [v/v]) and incubated for 15 min before treatment with or without light using a UV transilluminator at 365 nm for 180 s. Following additional incubation for designated times (ERRα 8 h, BRD4 5 h), cell lysis and protein extraction was carried out using RIPA lysis buffer (100 µL, 50 mM Tris pH 8.0, 150 mM NaCl, 0.5% [w/v] sodium deoxycholate, 1% [v/v] Triton X-100) supplemented with Halt Protease Inhibitor Cocktail (ThermoFisher). Whole cell lysates were boiled in Laemmli sample buffer and separated by 10% (v/v) SDS-PAGE gel electrophoresis. Following separate, proteins were transferred to a PVDF membrane (GE Healthcare) and the membrane was blocked in blocking buffer (5% BSA in 1X TBS with 0.1% [v/v] Tween 20) for 1 h at room temperature. The blots were probed with primary antibodies rabbit monoclonal antibody anti-ERRα (1:1000 dilution, Cell Signaling 13826S), rabbit monoclonal anti-BRD4 antibody (1:1000 dilution, Cell Signaling 13440S), rabbit monoclonal anti-GAPDH antibody (1:1000, Cell Signaling 2118S), mouse monoclonal anti-β-tubulin antibody (1:1000 dilution, Santa Cruz SC-5274) in blocking buffer (5 mL) at 4 ºC overnight with rocking, followed by secondary antibody

detection using an anti-rabbit IgG HRP-linked antibody (1:2500 dilution, Cell Signaling 7074S) or anti-mouse IgG HRP-linked antibody (1:2500 dilution, Cell Signaling 7076S) in blocking buffer (5 mL) for 1 h at room temperature. Chemiluminescence was developed using SuperSignal West Pico Chemiluminescent Substrate (5 mL, ThermoFisher 34580) and imaged on a ChemiDoc Imaging System (BioRad) using automated exposure settings.

ERRα luciferase reporter assay. MCF-7 cells were seeded into a white, clear-bottom, 96-well plate at a density of 25,000 cells/well (100 µL/well). Following overnight incubation, each well was transfected with 100 ng of 3xERRE/ERE-luc (Addgene #37852)[396] and 5 ng of control Renilla pGL4.74 (Promega) using Lipofectamine 2000 (Invitrogen) in OptiMEM (Gibco) for 3 h. Following incubation, media was removed and replace with fresh DMEM (100 µL) containing DMSO, **189**, or **190** (0.1% DMSO [v/v]). Cells were incubated for 15 min before treatment with or without UV light using a 405 nm LED at 700 mA for 30 s. Cells were incubated an additional 24 h before running a dual-luciferase assay (Promega E1980) to determine both firefly luciferase signal and control Renilla luciferase signal. Firefly luciferase signal was normalized to control Renilla luciferase signal to generate RLU values.

Live cell fluorescence imaging. HEK293T cells were seeded into a polyD-lysine treated 96-well black plate (15,000 cells/well, 100 µL) and incubated for 48 h. Following incubation, cells were transfected with 50 ng GFP-BRD4 (Addgene #65378)[397] with Lipofectamine 2000 following the manufacturer's protocol. After overnight transfection, media was removed and replaced with phenol red-free HyClone Dulbecco's Modified Eagles Medium (90 µL, GE Healthcare). Cells were treated with DMSO (0.1% [v/v]), **193**, or **194** (0.1% [v/v] DMSO). Cells were incubated for 1 h and then exposed to UV light using a UV transilluminator (365 nm, 180 s). Cells were imaged using a Tokai Hit (Inu) on a Zeiss Axio Observer Z1 using the LD-Plan-Neoflaur 20x objective

and a FITC (Chroma filter 49002; Ex. ET 470/40, Em. ET 525/50) filter set. GFP fluorescence was monitored over 4 h following irradiation. Image processing was completed in Slidebook 4.0 software (3i) and ImageJ software (National Institutes of Health).

Cell viability. 22Rv1 cells were seeded into a white, clear-bottom, 384-well plate at a density of 500 cells/well (45 μL/well). Following overnight incubation, wells were treated with DMSO, **193**, or **194** (5 μL/well, 0.1% [v/v] DMSO) and incubated for 15 min before treating with or without UV light using a UV transilluminator (365 nm, 180 s). Cells were incubated an additional 72 h before running a CellTiter-Glo assay (Promega G7572) following the manufacturer's protocol. Cell viability was normalized to the negative control (DMSO).

Caspase-3/7 assay. 22Rv1 cells were seeded into a white, clear-bottom 96-well plate at a density of 15,000 cells/well (90 μL/well). Following overnight incubation, cells were treated with either DMSO,(+)- JQ1 **195**, **193**, or **194** (10 μL/well, 0.1% [v/v] DMSO) and incubated for 15 min before treating with or without UV light using a UV transilluminator (365 nm, 180 s). Cells were incubated an additional 24 h before conducting a Caspase-Glo assay (Promega) to determine caspase-3/7 activation. Caspase-3/7 activation was monitored following the manufacturer's protocol.

Caged PROTAC photolysis. Caged PROTACs **190** or **194** (10 μL of a 5 mM stock solution in DMSO) were added to MeOH (490 μL) to generate a 100 μM solution. An aliquot (120 μL) was transferred into a ½-dram borosilicate glass vial and irradiated on a UV transilluminator (365 nm) for the indicated amount of time. A 25 μL aliquot of each sample was removed and analyzed on a Shimadzu LC-20AD (5-95% acetonitrile, 30 min gradient) using a 1 mL/min flow rate. Samples were monitored at 280 nm on a SPD-20AV UV/Vis detector using a Shimadzu 50 x 4.6 mm C18 column (Lot 140613P).

Proteasome and E3 ligase competition assays. Cells were seeded into a 12-well plate at a density of 150,000 cells/well (1 mL/well). Following 24 hr incubation, where indicated cells were treated with either MG132 (10 μM) or MLN4924 (3 μM). Cells were incubated at 37 ºC for 4 h (MG132) or 3 h (MLN4924) before treatment with DMSO (0.1% [v/v] or compounds (**189** 10 μM, **190** 20 μM, **193** 1 μM, **194** 1 μM). Cells were incubated for 15 min before treatment with or without light using a UV transilluminator at 365 nm for 180 s. Cells were incubated for a designated amount of time (ERRα overnight, BRD4 5 h) prior to cell lysis. Cells were lysed using RIPA lysis buffer (100 μL, 50 mM Tris pH 8.0, 150 mM NaCl, 0.5% [w/v] sodium deoxycholate, 1% [v/v] Triton X-100) supplemented with Halt Protease Inhibitor Cocktail (ThermoFisher 78429). Whole cell lysates were boiled in Laemmli sample buffer and separated by either 10% (v/v) SDS-PAGE (ERRα) or 8% (v/v) SDS-PAGE (BRD4) gel electrophoresis. Following separation, proteins were transferred to a PVDF membrane (MilliporeSigma IPV00010) and the membrane was blocked (5% nonfat milk in 1X TBS with 0.1% [v/v] Tween 20) for 2 h at room temperature. The blots were probed with primary antibodies rabbit monoclonal anti-ERRα antibody (1:1000 dilution, Cell Signaling 13826S), rabbit monoclonal anti-BRD4 antibody (1:1000 dilution, Cell Signaling 13440S), rabbit monoclonal anti-GAPDH monoclonal (1:5000, ProteinTech, 10494-1-AP), rabbit monoclonal anti-β-tubulin antibody (1:2000 dilution, ProteinTech, 10068-1-AP) in blocking buffer (5 mL) at 4 ºC overnight with rocking, followed by secondary antibody detection using an anti-rabbit IgG HRP-linked antibody (1:5000 dilution, ProteinTech, SA00001-2) in 1X TBST (4 mL) for 1 h at room temperature. Chemiluminescence was developed using SuperSignal West Pico Chemiluminescent Substrate (ThermoFisher, 4 mL) and imaged on a ChemiDoc Imaging System (BioRad) using automated exposure settings.

4.0 Expanded Methods

4.1 General Methods – Molecular Biology

4.1.1 Polymerase Chain Reaction (PCR)

PCR reactions were performed using commercial kits available from ThermoScientific. For amplicons < 1500 bp, DreamTaq polymerase (ThermoFisher EP0711) was used, while for amplicons >1500 bp or G/C rich, Phusion polymerase (ThermoFisher F530S) was used. A 10 mM dNTP solution (100 µL) was prepared by mixing 10 µL of each of the four dNTPs (dATP, dTTP, dGTP, and dCTP, 100 mM stocks, ThermoFisher FERR0181) with milliQ water (60 µL). The dNTP solution was stored at –20 ºC for up to 6 months. PCR primers were ordered from Sigma or Integrated DNA Technologies (IDT) and were resuspended in milliQ water to a final concentration of 100 µM. Working solutions of PCR primers (10 µM, 50 µL) were prepared by diluting 5 µL of the 100 µM stock into 45 µL milliQ water. Following dissolution in water, all primers were stored at –20 ºC.

DreamTaq PCR reactions were assembled and cycled on a Bio-Rad T100 Thermal Cycler according to the recipe and cycling conditions outlined in Table 4-1 below.

Table 4-1: DreamTaq PCR recipe and thermal cycling conditions

Reagent	Volume	Step	Temp.	Time
10X DreamTaq Green Buffer	5 µL	Initial Denaturation	95 ºC	1 min
dNTPs (10 mM)	2 µL	Denaturation	95 ºC	30 sec
Forward Primer (10 µM)	2.5 µL	Annealing	T_m – 5 ºC	30 sec
Reverse Primer (10 µM)	2.5 µL	Extension	72 ºC	1 min/kb
DNA Template (50-100 ng)	0.3 -1 µL	Repeat steps 2-4 34 times		
DreamTaq polymerase	0.5 µL	Final Extension	72 ºC	5 min
milliQ water to 50 µL		Cool to 12 ºC, hold at 25 ºC		

Phusion PCR reactions were assembled and cycled on a Bio-Rad T100 Thermal Cycler according to the recipe and cycling conditions outlined in Table 4-2 below.

Table 4-2: Phusion PCR recipe and thermal cycling conditions

Reagent	Volume	Step	Temp.	Time
5X Phusion HF buffer	10 µL	Initial Denaturation	98 ºC	30 sec
dNTPs (10 mM)	1 µL	Denaturation	98 ºC	10 sec
Forward Primer (10 µM)	2.5 µL	Annealing	T_m – 5 ºC	30 sec
Reverse Primer (10 µM)	2.5 µL	Extension	72 ºC	30 sec/kb
DNA Template (50-100 ng)	0.3 -1 µL	Repeat steps 2-4 34 times		
Phusion polymerase	0.5 µL	Final Extension	72 ºC	10 min
milliQ water to 50 µL		Cool to 12 ºC, hold at 25 ºC		

Reactions were scaled based on application. After completion of the PCR reactions, samples were diluted with a homemade purple loading dye (500 µL 30% glycerol in milliQ water + 250 µL 6X purple loading dye (NEB B7024S)) to a final concentration of 5% glycerol. DreamTaq PCR reactions were used as is because the 10X Green buffer contains a proprietary loading dye mixture. The entire PCR reaction (50-100 µL) was loaded alongside TriDye 1kb DNA ladder (7 µL, NEB N3272S) onto a 0.8% agarose gel (320 mg agarose dissolved in 40 mL 1X Tris/Borate/EDTA (TBE) buffer, and a drop of ethidium bromide solution (10 mg/mL)) and electrophoresed at 80 V for 40 minutes. The gel band containing the desired amplicon was excised from the gel and purified using the E.Z.N.A. Gel Extraction Kit (OmegaBioTek D2500-02, pre-

March 2020) or GeneJET Gel Extraction Kit (ThermoScientific K0692, post-March 2020) following the manufacturer's protocol.

4.1.2 Restriction Enzyme Digest

All restriction enzymes used herein were purchased from New England Biolabs. Restriction digests were set up to a final volume of 50 µL. For backbone digestions, the DNA template (5-8 µg) was mixed with 5 µL of 10X CutSmart buffer (provided with the purchased restriction enzymes) and 1 µL of the respective restriction enzymes. For linearization of plasmids to be transcribed via *in vitro* transcription (see Section 4.1.9), 5 µg DNA was digested. MilliQ water was added to a final volume of 50 µL. Reactions were incubated at 37 ºC for a total of 4 hours. For backbones that were digested and eventually used for restriction enzyme cloning (ligation reactions), reactions were incubated for 1 hour and then Antarctic Phosphatase (AP, 1 µL, NEB M0289S) and Antarctic phosphatase buffer (AP buffer, 5.6 µL) were added to the digest reaction mixture. Following addition of AP and AP buffer, the digest reaction was placed back in the 37 ºC incubator and was incubated at 37 ºC for an additional 3 hours before heat inactivation of the enzyme at the temperature specified by the manufacturer for the utilized enzyme. In the case where the two restriction enzymes were not compatible in the same buffer, sequential digests were performed as outlined above using the compatible buffer. Following completion of the first digest, the sample was electrophoresed on a 0.8% agarose gel (stained with ethidium bromide) and the band was purified via gel extraction. Then, the second digest was performed following the protocol specified above, electrophoresed, and purified by gel extraction.

For digests of inserts generated by PCR, the purified PCR amplicon (44 µL, typically within 100-250 ng/µL) was mixed with 10X CutSmart buffer (5 µL) and restriction enzyme (0.5

μL). The digest reaction was incubated at 37 ºC for 3-4 hours. The enzyme(s) was then heat inactivated, and samples were diluted with a homemade purple DNA loading dye (10 μL, final concentration of ~ 5% glycerol). The entire sample (60 μL) was loaded onto a 0.8% [w/v] agarose gel (prepped in TBE buffer, stained with ethidium bromide) electrophoresed at 80 V for 40 minutes. The desired gel band was purified by gel extraction as outlined in Section 4.1.1.

4.1.3 Plasmid Assembly - Ligation

For assembly of plasmids by enzymatic ligation, T4 DNA ligase (NEB M0203S) was utilized. Backbone DNA vectors were generated as described in Section 4.1.2 and the corresponding inserts were most often attained through PCR amplification of the gene of interest (Section 4.1.1) using primers designed to contain the restriction cut sites of interest, followed by restriction enzyme digestion (Section 4.1.2) and purification by gel extraction. Ligation reactions were always assembled to a final volume of 10 μL using a 3:1 molar ratio of insert:backbone. The amounts were calculated such that the total DNA (backbone and insert) accounted for 8.5 μL (100 ng backbone was always used). A negative control ligation was assembled identically to the experimental ligation reaction but replacing the volume of insert DNA with milliQ water. To the 8.5 μL DNA, 10X T4 DNA Ligase buffer (1 μL NEB, supplied with the purchased enzyme) and T4 DNA ligase (0.5 μL) were added. Ligation reactions were incubated in the thermal cycler at 16 ºC overnight. Following ligation, samples (5 μL) were transformed into Top10 competent cells (Section 4.1.7) and incubated at 37 ºC overnight. If a colony ratio of at least 3:1 experimental:negative control plate was observed, then a minimum of three colonies were selected and grown up in liquid culture overnight at 37 ºC, and then mini-prepped for Sanger sequencing (Genewiz).

If the ratio was lower, 15-30 colonies were screened for successful ligation through a PCR screen as specified in Section 4.1.5. If hits were identified in the PCR screen, then the corresponding colonies were grown up in liquid culture, mini-prepped, and submitted for Sanger sequencing (Genewiz).

4.1.4 Plasmid Assembly – Gibson Isothermal Assembly

The backbone used for Gibson assembly[181] was either prepared by PCR amplification (Section 4.1.1) or restriction enzyme digest (Section 4.1.2). Inserts for Gibson assembly were prepared through PCR amplification in order to introduce overlaps on the termini that were complementary to the desired backbone and/or other DNA fragment. Gibson reactions were assembled using 50-100 ng backbone in a molar ratio of 3:1 insert(s):backbone. Gibson reactions were always prepared on ice to final volume of 20 µL. Pre-prepared Gibson Isothermal master mix (10U/µL T5 Exonuclease (NEB M0363S), 2U/µL Phusion polymerase (ThermoScientific F530L), 40U/µL Taq DNA ligase (Applied Biomedical Materials E090) in 1X Isothermal Gibson Assembly Buffer) was provided as a gift from fellow lab member Amy Ryan. An aliquot of the Gibson master mix (15 µL, stored at –20 ºC) was mixed with DNA solutions (5 µL) in a PCR tube. If the total volume of DNA solutions exceeded 5 µL, the reaction was scaled down accordingly. The assembly reaction was incubated on the thermal cycler or a heat block at 50 ºC for 1 hour. Following Gibson assembly, an aliquot of the reaction (5 µL) was removed and transformed in to Top10 competent cells (Section 4.1.7) and incubated at 37 ºC overnight. If colonies grew, at least 5 colonies were selected and grown up in liquid culture overnight, purified by mini-prep, and submitted for Sanger sequencing (Genewiz).

4.1.5 PCR Screen

If transformation of a ligation reaction (more likely) or Gibson assembly (less likely) resulted in more than 15 colonies on the agarose plate, a PCR screen was typically conducted in order to identify hits. On average, 15-27 colonies were screened (including a negative control colony from the negative control ligation plate) and on average ~ 15-20% were identified as successful clones using a PCR screen.

Selected colonies were circled and assigned numbers on the agarose plate. Colonies were gently dabbed with a P2 pipette tip (ensuring that only a small portion of the colony was lifted from the plate) and the tip was placed into a PCR tube labeled with the colony number and loaded with 10 µL of milliQ water. A P2 pipette was loaded with the "colony-dabbed" tip and the small portion of the colony was rinsed off of the tip into the water in the PCR tube through vigorous pipetting up and down (~ 10 times). Once all colonies to be screened were resuspended, the PCR tubes were incubated at 95 ºC for 10 minutes. While samples were heated, a PCR master mix was prepared on ice (see Table 4-3), calculated for 15 colonies), scaled linearly according to the number of colonies that were being screened (calculated volume of master mix such that ~ 12-14 µL master mix was prepared per colony screened). The primers used for the PCR screen varied with the backbone and gene of interest. As a general guideline, one primer should anneal to the backbone and another should anneal to the insert that was either ligated or Gibson assembled into said backbone.

Table 4-3: PCR screen master mix and thermal cycling conditions

Reagent	Volume	Step	Temp.	Time
10X DreamTaq Green buffer	15 µL	Initial Denaturation	95 ºC	1 min
dNTPs (10 mM)	6 µL	Denaturation	95 ºC	30 sec
Forward Primer (10 µM)	7.5 µL	Annealing	T_m – 5 ºC	30 sec
Reverse Primer (10 µM)	7.5 µL	Extension	72 ºC	30 sec/kb
DreamTaq polymerase	1.5 µL	Repeat steps 2-4 for 34 cycles		
milliQ water	111 µL	Final Extension	72 ºC	5 min
		Cool to 12 ºC, hold at 25 ºC		

Once master mix was prepared, a PCR rack was loaded with the same number of tubes as colonies that were being screened and the entire rack was placed on ice. Following heating, the samples were removed from the heat block and cooled on ice. An aliquot of the PCR master mix (9 µL) was mixed with the boiled colony DNA (1 µL) on ice in the PCR tube labeled with the corresponding colony number. The assembled PCR reactions were then transferred to the thermal cycler and the PCR reaction was run according to the cycling conditions specified in Table 4-3. After the PCR was completed, the entire volume of the PCR reaction was loaded alongside the TriDye 1kb DNA ladder (7 µL, NEB N3272S) in a 0.8% [w/v] agarose gel (prepped in TBE buffer with a drop of ethidium bromide (10 mg/mL), solidified with a 15-well comb) and electrophoresed at 80 V for 40 minutes. The gel was imaged using the autoexposure settings on the pre-set ethidium bromide channel on the BioRad ChemiDoc XRS Imager and checked for the appearance of amplicons of the desired size (indicating successful cloning). If successful, the rest of the colony was inoculated into a liquid culture (LB media plus antibiotic) and grown up overnight, mini-prepped, and submitted for Sanger sequencing (Genewiz).

4.1.6 Calcium Competent Cell Preparation (for Cloning)

Top10 cells were used for cloning. All competent cell preparation was performed following the protocol outlined by the Krantz lab (U.C. Berkeley) with few modifications (specified below).[398]

Day 1. Top10 cells from a frozen glycerol stock were streaked onto a 10 cm LB agarose plate (no antibiotics) in the presence of a flame to ensure a sterile working environment. The streak plate can be used to select a colony for up to 7 days, after which it should be discarded. To ensure that the competent cells have not acquired antibiotic resistance, the stock can be streaked on to an LB plate(s) supplemented with antibiotic (Table 2-4). If the cells grow in the presence of the antibiotic, this indicates that they have acquired antibiotic resistance and should be discarded.

Day 2. Use a sterile, syringe filter to filter solutions of: a) 100 mM $CaCl_2$ (50 mL), b) 100 mM $MgCl_2$ (50 mL), c) 85 mM $CaCl_2$ (10 mL in 15% glycerol, prepped by mixing 8.5 mL of 100 mM $CaCl_2$ with 1.5 mL of glycerol). Store all sterile filtered solutions overnight at 4 ºC. A starter culture of the Top10 cells was prepared by selecting one colony from the streak plate and inoculating it into 10 mL of LB media (no antibiotics). The starter culture was grown in a 37 ºC shaker (250 rpm) overnight.

Day 3. Use the starter culture (500 µL) to inoculate LB media (50 mL) in an autoclaved, 250 mL Erlenmeyer flask under a flame to ensure a sterile environment. The culture was grown in the 37 ºC shaker (250 rpm) and the OD_{600} was monitored every hour. Once the OD_{600} reaches above 0.2, the OD_{600} was checked every 15 minutes until the OD_{600} reached 0.35-0.4. Once the OD_{600} reached 0.35-0.4, the flask was immediately placed on ice. The flask was chilled on ice for 30 minutes and swirled every 10 minutes to ensure even cooling. Concurrently, a 50 mL conical

was also chilled on ice. *Note:* it is imperative that the OD_{600} does not exceed 0.4. The OD_{600} should be checked frequently once it reaches ~ 0.2 as the cells will grow exponentially.

It is very important to keep the cells and all of the reagents and materials (tubes, pipette tips, etc.) cold for the remainder of the competent cell preparation. The liquid culture was gently poured into the pre-chilled 50 mL conical tube. The cells were pelleted through centrifugation at 3000 x g for 15 minutes at 4 ºC. The supernatant was decanted, and the pellet was resuspended in ice-cold $CaCl_2$ (10 mL, 100 mM) using a wide-orifice pipette tip. The suspended cells were kept on ice for at least 20 minutes (up to 40 minutes is fine as well). During this incubation, a rack of 1.7 mL Eppendorf tubes and the P200 pipette tips were placed in the – 80 ºC freezer to chill. The cells were re-pelleted by centrifugation at 2000 x g for 15 minutes at 4 ºC. The supernatant was decanted and the cell pellet was resuspended in ice cold $CaCl_2$ (5 mL of 85 mM $CaCl_2$ in 15% [v/v] glycerol) using a wide-orifice pipette tip.

The pre-chilled 1.7 mL Eppendorf tubes and the P200 pipette tips were removed from the –80 ºC freezer. The resuspended cell pellet was aliquoted (50 µL) into the sterile, pre-chilled microcentrifuge tubes and snap-frozen in a dry-ice or in a liquid nitrogen bath. Once frozen, the competent cells were transferred to a labeled freezer box and stored in the –80 ºC freezer.

The competency of the cells was evaluated by transforming 10 µg of pUC19 vector (obtained from former lab member, Dr. Taylor Courtney) into the newly prepared cells and then plating 50 µL of the transformation on a 10 cm LB agarose plate. The plate was incubated overnight at 37 ºC. The next morning, the plate was removed from the incubator and the number of colonies that grew were counted. The competency can be calculated using the following formula: competency = colony count * 500 µL / (plating volume, µL, in this case 50) / µg DNA

transformed (in this case 10). Per the protocol, competent cells should give a minimum of 1 x 10^6 transformants per µg of plamid DNA, however, competencies that are ~ 10^5 are also suitable.

4.1.7 Bacterial Transformation of Calcium Competent Cells

Frozen, competent cell stocks were removed from the freezer and thawed on ice for 15-20 minutes. The plasmid DNA (10-100 ng) or the cloning reaction mixture (5 µL ligation or Gibson assembly reaction) was pipetted into the tube of cells. The DNA was mixed with cells by gently stirring with the pipette tip (do not pipette up and down). The cells were incubated with the DNA mixture on ice for 30 minutes. The tubes were then heat shocked at 42 ºC in a water bath for 45 seconds. The tubes were immediately placed on ice, and then autoclaved SOC broth (250 µL, TekNova) was added to the cells. The tubes were placed into a foam microcentrifuge tube holder and placed in the 37 ºC shaker (250 rpm) and incubated for 45-60 minutes. For propagation of plasmid DNA, a 50 µL aliquot of the cell suspension was plated on a 10 cm LB agar plate supplemented with the correct antibiotic (see Table 4-4 for concentration). For cloning reactions, the entire 300 µL transformation reaction was split between two separate LB agarose plates supplemented with the correct antibiotic (150 µL cells plated per 10 cm plate). The cell suspension was spread throughout the plate using a flame-sterilized metal cell spreader and a turn table. Once sufficiently spread out, the plates were left to dry (with the lids open) next to the flame for ~ 5 minutes. The lids were then placed on the plates, and the plates were stored upside down in the 37 ºC incubator overnight.

The LB agar plate(s) were prepared by melting a 400 mL bottle of autoclaved LB agar in the microwave. The LB agar was microwaved for 45 seconds at a time. The lid on the LB agarose bottle should be unscrewed prior to microwaving to avoid pressure build up in the closed system

(i.e., the closed bottle) and avoid a potential explosion. The LB agar was microwaved until the amount of agar required for plating was accessible. Once melted, the tip of the bottle and the lid were flamed to ensure sterilization. The melted agarose (12 mL) was transferred out of the bottle and into a 15 mL conical tube using a sterile, plastic 10 mL pipette. The melted agarose was cooled until it could comfortably be touched against the skin on the forearm, at which point it was then supplemented with the appropriate volume of the desired antibiotic (Table 4-4). The tube was capped, inverted to mix, and the entire volume of the melted agarose (12 mL) was poured into a 10 cm petri dish. The plate(s) were allowed to solidify next to the Bunsen burner flame. Once solidified the plate(s) were labeled with my initials, the date, and the antibiotic. Once solidified, the plate(s) were stored upside-down in the 37 ºC incubator until plating.

Table 4-4: Antibiotic stocks and dilutions

Antibiotic	Stock concentration	Working concentration	Diluent
Kanamycin	50 mg/mL (1000X)	50 µg/mL	milliQ water
Ampicillin	100 mg/mL (1000X)	100 µg/mL	milliQ water
Tetracycline	5 mg/mL	25 µg/mL	70% ethanol
Chloramphenicol	34 mg/mL	25 µg/mL	milliQ water
Spectinomycin	50 mg/mL (1000X)	50 µg/mL	milliQ water

4.1.8 Plasmid Isolation

As mentioned previously, hit colonies from cloning reactions (see Sections 4.1.3, 4.1.4) or from plasmid propagation were inoculated into 6 mL LB media supplemented with the specific antibiotic and grown up overnight at 37 ºC in the shaker (250 rpm). The next morning, the cultures were pelleted by centrifugation at 7000 rpm at 4 ºC for 10 minutes. If a glycerol stock was needed, an aliquot of the culture (500 µL) was removed and mixed with 50% glycerol (500 µL) prior to

centrifugation. The glycerol stock was stored at –80 ºC. Following centrifugation, the supernatant was decanted. Plasmid samples were purified following the manufacturer's protocol using either the E.Z.N.A. Plasmid Mini Kit I Q-spin (Omega Bio-Tek, pre-March 2020) or GeneJet Plasmid Miniprep Kit (ThermoScientific K0503, post-March 2020). The elution steps were performed with 30-50 µL of nuclease-free water (pre-heated to 65 ºC in a heat block). Plasmid concentrations (ng/µL) were determined using the pre-set DNA program a NanoDrop ND-1000 spectrophotometer. Typically, 50 – 700 ng/µL solutions were obtained.

4.1.9 *In vitro* Transcription and Purification of Synthetic mRNAs

For the expression of proteins in zebrafish embryos, the coding sequence of the gene of interest was sub-cloned into the pCS2+ backbone and the corresponding synthetic mRNA was prepared using the mMessage mMachine SP6 *in vitro* transcription kit (ThermoScientific AM1340). First, the plasmid was linearized with NotI-HF (NEB, 0.5 µL) at 37 ºC following the standard restriction enzyme digestion protocol outlined in Section 4.1.2. Following digest, the linearized construct was electrophoresed on a 0.8% agarose gel (stained with ethidium bromide, 80 V, 40 minutes) and then purified by gel extraction. The linearized plasmid (1 µg) was *in vitro* transcribed using the mMessage mMachine SP6 *in vitro* transcription kit (ThermoScientific AM1340) following the manufacturer's protocol. The transcription reaction was incubated at 37 ºC for 4-5 hours. At the end of the incubation, the template DNA was degraded following the addition of TURBO DNAse (1 µL, provided with the mMessage mMachine *in vitro* transcription kit). The reaction was incubated at 37 ºC with TURBO DNAse for an additional 15 minutes. The transcription reaction was removed from the incubator and diluted to 50 µL with water. An equal volume of phenol:chloroform:isoamyl alcohol (PCIA, Sigma P1944) was added directly to the

reaction mixture and vortexed to mix. The reaction eventually settled into two layers and the PCIA layer was removed by careful pipetting. Then, a volume equal to 1/10th of the total reaction volume of 3 M sodium acetate pH 5.2 buffer (5 µL) was added to the reaction mixture, which was vortexed to mix and then immediately placed on ice. Ice cold 100% ethanol equal to 3-5x the reaction volume (150 – 250 µL) was added to the transcription reaction and was either incubated at –20 ºC overnight or –80 ºC for a few hours to precipitate the synthetic mRNA. After incubation, the mRNA solution was centrifuged at max speed at 4 ºC for 10 minutes to pellet the mRNA. The supernatant was removed by careful pipetting and the resulting white pellet was rinsed with ice cold 70% ethanol (150 – 250 µL). The tube was centrifuged again at max speed at 4 ºC for 10 minutes and the ethanol was removed by careful pipetting. The pellet was dried leaving the lid of the microcentrifuge tube open while incubating on ice for 5 minutes and then was resuspended in nuclease-free water. The concentration of the mRNA was determined on the NanoDrop ND-1000 spectrophotometer using the pre-set RNA program. The mRNA stock was diluted to a working concentration of ~ 1000 ng/µL and stored as 3 µL aliquots at –20 ºC. For long term storage (> 6 months), mRNA stocks should be kept at –80 ºC.

4.1.10 Agarose Gel Electrophoresis

All DNA samples (PCR, restriction digests, etc.) were resolved on a 0.8% [w/v] agarose gel. Agarose (320 mg, Fisher BP160-500) was weighed into a 125 mL Erlenmeyer flask. The agarose was suspended in 40 mL of 1X Tris/Borate/EDTA (TBE) buffer. TBE buffered is prepared by diluting 100 mL of a 10X TBE stock into 900 mL of milliQ water. 10X TBE was prepared by dissolving Tris base (121 g), boric acid (61.8 g) and ethylenediaminetetraacetic acid disodium salt (7.4 g) in 1 L of milliQ water. Once suspended, the agarose and TBE suspension was microwaved

for 30 seconds and then swirled. The agarose was microwaved again for 15 seconds, swirled, and then if necessary, another 10 seconds. Once fully dissolved, the flask was cooled under cold, running water from the faucet. Once cooled, ethidium bromide (2-5 µL of a 10 mg/mL solution in water) was pipetted into the warm, agarose solution and swirled to mix. The agarose mixture was poured into the 7 x 7 cm cassette mold, and the comb containing the desired number of wells (depending on application), was added. Bubbles introduced from pouring the agarose mixture into the gel cassette were removed using a P10 pipette tip. The gel was allowed to solidify at room temperature for ~ 30 minutes, at which point the comb was carefully removed so as to maintain the integrity of the wells. The 2-well comb can hold ~ 120 µL, the 8-well comb can hold ~ 50 µL, and the 15 well comb can hold ~ 25 µL in each well. Alongside loaded samples, TriDye 1kb DNA ladder (7 µL, NEB N3272S) was loaded onto each side of the gel. The samples were electrophoresed at 80 V for 40 minutes. Once complete, the gels were imaged on a BioRad ChemiDoc XRS imager, and bands were visualized on a UV transilluminator (365 nm) for gel excision.

4.1.11 SDS-PAGE Preparation and Gel Electrophoresis

SDS-PAGE gels were prepared in house following the recipe specified in Table 4-5 (recipe specified for a single gel, can be scaled linearly for preparation of multiple gels at once) in a 50 mL conical tube. A solution of 40% acrylamide (19:1) was purchased from Fisher (BP1406-1). Tetramethylenediamine (TEMED) was purchased from ACROS Organics (CAS 110-18-9, AC138450500). The remaining solutions were prepared as common-use lab solutions by fellow lab members. Tris buffer for the preparation of the resolving gels (1.5 M Tris pH 8.8) was prepared by dissolving Tris-base (91 g) in 450 mL of milliQ water. The pH was adjusted to pH 8.8 with

65% aqueous hydrochloric acid and monitoring using the benchtop Mettler Toledo FiveEasy pH meter. Once at the desired pH, the buffer was filled to volume (500 mL) with milliQ water. Tris buffer for the preparation of the stacking gel was prepared by identically as specified above, except that the pH was adjusted to 6.8 (as opposed to pH 8.8). Solutions containing 10%[w/v] sodium dodecyl sulfate (SDS) and 10% ammonium persulfate (APS) were prepared by dissolving the corresponding solid (5 g) in milliQ water (50 mL). The 10% [w/v] SDS solution can be stored at room temperature, while the 10% [w/v] APS should be stored at 4 ºC. The percent acrylamide was determined based on the molecular weight of the desired protein of interest. For most applications, a 10% SDS-PAGE gel provided sufficient resolution.

Table 4-5: SDS-PAGE and stacking gel recipe

Resolving gel				Stacking gel	
	8% gel	10% gel	12% gel		4%
water	7.95 mL	7.2 mL	6.45 mL	water	4.4 mL
40% acrylamide	3 mL	3.75 mL	4.5 mL	40% acrylamide	750 µL
1.5M Tris pH 8.8	3.75 mL	3.75 mL	3.75 mL	1.5 M Tris pH 6.8	750 µL
10% SDS	150 µL	150 µL	150 µL	10% SDS	60 µL
10% APS	150 µL	150 µL	150 µL	10% APS	60 µL
TEMED	9 µL	9 µL	9 µL	TEMED	6 µL

Once combined, the gel solution was briefly vortexed to mix and poured between the faceplate and back-plate of a 1.5 mm thick gel cassette using the BioRad Mini-PROTAN Tetra Cell system. To ensure that the top of the gel was flat, ~ 2.5 mL of a saturated butanol solution (35-40 mL butanol mixed with 10-15 mL milliQ water, pipetted from the top layer) was pipetted on top of the resolving gel in the cassette. The resolving gel was left to polymerize at room temperature for ~ 30-40 minutes. Once solidified, the butanol was poured off and the top of the gel was rinsed thoroughly with water. The stacking gel solution was then poured on top of the

resolving gel to fill the gel cassette. The appropriate comb (10-well or 15-well, 1.5 mm thick) was added to the cassette, and the stacking gel was left to polymerize at room temperature for 20 minutes. *Note:* gels were usually prepared as needed. However, SDS-PAGE gels can be stored in the faceplates, wrapped in wet paper towels at 4 ºC overnight with no negative effects observed. Once fully solidified the gel cassette was removed and rinse with deionized water.

Using the Mini-PROTEAN Tetra Electrode assembly, the gel and a buffer dam (for running one gel) or both gels were loaded into the gel chamber and placed in the gel tank. Fresh SDS running buffer was prepared by diluting 100 mL from a 10X stock of SDS running buffer (30 g Tris base, 144 g glycine, 10 g sodium dodecyl sulfate dissolved in 1 L milliQ water) into 900 mL milliQ water. The fresh SDS running buffer was used to fill the chamber between the gel(s) and buffer dam (when only one gel was being run), and the rest of the gel tank was filled with previously used SDS running buffer. An ice pack was placed in the gel tank in order to counter act the residual heat from the current, which can disrupt protein electrophoresis. The samples were loaded into the respective wells by pipetting with a P10 pipette tip. Pre-stained protein ladder (7 µL, ThermoScientific 26617) was loaded into the first well and the well after the final sample. The gel was run at 60 V for 15-20 minutes for samples to first run through the stacking gel, and then run through the resolving gel at 150 V for 90 minutes, or until the dye front was run off the bottom of the gel.

Once the gel was complete, it was typically used for analysis of protein levels by western blot (Section 4.2.5). In some cases, the gels were stained overnight with Coomassie stain (1 g of Brilliant Blue G-250 dissolved in 100 mL of glacial acetic acid, 200 mL of methanol, and 700 mL of milliQ water) and then destained using the destaining buffer (100 mL of glacial acetic acid, 200 mL of methanol, 700 mL of milliQ water) the next day. The gels were imaged using the

autoexposure settings and the appropriate pre-set imaging program on the BioRad ChemiDoc XRS Imager.

4.1.12 Native PAGE Preparation and Gel Electrophoresis

Native PAGE gels were prepared in house following the recipe outlined in Table 4-6. For most applications, a 15% PAGE gel sufficed, but the percentage can be adjusted based on the application. Accordingly, if more than one gel was needed, then the recipe was scaled linearly. Once mixed together, the gel was vortexed to mix and poured between the face-plate and back-plate of a 1.5 mm thick gel cassette using the BioRad Mini-PROTAN Tetra Cell system. Native PAGE gels were prepared as needed, but could be prepared the day before and stored, wrapped in wet paper towels, at 4 ºC overnight if needed. Once poured, the desired comb of interest (10-well or 15-well, 1.5 mm) was placed into the cassette and the gel was left to solidify at room temperature for ~ 30-40 minutes. Once the gel was solidified, the gel running apparatus was set up using the Mini PROTEAN Tetra Electrode assembly. Fresh TBE buffer was poured between the gel(s) and/or buffer dam (used when only one gel was being run) and the rest of the tank was filled with used TBE buffer. The samples were loaded into the respective well using a P20 pipette and the gel was run at 150 V for 75 minutes. Once complete, DNA gels were stained with SYBR Gold Nucleic Acid Stain (Invitrogen S11494, 1:10,000 in TBE, 50 mL) at room temperature for 15-20 minutes. Then, the gels were destained in TBE for 5 minutes before imaging on the BioRad ChemiDoc XRS Imager using the autoexposure settings on the SYBR Gold channel.

Table 4-6: Native PAGE gel recipe

Reagent	Volume
10X TBE buffer	1 mL
40% acrylamide	3.8 mL
milliQ water	4.2 mL
10% APS	100 µL
TEMED	10 µL

4.2 General Methods – Cell Biology

4.2.1 Mammalian Cell Culture

All mammalian cell lines were grown and maintained at 37 ºC in a 5% CO_2 humidified atmosphere. Mammalian cell lines were kept in tissue culture-treated 10 cm plates (Corning 353003) with 10 mL of media. HEK293T (CRL-11268) and HeLa (CCL-2) cell lines were obtained from ATCC and grown in Dulbecco's Modified Eagle Medium high glucose with 4.5 mM L-glutamine (DMEM, GE Life Sciences, SH30003.03) supplemented with 10% fetal bovine serum (FBS; Sigma Aldrich F0926 through March 2019; HyClone March 2019 to present). DMEM media was prepared by dissolving 6.7 g of DMEM (GE catalog no. SH3000303), 1.85 g of sodium bicarbonate, and 55 mg of sodium pyruvate (Alfa, A11148) in 450 mL of milliQ water in a 500 mL glass bottle until completely dissolved. A frozen aliquot of FBS (50 mL) was thawed in the 37 ºC water bath, inverted to mix, and then added to the media. The media was mixed by gently inverting the bottle three times. In preparation of media supplemented with antibiotic, 5 mL of 100X penicillin/streptomycin (Corning, 30-002-CI) was added to the media (500 mL). The media was sterile filtered in a 500 mL filter flask (0.2 µm PES filter, ThermoScientific 09-741-

02). After sterile filtering, the lid of the bottle was labeled with the media type and the date of preparation. All media was stored at 4 ºC. Prior to cell work, media was removed and either warmed to room temperature over the course of a few hours or warmed to 37 ºC in a water bath. MCF-7 cells (HTB-22) were obtained from ATCC and cultured in Eagles Minimum Essential Medium (EMEM, ATCC 30-2003) supplemented with 10% FBS. 22Rv1 cells (CRL-2505) were obtained from ATCC and cultured in RPMI-1640 medium (ATCC 30-2001). For general cell passaging, cells were maintained in the indicated growth medium supplemented with antibiotics (1% penicillin/streptomycin, Corning). For experiments, all cells were plated into and maintained within multi-well plates in the indicated medium minus antibiotics. Every 3 months, the media from confluent plates and aliquots from sterile media bottles were analyzed for mycoplasma contamination using the Genlantis MycoScope PCR detection kit (MY01100).

All cell passaging and cell-related experiments were performed in a certified biosafety cabinet. Cell passaging was performed once cells reached 90-100% confluence (typically 1-2 times per week). The cells were passaged by carefully removing the 10 mL of media using a sterile pipette and an autopipettor. Adherent cells were rinsed with TrypLe (1 mL, Gibco 12604021) and then incubated with TrypLe (1 mL) for ~ 1-2 minutes at room temperature. Cells were lifted by gentle pipetting of the TrypLe solution around the plate. Once most/all cells were lifted from the bottom of the plate, the TrypLe was inactivated through the addition of 9 mL of the indicated media and mixed through gentle pipetting. In a separate 10 mL plate, the cell suspension (1 mL) was diluted into fresh media (9 mL) and gently mixed by pipetting. The plate was labeled with the owner's initials, the date of passage, the passage number, and the cell line. *Note:* depending on the experiment timeline or urgency, the cells could also be passaged "low" (500 µL of the cell

suspension into 9.5 mL of media) or “high” (2-3 mL of the cell suspension in 7-8 mL of media), with no noticeable effects on cell health or growth.

When the cells reached passage 30, they were discarded, and a new cell stock was thawed. The cells were thawed by removing the desired vial from the liquid nitrogen dewar and placing it in the 37 ºC water bath only until complete thawing was observed. The cells were then carefully poured into a 10 cm plate containing 10 mL of media. The following day, media was removed and replaced with fresh 10 mL of media. This step is essential as the thawed aliquot contains DMSO which can hinder the cells recovery after thawing. In some cases, the cells from the initial thawing do not adhere to the plate and instead are resuspended in the media that is removed prior to refreshment. If this is the case, the media that is removed from the freshly thawed cells should be cultured in a separate 10 cmplate for 48-72 hours and cell health and adherence should be monitored daily. The media can be changed after 48-72 hours or once sufficient numbers of cells have adhered to the plate.

To ensure that ample vials of cells are stored for future use, or if a new cell line is obtained from ATCC or as a gift from another lab, cell stocks should be frozen down. In preparation for freezing down cells, during the next passage, 3 mL of the cell suspension was plated into a 15 cm plate in 20 mL of the indicated growth medium. On the day of freezing, the Mr. Frosty Freezing Container (ThermoScientific 5100-0001) should be filled with the appropriate volume of isopropanol and stored at room temperature. Once cells reach 100% confluency, media was removed, and the adherent cells were rinsed with 2 mL TrypLe. Cells were lifted in 2 mL TrypLe, transferred to a sterile 15 mL conical tube, and then diluted with 12 mL media (14 mL final volume in the conical tube). A small aliquot of the suspended cells (10 μL) was removed for counting and the rest of the cells were pelleted at 1000 x g for 10 minutes at room temperature. The supernatant

was discarded and the cells were resuspended such that the final cell concentration was 1 million cells per mL in media supplemented with 5% DMSO: The cells were resuspended in 3 mL of media by gentle pipetting with a P1000 pipette, and then the remaining volume was added (if all resuspension media is added initially, the resuspension itself is very challenging). DMSO (5% final concentration) was added to the cell suspension last, and the tube was mixed by gently inverting the tube 5 times. *Note:* once DMSO is added, it is important to work quickly. The cell suspension (1 mL) was transferred to cryogenic tubes and then placed in the Mr. Frosty Freezing Container. The lid was placed on the Mr. Frosty and the cells should be stored at –80 ºC for 24 hours prior to transfer and long-term storage in the liquid nitrogen dewar.

4.2.2 Poly-D Lysine (PDK) Treatment

For imaging experiments or experiments where several media changes were required, multi-well plates were treated with poly-D Lysine (PDK, MP Biomedicals 0215017550, 70-150 kDa) prior to plating in order to improve cell adherence. This was typically only required for experiments where HEK293T cells were used. A stock solution of 10 mg/mL was prepared by dissolving 12 mg of PDK into 1.2 mL of sterile milliQ water and stored at 4 ºC. A working solution of 1 mg/mL of PDK in sterile milliQ water was freshly prepared by diluting from the 10 mg/mL stock prior to each use. The 1 mg/mL PDK solution was pipetted into each well that cells would eventually be plated in for the experiment in a sufficient volume to cover the entire bottom of the well. The plate was incubated with the PDK solution for ~ 20-30 minutes, at which point it was removed. The treated wells were washed twice with an equal volume of autoclaved and sterile-filtered water and then dried in the biosafety cabinet with the lids opened slightly for at least two hours at room temperature.

4.2.3 Mammalian Cell Transfection – Lipofectamine 2000

Lipofectamine 2000 (L2k, ThermoFisher 11668-019) was used for all mammalian cell transfections. L2k was stored as 100 µL aliquots at 4 ºC. Cells were checked for confluency and viability under the microscope the morning of transfections. For transfections to be amenable to the varying plate size, the manufacturer's recommendation was followed (see Table 4-7).[399] Generally, plasmid DNA (the amount varies based on the experiment) was diluted in OptiMEM to the desired "dilution volume" in a 1.7 mL Eppendorf tube ("DNA solution"). In a separate tube, the total amount of L2k required for the entire transfection was diluted in OptiMEM either in a 1.7 mL Eppendorf tube (< 1.5 mL) or a 15 mL conical tube (>1.5 mL) ("L2k solution"). Both of the individual solutions were gently pipetted to mix. Then, an equal volume of the L2k solution was added to the DNA solution ("transfection solution") and gently pipetted to mix. The transfection solution was incubated at room temperature for 20 minutes per the manufacturer's protocol. Following incubation, the transfection solution was added to the plated cells (volumes dependent on plate size, indicated in Table 4-7) and the cells were incubated overnight. The next morning, the transfection media was removed and replaced with an equal volume of fresh media.

Table 4-7: Lipofectamine2000 transfection reagent volumes

Plate size	Plating volume	Dilution volume	L2k (µL/well)
96-well	100 µL	2 x 25 µL	0.5 µL
24-well	500 µL	2 x 50 µL	2 µL
12-well	1 mL	2 x 100 µL	4 µL
6-well	2 mL	2 x 250 µL	10 µL

4.2.4 Mammalian Cell Lysis

For western blot analysis, transfected cells in a 6-, 12-, or 24-well plate were usually lysed ~ 24-72 hours post-transfection. The cells were removed from the incubator and media was removed. Cells were rinsed with cold phosphate-buffered saline (PBS, 500 µL – 1 mL, volume dependent on plate size). PBS was prepared by diluting 100 mL of 10X PBS (prepared by dissolving 17.8 g of Na_2HPO_4, 2.4 g of KH_2PO_4, 80 g of NaCl, and 2 g of KCl in 1000 mL of milliQ water) into 900 mL of milliQ water. Radioimmunoprecipitation assay (RIPA) lysis buffer was prepared and supplemented with Halt Protease Inhibitor Cocktail (1X, diluted from 100X stock, ThermoScientific 78429). The amount of RIPA lysis buffer added to each well was dependent on plate size; for a 6-well plate, 200 µL was added to each well, for a 12-well plate, 100 µL was added to each well, for a 24-well plate, 50 µL was added to each well. Once added, the plate was shaken (250 rpm) on ice for 20 minutes. After shaking, all liquid was removed from each well and transferred into a labeled 1.7 mL Eppendorf tubes. Lysates were centrifuged at max speed at 4 ºC for 15 minutes to pellet the cellular debris. While samples were centrifuging, loading buffer was prepared by combining 450 µL of 4X Laemlli buffer with 50 µL of 2-mercaptoethanol (BME). Laemlli buffer (4X) was prepared by mixing 2 mL of Tris-HCl pH 6.8, 0.8 g of SDS, 4 mL of glycerol, and 8 mg of bromophenol blue and diluted to a final volume of 10 mL with milliQ water. Following centrifugation, the lysate supernatant was carefully removed by pipetting and mixed with $1/3^{rd}$ the volume of the 4X Laemlli buffer supplemented with BME. Samples were heated at 95 ºC for 10 minutes and then stored at –20 ºC until western blot analysis.

4.2.5 Western Blot Analysis

Lysates (12-25 µL) were resolved on either an 8, 10, or 12% SDS-PAGE gel topped with a 4% stacking gel. The percentage of the resolving gel was dependent on the size of the protein-of-interest. The gels were run at 60 V for 20 minutes and then increased to 150 V for 90 minutes or until the dye front ran off the gel. Immediately after the gel was started, transfer buffer was prepared by diluting 100 mL of 10X transfer buffer (30.3 g of Tris base and 144 g of glycine dissolved in 1000 mL of milliQ water), with 200 mL of methanol, and 700 mL of milliQ water. The transfer buffer was immediately placed in the –20 ºC freezer and left there the entire time that the gel is running, as it must be chilled prior to the transfer step. While the gel was running, the PVDF membrane (Millipore, IPVH00010) was cut with scissors such that it was the same approximate size as the SDS PAGE gel. Additionally, two pieces of Whatman filter paper (GE Healthcare 100115) were cut the same size as the PVDF membrane. With ~ 10 minutes remaining, the PVDF membrane was soaked in 100% methanol to activate the membrane. A gel tank was placed in a Nalgene autoclave bin that was filled with ice around the gel tank, generating an ice moat so as to ensure that everything remained cold for the transfer step.

Once the gel was finished electrophoresing, the gel was removed from the glass plates and the stacking gel was removed by cutting with a clean razor blade. The gel was rinsed with water and temporarily stored in an old plastic pipette box. The transfer cassette was assembled in a glass casserole dish filled with the ~ 800 mL of the chilled transfer buffer using the BioRad Mini Trans-Blot Cell. The transfer cassette was assembled as follows (from bottom to top): plastic casing was laid black side down, then sponge, filter paper, gel (with lane 1 aligned at the top left corner), PVDF membrane, filter paper, sponge, clear side of plastic casing. Prior to placement of the second piece of filter paper, the contact between the membrane and the gel was carefully examined for

bubbles. If present, the bubbles were rubbed out by gently pressing the filter paper. It is imperative that the bubbles are removed as these will prevent uniform protein transfer and will present as artifacts on the developed blot. Once assembled, the plastic casing was latched shut by locking the clip. The cassette was then placed into the Trans-Blot Cell by matching the black side of the cassette casing with the black side of the transfer cell. Matching the colors ensures proper directionality of the protein transfer from the SDS PAGE gel to the PVDF membrane. If the cassette is backwards (i.e., clear side of the cassette casing to the black side of the transfer cell), the protein will be transferred onto filter paper, which cannot retain it, and subsequently lost in the buffer. The gel tank was filled with the transfer buffer from the baking dish and then an ice pack was placed inside the gel tank. The protein transfer was run at 80 V for 90 minutes.

After the transfer, the cassette was disassembled, and the membrane was trimmed and placed in a clear, plastic box of appropriate size. The membrane was washed with ~ 5 mL of cold Tris-buffered saline with Tween-20 (TBST) buffer three times. TBST buffer was prepared by diluting 100 mL of 10X Tris-buffered saline (TBS) with 900 mL of milliQ water, and then adding 1 mL of Tween-20 (Fisher BP337-500). The 10X TBS buffer was prepared by dissolving 88 g of NaCl and 12.1 g of Tris-base in 1000 mL of milliQ water. In the first two rinses, TBST (~ 5-10 mL) was pipetted onto the membrane and then immediately poured off ("quick rinses"). On the third rinse, TBST was pipetted onto the membrane and then the membrane was placed on the rocking shaker for ~ 2-3 minutes ("long rinse"). This rinsing scheme (i.e., 2 "quick" rinses, and 1 "long" rinse) was repeated two times for a total of six washes. *Note:* from this point on it is important that the membrane remain wet and to not let it dry out.

After rinsing, the membrane was blocked using the blocking buffer that was specified for the primary antibody that would be used for probing the protein-of-interest. Blocking buffers

consisted of either 5% non-fat milk powder [w/v] diluted in TBST or 5% BSA [w/v] diluted in TBST. Non-fat dry milk powder was purchased from LabScientific (M0841) and Fraction V BSA was purchased from ThermoScientific (J1085722). The membrane was blocked in blocking buffer for a minimum of 2 hours while rocking at room temperature. The primary antibody solutions were prepared in the corresponding blocking buffer (specified by the manufacturer) following the dilutions recommended by the manufacturer (antibody, dilutions, manufacturer, and blocking buffer are specified in the western blot protocols presented in the Materials and Methods sections at the end of each project's chapter throughout this thesis). Primary antibody was incubated with the membrane overnight at 4 ºC while rocking. The next morning, the primary antibody solution was poured off the membrane and the membrane was rinsed thoroughly with TBST buffer following the same rinsing scheme that is specified for post-transfer (i.e., 2 "quick" rinses and 1 "long" rinse, two times). The secondary antibody was prepared in TBST buffer following the manufacturer's recommended dilution. Secondary antibody was added to the rinsed membrane and incubated at room temperature (while rocking) for no longer than 90 minutes. At the end of the secondary antibody incubation, the membrane was rinsed following the same rinsing scheme specified above (i.e., 2 "quick" rinses and 1 "long" rinse, two times) with TBST. The blot was then developed using SuperSignal West Pico PLUS Chemiluminescent Substrate (ThermoScientific 34580). Equal volumes of the "Luminol" and "Enhancer" solutions (usually no more than 2 mL of each) were mixed in a 15 mL conical tube and gently inverted to mix. The entire developing solution was poured over the membrane and incubated at room temperature while shaking for 5 minutes. The membrane was then carefully placed between two sheets of plastic and imaged using the autoexposure settings of the "Chemi HiSensitivity" program on the BioRad ChemiDoc XRS imager. If the exposure time determined by the autoexposure settings was greater than 300

seconds, a manual exposure time was programmed, and the blot was re-imaged. The blot was also imaged using the autoexposure settings on the Cy3 and Cy5 channels in order to visualize the protein ladder. Images were captured using the ImageLab software and exported using the "Export for Publication" feature.

4.3 General Methods – Morpholino Preparation and Handling

4.3.1 Morpholino Preparation

All morpholinos were purchased from GeneTools, LLC (Philomath, OR). The control MO ("control MO") is a standard control MO offered by GeneTools and should have no endogenous target and very little biological activity, and therefore serves as a negative control. Morpholinos were received as a dry, lyophilized solids in glass vials. The dry solid was dissolved with milliQ water to a final concentration of 1 mM (300 nmol scale resuspended in 300 µL, 1000 nmol scale resuspended in 1000 µL). The resuspended MO was stored at room temperature on the benchtop per Gene-Tools recommendation. When needed for synthesis reactions, an aliquot of the MO solution was pipetted into a 1.7 mL microcentrifuge tube. The MO solution was vortexed, heated at 95 ºC for 30-60 seconds, and then vortexed again to mix. According to the manufacturer's instructions, heating and/or autoclaving can help dissolve any MO aggregates that may form.

4.3.2 Determination of MO Concentration

The concentration of the MO was determined following the manufacturer's protocol.[180] The MO solution was diluted 1:10 and 1:20 into 0.1 N HCl and pipetted to mix. For synthetic intermediates, the diluted MO solutions were prepared by diluting 1:5 or 1:10 in 0.1 N HCl as they may not be as concentrated as the stock solutions prepared from GeneTools. The concentration of each of the diluted MO solutions was determined by measuring the absorbance using the "Other" program on the ND-1000 NanoDrop spectrophotometer. The absorbance wavelength was set to 265 nm and the constant (specific to each MO intermediate) can be calculated by multiplying the molecular weight of the MO by 1000 and then dividing by the extinction coefficient of the MO sequence (provided by the manufacturer on the MO data sheet, but listed here for convenience, control MO 259160, *spt* MO 254250, *ntla* MO 262310). The concentration (ng/µL) for each diluted solution was measured 3-5 times and then the average concentration for each solution was calculated. The concentration (ng/µL) were then multiplied by their corresponding dilution factors (5, 10, or 20) to give the actual concentration of the MO (ng/µL). This value can then be used to calculate the molar concentration of the MO solution. *Note:* concentrations for synthetic cMO intermediates was not measured in cases where MO concentration was not essential the reaction (i.e., cyclization with immobilized TCEP, NHS-agarose purification, SulfoLink purification). This is because the MO concentration is already dilute, and in order to get an accurate concentration measurement on the NanoDrop ND-1000, the MO solution must be further diluted in 0.1N HCl, and therefore the concentration would likely be below the detection limit of the NanoDrop.

4.3.3 MALDI-TOF Analysis of MOs

All morpholinos, synthetic MO intermediates, and cMO products were characterized by spotting on a MSP 96 target ground steel BC MALDI plate (Bruker Daltonics 8280799) and analyzed by MALDI-TOF mass spectrometry on the Bruker Daltonics UltrafleXtreme MALDI-TOF mass spectrometer in linear positive mode. In most cases, an aliquot of the MO solution (2 μL) was co-spotted with 1 mg/mL sinapic acid (SA) matrix (Proteochem Inc, NC1485903). MOs were spotted using the "sandwich method" in which the SA matrix (2 μL) was spotted on the plate and evaporated under a constant stream of air. Next, the MO solution (2 μL) was added to this same spot and evaporated to dryness under a constant stream of air. Then, another 2 μL of SA matrix was pipetted onto the spot and dried (final 2:1 matrix to analyte ratio). Once dried, the crystalline spot was analyzed by MALDI-TOF MS using the pre-set "LP5-20 kDa" method prepared by the University of Pittsburgh Mass Spectrometry Facility. The MOs were analyzed using 100% laser power and the sample was analyzed at different regions of the spot (~ 5-10 mouse clicks per sample). In some cases (i.e., crude MO bioconjugation reaction mixtures), DMSO is present in the reaction mixture and the evaporation of the spot requires subsequent additions of water or matrix to facilitate co-evaporation. This often leads to a much larger matrix to analyte ratios in the sample (> 5 μL matrix per 1 μL analyte with DMSO) and requires excess time under a constant stream of air to obtain a dry, crystalline spot for analysis. The excess of matrix does not interfere with ionization or MALDI analysis.

4.3.4 HPLC Purification of MOs

All synthetic MO intermediates and cMOs are subject to purification or buffer exchange by HPLC on a Shimadzu LC20 HPLC system using a gradient of either 5-50% or 5-60% acetonitrile in 0.1 M triethylammonium acetate (TEAA) buffer over 20 minutes. MOs were resolved on an ACE Excel 3 Oligo Beta Test HPLC column (100 x 4.6 mm, serial no, A252326) using a 1 mL/min flow rate. The MO was monitored via absorbance at 260 nm on a SP-20AD UV/Vis detector. Prior to purification, a test run (~15-25 µL injection) of the crude MO reaction mixture (30-50 µM) was performed to analyze the crude reaction mixtures before larger injection amounts (50-100 µL) for batch purification were used. All peaks eluted in the initial test run were manually collected (typically 500-1000 µL, collected in ½ dram borosilicate glass vials) and analyzed by MALDI-TOF MS as outlined above (Section 4.3.3) for determine which peak contained the desired MO intermediate. Typically, conjugated MO products elute as a single, broad peak between 9-12 minutes. The amount of MO fractions collected depended on reaction scale. A 100 µL injection on the HPLC yielded ~ 1-1.2 mL of purified MO product that eluted from the HPLC. Following purification, all MO containing elutions were pooled, diluted with water (typically ~ 1 mL for every 4 mL eluted HPLC fractions as diluting with water prevents the sample from melting on the lyophilizer) and lyophilized to dryness overnight.

4.3.5 Purification Using NHS-activated Agarose Resin

Pierce dry NHS-activated agarose (Cat. No. 26196) was purchased from ThermoScientific. The dried, cyclic cMO was resuspended in water (100 µL). In a Pierce spin cup filter (ThermoScientific, paper filter – Cat. No. 69700 – discontinued or cellulose acetate filter – Cat.

No. 69702), dry NHS-activated agarose resin (20 mg) was swollen in phosphate-buffered saline (PBS, 400 µL) for 20 minutes at room temperature. After swelling, the spin cup filter was centrifuged at 2,000 rpm for 1 minute and the flow-through was discarded. The resin was washed two more times with PBS (400 µL per rinse). Following the final rinse, PBS (100 µL) and the MO solution (100 µL) were added directly to the resin. The heterogenous solution was mixed by brief, gentle shaking. The reaction mixture was incubated at room temperature for 30 minutes, as the manufacturer's protocol states that the majority of the reaction occurs within this time frame. Following incubation, the spin cup filter was centrifuged at 2,000 rpm for 2 minutes and the flow-through was collected. To ensure complete elution of all MO solution from the resin, the spin cup filter was centrifuged at 5,000 rpm for 5 minutes and the remaining flow-through was collected and combined with that from the first spin. The NHS-purified MO solution was then purified on the Shimadzu LC-20AD HPLC as described in Section 4.3.4. Fractions containing the purified cMO were pooled and lyophilized to dryness overnight.

4.3.6 Purification Using SulfoLink Resin

Pierce SulfoLink coupling resin (Cat. No. 20401) was purchased from ThermoScientific. The cyclic cMO was resuspended in water (100 µL) and SulfoLink coupling buffer (100 µL, 50 mM Tris, 5 mM EDTA-Na pH 8.5) was added. SulfoLink slurry (120 µL) was pipetted into Pierce spin cup filter and mixed with coupling buffer (400 µL). The spin cup filter was centrifuged at 2,000 rpm for 2 minutes and the flow-through was discarded. The SulfoLink resin was rinsed two more times with coupling buffer (400 µL per rinse) and the flow-through was discarded. After the final rinse, the cMO solution (200 µL) was added directly to the resin and was rocked end-over-end on a shaker for 20 minutes. The resin was allowed to settle at room temperature for 30 minutes

and then the spin cup filter was centrifuged at 5,000 rpm for 2 min and the flow-through was collected. To ensure complete elution of the purified cMO solution from the resin, the resin was centrifuged a second time at 10,000 rpm for 2 minutes and the flow-through was collected and combined with that from the initial spin. The purified cMO solution was then buffer exchanged by HPLC following the protocol outlined in Section 4.3.4. Fractions containing purified cMO were pooled and lyophilized to dryness overnight.

4.4 General Methods – Zebrafish

4.4.1 Zebrafish Aquaculture and Husbandry

All zebrafish manipulations were performed in accordance with IACUC regulations and approved by the University of Pittsburgh. The AB* strain was maintained under standard conditions at the University of Pittsburgh School of Medicine in accordance with Institutional and Federal guidelines. All feeding schedules, temperature control, water quality monitoring, and light cycles were controlled by the veterinary staff at the University of Pittsburgh Division of Laboratory Animal Research (DLAR).

4.4.2 Zebrafish Breeding

Natural mating of adult zebrafish were set up in the afternoon or early evening the day before injections (4-6 pm). Male and female zebrafish (5-10 of each) were placed in a breeding tank with a separated divider. It is preferred that these fish have not been bred for ~ 2 weeks,

however, sufficient breeding has been observed with fish that are bred every 7-10 days. Fertile fish should range in age anywhere from 6 months to 2 years old and should be euthanized after 2 years old. The following morning between 8-9 am, the divider was removed, and fish were allowed to breed. The embryos from the natural mating were collected and stored in E3 water (5 mM NaCl, 0.17 mM KCl, 0.33 mM $CaCl_2$, 0.33 mM $MgSO_4$, and 0.00001% methylene blue). Zebrafish were allowed to breed for 2-3 hours and then the male and female fish were separated and placed back onto the maintenance shelves. The dates and success of breeding (+/–) were recorded on the respective fish tanks.

4.4.3 Zebrafish Microinjection

Borosilicate glass capillary tube needles (World Precision Instruments, 1 mm, 4 inches) were heated and pulled to form micropipette needles. The needs were marked every 1 mm, indicating a volume of 30 nL between the hash marks. Injection solutions were prepared and diluted with phenol red to a final concentration of 0.05% as a tracer for injection. The injection solutions (~ 3-5 μL) were pipetted into 35 mm petri dishes and covered in mineral oil to prevent evaporation. At most, four separate, injection solutions can be placed on one plate. Once pipetted, ~ 2-3 mL of mineral oil is The very tip of the needle was cut using a razor blade to form an opening at the tip and then loaded with the injection solution. Microinjections were performed using a World Precision Instruments Pneumatic PicoPump injector. The flow rate of the needle (nL/sec) was determined by first measuring the time (measured with a stopwatch) required to dispense 30 nL from the needle at the desired pump pressure output. This was measured twice and the timings were averaged, then divided by 30 (volume dispensed) to determine the gating time to inject a single nanoliter. Gating times were then multiplied by the volume necessary to deliver the desired

amount of reagent. Once embryos were obtained, the embryos were placed into a 3% agarose injection tray containing divots to hold single embryos in place. Embryos were properly positioned using an inoculation loop or an eyelash brush (although the inoculation loop always worked better in my hands). The loaded needle was then lowered to penetrate the chorion and the embryo. Most morpholino and mRNA solutions were injected into the yolk sac just under the blastomere. No more than 6 nL volume should be injected into the embryo at a time. Embryos were injected up to the 8-cell stage, after which they were deemed too developed for efficient global delivery of the injected material. Once completed, the embryos were rinsed from the agarose tray with E3 water into 10 cm petri dishes. The embryos were incubated at 29 ºC until the desired developmental stage. Unfertilized embryos (which do not develop past the 1-cell stage) were removed and discarded usually around 3-5 hpf. Following injections, it is imperative to take a quick coffee and treat break at RedHawk with your injection partner (Wesley Brown) as embryo microinjections call for long mornings and you will deserve the break.

4.4.4 Zebrafish Imaging

Early-stage zebrafish embryos (<10 hpf) were pooled and imaged as is. Later stage embryos (24 – 72 hpf) were anesthetized with tricaine (Sigma MS-222) in E3 water. Unhatched embryos (24-32 hpf) were manually dechorionated using forceps. In cases where only brightfield images were required, imaging was performed on a Leica MZ16 stereoscope equipped with a QImaging Retiga 1300 camera and captured using the QCapture software. In experiments where fluorescence imaging was required, imaging was performed on the Leica M205FA fluorescent stereoscope using the 0.93X or 1.6X objective at zoom settings dictated by the number and size of the zebrafish embryos. Fluorescent images were obtained using the EGFP (filter 41017) or

mCherry (filter 41043) filter sets. All imaging parameters were set using the Leica software and images were collected with a QImaging Reiga-EXi Fast 1394 digital camera.

4.4.5 Zebrafish Embryo Lysis for Luminescence or Colorimetric Assays

Embryos at 24 hpf, were pooled, and anesthetized in tricaine, and manually dechorionated using forceps. Embryos were counted and equal numbers per condition were transferred in 1.7 mL Eppendorf tubes. Excess E3 water was pipetted off. Embryos were centrifuged at room temperature at 1100 rpm for 10 minutes and residual E3 was removed. Then, lysis buffer was prepared by diluting 500 µL 5X passive lysis buffer (Promega E1941) in 2.5 mL milliQ water. A volume equal to ~ 2 µL lysis buffer per embryo was added to each tube. Embryos were homogenized on ice for 90 seconds using a Pellet Pestle Cordless Motor (Fisher 12-141-361) equipped with an RNAse-Free Disposable Pellet Pestle (Fisher 12-141-364). Following homogenization, samples were analyzed in accordance with the assay under experimentation.

4.4.6 Zebrafish Embryos Lysis for Western Blot Analysis

At the desired time point (24-48 hpf), embryos were pooled (n = 60-100 embryos / condition is usually sufficient for western blot analysis), anesthetized in tricaine, and manually dechorionated using forceps. Embryos were then transferred to 1.7 mL Eppendorf tubes and excess E3 water was removed by pipetting. Embryos were lysed following a modified version of a previously reported protocol.[400] Embryos were deyolked in 100 µL of de-yolking buffer (55 mM of NaCl, 1.8 mM of KCl, 1.25 mM of $NaHCO_3$ in milliQ water) by vigorous pipetting with a P200 pipette tip. Deyolked embryos were centrifuged at 1100 rpm at room temperature for 10 minutes

and the supernatant was discarded. Lysis buffer was prepared fresh by combining 900 µL of T-PER (ThermoScientific 78510) and 100 µL of 10X cOmplete Mini EDTA-free Protease Inhibitor Cocktail (Sigma 11836170001). A 10X stock of Protease Inhibitor Cocktail was prepared by diluting 1 tablet of the inhibitor cocktail into 1 mL of deionized water. When phospho-proteins were to be analyzed, lysis was supplemented with 20 µL of 50X phosphatase inhibitors (100 mM each of sodium fluoride and sodium orthovanadate, prepped by fellow, former lab member Dr. Taylor Courtney).

Embryo pellets were resuspended in the lysis buffer at ~ 2 µL/embryo, then homogenized on ice for 90 seconds using a Pellet Pestle Cordless Motor (Fisher 12-141-361) equipped with an RNAse-Free Disposable Pellet Pestle (Fisher 12-141-364). Following homogenization, the lysates were incubated on ice for 30 minutes. The samples were centrifuged at 15,000 g for 15 minutes at 4 ºC, then the supernatant was transferred to a fresh 1.7 mL Eppendorf tube. An aliquot (5 µL) of the lysate was set aside for protein quantification by Bradford assay, and 4X Laemlli buffer (to a final 1X concentration) was added to the remainder of the solution. Lysates were heated for 10 minutes at 95 ºC, then stored at –80 ºC until analysis by western blot.

A detergent compatible Bradford assay (Pierce PI23246) was performed to quantify protein concentration in the embryo lysates. A BSA standard curve was generated by mixing 5 µL of BSA standards (5, 2.5, 1, 0.5, 0.25, 0.125, 0.0625, and 0 mg/mL) with 150 µL of the Bradford reagent. Samples were shaken on an orbital shaker (50 rpm) at room temperature for 10 minutes. Absorbance measurements were acquired on a Tecan M1000 plate reader at 595 nm. To determine protein concentration in the lysates, a 2.5 µL aliquot of lysate was diluted with 2.5 µL T-PER (ThermoScientific) and the protein concentration was measured identically as described for the BSA standards. Following background subtraction of a “buffer only” sample, the protein

concentration in the lysate samples was determined using the standard curve. The volume necessary for 20 and 15 µg was determined by dividing by the concentration. Western blot analysis was performed identically as described above for the cell-based experiments (Section 4.2.5) , except the appropriate volume of lysate was loaded per lane to obtain 20 µg analyte protein and 15 µg loading control.

4.4.7 General Reagent and Buffer Recipes

4.4.7.1 dNTPs

- 10 µL of dATP (100 mM)
- 10 µL 0f dTTP (100 mM)
- 10 µL of dGTP (100 mM)
- 10 µL of dCTP (100 mM)
- 60 µL of milliQ water

dNTPs were purchased as 100 mM stocks from ThermoScientific (FERR0181). dNTPs were diluted in milliQ water and stored at –20 ºC.

4.4.7.2 5X Isothermal Gibson Assembly Buffer

- 3 mL of 1M Tris-HCl pH 7.5
- 150 µL 2M $MgCl_2$
- 600 µL of 10 mM dNTPs
- 300 µL 1M DTT
- 1.5 g of PEG-8000
- 20 mg of NAD+ hydrate

Combine all reagents in a 15 mL conical tube and fill to volume (6 mL) with autoclaved milliQ water. Store at –20 ºC in 320 µL aliquots.

4.4.7.3 Gibson Assembly Master Mix

- 320 µL of 5X Isothermal Gibson Assembly Buffer (see 4.4.7.3)
- 0.64 µL of T5 Exonuclease (10U/µL, NEB M0363S)
- 20 µL of Phusion polymerase (2U/µL, ThermoScientific F530L)
- 160 µL of Taq DNA ligase (40U/µL, Applied Biomedical Materials E090)
- 699 µL of autoclave milliQ water

Keep all reagents on ice during preparation. Combine all reagents in a 1.7 mL Eppendorf tube. Gently invert to mix (do not vortex). Prepare aliquots of master mix (15 µL) in pre-chilled autoclaved PCR tubes on ice (recipe makes 80 aliquots). Store at –20 ºC until needed.

4.4.7.4 LB Agar

- 10 g of LB broth
- 6 g Agarose powder
- 400 mL of milliQ water

LB Broth (Cat. No. BP14262) and agarose powder (Cat. No. BP1423-2) were purchased from Fisher. Agarose and broth were mixed in 400 mL of milliQ water. The solution was autoclaved to fully dissolve the agarose and sterilize for bacterial cell work. While still hot, the bottle was gently inverted to mix. Store at room temperature and only use in a sterile working environment (ethanol sanitized bench and next to Bunsen burner flame) to avoid contamination.

4.4.7.5 LB Broth

- 10 g of LB broth
- 400 mL of milliQ water

Dissolve LB broth in 400 mL milliQ water and autoclave to sterilize. Store at room temperature and only use while working in a sterile environment (ethanol sanitized bench and next to a Bunsen burner flame) to avoid contamination.

4.4.7.6 10X Phosphate Buffered Saline (PBS)

- 80 g of NaCl
- 2.0 g of KCl
- 14.4 g of Na_2HPO_4
- 2.4 g KH_2PO_4

Recipe obtained from Cold Spring Harbor. Dissolve all contents in milliQ water (950 mL). Adjust the pH to 7.4 with 65% [v/v] aq. HCl. Fill to volume (1000 mL) with milliQ water and store at room temperature. To make a 1X solution, dilute 100 mL of the 10X PBS stock into 900 mL milliQ water. For use in mammalian cell culture, be sure to sterile filter as needed.

4.4.7.7 10X Tris/Borate/EDTA (TBE) Buffer

- 121 g of Tris base
- 61.8 g of boric acid
- 7.4 g EDTA disodium salt

Dissolve salts in 900 mL of milliQ water. Once completely dissolved, fill to volume (1000 mL). Store at room temperature. Dilute to 1X by mixing 100 mL 10X stock with 900 mL milliQ water for gel electrophoresis as needed. If precipitation of buffer components is observed over time, autoclave to redissolve. Recipe from Cold Spring Harbor.

4.4.7.8 Agarose Gels (for Electrophoresis)

- 320 mg agarose
- 40 mL TBE buffer

Agarose was purchased from Fisher (Cat. No. BP160-100). Agarose was resuspended in TBE buffer in a 50 mL Erlenmeyer flask and swirled to mix. The suspension was microwaved for 30 seconds to dissolve the agarose and then swirled to mix. The flask was microwaved for an additional 15 seconds, swirled to mix, and then an additional 10 seconds if the agarose was not fully dissolved. The flask was cooled under running water from the faucet. For visualizing DNA, a drop (1-5 µL) of ethidium bromide (from 10 mg/mL stock) was added to the cooled agarose and swirled to mix. Once the gel was poured into the cassette, the desired comb was inserted into the mold, and the gel was left to solidify at room temperature.

4.4.7.9 1.5M Tris-HCl buffers (for PAGE Gel Preparation)

- 91.05 g Tris base

Dissolve Tris base in 450 mL milliQ water. Adjust to pH 8 or pH 6.8 (depending on solution) with 65% [v/v] aq. HCl and monitoring with the pH meter. Once at desired pH, fill to volume (500 mL). Store at room temperature.

4.4.7.10 10% SDS solution (for SDS-PAGE Gel Electrophoresis)

- 5 g of sodium dodecyl sulfate (SDS)

Dissolve SDS in 40 mL of milliQ water in a 50 mL conical tube. Vortex to mix. Let bubbles settle and once fully dissolved, fill to volume (50 mL) with milliQ water. Store at room temperature.

4.4.7.11 10% Ammonium Persulfate (APS) (for PAGE Gel Preparation)

- 1 g of ammonium persulfate

Dissolve APS in 9 mL of milliQ water in a 15 mL conical tube. Vortex to mix. Once fully dissolved, fill to volume (10 mL) with milliQ water. Store at 4 ºC.

4.4.7.12 10X SDS-PAGE Running Buffer

- 30.3 g of Tris base
- 144 g of glycine
- 10 g of sodium dodecyl sulfate (SDS)

Dissolve solids in 900 mL of milliQ water. If SDS does not go into solution, sonicate the solution and periodically invert to mix (this will take awhile). Fill to volume (1000 mL) with milliQ water. Plan to make this solution at least 1 day in advance of actually needing it. For SDS-PAGE gel electrophoresis, prepare 1X running buffer by diluting 100 mL of the 10X stock with 900 mL of milliQ water. Both the 10X and 1X stocks can be stored at room temperature. Fresh buffer should be used to fill the dam between the gel(s) and buffer dam. Following gel electrophoresis, the used buffer was collected and stored in a separate, labeled 1-L bottle. The used buffer can be recycled and used to fill the gel tank, but should be discarded after ~ a month if gels were not run.

4.4.7.13 Laemlli Buffer

- 2 mL 1 M Tris-HCl pH 6.8
- 0.8 g sodium dodecyl sulfate
- 4 mL glycerol
- 8 mg bromophenol blue

Combine all components in a 15 mL conical tube and fill to 10 mL with milliQ water. Buffer can be stored at room temperature. Before diluting into lysate(s), a 900 µL aliquot of buffer should be mixed with 100 µL β-mercaptoethanol.

4.4.7.14 Purple Loading Dye

- 500 µL 30% glycerol
- 250 µL 6X Purple loading dye

Purple loading dye was purchased from NEB (Cat. No. B7024S). Solutions were mixed together and stored at room temperature. Samples were mixed with homemade loading dye to a final concentration of 5% glycerol before loading into agarose or native PAGE gels.

4.4.7.15 Radioimmunoprecipitation Assay (RIPA) Buffer

- 2.5 mL 1 M Tris-HCl pH 7.6
- 5 mL 3 M NaCl
- 10 mL 10% NP-40 (borrowed from the Islam lab)
- 10 mL 10% aqueous sodium deoxycholate
- 1 mL 10% aqueous sodium dodecyl sulfate

Combine reagents in a 100 mL bottle and dilute to volume with milliQ water. Buffer can be stored indefinitely at 4 ºC. Final concentrations of each component are: 25 mM Tris-HCl pH 7.5, 150 mM NaCl, 1% NP-40, 1% sodium deoxycholate, 0.1% SDS.

4.4.7.16 10X Transfer Buffer (for Western Blot)

- 30.3 g Tris base
- 144 g glycine

Dissolve solids in 900 mL of milliQ water. Once dissolved, fill to volume (1000 mL) with milliQ water. Store at 4 ºC indefinitely.

4.4.7.17 1X Transfer Buffer

- 100 mL of 10X Transfer buffer (see 4.4.7.16)
- 200 mL methanol
- 700 mL of dI water (or milliQ water)

Dilute 100 mL of the 10X stock into 700 mL of dI or milliQ water. Fill to volume with 200 mL of methanol. Mix thoroughly by inverting bottle and shaking. Prepare fresh before use. For western blot applications, be sure to chill at 4 ºC or –20 ºC for ~ 1-2 hours before the transfer step. The final concentrations of each component are: 25 mM Tris-HCl, 192 mM glycine, 20% [v/v] methanol.

4.4.7.18 10X Tris-buffered Saline (TBS)

- 88 g of NaCl
- 121.1 g Tris-base

Dissolve solids in 900 mL milliQ or dI water. Once fully dissolved, fill to volume (1000 mL) with milliQ for dI water. Store at 4 ºC.

4.4.7.19 Tris-buffered Saline + Tween-20 (TBST)

- 100 mL of 10X TBS
- 1 mL of Tween-20
- 900 mL of dI water

Dilute 100 mL of the 10X TBS stock solution with 900 mL of dI water and invert bottle to mix. Using a wide-orifice pipette tip, add 1 mL Tween-20 to the solution. Mix thoroughly. Store at 4 ºC.

4.4.7.20 Western Blot Blocking Buffers

- 2.5 g of either non-fat dry milk powder or bovine serum albumin (BSA)

Choice of blocking buffer is specified on the antibody data sheet. Dissolve the solid (milk or BSA) in 40 mL of TBST. Vortex to mix. Once fully dissolved, fill to volume with TBST and invert to mix. Store at 4 ºC. These solutions should be made fresh prior to use, however, in my experience, can be used for up to 3 days (if several blots are being run). Blocking buffers are 2.5% [w/v] solutions of the solid in TBST buffer.

4.4.7.21 Coomassie Destain Buffer

- 100 mL of glacial acetic acid
- 200 mL of methanol
- 700 mL of dI or milliQ water

Dilute glacial acetic acid with milliQ water, then add methanol. Mix solution thoroughly. Following staining with Coomasie, the Coomassie Destain Buffer is added to the gel box and rocked at room temperature (refreshing as needed), until the protein bands are visibly detectable above background (typically an overnight incubation will suffice).

4.4.7.22 Coomassie Stain Solution

- 50 mg Brilliant Blue G-250
- 50 mL Coomassie Destain buffer

Dissolve solid in Coomassie Destain buffer in a 50 mL conical tube. Invert to mix. Prepare fresh before use. Can be stored at room temperature. Following staining with Coomassie, the staining solution can be recycled by filtering through decolorizing carbon to remove the blue dye and added back to the Coomassie Destain Buffer stock bottle.

4.4.7.23 DMEM Media (for Mammalian Cell Culture)

- 6.7 g DMEM (GE SH3000303)
- 1.85 g sodium bicarbonate
- 55 mg sodium pyruvate

Combine all solids in an autoclaved 500 mL glass bottle. Dissolve in 450 mL of milliQ water and mix thoroughly until completely dissolved. In a tissue culture hood, pour the dissolved media into a 500 mL sterile filter flask (0.2 μm PES filter). Then, add 5 mL of 100X penicillin/streptomycin (if making media supplemented with antibiotics) and/or 50 mL fetal bovine serum (FBS). Sterile filter in the tissue culture hood and then store at 4 ºC in the cell culture room. Prior to use, warm media to 37 ºC in the water bath in the tissue culture room.

4.4.7.24 25X Tricaine Solution

- 200 mg of ethyl 3-aminobenzoate
- 1.05 mL of 1M Tris pH 9
- 49 mL of dI water

Dissolve ethyl 3-aminobenzoate in ~ 45 mL of dI water. Pipette in 1M Tris pH 9 buffer. Adjust pH to ~ 7 with 65% [v/v] aq. HCl. Once at pH, fill to volume (50 mL) with dI water. Store at 4 ºC. For anesthetizing embryos, mix ~ 200 μL of the 25X tricaine stock with ~ 3 mL of E3 water in embryo plate. Embryos should become static within 5 minutes and remain static for up to 3 hours.

4.4.7.25 10X Protease Inhibitor Cocktail (for Zebrafish Embryo Lysis)

Dissolve 1 tablet of cOmplete, Mini, EDTA-free Protease Inhibitor Cocktail in 1000 µL of E3 water. Store at –20 ºC. Discard after ~ 2 months.

4.4.7.26 Zebrafish Embryo Deyolking Buffer

- 160.6 mg of NaCl
- 6.7 mg of KCl
- 5.3 mg of sodium bicarbonate

Combine solids in a 50 mL conical tube. Dissolve in 45 mL of milliQ water. Once dissolved, fill to volume (50 mL) with milliQ water. Store at 4 ºC. Prior to deyolking embryos, mix 900 mL of deyolking buffer with 100 µL of 10X Protease Inhibitor Cocktail, and deyolk embryos with protease inhibitor-supplemented buffer.

4.4.7.27 Zebrafish Embryo Lysis Buffer (for Western Blot)

Over the course of this work, the protocol for analyzing zebrafish embryo lysates by western blot was optimized. For western blot analysis of TEVp and HA-β-lactamase expression in zebrafish embryos lysates, **lysis buffer 1** was used. For western blot analysis of mTOR signaling in zebrafish embryos (see Dr. Taylor Courtney's thesis or the Deiters lab ANB-rapamycin paper), **lysis buffer 2** was used. *Note:* Western blot analysis of zebrafish embryo lysates that were lysed using **lysis buffer 2** provided more blot-to-blot consistency (and better protein signal) and is the preferred lysis buffer for preparation of embryo lysates for analysis by western blot.

Lysis buffer 1 (makes 2X stock)

- 242 mg of Tris base
- 876 mg of NaCl
- 37.24 mg EDTA disodium salt
- 38 mg of EGTA

- 1 mL of Triton X-100

Dissolve solids in 45 mL of milliQ water in a 50 mL conical tube. Add 1 mL of Triton X-100. Mix thoroughly through inverting the tube or by vortexing. Once fully dissolved, fill to volume (50 mL) with milliQ water. Store at 4 ºC. Prior to lysis, mix 500 µL of lysis buffer 1, 100 µL of 10X Protease Inhibitor Cocktail, and 400 µL of milliQ water in a 1.7 mL Eppendorf tube to make 1X lysis buffer stock. Keep on ice through embryos lysis procedure. The final concentrations of each component in the 2X lysis buffer stock are as follows: 40 mM Tris, 300 mM NaCl, 2 mM EDTA, 2 mM EGTA, 2% Triton X-100.

Lysis buffer 2

Dilute 900 µL of Tissue Protein Extraction Reagent (T-PER, ThermoScientific 78510) with 100 µL of 10X Protease Inhibitor Cocktail in a 1.7 mL Eppendorf tube. For western blot analysis of phospho-proteins, 880 µL of T-PER was diluted with 100 µL 10X Protease Inhibitor Cocktail and 20 µL of 50X phosphatase inhibitors (100 mM each of sodium fluoride and sodium orthovanadate, prepped by Dr. Taylor Courtney). Prepare fresh before every use and keep on ice during lysis. *Note:* Use ~ 2 µL lysis buffer per embryo.

4.4.7.28 0.1M Tris-HCl pH 8

- 607 mg Tris base

Dilute Tris base in 45 mL of milliQ water. Adjust to pH 8 with 65% [v/v] aq. HCl. Once at pH, fill to volume (50 mL) with milliQ water. Store at room temperature.

4.4.7.29 β-lactamase Activity Buffer

- 2.11 mL of 1M sodium phosphate buffer (monobasic)

- 2.88 mL of 1M sodium phosphate buffer (dibasic)
- 45 mL of milliQ water

Prepare 1M sodium phosphate buffer (monobasic) by dissolving 6.9 g of NaH_2PO_4 in 50 mL of milliQ water. Prepare 1M sodium phosphate buffer (dibasic) by dissolving 7.1 g of Na_2HPO_4 in 50 mL of milliQ water. To make β-lactamase activity buffer, mix 2.11 mL of 1M sodium phosphate buffer (monobasic) and 2.88 mL of 1M sodium phosphate buffer (dibasic) with 40 mL milliQ water. Adjust pH to 7 with 65% [v/v] aq. HCl or 2M NaOH. Once at desired pH, fill to volume (50 mL) with milliQ water. Store at room temperature. Final concentration of buffer is 50 mM sodium phosphate.

4.4.7.30 TEV Protease Activity Buffer

- 304 mg of Tris base
- 9.4 mg of EDTA disodium salt
- 7.7 mg DTT

Dissolve solids in 45 mL milliQ water. Adjust pH to 8 with either 65% [v/v] aq. HCl. Fill to volume (50 mL) with milliQ water. Store at room temperature. Discard after ~ 1 month. Final concentrations of buffer components are as follows: 50 mM Tris-HCl, 0.5 mM EDTA, 1 mM DTT.

4.4.7.31 Sinapinic Acid (SA) MALDI Matrix

- 12 mg of sinapic acid (4-hydroxy-3,5-dimethoxy cinnamic acid, CAS 530-59-6)
- 600 µL of acetonitrile
- 600 µL of milliQ water
- 1.2 µLof trifluoroacetic acid

Weigh out sinapinic acid in a 1.7 mL Eppendorf tube. In a separate tube, mix 600 µL of acetonitrile, 600 µL of milliQ water, and 1.2 µL of trifluoroacetic acid. Transfer the solvent in the

tube to the tube containing the solid SA and dissolve to make the SA matrix. Vortex until SA is completely dissolved. Label tube with the date prepared. SA matrix can be stored at room temperature for ~ 1 month. To prolong shelf-life, store at 4 ºC. The final concentration of SA in the matrix is 10 mg/mL. Sinapinic Acid was purchased from Alfa (Cat. No. AAA1567603).

4.4.7.32 CHCA MALDI Matrix

- 12 mg of α-cyano-4-hydroxycinnamic acid (CHCA, CAS 28166-41-8)
- 600 µL of acetonitrile
- 600 µL of milliQ water
- 1.2 µL of trifluoroacetic acid

Weigh out CHCA in a 1.7 mL Eppendorf tube. In a separate tube, mix 600 µL of acetonitrile, 600 µL of milliQ water, and 1.2 µL of trifluoroacetic acid. Transfer the solvent in the tube to the tube containing the solid CHCA and dissolve to make the CHCA matrix. Vortex until CHCA is completely dissolved. Label tube with the date prepared. CHCA matrix can be stored at room temperature for ~ 1 month. To prolong shelf-life, store at 4 ºC. The final concentration of CHCA in the matrix is 10 mg/mL. Solid CHCA was purchased from Sigma (Cat. No. 476870-2G).

Appendix A – Plasmid Maps

Maps of all plasmids within this document are included in this Appendix section. Plasmids assembled by me are denoted with a black color-coded plasmid name. While plasmids obtained from fellow lab members, provided as gifts from other labs, or purchased from Addgene are denoted using a blue color-coded plasmid name with the name of the lab member or source as specified within the figure caption.

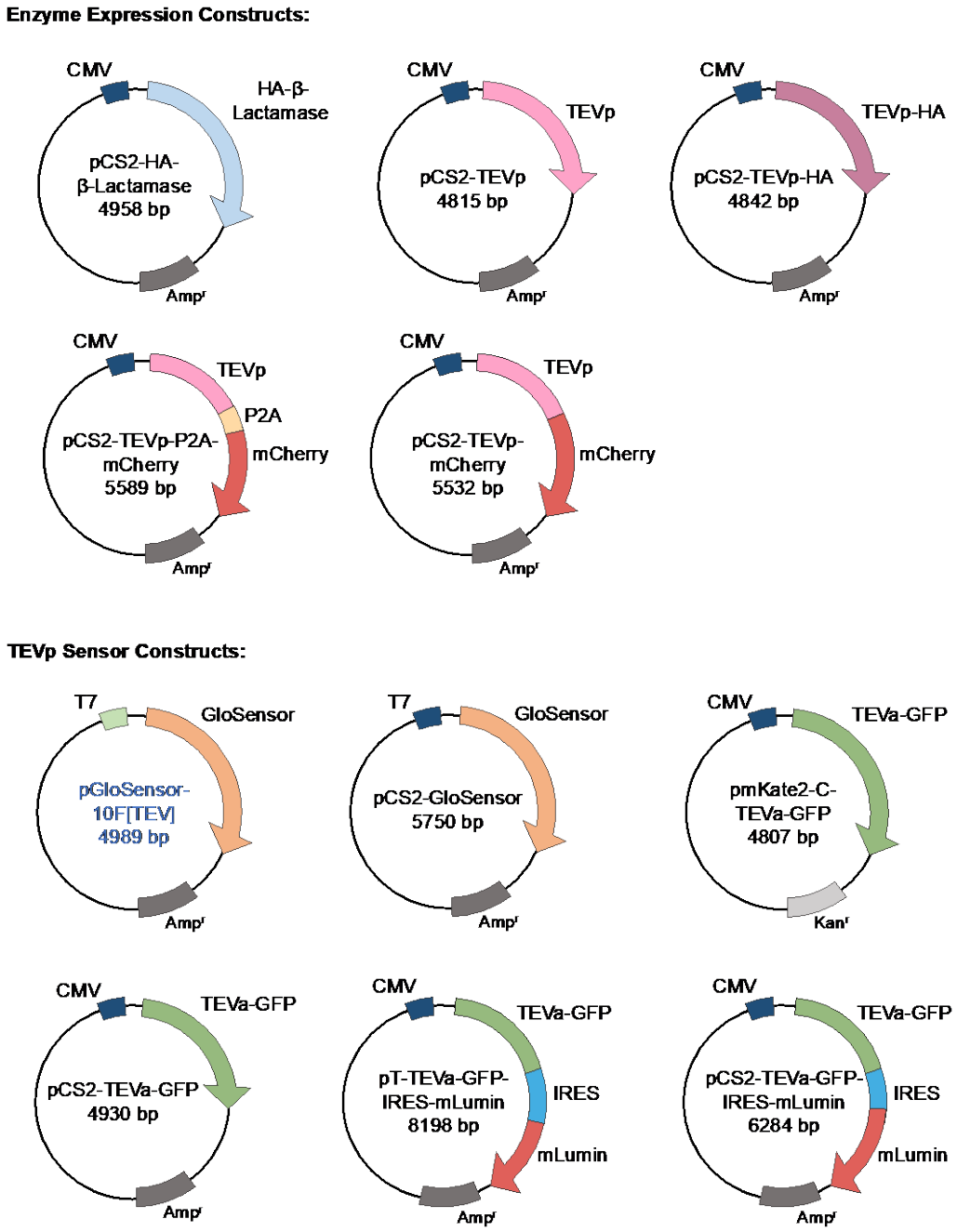

Appendix Figure A-1: Plasmids used for enzyme expression and activity in Chapter 1 Enzyme expression and TEVp sensor constructs used in Chapter 1. pGloSensor-10F[TEV] (also referred to as pTriEx-GloSensor) was obtained from former lab member, Dr. Kalyn Brown.

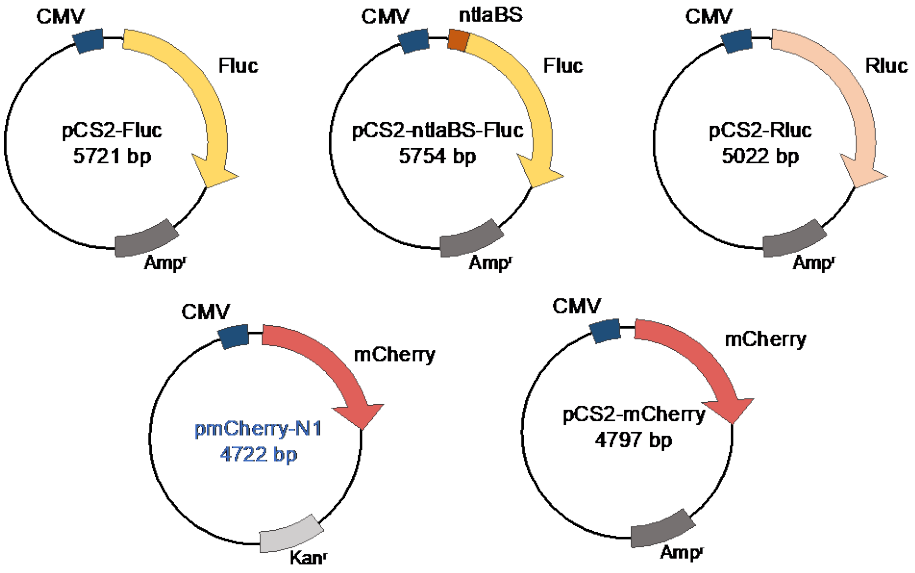

Appendix Figure A-2: Plasmids used for reporter assays in Chapter 1 pmCherry-N1 was obtained from former lab member, Dr. Taylor Courtney.

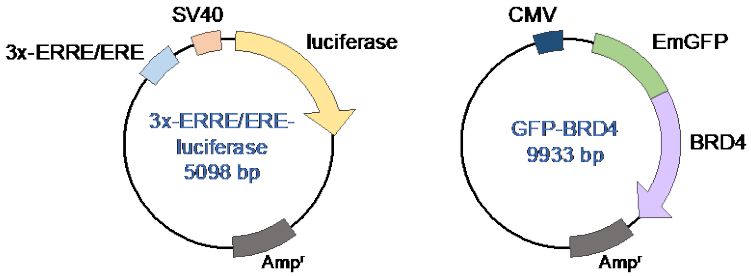

Appendix Figure A-3: Plasmids used in Chapter 3 3X-ERRE/ERE-luciferase was provided as a gift from Dr. Rebecca Riggins (Addgene #37852). GFP-BRD4 was provided as a gift from Dr. Kyle Richards (Addgene #65378).

Bibliography

1. Setten, R. L.; Rossi, J. J.; Han, S. P., The current state and future directions of RNAi-based therapeutics. *Nat Rev Drug Discov* **2019,** *18* (6), 421-446.

2. Shen, X.; Corey, D. R., Chemistry, mechanism and clinical status of antisense oligonucleotides and duplex RNAs. *Nucleic Acids Res* **2018,** *46* (4), 1584-1600.

3. Havens, M. A.; Hastings, M. L., Splice-switching antisense oligonucleotides as therapeutic drugs. *Nucleic Acids Res* **2016,** *44* (14), 6549-63.

4. Chakraborty, S.; Mehtab, S.; Krishnan, Y., The predictive power of synthetic nucleic acid technologies in RNA biology. *Acc Chem Res* **2014,** *47* (6), 1710-9.

5. Khvorova, A.; Watts, J. K., The chemical evolution of oligonucleotide therapies of clinical utility. *Nat Biotechnol* **2017,** *35* (3), 238-248.

6. Pauli, A.; Montague, T. G.; Lennox, K. A.; Behlke, M. A.; Schier, A. F., Antisense Oligonucleotide-Mediated Transcript Knockdown in Zebrafish. *PloS one* **2015,** *10* (10), e0139504.

7. Rinaldi, C.; Wood, M. J. A., Antisense oligonucleotides: the next frontier for treatment of neurological disorders. *Nat Rev Neurol* **2018,** *14* (1), 9-21.

8. Goyal, N.; Narayanaswami, P., Making sense of antisense oligonucleotides: A narrative review. *Muscle Nerve* **2018,** *57* (3), 356-370.

9. Scoles, D. R.; Minikel, E. V.; Pulst, S. M., Antisense oligonucleotides: A primer. *Neurol Genet* **2019,** *5* (2), e323.

10. Nasevicius, A.; Ekker, S. C., Effective targeted gene 'knockdown' in zebrafish. *Nat Genet* **2000,** *26* (2), 216-20.

11. Norris, A.; Streit, A., Morpholinos: studying gene function in the chick. *Methods* **2014,** *66* (3), 454-65.

12. Ochoa, S.; Milam, V. T., Modified Nucleic Acids: Expanding the Capabilities of Functional Oligonucleotides. *Molecules* **2020,** *25* (20).

13. Siva, K.; Covello, G.; Denti, M. A., Exon-skipping antisense oligonucleotides to correct missplicing in neurogenetic diseases. *Nucleic Acid Ther* **2014,** *24* (1), 69-86.

14. Crooke, S. T.; Bennett, C. F., Progress in antisense oligonucleotide therapeutics. *Annu Rev Pharmacol Toxicol* **1996,** *36*, 107-29.

15. Iwamoto, N.; Butler, D. C. D.; Svrzikapa, N.; Mohapatra, S.; Zlatev, I.; Sah, D. W. Y.; Meena; Standley, S. M.; Lu, G.; Apponi, L. H., et al., Control of phosphorothioate stereochemistry substantially increases the efficacy of antisense oligonucleotides. *Nat Biotechnol* **2017,** *35* (9), 845-851.

16. Maio, G.; Enweronye, O.; Zumrut, H. E.; Batool, S.; Van, N.; Mallikaratchy, P., Systematic optimization and modification of a DNA aptamer with 2'-O-methyl RNA analogues. *ChemistrySelect* **2017,** *2* (7), 2335-2340.

17. Ruckman, J.; Green, L. S.; Beeson, J.; Waugh, S.; Gillette, W. L.; Henninger, D. D.; Claesson-Welsh, L.; Janjic, N., 2'-Fluoropyrimidine RNA-based aptamers to the 165-amino acid form of vascular endothelial growth factor (VEGF165). Inhibition of receptor binding and VEGF-induced vascular permeability through interactions requiring the exon 7-encoded domain. *J Biol Chem* **1998,** *273* (32), 20556-67.

18. Kurreck, J.; Wyszko, E.; Gillen, C.; Erdmann, V. A., Design of antisense oligonucleotides stabilized by locked nucleic acids. *Nucleic Acids Res* **2002,** *30* (9), 1911-8.

19. Di Martino, M. T.; Gulla, A.; Gallo Cantafio, M. E.; Altomare, E.; Amodio, N.; Leone, E.; Morelli, E.; Lio, S. G.; Caracciolo, D.; Rossi, M., et al., In vitro and in vivo activity of a novel locked nucleic acid (LNA)-inhibitor-miR-221 against multiple myeloma cells. *PloS one* **2014,** *9* (2), e89659.

20. Eze, N. A.; Milam, V. T., Exploring locked nucleic acids as a bio-inspired materials assembly and disassembly tool. *Soft Matter* **2013,** *9* (8), 2403-2411.

21. Summerton, J.; Weller, D., Morpholino antisense oligomers: design, preparation, and properties. *Antisense Nucleic Acid Drug Dev* **1997,** *7* (3), 187-95.

22. Hardy, S.; Legagneux, V.; Audic, Y.; Paillard, L., Reverse genetics in eukaryotes. *Biol Cell* **2010,** *102* (10), 561-80.

23. Kole, R.; Krainer, A. R.; Altman, S., RNA therapeutics: beyond RNA interference and antisense oligonucleotides. *Nat Rev Drug Discov* **2012,** *11* (2), 125-40.

24. Corey, D. R.; Abrams, J. M., Morpholino antisense oligonucleotides: tools for investigating vertebrate development. *Genome Biol* **2001,** *2* (5), REVIEWS1015.

25. Dhuri, K.; Bechtold, C.; Quijano, E.; Pham, H.; Gupta, A.; Vikram, A.; Bahal, R., Antisense Oligonucleotides: An Emerging Area in Drug Discovery and Development. *J Clin Med* **2020,** *9* (6).

26. Pellestor, F.; Paulasova, P., The peptide nucleic acids (PNAs), powerful tools for molecular genetics and cytogenetics. *Eur J Hum Genet* **2004,** *12* (9), 694-700.

27. Moulton, J. D.; Jiang, S., Gene knockdowns in adult animals: PPMOs and vivo-morpholinos. *Molecules* **2009,** *14* (3), 1304-23.

28. Montazersaheb, S.; Hejazi, M. S.; Nozad Charoudeh, H., Potential of Peptide Nucleic Acids in Future Therapeutic Applications. *Adv Pharm Bull* **2018,** *8* (4), 551-563.

29. Dean, N. M.; Bennett, C. F., Antisense oligonucleotide-based therapeutics for cancer. *Oncogene* **2003,** *22* (56), 9087-96.

30. Yin, H.; Kanasty, R. L.; Eltoukhy, A. A.; Vegas, A. J.; Dorkin, J. R.; Anderson, D. G., Non-viral vectors for gene-based therapy. *Nat Rev Genet* **2014,** *15* (8), 541-55.

31. Juliano, R. L., The delivery of therapeutic oligonucleotides. *Nucleic Acids Res* **2016,** *44* (14), 6518-48.

32. Roberts, T. C.; Langer, R.; Wood, M. J. A., Advances in oligonucleotide drug delivery. *Nature Reviews Drug Discovery* **2020,** *19* (10), 673-694.

33. Suk, J. S.; Xu, Q.; Kim, N.; Hanes, J.; Ensign, L. M., PEGylation as a strategy for improving nanoparticle-based drug and gene delivery. *Advanced Drug Delivery Reviews* **2016,** *99*, 28-51.

34. Danhier, F.; Ansorena, E.; Silva, J. M.; Coco, R.; Le Breton, A.; Préat, V., PLGA-based nanoparticles: An overview of biomedical applications. *Journal of Controlled Release* **2012,** *161* (2), 505-522.

35. McClorey, G.; Banerjee, S., Cell-Penetrating Peptides to Enhance Delivery of Oligonucleotide-Based Therapeutics. *Biomedicines* **2018,** *6* (2).

36. Sharma, V. K.; Sharma, R. K.; Singh, S. K., Antisense oligonucleotides: modifications and clinical trials. *MedChemComm* **2014,** *5* (10), 1454-1471.

37. Aartsma-Rus, A.; Krieg, A. M., FDA Approves Eteplirsen for Duchenne Muscular Dystrophy: The Next Chapter in the Eteplirsen Saga. *Nucleic Acid Ther* **2017,** *27* (1), 1-3.

38. Veldman, M. B.; Lin, S., Zebrafish as a developmental model organism for pediatric research. *Pediatr Res* **2008,** *64* (5), 470-6.

39. Choi, T. Y.; Choi, T. I.; Lee, Y. R.; Choe, S. K.; Kim, C. H., Zebrafish as an animal model for biomedical research. *Exp Mol Med* **2021,** *53* (3), 310-317.

40. Lieschke, G. J.; Currie, P. D., Animal models of human disease: zebrafish swim into view. *Nat Rev Genet* **2007,** *8* (5), 353-67.

41. Howe, K.; Clark, M. D.; Torroja, C. F.; Torrance, J.; Berthelot, C.; Muffato, M.; Collins, J. E.; Humphray, S.; McLaren, K.; Matthews, L., et al., The zebrafish reference genome sequence and its relationship to the human genome. *Nature* **2013,** *496* (7446), 498-503.

42. Kimmel, C. B.; Ballard, W. W.; Kimmel, S. R.; Ullmann, B.; Schilling, T. F., Stages of embryonic development of the zebrafish. *Dev Dyn* **1995,** *203* (3), 253-310.

43. Summerton, J. E., Morpholino, siRNA, and S-DNA compared: impact of structure and mechanism of action on off-target effects and sequence specificity. *Curr Top Med Chem* **2007,** *7* (7), 651-60.

44. Ciruna, B.; Weidinger, G.; Knaut, H.; Thisse, B.; Thisse, C.; Raz, E.; Schier, A. F., Production of maternal-zygotic mutant zebrafish by germ-line replacement. *Proc Natl Acad Sci U S A* **2002,** *99* (23), 14919-24.

45. Bill, B. R.; Petzold, A. M.; Clark, K. J.; Schimmenti, L. A.; Ekker, S. C., A primer for morpholino use in zebrafish. *Zebrafish* **2009,** *6* (1), 69-77.

46. Timme-Laragy, A. R.; Karchner, S. I.; Hahn, M. E., Gene knockdown by morpholino-modified oligonucleotides in the zebrafish (Danio rerio) model: applications for developmental toxicology. *Methods Mol Biol* **2012,** *889*, 51-71.

47. Shestopalov, I. A.; Chen, J. K., Oligonucleotide-based tools for studying zebrafish development. *Zebrafish* **2010,** *7* (1), 31-40.

48. Tomasini, A. J.; Schuler, A. D.; Zebala, J. A.; Mayer, A. N., PhotoMorphs: a novel light-activated reagent for controlling gene expression in zebrafish. *Genesis* **2009,** *47* (11), 736-43.

49. Köster, R.; Sassen, W., A molecular toolbox for genetic manipulation of zebrafish. *Advances in Genomics and Genetics* **2015,** *5*, 151.

50. Urtishak, K. A.; Choob, M.; Tian, X.; Sternheim, N.; Talbot, W. S.; Wickstrom, E.; Farber, S. A., Targeted gene knockdown in zebrafish using negatively charged peptide nucleic acid mimics. *Dev Dyn* **2003,** *228* (3), 405-13.

51. Tang, X.; Maegawa, S.; Weinberg, E. S.; Dmochowski, I. J., Regulating gene expression in zebrafish embryos using light-activated, negatively charged peptide nucleic acids. *J Am Chem Soc* **2007,** *129* (36), 11000-1.

52. Moulton, J. D.; Yan, Y. L., Using Morpholinos to control gene expression. *Curr Protoc Mol Biol* **2008,** *Chapter 26*, Unit 26 8.

53. Kimmel, C. B.; Law, R. D., Cell lineage of zebrafish blastomeres. I. Cleavage pattern and cytoplasmic bridges between cells. *Dev Biol* **1985,** *108* (1), 78-85.

54. Kloosterman, W. P.; Lagendijk, A. K.; Ketting, R. F.; Moulton, J. D.; Plasterk, R. H., Targeted inhibition of miRNA maturation with morpholinos reveals a role for miR-375 in pancreatic islet development. *PLoS Biol* **2007,** *5* (8), e203.

55. Staton, A. A.; Giraldez, A. J., Use of target protector morpholinos to analyze the physiological roles of specific miRNA-mRNA pairs in vivo. *Nat Protoc* **2011,** *6* (12), 2035-49.

56. Giraldez, A. J.; Cinalli, R. M.; Glasner, M. E.; Enright, A. J.; Thomson, J. M.; Baskerville, S.; Hammond, S. M.; Bartel, D. P.; Schier, A. F., MicroRNAs regulate brain morphogenesis in zebrafish. *Science* **2005,** *308* (5723), 833-8.

57. Kamachi, Y.; Okuda, Y.; Kondoh, H., Quantitative assessment of the knockdown efficiency of morpholino antisense oligonucleotides in zebrafish embryos using a luciferase assay. *Genesis* **2008,** *46* (1), 1-7.

58. Schulte-Merker, S.; Stainier, D. Y., Out with the old, in with the new: reassessing morpholino knockdowns in light of genome editing technology. *Development* **2014,** *141* (16), 3103-4.

59. Robu, M. E.; Larson, J. D.; Nasevicius, A.; Beiraghi, S.; Brenner, C.; Farber, S. A.; Ekker, S. C., p53 activation by knockdown technologies. *PLoS Genet* **2007,** *3* (5), e78.

60. Eisen, J. S.; Smith, J. C., Controlling morpholino experiments: don't stop making antisense. *Development* **2008,** *135* (10), 1735-43.

61. Stainier, D. Y. R.; Raz, E.; Lawson, N. D.; Ekker, S. C.; Burdine, R. D.; Eisen, J. S.; Ingham, P. W.; Schulte-Merker, S.; Yelon, D.; Weinstein, B. M., et al., Guidelines for morpholino use in zebrafish. *PLoS Genet* **2017,** *13* (10), e1007000.

62. Stainier, D. Y.; Kontarakis, Z.; Rossi, A., Making sense of anti-sense data. *Developmental cell* **2015,** *32* (1), 7-8.

63. Shestopalov, I. A.; Sinha, S.; Chen, J. K., Light-controlled gene silencing in zebrafish embryos. *Nat Chem Biol* **2007,** *3* (10), 650-1.

64. Ouyang, X.; Shestopalov, I. A.; Sinha, S.; Zheng, G.; Pitt, C. L. W.; Li, W.; Olson, A. J.; Chen, J. K., Versatile Synthesis and Rational Design of Caged Morpholinos. *J. Am. Chem. Soc.* **2009,** *131*, 13255-13269.

65. Deiters, A.; Garner, R. A.; Lusic, H.; Govan, J. M.; Dush, M.; Nascone-Yoder, N. M.; Yoder, J. A., Photocaged morpholino oligomers for the light-regulation of gene function in zebrafish and Xenopus embryos. *J Am Chem Soc* **2010,** *132* (44), 15644-50.

66. Yamazoe, S.; Shestopalov, I. A.; Provost, E.; Leach, S. D.; Chen, J. K., Cyclic caged morpholinos: conformationally gated probes of embryonic gene function. *Angew Chem Int Ed Engl* **2012,** *51* (28), 6908-11.

67. Yamazoe, S.; Liu, Q.; McQuade, L. E.; Deiters, A.; Chen, J. K., Sequential gene silencing using wavelength-selective caged morpholino oligonucleotides. *Angew Chem Int Ed Engl* **2014,** *53* (38), 10114-8.

68. Wang, Y.; Wu, L.; Wang, P.; Lv, C.; Yang, Z.; Tang, X., Manipulation of gene expression in zebrafish using caged circular morpholino oligomers. *Nucleic Acids Res* **2012,** *40* (21), 11155-62.

69. Griepenburg, J. C.; Rapp, T. L.; Carroll, P. J.; Eberwine, J.; Dmochowski, I. J., Ruthenium-Caged Antisense Morpholinos for Regulating Gene Expression in Zebrafish Embryos. *Chem Sci* **2015,** *6* (4), 2342-2346.

70. O'Connor, M. J.; Beebe, L. L.; Deodato, D.; Ball, R. E.; Page, A. T.; VanLeuven, A. J.; Harris, K. T.; Park, S.; Hariharan, V.; Lauderdale, J. D., et al., Bypassing Glutamic Acid Decarboxylase 1 (Gad1) Induced Craniofacial Defects with a Photoactivatable Translation Blocker Morpholino. *ACS Chem Neurosci* **2019,** *10* (1), 266-278.

71. Tallafuss, A.; Gibson, D.; Morcos, P.; Li, Y.; Seredick, S.; Eisen, J.; Washbourne, P., Turning gene function ON and OFF using sense and antisense photo-morpholinos in zebrafish. *Development* **2012,** *139* (9), 1691-9.

72. Liu, Q.; Deiters, A., Optochemical control of deoxyoligonucleotide function via a nucleobase-caging approach. *Acc Chem Res* **2014,** *47* (1), 45-55.

73. Rodrigues-Correia, A.; Koeppel, M. B.; Schafer, F.; Joshi, K. B.; Mack, T.; Heckel, A., Comparison of the duplex-destabilizing effects of nucleobase-caged oligonucleotides. *Anal Bioanal Chem* **2011,** *399* (1), 441-7.

74. Young, D. D.; Lively, M. O.; Deiters, A., Activation and Deactivation of DNAzyme and Antisense Function with Light for the Photochemical Regulation of Gene Expression in Mammalian Cells. *J Am Chem Soc* **2010,** *132* (17), 6183-6193.

75. Govan, J. M.; Uprety, R.; Thomas, M.; Lusic, H.; Lively, M. O.; Deiters, A., Cellular delivery and photochemical activation of antisense agents through a nucleobase caging strategy. *ACS Chem Biol* **2013,** *8* (10), 2272-82.

76. Bardhan, A.; Deiters, A.; Ettensohn, C. A., Conditional gene knockdowns in sea urchins using caged morpholinos. *Dev Biol* **2021,** *475*, 21-29.

77. Pattanayak, S.; Vazquez-Maldonado, L. A.; Deiters, A.; Chen, J. K., Combinatorial control of gene function with wavelength-selective caged morpholinos. *Methods Enzymol* **2019,** *624*, 69-88.

78. Bardhan, A.; Deiters, A., Development of photolabile protecting groups and their application to the optochemical control of cell signaling. *Curr Opin Struct Biol* **2019,** *57*, 164-175.

79. Klan, P.; Solomek, T.; Bochet, C. G.; Blanc, A.; Givens, R.; Rubina, M.; Popik, V.; Kostikov, A.; Wirz, J., Photoremovable protecting groups in chemistry and biology: reaction mechanisms and efficacy. *Chem Rev* **2013,** *113* (1), 119-91.

80. Bardhan, A.; Deiters, A., Development of photolabile protecting groups and their application to the optochemical control of cell signaling. *Current Opinion in Structural Biology* **2019,** *57*, 164-175.

81. Yamazoe, S.; McQuade, L. E.; Chen, J. K., Nitroreductase-activatable morpholino oligonucleotides for in vivo gene silencing. *ACS Chem Biol* **2014,** *9* (9), 1985-90.

82. Clark, A. J.; Iwobi, M.; Cui, W.; Crompton, M.; Harold, G.; Hobbs, S.; Kamalati, T.; Knox, R.; Neil, C.; Yull, F., et al., Selective cell ablation in transgenic mice expression E. coli nitroreductase. *Gene Ther* **1997,** *4* (2), 101-10.

83. Pisharath, H.; Rhee, J. M.; Swanson, M. A.; Leach, S. D.; Parsons, M. J., Targeted ablation of beta cells in the embryonic zebrafish pancreas using E. coli nitroreductase. *Mech Dev* **2007,** *124* (3), 218-29.

84. Yang, L.; Eberwine, J. H.; Dmochowski, I. J., Caspase-Activated Oligonucleotide Probe. *Bioconjug Chem* **2020,** *31* (9), 2172-2178.

85. Fleming, A., On the Antibacterial Action of Cultures of a Penicillium, with Special Reference to their Use in the Isolation of B. influenzae. *Br J Exp Pathol* **1929,** *10* (3), 226-236.

86. Tooke, C. L.; Hinchliffe, P.; Bragginton, E. C.; Colenso, C. K.; Hirvonen, V. H. A.; Takebayashi, Y.; Spencer, J., beta-Lactamases and beta-Lactamase Inhibitors in the 21st Century. *J Mol Biol* **2019,** *431* (18), 3472-3500.

87. Bonomo, R. A., beta-Lactamases: A Focus on Current Challenges. *Cold Spring Harb Perspect Med* **2017,** *7* (1).

88. Bush, K.; Bradford, P. A., Interplay between beta-lactamases and new beta-lactamase inhibitors. *Nat Rev Microbiol* **2019,** *17* (5), 295-306.

89. Mojica, M. F.; Bonomo, R. A.; Fast, W., B1-Metallo-beta-Lactamases: Where Do We Stand? *Curr Drug Targets* **2016,** *17* (9), 1029-50.

90. Perry, C. M.; Markham, A., Piperacillin/tazobactam: an updated review of its use in the treatment of bacterial infections. *Drugs* **1999,** *57* (5), 805-43.

91. Drawz, S. M.; Bonomo, R. A., Three decades of beta-lactamase inhibitors. *Clin Microbiol Rev* **2010,** *23* (1), 160-201.

92. Lee, N.; Yuen, K. Y.; Kumana, C. R., Clinical role of beta-lactam/beta-lactamase inhibitor combinations. *Drugs* **2003,** *63* (14), 1511-24.

93. Schellmann, N.; Deckert, P. M.; Bachran, D.; Fuchs, H.; Bachran, C., Targeted enzyme prodrug therapies. *Mini Rev Med Chem* **2010,** *10* (10), 887-904.

94. Bagshawe, K. D., Antibody-directed enzyme prodrug therapy (ADEPT) for cancer. *Expert Rev Anticancer Ther* **2006,** *6* (10), 1421-31.

95. Zhang, J.; Kale, V.; Chen, M., Gene-directed enzyme prodrug therapy. *AAPS J* **2015,** *17* (1), 102-10.

96. Harding, F. A.; Liu, A. D.; Stickler, M.; Razo, O. J.; Chin, R.; Faravashi, N.; Viola, W.; Graycar, T.; Yeung, V. P.; Aehle, W., et al., A beta-lactamase with reduced immunogenicity for the targeted delivery of chemotherapeutics using antibody-directed enzyme prodrug therapy. *Mol Cancer Ther* **2005,** *4* (11), 1791-800.

97. Vrudhula, V. M.; Svensson, H. P.; Senter, P. D., Cephalosporin derivatives of doxorubicin as prodrugs for activation by monoclonal antibody-beta-lactamase conjugates. *J Med Chem* **1995,** *38* (8), 1380-5.

98. Rodrigues, M. L.; Carter, P.; Wirth, C.; Mullins, S.; Lee, A.; Blackburn, B. K., Synthesis and beta-lactamase-mediated activation of a cephalosporin-taxol prodrug. *Chem Biol* **1995,** *2* (4), 223-7.

99. Vrudhula, V. M.; Kerr, D. E.; Siemers, N. O.; Dubowchik, G. M.; Senter, P. D., Cephalosporin prodrugs of paclitaxel for immunologically specific activation by L-49-sFv-beta-lactamase fusion protein. *Bioorg Med Chem Lett* **2003,** *13* (3), 539-42.

100. Meyer, D. L.; Jungheim, L. N.; Law, K. L.; Mikolajczyk, S. D.; Shepherd, T. A.; Mackensen, D. G.; Briggs, S. L.; Starling, J. J., Site-specific prodrug activation by antibody-beta-lactamase conjugates: regression and long-term growth inhibition of human colon carcinoma xenograft models. *Cancer Res* **1993,** *53* (17), 3956-63.

101. Zhou, X.; Wang, H.; Shi, P.; Meng, A. M., Characterization of a fusion protein of RGD4C and the beta-lactamase variant for antibody-directed enzyme prodrug therapy. *Onco Targets Ther* **2014,** *7*, 535-41.

102. Zlokarnik, G.; Negulescu, P. A.; Knapp, T. E.; Mere, L.; Burres, N.; Feng, L.; Whitney, M.; Roemer, K.; Tsien, R. Y., Quantitation of transcription and clonal selection of single living cells with beta-lactamase as reporter. *Science* **1998,** *279* (5347), 84-8.

103. Boyd, D. B., Electronic structures of cephalosporins and penicillins. 15. Inductive effect of the 3-position side chain in cephalosporins. *J Med Chem* **1984,** *27* (1), 63-6.

104. Faraci, W. S.; Pratt, R. F., Elimination of a good leaving group from the 3'-position of a cephalosporin need not be concerted with .beta.-lactam ring opening: TEM-2 .beta.-lactamase-catalyzed hydrolysis of pyridine-2-azo-4'-(N',N'-dimethylaniline) cephalosporin (PADAC) and of cephaloridine. *Journal of the American Chemical Society* **1984,** *106* (5), 1489-1490.

105. Raz, E.; Zlokarnik, G.; Tsien, R. Y.; Driever, W., beta-lactamase as a marker for gene expression in live zebrafish embryos. *Dev Biol* **1998,** *203* (2), 290-4.

106. Shabanpoor, F.; Gait, M. J., Development of a general methodology for labelling peptide–morpholino oligonucleotide conjugates using alkyne–azide click chemistry. *Chemical Communications* **2013,** *49* (87), 10260-10262.

107. Miller, L. M.; Herman, R.; Gyulev, I.; Krauss, T. F.; Thomas, G. H.; Duhme-Klair, A.-K., Synthesis and biochemical evaluation of cephalosporin analogues equipped with chemical tethers. *RSC Advances* **2020,** *10* (60), 36485-36494.

108. Jung, F.; Delvare, C.; Boucherot, D.; Hamon, A.; Ackerley, N.; Betts, M. J., Synthesis and structure-activity relationship of new cephalosporins with amino heterocycles at C-7. Dependence of the antibacterial spectrum and .beta.-lactamase stability on the pKa of the C-7 heterocycle. *Journal of Medicinal Chemistry* **1991,** *34* (3), 1110-1116.

109. D'Astolfo, D. S.; Pagliero, R. J.; Pras, A.; Karthaus, W. R.; Clevers, H.; Prasad, V.; Lebbink, R. J.; Rehmann, H.; Geijsen, N., Efficient intracellular delivery of native proteins. *Cell* **2015,** *161* (3), 674-690.

110. O'Callaghan, C. H.; Morris, A.; Kirby, S. M.; Shingler, A. H., Novel method for detection of beta-lactamases by using a chromogenic cephalosporin substrate. *Antimicrob Agents Chemother* **1972,** *1* (4), 283-8.

111. Yuan, S.; Sun, Z., Microinjection of mRNA and morpholino antisense oligonucleotides in zebrafish embryos. *J Vis Exp* **2009,** (27).

112. Schulte-Merker, S.; van Eeden, F. J.; Halpern, M. E.; Kimmel, C. B.; Nusslein-Volhard, C., no tail (ntl) is the zebrafish homologue of the mouse T (Brachyury) gene. *Development* **1994,** *120* (4), 1009-15.

113. Halpern, M. E.; Ho, R. K.; Walker, C.; Kimmel, C. B., Induction of muscle pioneers and floor plate is distinguished by the zebrafish no tail mutation. *Cell* **1993,** *75* (1), 99-111.

114. Horatscheck, A.; Wagner, S.; Ortwein, J.; Kim, B. G.; Lisurek, M.; Beligny, S.; Schutz, A.; Rademann, J., Benzoylphosphonate-based photoactive phosphopeptide mimetics for modulation of protein tyrosine phosphatases and highly specific labeling of SH2 domains. *Angew Chem Int Ed Engl* **2012,** *51* (37), 9441-7.

115. IDT Codon Optimization Tool. https://www.idtdna.com/CodonOpt.

116. Carrington, J. C.; Dougherty, W. G., Small nuclear inclusion protein encoded by a plant potyvirus genome is a protease. *J Virol* **1987,** *61* (8), 2540-8.

117. Dougherty, W. G.; Parks, T. D.; Cary, S. M.; Bazan, J. F.; Fletterick, R. J., Characterization of the catalytic residues of the tobacco etch virus 49-kDa proteinase. *Virology* **1989,** *172* (1), 302-10.

118. Bazan, J. F.; Fletterick, R. J., Viral cysteine proteases are homologous to the trypsin-like family of serine proteases: structural and functional implications. *Proc Natl Acad Sci U S A* **1988,** *85* (21), 7872-6.

119. Carrington, J. C.; Dougherty, W. G., A viral cleavage site cassette: identification of amino acid sequences required for tobacco etch virus polyprotein processing. *Proc Natl Acad Sci U S A* **1988,** *85* (10), 3391-5.

120. Polayes, D. A.; Parks, T. D.; Johnston, S. A.; Dougherty, W. G., Application of TEV Protease in Protein Production. *Methods Mol Med* **1998,** *13*, 169-83.

121. Phan, J.; Zdanov, A.; Evdokimov, A. G.; Tropea, J. E.; Peters, H. K., 3rd; Kapust, R. B.; Li, M.; Wlodawer, A.; Waugh, D. S., Structural basis for the substrate specificity of tobacco etch virus protease. *J Biol Chem* **2002,** *277* (52), 50564-72.

122. Verhoeven, K. D.; Altstadt, O. C.; Savinov, S. N., Intracellular detection and evolution of site-specific proteases using a genetic selection system. *Appl Biochem Biotechnol* **2012,** *166* (5), 1340-54.

123. Packer, M. S.; Rees, H. A.; Liu, D. R., Phage-assisted continuous evolution of proteases with altered substrate specificity. *Nat Commun* **2017,** *8* (1), 956.

124. Denard, C. A.; Paresi, C.; Yaghi, R.; McGinnis, N.; Bennett, Z.; Yi, L.; Georgiou, G.; Iverson, B. L., YESS 2.0, a Tunable Platform for Enzyme Evolution, Yields Highly Active TEV Protease Variants. *ACS Synth Biol* **2021,** *10* (1), 63-71.

125. Williams, D. J.; Puhl, H. L., 3rd; Ikeda, S. R., Rapid modification of proteins using a rapamycin-inducible tobacco etch virus protease system. *PloS one* **2009,** *4* (10), e7474.

126. Wehr, M. C.; Laage, R.; Bolz, U.; Fischer, T. M.; Grunewald, S.; Scheek, S.; Bach, A.; Nave, K. A.; Rossner, M. J., Monitoring regulated protein-protein interactions using split TEV. *Nat Methods* **2006,** *3* (12), 985-93.

127. Blommel, P. G.; Fox, B. G., A combined approach to improving large-scale production of tobacco etch virus protease. *Protein Expr Purif* **2007,** *55* (1), 53-68.

128. Cabrita, L. D.; Gilis, D.; Robertson, A. L.; Dehouck, Y.; Rooman, M.; Bottomley, S. P., Enhancing the stability and solubility of TEV protease using in silico design. *Protein Sci* **2007,** *16* (11), 2360-7.

129. Fang, L.; Jia, K.-Z.; Tang, Y.-L.; Ma, D.-Y.; Yu, M.; Hua, Z.-C., An improved strategy for high-level production of TEV protease in Escherichia coli and its purification and characterization. *Protein Expression and Purification* **2007,** *51* (1), 102-109.

130. Harder, B.; Schomburg, A.; Pflanz, R.; Kustner, K.; Gerlach, N.; Schuh, R., TEV protease-mediated cleavage in Drosophila as a tool to analyze protein functions in living organisms. *Biotechniques* **2008,** *44* (6), 765-72.

131. Pauli, A.; Althoff, F.; Oliveira, R. A.; Heidmann, S.; Schuldiner, O.; Lehner, C. F.; Dickson, B. J.; Nasmyth, K., Cell-type-specific TEV protease cleavage reveals cohesin functions in Drosophila neurons. *Developmental cell* **2008,** *14* (2), 239-51.

132. Dougherty, W. G.; Carrington, J. C.; Cary, S. M.; Parks, T. D., Biochemical and mutational analysis of a plant virus polyprotein cleavage site. *EMBO J* **1988,** *7* (5), 1281-7.

133. Dougherty, W. G.; Cary, S. M.; Parks, T. D., Molecular genetic analysis of a plant virus polyprotein cleavage site: a model. *Virology* **1989,** *171* (2), 356-64.

134. Wei, L.; Cai, X.; Qi, Z.; Rong, L.; Cheng, B.; Fan, J., In vivo and in vitro characterization of TEV protease mutants. *Protein Expr Purif* **2012,** *83* (2), 157-63.

135. Kapust, R. B.; Tözsér, J.; Fox, J. D.; Anderson, D. E.; Cherry, S.; Copeland, T. D.; Waugh, D. S., Tobacco etch virus protease: mechanism of autolysis and rational design of stable mutants with wild-type catalytic proficiency. *Protein Engineering, Design and Selection* **2001,** *14* (12), 993-1000.

136. Kim, J. H.; Lee, S. R.; Li, L. H.; Park, H. J.; Park, J. H.; Lee, K. Y.; Kim, M. K.; Shin, B. A.; Choi, S. Y., High cleavage efficiency of a 2A peptide derived from porcine teschovirus-1 in human cell lines, zebrafish and mice. *PloS one* **2011,** *6* (4), e18556.

137. To, T. L.; Schepis, A.; Ruiz-Gonzalez, R.; Zhang, Q.; Yu, D.; Dong, Z.; Coughlin, S. R.; Shu, X., Rational Design of a GFP-Based Fluorogenic Caspase Reporter for Imaging Apoptosis In Vivo. *Cell chemical biology* **2016,** *23* (7), 875-882.

138. Nicholls, S. B.; Chu, J.; Abbruzzese, G.; Tremblay, K. D.; Hardy, J. A., Mechanism of a genetically encoded dark-to-bright reporter for caspase activity. *J Biol Chem* **2011,** *286* (28), 24977-86.

139. Waldo, G. S.; Standish, B. M.; Berendzen, J.; Terwilliger, T. C., Rapid protein-folding assay using green fluorescent protein. *Nat Biotechnol* **1999,** *17* (7), 691-5.

140. Fahrenkrug, S. C.; Clark, K. J.; Dahlquist, M. O.; Hackett, P. B., Jr., Dicistronic Gene Expression in Developing Zebrafish. *Mar Biotechnol (NY)* **1999,** *1* (6), 552-561.

141. Banaszynski, L. A.; Wandless, T. J., Conditional control of protein function. *Chem Biol* **2006,** *13* (1), 11-21.

142. Gangopadhyay, S. A.; Cox, K. J.; Manna, D.; Lim, D.; Maji, B.; Zhou, Q.; Choudhary, A., Precision Control of CRISPR-Cas9 Using Small Molecules and Light. *Biochemistry* **2019,** *58* (4), 234-244.

143. Buskirk, A. R.; Liu, D. R., Creating small-molecule-dependent switches to modulate biological functions. *Chem Biol* **2005,** *12* (2), 151-61.

144. Chang, A. L.; Wolf, J. J.; Smolke, C. D., Synthetic RNA switches as a tool for temporal and spatial control over gene expression. *Curr Opin Biotechnol* **2012,** *23* (5), 679-88.

145. Bugaut, A.; Balasubramanian, S., 5'-UTR RNA G-quadruplexes: translation regulation and targeting. *Nucleic Acids Res* **2012,** *40* (11), 4727-41.

146. Topp, S.; Gallivan, J. P., Emerging applications of riboswitches in chemical biology. *ACS Chem Biol* **2010,** *5* (1), 139-48.

147. Nguyen, S. S.; Prescher, J. A., Developing bioorthogonal probes to span a spectrum of reactivities. *Nature Reviews Chemistry* **2020,** *4* (9), 476-489.

148. Agard, N. J.; Baskin, J. M.; Prescher, J. A.; Lo, A.; Bertozzi, C. R., A comparative study of bioorthogonal reactions with azides. *ACS Chem Biol* **2006,** *1* (10), 644-8.

149. Sletten, E. M.; Bertozzi, C. R., From mechanism to mouse: a tale of two bioorthogonal reactions. *Acc Chem Res* **2011,** *44* (9), 666-76.

150. Azoulay, M.; Tuffin, G.; Sallem, W.; Florent, J. C., A new drug-release method using the Staudinger ligation. *Bioorg Med Chem Lett* **2006,** *16* (12), 3147-9.

151. van Brakel, R.; Vulders, R. C.; Bokdam, R. J.; Grull, H.; Robillard, M. S., A doxorubicin prodrug activated by the staudinger reaction. *Bioconjug Chem* **2008,** *19* (3), 714-8.

152. Alouane, A.; Labruere, R.; Le Saux, T.; Schmidt, F.; Jullien, L., Self-immolative spacers: kinetic aspects, structure-property relationships, and applications. *Angew Chem Int Ed Engl* **2015,** *54* (26), 7492-509.

153. Erez, R.; Shabat, D., The azaquinone-methide elimination: comparison study of 1,6- and 1,4-eliminations under physiological conditions. *Organic & Biomolecular Chemistry* **2008,** *6* (15), 2669-2672.

154. Mosey, R. A.; Floreancig, P. E., Versatile approach to α-alkoxy carbamate synthesis and stimulus-responsive alcohol release. *Organic & Biomolecular Chemistry* **2012,** *10* (39), 7980-7985.

155. Lukasak, B.; Morihiro, K.; Deiters, A., Aryl Azides as Phosphine-Activated Switches for Small Molecule Function. *Sci Rep* **2019,** *9* (1), 1470.

156. Wesalo, J. S.; Luo, J.; Morihiro, K.; Liu, J.; Deiters, A., Phosphine-Activated Lysine Analogues for Fast Chemical Control of Protein Subcellular Localization and Protein SUMOylation. *Chembiochem* **2020,** *21* (1-2), 141-148.

157. Habeeb, A. G.; Praveen Rao, P. N.; Knaus, E. E., Design and Synthesis of Celecoxib and Rofecoxib Analogues as Selective Cyclooxygenase-2 (COX-2) Inhibitors: Replacement of Sulfonamide and Methylsulfonyl Pharmacophores by an Azido Bioisostere. *Journal of Medicinal Chemistry* **2001,** *44* (18), 3039-3042.

158. Mitchison, T. J.; Sawin, K. E.; Theriot, J. A.; Gee, K.; Mallavarapu, A., Caged fluorescent probes. *Methods Enzymol* **1998,** *291*, 63-78.

159. Karstens, T.; Kobs, K., Rhodamine B and rhodamine 101 as reference substances for fluorescence quantum yield measurements. *The Journal of Physical Chemistry* **1980,** *84* (14), 1871-1872.

160. Wysocki, L. M.; Grimm, J. B.; Tkachuk, A. N.; Brown, T. A.; Betzig, E.; Lavis, L. D., Facile and general synthesis of photoactivatable xanthene dyes. *Angew Chem Int Ed Engl* **2011,** *50* (47), 11206-9.

161. Luo, J.; Liu, Q.; Morihiro, K.; Deiters, A., Small-molecule control of protein function through Staudinger reduction. *Nat Chem* **2016,** *8* (11), 1027-1034.

162. Saneyoshi, H.; Ochikubo, T.; Mashimo, T.; Hatano, K.; Ito, Y.; Abe, H., Triphenylphosphinecarboxamide: An Effective Reagent for the Reduction of Azides and Its Application to Nucleic Acid Detection. *Organic Letters* **2014,** *16* (1), 30-33.

163. Gee, K. R.; Weinberg, E. S.; Kozlowski, D. J., Caged Q-rhodamine dextran: a new photoactivated fluorescent tracer. *Bioorganic & Medicinal Chemistry Letters* **2001,** *11* (16), 2181-2183.

164. Kozlowski, D. J.; Weinberg, E. S., Photoactivatable (Caged) Fluorescein as a Cell Tracer for Fate Mapping in the Zebrafish Embryo. In *Developmental Biology Protocols: Volume I*, Walker, J. M.; Tuan, R. S.; Lo, C. W., Eds. Humana Press: Totowa, NJ, 2000; pp 349-355.

165. Kimmel, C. B.; Law, R. D., Cell lineage of zebrafish blastomeres: I. Cleavage pattern and cytoplasmic bridges between cells. *Developmental Biology* **1985,** *108* (1), 78-85.

166. Woo, K.; Fraser, S. E., Order and coherence in the fate map of the zebrafish nervous system. *Development* **1995,** *121* (8), 2595-2609.

167. Au - Clanton, J. A.; Au - Shestopalov, I. A.; Au - Chen, J. K.; Au - Gamse, J. T., Lineage Labeling of Zebrafish Cells with Laser Uncagable Fluorescein Dextran. *JoVE* **2011,** (50), e2672.

168. Wetts, R.; Fraser, S. E., Microinjection of fluorescent tracers to study neural cell lineages. *Development* **1991,** *113* (Supplement_2), 1-8.

169. Strehlow, D.; Gilbert, W., A fate map for the first cleavages of the zebrafish. *Nature* **1993,** *361* (6411), 451-453.

170. Burns, C. G.; Milan, D. J.; Grande, E. J.; Rottbauer, W.; MacRae, C. A.; Fishman, M. C., High-throughput assay for small molecules that modulate zebrafish embryonic heart rate. *Nat Chem Biol* **2005,** *1* (5), 263-4.

171. Sasmal, P. K.; Carregal-Romero, S.; Han, A. A.; Streu, C. N.; Lin, Z.; Namikawa, K.; Elliott, S. L.; Koster, R. W.; Parak, W. J.; Meggers, E., Catalytic azide reduction in biological environments. *Chembiochem* **2012,** *13* (8), 1116-20.

172. Showell, C.; Binder, O.; Conlon, F. L., T-box genes in early embryogenesis. *Dev Dyn* **2004,** *229* (1), 201-18.

173. Taylor, M. F.; Paulauskis, J. D.; Weller, D. D.; Kobzik, L., In vitro efficacy of morpholino-modified antisense oligomers directed against tumor necrosis factor-alpha mRNA. *J Biol Chem* **1996,** *271* (29), 17445-52.

174. Schulte-Merker, S.; Ho, R. K.; Herrmann, B. G.; Nusslein-Volhard, C., The protein product of the zebrafish homologue of the mouse T gene is expressed in nuclei of the germ ring and the notochord of the early embryo. *Development* **1992,** *116* (4), 1021-32.

175. Ruvinsky, I.; Silver, L. M.; Ho, R. K., Characterization of the zebrafish tbx16 gene and evolution of the vertebrate T-box family. *Dev Genes Evol* **1998,** *208* (2), 94-9.

176. Warga, R. M.; Mueller, R. L.; Ho, R. K.; Kane, D. A., Zebrafish Tbx16 regulates intermediate mesoderm cell fate by attenuating Fgf activity. *Dev Biol* **2013,** *383* (1), 75-89.

177. Amacher, S. L.; Draper, B. W.; Summers, B. R.; Kimmel, C. B., The zebrafish T-box genes no tail and spadetail are required for development of trunk and tail mesoderm and medial floor plate. *Development* **2002,** *129* (14), 3311-23.

178. Griffin, K. J.; Amacher, S. L.; Kimmel, C. B.; Kimelman, D., Molecular identification of spadetail: regulation of zebrafish trunk and tail mesoderm formation by T-box genes. *Development* **1998,** *125* (17), 3379-88.

179. Ho, R. K.; Kane, D. A., Cell-autonomous action of zebrafish spt-1 mutation in specific mesodermal precursors. *Nature* **1990,** *348* (6303), 728-30.

180. Arbogast, D. Determining the Concentration of your Morpholino in Solution using the NanoDrop ND-1000 Spectrophotometer. https://www.gene-tools.com/sites/default/files/NanoDrop%20ND-2.pdf.

181. Gibson, D. G.; Young, L.; Chuang, R. Y.; Venter, J. C.; Hutchison, C. A., 3rd; Smith, H. O., Enzymatic assembly of DNA molecules up to several hundred kilobases. *Nat Methods* **2009,** *6* (5), 343-5.

182. Brown, W.; Deiters, A., Light-activation of Cre recombinase in zebrafish embryos through genetic code expansion. *Methods Enzymol* **2019,** *624*, 265-281.

183. Kirchmair, J.; Goller, A. H.; Lang, D.; Kunze, J.; Testa, B.; Wilson, I. D.; Glen, R. C.; Schneider, G., Predicting drug metabolism: experiment and/or computation? *Nat Rev Drug Discov* **2015,** *14* (6), 387-404.

184. Wienkers, L. C.; Heath, T. G., Predicting in vivo drug interactions from in vitro drug discovery data. *Nat Rev Drug Discov* **2005,** *4* (10), 825-33.

185. Di, L., The role of drug metabolizing enzymes in clearance. *Expert Opin Drug Metab Toxicol* **2014,** *10* (3), 373-393.

186. Iyanagi, T., Molecular mechanism of phase I and phase II drug-metabolizing enzymes: implications for detoxification. *Int Rev Cytol* **2007,** *260*, 35-112.

187. Penner, N.; Woodward, C.; Prakash, C., Drug Metabolizing Enzymes and Biotransformation Reactions. In *ADME-Enabling Technologies in Drug Design and Development*, 1st ed.; Zhang, D.; Surapanemi, S., Eds. John Wiley & Sons, Inc.: 2012.

188. Jancova, P.; Anzenbacher, P.; Anzenbacherova, E., Phase II drug metabolizing enzymes. *Biomed Pap Med Fac Univ Palacky Olomouc Czech Repub* **2010,** *154* (2), 103-116.

189. Chapman, E.; Best, M. D.; Hanson, S. R.; Wong, C. H., Sulfotransferases: structure, mechanism, biological activity, inhibition, and synthetic utility. *Angew Chem Int Ed Engl* **2004,** *43* (27), 3526-48.

190. Visser, T. J., Role of sulfonation in thyroid hormone metabolism. *Chem Biol Interact* **1994,** *92* (1-3), 293-303.

191. Nagar, S.; Walther, S.; Blanchard, R. L., Sulfotransferase (SULT) 1A1 polymorphic variants *1, *2, and *3 are associated with altered enzymatic activity, cellular phenotype, and protein degradation. *Mol Pharmacol* **2006,** *69* (6), 2084-92.

192. James, M. O.; Ambadapadi, S., Interactions of cytosolic sulfotransferases with xenobiotics. *Drug Metab Rev* **2013,** *45* (4), 401-414.

193. Barnett, A. C.; Tsvetanov, S.; Gamage, N.; Martin, J. L.; Duggleby, R. G.; McManus, M. E., Active site mutations and substrate inhibition in human sulfotransferase 1A1 and 1A3. *J Biol Chem* **2004,** *279* (18), 18799-805.

194. Berger, I.; Guttman, C.; Amar, D.; Zarivach, R.; Aharoni, A., The molecular basis for the broad substrate specificity of human sulfotransferase 1A1. *PloS one* **2011,** *6* (11), e26794.

195. Brix, L. A.; Barnett, A. C.; Duggleby, R. G.; Leggett, B.; McManus, M. E., Analysis of the Substrate Specificity of Human Sulfotransferases SULT1A1 and SULT1A3: Site-Directed Mutagenesis and Kinetic Studies. *Biochemistry* **1999,** *38*, 10474-10479.

196. Cook, I.; Wang, T.; Falany, C. N.; Leyh, T. S., A nucleotide-gated molecular pore selects sulfotransferase substrates. *Biochemistry* **2012,** *51* (28), 5674-83.

197. Cook, I.; Wang, T.; Almo, S. C.; Kim, J.; Falany, C. N.; Leyh, T. S., The Gate That Governs Sulfotransferase Selectivity. *Biochemistry* **2012,** *52* (2), 415-424.

198. Driscoll, W. J.; Komatsu, K.; Strott, C. A., Proposed active site domain in estrogen sulfotransferase as determined by mutational analysis. *Proc Natl Acad Sci USA* **1995,** *92*, 12328-12332.

199. Wang, T.; Cook, I.; Falany, C. N.; Leyh, T. S., Paradigms of sulfotransferase catalysis: the mechanism of SULT2A1. *J Biol Chem* **2014,** *289* (38), 26474-80.

200. Chen, G., Histidine residues in human phenol sulfotransferases. *Biochem Pharmacol* **2004,** *67* (7), 1355-61.

201. Kakuta, Y.; Petrotchenko, E. V.; Pedersen, L. C.; Negishi, M., The Sulfuryl Transfer Mechanism. *J Biol Chem* **1998,** *273* (42), 27325-27330.

202. Gamage, N.; Barnett, A.; Hempel, N.; Duggleby, R. G.; Windmill, K. F.; Martin, J. L.; McManus, M. E., Human sulfotransferases and their role in chemical metabolism. *Toxicol Sci* **2006,** *90* (1), 5-22.

203. Steventon, G. B.; Heafield, M. T.; Waring, R. H.; Williams, A. C., Xenobiotic metabolism in Parkinson's disease. *Neurology* **1989,** *39* (7), 883-887.

204. Li, L.; Falany, C. N., Elevated hepatic SULT1E1 activity in mouse models of cystic fibrosis alters the regulation of estrogen responsive proteins. *J Cyst Fibros* **2007,** *6* (1), 23-30.

205. Bischoff, E. D.; Daige, C. L.; Petrowski, M.; Dedman, H.; Pattison, J.; Juliano, J.; Li, A. C.; Schulman, I. G., Non-redundant roles for LXRα and LXRβ in atherosclerosis susceptibility in low density lipoprotein receptor knockout mice. *Journal of Lipid Research* **2010,** *51* (5), 900-906.

206. Sidharthan, N. P.; Minchin, R. F.; Butcher, N. J., Cytosolic sulfotransferase 1A3 is induced by dopamine and protects neuronal cells from dopamine toxicity: role of D1 receptor-N-methyl-D-aspartate receptor coupling. *J Biol Chem* **2013,** *288* (48), 34364-74.

207. Gamage, N. U.; Duggleby, R. G.; Barnett, A. C.; Tresillian, M.; Latham, C. F.; Liyou, N. E.; McManus, M. E.; Martin, J. L., Structure of a human carcinogen-converting enzyme, SULT1A1. Structural and kinetic implications of substrate inhibition. *J Biol Chem* **2003,** *278* (9), 7655-62.

208. Shukla, D.; Liu, J.; Blaiklock, P.; Shworak, N. W.; Bai, X.; Esko, J. D.; Cohen, G. H.; Eisenberg, R. J.; Rosenberg, R. D.; Spear, P. G., A novel role for 3-O-sulfated heparan sulfate in herpes simplex virus 1 entry. *Cell* **1999,** *99* (1), 13-22.

209. Yao-Borengasser, A.; Rogers, L. J.; Edavana, V. K.; Penney, R. B.; Yu, X.; Dhakal, I. B.; Williams, S.; Kadlubar, S. A., Sulfotransferase 1A1 (SULT1A1) gene expression is regulated by members of the NFI transcription factors in human breast cancer cells. *BMC Clin Pathol* **2014,** *14* (1).

210. Falany, J. L.; Falany, C. N., Expression of cytosolic sulfotransferases in normal mammary epithelial cells and breast cancer cell lines. *Cancer Res* **1996,** *56* (7), 1551-1555.

211. Goldstein, D. S.; Swoboda, K. J.; Miles, J. M.; Coppack, S. W.; Aneman, A.; Holmes, C.; Lamensdorf, I.; Eisenhofer, G., Sources and physiological significance of plasma dopamine sulfate. *J Clin Endocrinol Metab* **1999,** *84* (7), 2523-2531.

212. Strott, C. A., Sulfonation and molecular action. *Endocr Rev* **2002,** *23* (5), 703-32.

213. Yamamoto, T.; Yamatodani, A.; Nishimura, M.; Wada, H., Determination of dopamine-3- and 4-O-sulphate in human plasma and urine by anion exchange high performance liquid chromatography with fluorimetric detection. *J Chromatogr* **1985,** *342* (2), 261-267.

214. Le Corre, P.; Malledant, Y.; Tanguy, M.; Le Verge, R., Steady-state pharmacokinetics of dopamine in adult patients. *Crit Care Med* **1993,** *21* (11), 1652-1657.

215. Chen, J. J.; Swope, D. M.; Dashtipour, K., Comprehensive review of rasagiline, a second-generation monoamine oxidase inhibitor, for the treatment of Parkinson's disease. *Clin Ther* **2007,** *29* (9), 1825-1849.

216. Lotufo-Neto, F.; Trivedi, M.; Thase, M. E., Meta-analysis of the reversible inhibitors of monoamine oxidase type A moclobemide and brofaromine for the treatment of depression. *Neuropsychopharmacology* **1999,** *20* (3), 226-247.

217. Bucci, L., The negative symptoms of schizophrenia and the monoamine oxidase inhibitors. *Psychopharmacology* **1987,** *91* (1), 104-108.

218. Jungerman, T.; Rabinowitz, D.; Klein, E., Deprenyl augmentation for treating negative symptoms of schizophrenia: a double-blind, controlled study. *J Clin Psychopharmacol* **1999,** *19* (6), 522-525.

219. Berton, O.; Nestler, E. J., New approaches to antidepressant drug discovery: beyond monoamines. *Nat Rev Neurosci* **2006,** *7* (2), 137-51.

220. Blackwell, B., Monoamine Oxidase Inhibitor Interactions with Other Drugs. *J Clin Psychopharmacol* **1991,** *11* (1), 55-58.

221. Yamada, M., Clinical Pharmacology of MAO Inhibitors: Safety and Future. *NeuroToxicology* **2004,** *25* (1-2), 215-221.

222. Souery, D.; Amsterdam, J.; de Montigny, C.; Lecrubier, Y.; Montgomery, S.; Lipp, O.; Racagni, G.; Zohar, J.; Mendlewicz, J., Treatment resistant depression: methodological overview and operational criteria. *Eur Neuropsychopharmacol* **1999,** *9* (1-2), 83-91.

223. Olgiati, P.; Serretti, A.; Souery, D.; Dold, M.; Kasper, S.; Montgomery, S.; Zohar, J.; Mendlewicz, J., Early improvement and response to antidepressant medications in adults with major depressive disorder. Meta-analysis and study of a sample with treatment-resistant depression. *J Affect Disord* **2018,** *227* (777-786).

224. Thomas, S. J.; Shin, M.; McInnis, M. G.; Bostwick, J. R., Combination therapy with monoamine oxidase inhibitors and other antidepressants or stimulus: strategies for the management of treatment-resistant depression. *Pharmacotherapy* **2015,** *35* (4), 433-449.

225. Suominen, T.; Uutela, P.; Ketola, R. A.; Bergquist, J.; Hillered, L.; Finel, M.; Zhang, H.; Laakso, A.; Kostiainen, R., Determination of Serotonin and Dopamine Metabolites in Human Brain Microdialysis and Cerebrospinal Fluid Samples by UPLC-MS/MS: Discovery of Intact Glucuronide and Sulfate Conjugates. *PloS one* **2013,** *8* (6), e68007.

226. Runge-Morris, M., Regulation of sulfotransferase gene expression by glucocorticoid hormones and xenobiotics in primary rat hepatocyte culture. *Chem Biol Interact* **1998,** *109* (1-3), 315-327.

227. Maglich, J. M.; Parks, D. J.; Moore, L. B.; Collins, J. L.; Goodwin, B.; Billin, A. N.; Stoltz, C. A.; Kliewer, S. A.; Lambert, M. H.; Willson, T. M., et al., Identification of a novel human constitutive androstane receptor (CAR) agonist and its use in the identification of CAR target genes. *J Biol Chem* **2003,** *278* (19), 17277-83.

228. Falany, J. L.; Falany, C. N., Regulation of estrogen sulfotransferase in human endometrial adenocarcinoma cells by progesterone. *Endocrinology* **1996,** *137* (4), 1395-1401.

229. Hellriegel, E. T.; Matwyshyn, G. A.; Fei, P.; Dragnev, K. H.; Nims, R. W.; Lubet, R. A.; Kong, A. N. T., Regulation of gene expression of various Phase I and Phase II drug-metabolizing enzymes by tamoxifen in rat liver. *Biochem Pharmacol* **1996,** *52* (10), 1561-1568.

230. Ou, Z.; Shi, X.; Gilroy, R. K.; Kirisci, L.; Romkes, M.; Lynch, C.; Wang, H.; Xu, M.; Jiang, M.; Ren, S., et al., Regulation of the human hydroxysteroid sulfotransferase (SULT2A1) by RORalpha and RORgamma and its potential relevance to human liver diseases. *Mol Endocrinol* **2013,** *27* (1), 106-15.

231. Bian, H. S.; Ngo, S. Y.; Tan, W.; Wong, C. H.; Boelsterli, U. A.; Tan, T. M., Induction of human sulfotransferase 1A3 (SULT1A3) by glucocorticoids. *Life Sci* **2007,** *81* (25-26), 1659-67.

232. Hempel, N.; Wang, H.; LeCluyse, E. L.; McManus, M. E.; Negishi, M., The human sulfotransferase SULT1A1 gene is regulated in a synergistic manner by Sp1 and GA binding protein. *Mol Pharmacol* **2004,** *66* (6), 1690-701.

233. Wang, T.; Cook, I.; Leyh, T. S., 3'-Phosphoadenosine 5'-phosphosulfate allosterically regulates sulfotransferase turnover. *Biochemistry* **2014,** *53* (44), 6893-900.

234. Armstrong, J. I.; Portley, A. R.; Chang, Y. T.; Nierengarten, D. M.; Cook, B. N.; Bowman, K. G.; Bishop, A.; Gray, N. S.; Shokat, K. M.; Schultz, P. G., et al., Discovery of Carbohydrate Sulfotransferase Inhibitors from a Kinase-Directed Library. *Angew Chem Int Ed Engl* **2000,** *39* (7), 1303-1306.

235. Chapman, E.; Ding, S.; Schultz, P. G.; Wong, C. H., A Potent and Highly Selective Sulfotransferase Inhibitor. *J Am Chem Soc* **2002,** *124* (49), 14524-14525.

236. Verdugo, D. E.; Cancilla, M. T.; Ge, X.; Gray, N. S.; Chang, Y. T.; Schultz, P. G.; Negishi, M.; Leary, J. A.; Bertozzi, C. R., Discovery of Estrogen Sulfotransferase Inhibitors from a Purine Library Screen. *J Med Chem* **2001,** *44* (17), 2683-2686.

237. Gower, C. M.; Chang, M. E.; Maly, D. J., Bivalent inhibitors of protein kinases. *Crit Rev Biochem Mol Biol* **2014,** *49* (2), 102-15.

238. Parang, K.; Till, J. H.; Ablooglu, A. J.; Kohanski, R. A.; Hubbard, S. R.; Cole, P. A., Mechanism-based design of a protein kinase inhibitor. *Nat Struct Biol* **2001,** *8* (1), 37-41.

239. Wong, C. H., Mimics of complex carbohydrates recognized by receptors. *Acc Chem Res* **1999,** *32* (4), 376-385.

240. Armstrong, J. I.; Ge, X.; Verdugo, D. E.; Winans, K. A.; Leary, J. A.; Bertozzi, C. R., A Library Approach to the Generation of Bisubstrate Analogue Sulfotransferase Inhibitors. *Org Lett* **2001,** *3* (17), 2657-2660.

241. Armstrong, J. I.; Verdugo, D. E.; Bertozzi, C. R., Synthesis of a Bisubstrate Analogue Targeting Estrogen Sulfotransferase. *J Org Chem* **2003,** *68* (1), 170-173.

242. Best, M. D.; Brik, A.; Chapman, E.; Lee, L. V.; Cheng, W. C.; Wong, C. H., Rapid discovery of potent sulfotransferase inhibitors by diversity-oriented reaction in microplates followed by in situ screening. *Chembiochem* **2004,** *5* (6), 811-9.

243. Kester, M. A.; Bulduk, S.; Tibboel, D.; Meinl, W.; Glatt, H.; Falany, C. N.; Coughtrie, M. W. H.; Bergman, A.; Safe, S. H.; Kuiper, G. G. J. M., et al., Potent Inhibition of Estrogen Sulfotransferase by Hydroxylated PCB Metabolites: A Novel Pathway Explaining the Estrogenic Activity of PCBs. *Endocrinology* **2000,** *141* (5), 1897-1900.

244. Vietri, M.; De Santi, C.; Pietrabissa, A.; Mosca, F.; Pacifici, G. M., Inhibition of human liver phenol sulfotransferase by nonsteroidal anti-inflammatory drugs. *Eur J Clin Pharmacol* **2000,** *56* (1), 81-87.

245. Coughtrie, M. W.; Johnston, L. E., Interactions between Dietary Chemicals and Human Sulfotransferases – Molecular Mechanisms and Clinical Significance. *Drug Metab Dispos* **2001,** *29* (4 Pt 2), 522-528.

246. Cook, I.; Wang, T.; Falany, C. N.; Leyh, T. S., The allosteric binding sites of sulfotransferase 1A1. *Drug Metab Dispos* **2015,** *43* (3), 418-23.

247. Cook, I.; Wang, T.; Girvin, M.; Leyh, T. S., The structure of the catechin-binding site of human sulfotransferase 1A1. *Proc Natl Acad Sci U S A* **2016,** *113* (50), 14312-14317.

248. Wang, T.; Cook, I.; Leyh, T. S., Isozyme Specific Allosteric Regulation of Human Sulfotransferase 1A1. *Biochemistry* **2016,** *55* (29), 4036-46.

249. Cook, I.; Wang, T.; Leyh, T. S., Tetrahydrobiopterin regulates monoamine neurotransmitter sulfonation. *Proc Natl Acad Sci U S A* **2017,** *114* (27), E5317-E5324.

250. Wu, P.; Clausen, M. H.; Nielsen, T. E., Allosteric small-molecule kinase inhibitors. *Pharmacol Ther* **2015,** *156*, 59-68.

251. Darrah, K.; Wang, T.; Cook, I.; Cacace, M.; Deiters, A.; Leyh, T. S., Allosteres to regulate neurotransmitter sulfonation. *J Biol Chem* **2019,** *294* (7), 2293-2301.

252. Yalcin, E. B.; More, V.; Neira, K. L.; Lu, Z. J.; Cherrington, N. J.; Slitt, A. L.; King, R. S., Downregulation of sulfotransferase expression and activity in diseased human livers. *Drug Metab Dispos* **2013,** *41* (9), 1642-50.

253. Runge-Morris, M.; Kocarek, T. A.; Falany, C. N., Regulation of the cytosolic sulfotransferases by nuclear receptors. *Drug Metab Rev* **2013,** *45* (1), 15-33.

254. Cook, I.; Wang, T.; Falany, C. N.; Leyh, T. S., High accuracy in silico sulfotransferase models. *J Biol Chem* **2013,** *288* (48), 34494-501.

255. Verdonk, M. L.; Cole, J. C.; Hartshorn, M. J.; Murray, C. W.; Taylor, R. D., Improved protein-ligand docking using GOLD. *Proteins* **2003,** *52* (4), 609-23.

256. Dormer, P. G.; Eng, K. K.; Farr, R. N.; Humphrey, G. R.; McWilliams, J. C.; Reider, P. J.; Sager, J. W.; Volante, R. P., Highly regioselective Friedlander annulations with unmodified ketones employing novel amine catalysts: syntheses of 2-substituted quinolines, 1,8-naphthyridines, and related heterocycles. *J Org Chem* **2003,** *68* (2), 467-477.

257. Yasu, Y.; Koike, T.; Akita, M., Visible-light-induced synthesis of a variety of trifluoromethylated alkenes from potassium vinyltrifluoroborates by photoredox catalysis. *Chem Commun (Camb)* **2013,** *49* (20), 2037-9.

258. Ma, B.; Shou, M.; Schrag, M. L., Solvent effect on cDNA-expressed human sulfotransferase (SULT) activities in vitro. *Drug Metab Dispos* **2003,** *31* (11), 1300-1305.

259. Brak, K.; Doyle, P. S.; McKerrow, J. H.; Ellman, J. A., Identification of a new class of nonpeptidic inhibitors of cruzain. *J Am Chem Soc* **2008,** *130* (20), 6404-6410.

260. Cook, I.; Wang, T.; Almo, S. C.; Kim, J.; Falany, C. N.; Leyh, T. S., The gate that governs sulfotransferase selectivity. *Biochemistry* **2013,** *52* (2), 415-24.

261. Dong, D.; Ako, R.; Wu, B., Crystal structures of human sulfotransferases: insights into the mechanisms of action and substrate selectivity. *Expert Opin Drug Metab Toxicol* **2012,** *8* (6), 635-46.

262. Pedersen, L. C.; Petrotchenko, E.; Shevtsov, S.; Negishi, M., Crystal structure of the human estrogen sulfotransferase-PAPS complex: evidence for catalytic role of Ser137 in the sulfuryl transfer reaction. *J Biol Chem* **2002,** *277* (20), 17928-32.

263. Wang, T.; Cook, I.; Leyh, T. S., Design and Interpretation of Human Sulfotransferase 1A1 Assays. *Drug Metab Dispos* **2016,** *44* (4), 481-4.

264. Hoegberg, T.; Stroem, P.; Ebner, M.; Raemsby, S., Cyanide as an efficient and mild catalyst in the aminolysis of esters. *J Org Chem* **1987,** *52* (10), 2033-2036.

265. Cook, I.; Cacace, M.; Wang, T.; Darrah, K.; Deiters, A.; Leyh, T. S., Small-molecule control of neurotransmitter sulfonation. *J Biol Chem* **2020,** *296*, 100094.

266. Wang, T.; Cook, I.; Leyh, T. S., The NSAID allosteric site of human cytosolic sulfotransferases. *J Biol Chem* **2017,** *292* (49), 20305-20312.

267. Weisz, J.; Fritz-Wolz, G.; Gestl, S.; Clawson, G. A.; Creveling, C. R.; Liehr, J. G.; Dabbs, D., Nuclear localization of catechol-O-methyltransferase in neoplastic and nonneoplastic mammary epithelial cells. *Am J Pathol* **2000,** *156* (6), 1841-8.

268. Falany, J. L.; Falany, C. N., Expression of Cytosolic Sulfotransferases in Normal Mammary Epithelial Cells and Breast Cancer Cell Lines. *Cancer Research* **1996,** *56* (7), 1551-1555.

269. Cook, I.; Wang, T.; Wang, W.; Kopp, F.; Wu, P.; Leyh, T. S., Controlling Sulfuryl-Transfer Biology. *Cell chemical biology* **2016,** *23* (5), 579-586.

270. Salman, E. D.; Kadlubar, S. A.; Falany, C. N., Expression and localization of cytosolic sulfotransferase (SULT) 1A1 and SULT1A3 in normal human brain. *Drug Metab Dispos* **2009,** *37* (4), 706-9.

271. Eisenhofer, G.; Coughtrie, M. W.; Goldstein, D. S., Dopamine sulphate: an enigma resolved. *Clin Exp Pharmacol Physiol Suppl* **1999,** *26*, S41-53.

272. Zhu, W.; Xu, H.; Wang, S. W.; Hu, M., Breast cancer resistance protein (BCRP) and sulfotransferases contribute significantly to the disposition of genistein in mouse intestine. *AAPS J* **2010,** *12* (4), 525-36.

273. Cook, I. T.; Duniec-Dmuchowski, Z.; Kocarek, T. A.; Runge-Morris, M.; Falany, C. N., 24-hydroxycholesterol sulfation by human cytosolic sulfotransferases: formation of monosulfates and disulfates, molecular modeling, sulfatase sensitivity, and inhibition of liver x receptor activation. *Drug Metab Dispos* **2009,** *37* (10), 2069-78.

274. Herrmann, K.; Engst, W.; Meinl, W.; Florian, S.; Cartus, A. T.; Schrenk, D.; Appel, K. E.; Nolden, T.; Himmelbauer, H.; Glatt, H., Formation of hepatic DNA adducts by methyleugenol in mouse models: drastic decrease by Sult1a1 knockout and strong increase by transgenic human SULT1A1/2. *Carcinogenesis* **2014,** *35* (4), 935-41.

275. Otte, C.; Gold, S. M.; Penninx, B. W.; Pariante, C. M.; Etkin, A.; Fava, M.; Mohr, D. C.; Schatzberg, A. F., Major depressive disorder. *Nat Rev Dis Primers* **2016,** *2*, 16065.

276. Penn, E.; Tracy, D. K., The drugs don't work? antidepressants and the current and future pharmacological management of depression. *Ther Adv Psychopharmacol* **2012,** *2* (5), 179-88.

277. Fava, M.; Rush, A. J.; Trivedi, M. H.; Nierenberg, A. A.; Thase, M. E.; Sackeim, H. A.; Quitkin, F. M.; Wisniewski, S.; Lavori, P. W.; Rosenbaum, J. F., et al., Background and rationale for the sequenced treatment alternatives to relieve depression (STAR*D) study. *Psychiatr Clin North Am* **2003,** *26* (2), 457-94, x.

278. Sinyor, M.; Schaffer, A.; Levitt, A., The sequenced treatment alternatives to relieve depression (STAR*D) trial: a review. *Can J Psychiatry* **2010,** *55* (3), 126-35.

279. Gulykina, N. S.; Dolgina, T. M.; Bondarenko, G. N.; Beletskaya, I. P., Hydrophosphorylation of Terminal Alkynes Catalyzed by Palladium. *Russian Journal of Organic Chemistry* **2003,** *39* (6), 797-807.

280. Paridala, K.; Lu, S.-M.; Wang, M.-M.; Li, C., Tandem one-pot CO2 reduction by PMHS and silyloxycarbonylation of aryl/vinyl halides to access carboxylic acids. *Chemical Communications* **2018,** *54* (82), 11574-11577.

281. Myers, A. G.; Zhong, B.; Movassaghi, M.; Kung, D. W.; Lanman, B. A.; Kwon, S., Synthesis of Highly Epimerizable N-protected Alpha-Amino Aldehydes of High Enatiomeric Excess. *Tetrahedron Letters* **2000,** *41* (9), 1359-1362.

282. Hershko, A.; Ciechanover, A., The ubiquitin system. *Annu Rev Biochem* **1998,** *67*, 425-79.

283. Pines, J.; Lindon, C., Proteolysis: anytime, any place, anywhere? *Nat Cell Biol* **2005,** *7* (8), 731-5.

284. Ronai, Z. A., Monoubiquitination in proteasomal degradation. *Proc Natl Acad Sci U S A* **2016,** *113* (32), 8894-6.

285. Nandi, D.; Tahiliani, P.; Kumar, A.; Chandu, D., The ubiquitin-proteasome system. *J Biosci* **2006,** *31* (1), 137-55.

286. Buetow, L.; Huang, D. T., Structural insights into the catalysis and regulation of E3 ubiquitin ligases. *Nat Rev Mol Cell Biol* **2016,** *17* (10), 626-42.

287. Zheng, N.; Shabek, N., Ubiquitin Ligases: Structure, Function, and Regulation. *Annu Rev Biochem* **2017,** *86*, 129-157.

288. Reiter, K. H.; Klevit, R. E., Characterization of RING-Between-RING E3 Ubiquitin Transfer Mechanisms. *Methods Mol Biol* **2018,** *1844*, 3-17.

289. Huang, X.; Dixit, V. M., Drugging the undruggables: exploring the ubiquitin system for drug development. *Cell Research* **2016,** *26* (4), 484-498.

290. Li, W.; Ye, Y., Polyubiquitin chains: functions, structures, and mechanisms. *Cell Mol Life Sci* **2008,** *65* (15), 2397-406.

291. French, M. E.; Koehler, C. F.; Hunter, T., Emerging functions of branched ubiquitin chains. *Cell Discov* **2021,** *7* (1), 6.

292. Tracz, M.; Bialek, W., Beyond K48 and K63: non-canonical protein ubiquitination. *Cell Mol Biol Lett* **2021,** *26* (1), 1.

293. Oh, E.; Akopian, D.; Rape, M., Principles of Ubiquitin-Dependent Signaling. *Annu Rev Cell Dev Biol* **2018,** *34*, 137-162.

294. Petroski, M. D.; Deshaies, R. J., Mechanism of lysine 48-linked ubiquitin-chain synthesis by the cullin-RING ubiquitin-ligase complex SCF-Cdc34. *Cell* **2005,** *123* (6), 1107-20.

295. Christensen, D. E.; Brzovic, P. S.; Klevit, R. E., E2-BRCA1 RING interactions dictate synthesis of mono- or specific polyubiquitin chain linkages. *Nat Struct Mol Biol* **2007,** *14* (10), 941-8.

296. Rodrigo-Brenni, M. C.; Morgan, D. O., Sequential E2s drive polyubiquitin chain assembly on APC targets. *Cell* **2007,** *130* (1), 127-39.

297. Sadowski, M.; Suryadinata, R.; Tan, A. R.; Roesley, S. N.; Sarcevic, B., Protein monoubiquitination and polyubiquitination generate structural diversity to control distinct biological processes. *IUBMB Life* **2012,** *64* (2), 136-42.

298. Komander, D.; Rape, M., The ubiquitin code. *Annu Rev Biochem* **2012,** *81*, 203-29.

299. Bondeson, D. P.; Crews, C. M., Targeted Protein Degradation by Small Molecules. *Annu Rev Pharmacol Toxicol* **2017,** *57*, 107-123.

300. Neklesa, T. K.; Winkler, J. D.; Crews, C. M., Targeted protein degradation by PROTACs. *Pharmacol Ther* **2017,** *174*, 138-144.

301. Pettersson, M.; Crews, C. M., PROteolysis TArgeting Chimeras (PROTACs) - Past, present and future. *Drug Discov Today Technol* **2019,** *31*, 15-27.

302. Xi, M.; Chen, Y.; Yang, H.; Xu, H.; Du, K.; Wu, C.; Xu, Y.; Deng, L.; Luo, X.; Yu, L., et al., Small molecule PROTACs in targeted therapy: An emerging strategy to induce protein degradation. *Eur J Med Chem* **2019,** *174*, 159-180.

303. Burslem, G. M.; Crews, C. M., Proteolysis-Targeting Chimeras as Therapeutics and Tools for Biological Discovery. *Cell* **2020,** *181* (1), 102-114.

304. Chamberlain, P. P.; Hamann, L. G., Development of targeted protein degradation therapeutics. *Nat Chem Biol* **2019,** *15* (10), 937-944.

305. Cromm, P. M.; Crews, C. M., Targeted Protein Degradation: from Chemical Biology to Drug Discovery. *Cell chemical biology* **2017,** *24* (9), 1181-1190.

306. Khan, S.; He, Y.; Zhang, X.; Yuan, Y.; Pu, S.; Kong, Q.; Zheng, G.; Zhou, D., PROteolysis TArgeting Chimeras (PROTACs) as emerging anticancer therapeutics. *Oncogene* **2020,** *39* (26), 4909-4924.

307. Liu, J.; Ma, J.; Liu, Y.; Xia, J.; Li, Y.; Wang, Z. P.; Wei, W., PROTACs: A novel strategy for cancer therapy. *Semin Cancer Biol* **2020,** *67* (Pt 2), 171-179.

308. Wan, Y.; Yan, C.; Gao, H.; Liu, T., Small-molecule PROTACs: novel agents for cancer therapy. *Future Med Chem* **2020,** *12* (10), 915-938.

309. Tomoshige, S.; Ishikawa, M., PROTACs and Other Chemical Protein Degradation Technologies for the Treatment of Neurodegenerative Disorders. *Angew Chem Int Ed Engl* **2021,** *60* (7), 3346-3354.

310. Zhou, X.; Dong, R.; Zhang, J. Y.; Zheng, X.; Sun, L. P., PROTAC: A promising technology for cancer treatment. *Eur J Med Chem* **2020,** *203*, 112539.

311. Kargbo, R. B., PROTAC Molecules for the Treatment of Autoimmune Disorders. *ACS Medicinal Chemistry Letters* **2019,** *10* (3), 276-277.

312. de Wispelaere, M.; Du, G.; Donovan, K. A.; Zhang, T.; Eleuteri, N. A.; Yuan, J. C.; Kalabathula, J.; Nowak, R. P.; Fischer, E. S.; Gray, N. S., et al., Small molecule degraders of the hepatitis C virus protease reduce susceptibility to resistance mutations. *Nat Commun* **2019,** *10* (1), 3468.

313. Ottis, P.; Crews, C. M., Proteolysis-Targeting Chimeras: Induced Protein Degradation as a Therapeutic Strategy. *ACS Chem Biol* **2017,** *12* (4), 892-898.

314. Lai, A. C.; Crews, C. M., Induced protein degradation: an emerging drug discovery paradigm. *Nat Rev Drug Discov* **2017,** *16* (2), 101-114.

315. Zeng, S.; Huang, W.; Zheng, X.; Liyan, C.; Zhang, Z.; Wang, J.; Shen, Z., Proteolysis targeting chimera (PROTAC) in drug discovery paradigm: Recent progress and future challenges. *Eur J Med Chem* **2021,** *210*, 112981.

316. Bondeson, D. P.; Mares, A.; Smith, I. E.; Ko, E.; Campos, S.; Miah, A. H.; Mulholland, K. E.; Routly, N.; Buckley, D. L.; Gustafson, J. L., et al., Catalytic in vivo protein knockdown by small-molecule PROTACs. *Nat Chem Biol* **2015,** *11* (8), 611-7.

317. Bondeson, D. P.; Smith, B. E.; Burslem, G. M.; Buhimschi, A. D.; Hines, J.; Jaime-Figueroa, S.; Wang, J.; Hamman, B. D.; Ishchenko, A.; Crews, C. M., Lessons in PROTAC Design from Selective Degradation with a Promiscuous Warhead. *Cell chemical biology* **2018,** *25* (1), 78-87 e5.

318. Smith, B. E.; Wang, S. L.; Jaime-Figueroa, S.; Harbin, A.; Wang, J.; Hamman, B. D.; Crews, C. M., Differential PROTAC substrate specificity dictated by orientation of recruited E3 ligase. *Nat Commun* **2019,** *10* (1), 131.

319. Hines, J.; Gough, J. D.; Corson, T. W.; Crews, C. M., Posttranslational protein knockdown coupled to receptor tyrosine kinase activation with phosphoPROTACs. *Proc Natl Acad Sci U S A* **2013,** *110* (22), 8942-7.

320. Farnaby, W.; Koegl, M.; Roy, M. J.; Whitworth, C.; Diers, E.; Trainor, N.; Zollman, D.; Steurer, S.; Karolyi-Oezguer, J.; Riedmueller, C., et al., BAF complex vulnerabilities

in cancer demonstrated via structure-based PROTAC design. *Nat Chem Biol* **2019,** *15* (7), 672-680.

321. Bai, L.; Zhou, H.; Xu, R.; Zhao, Y.; Chinnaswamy, K.; McEachern, D.; Chen, J.; Yang, C. Y.; Liu, Z.; Wang, M., et al., A Potent and Selective Small-Molecule Degrader of STAT3 Achieves Complete Tumor Regression In Vivo. *Cancer Cell* **2019,** *36* (5), 498-511 e17.

322. Liu, J.; Chen, H.; Kaniskan, H. Ü.; Xie, L.; Chen, X.; Jin, J.; Wei, W., TF-PROTACs Enable Targeted Degradation of Transcription Factors. *Journal of the American Chemical Society* **2021,** *143* (23), 8902-8910.

323. Sakamoto, K. M.; Kim, K. B.; Kumagai, A.; Mercurio, F.; Crews, C. M.; Deshaies, R. J., Protacs: chimeric molecules that target proteins to the Skp1-Cullin-F box complex for ubiquitination and degradation. *Proc Natl Acad Sci U S A* **2001,** *98* (15), 8554-9.

324. Schneekloth, J. S., Jr.; Fonseca, F. N.; Koldobskiy, M.; Mandal, A.; Deshaies, R.; Sakamoto, K.; Crews, C. M., Chemical genetic control of protein levels: selective in vivo targeted degradation. *J Am Chem Soc* **2004,** *126* (12), 3748-54.

325. Lai, A. C.; Toure, M.; Hellerschmied, D.; Salami, J.; Jaime-Figueroa, S.; Ko, E.; Hines, J.; Crews, C. M., Modular PROTAC Design for the Degradation of Oncogenic BCR-ABL. *Angew Chem Int Ed Engl* **2016,** *55* (2), 807-10.

326. Winter, G. E.; Buckley, D. L.; Paulk, J.; Roberts, J. M.; Souza, A.; Dhe-Paganon, S.; Bradner, J. E., DRUG DEVELOPMENT. Phthalimide conjugation as a strategy for in vivo target protein degradation. *Science* **2015,** *348* (6241), 1376-81.

327. Lu, J.; Qian, Y.; Altieri, M.; Dong, H.; Wang, J.; Raina, K.; Hines, J.; Winkler, J. D.; Crew, A. P.; Coleman, K., et al., Hijacking the E3 Ubiquitin Ligase Cereblon to Efficiently Target BRD4. *Chem Biol* **2015,** *22* (6), 755-63.

328. Zhang, D.; Baek, S. H.; Ho, A.; Kim, K., Degradation of target protein in living cells by small-molecule proteolysis inducer. *Bioorg Med Chem Lett* **2004,** *14* (3), 645-8.

329. Lee, H.; Puppala, D.; Choi, E. Y.; Swanson, H.; Kim, K. B., Targeted degradation of the aryl hydrocarbon receptor by the PROTAC approach: a useful chemical genetic tool. *Chembiochem* **2007,** *8* (17), 2058-62.

330. Galdeano, C.; Gadd, M. S.; Soares, P.; Scaffidi, S.; Van Molle, I.; Birced, I.; Hewitt, S.; Dias, D. M.; Ciulli, A., Structure-guided design and optimization of small molecules targeting the protein-protein interaction between the von Hippel-Lindau (VHL) E3 ubiquitin ligase and the hypoxia inducible factor (HIF) alpha subunit with in vitro nanomolar affinities. *J Med Chem* **2014,** *57* (20), 8657-63.

331. Ito, T.; Ando, H.; Suzuki, T.; Ogura, T.; Hotta, K.; Imamura, Y.; Yamaguchi, Y.; Handa, H., Identification of a primary target of thalidomide teratogenicity. *Science* **2010,** *327* (5971), 1345-50.

332. Ito, T.; Handa, H., Molecular mechanisms of thalidomide and its derivatives. *Proc Jpn Acad Ser B Phys Biol Sci* **2020,** *96* (6), 189-203.

333. Fischer, E. S.; Bohm, K.; Lydeard, J. R.; Yang, H.; Stadler, M. B.; Cavadini, S.; Nagel, J.; Serluca, F.; Acker, V.; Lingaraju, G. M., et al., Structure of the DDB1-CRBN E3 ubiquitin ligase in complex with thalidomide. *Nature* **2014,** *512* (7512), 49-53.

334. Weng, G.; Shen, C.; Cao, D.; Gao, J.; Dong, X.; He, Q.; Yang, B.; Li, D.; Wu, J.; Hou, T., PROTAC-DB: an online database of PROTACs. *Nucleic Acids Res* **2021,** *49* (D1), D1381-D1387.

335. Mullard, A., Targeted protein degraders crowd into the clinic. *Nat Rev Drug Discov* **2021,** *20* (4), 247-250.

336. Neklesa, T.; Snyder, L. B.; Willard, R. R.; Vitale, N.; Pizzano, J.; Gordon, D. A.; Bookbinder, M.; Macaluso, J.; Dong, H.; Ferraro, C., et al., ARV-110: An oral androgen receptor PROTAC degrader for prostate cancer. *Journal of Clinical Oncology* **2019,** *37* (7_suppl), 259-259.

337. Flanagan, J. J.; Qian, Y.; Gough, S. M.; Andreoli, M.; Bookbinder, M.; Cadelina, G.; Bradley, J.; Rousseau, E.; Chandler, J.; Willard, R., et al. In *ARV-471, an oral estrogen receptor PROTAC protein degrader for breast cancer*, SABCS, San Antonio, Texas, USA, San Antonio, Texas, USA, 2018.

338. Zorba, A.; Nguyen, C.; Xu, Y.; Starr, J.; Borzilleri, K.; Smith, J.; Zhu, H.; Farley, K. A.; Ding, W.; Schiemer, J., et al., Delineating the role of cooperativity in the design of potent PROTACs for BTK. *Proc Natl Acad Sci U S A* **2018,** *115* (31), E7285-E7292.

339. McCoull, W.; Cheung, T.; Anderson, E.; Barton, P.; Burgess, J.; Byth, K.; Cao, Q.; Castaldi, M. P.; Chen, H.; Chiarparin, E., et al., Development of a Novel B-Cell Lymphoma 6 (BCL6) PROTAC To Provide Insight into Small Molecule Targeting of BCL6. *ACS Chem Biol* **2018,** *13* (11), 3131-3141.

340. Popow, J.; Arnhof, H.; Bader, G.; Berger, H.; Ciulli, A.; Covini, D.; Dank, C.; Gmaschitz, T.; Greb, P.; Karolyi-Ozguer, J., et al., Highly Selective PTK2 Proteolysis Targeting Chimeras to Probe Focal Adhesion Kinase Scaffolding Functions. *J Med Chem* **2019,** *62* (5), 2508-2520.

341. Bassi, Z. I.; Fillmore, M. C.; Miah, A. H.; Chapman, T. D.; Maller, C.; Roberts, E. J.; Davis, L. C.; Lewis, D. E.; Galwey, N. W.; Waddington, K. E., et al., Modulating PCAF/GCN5 Immune Cell Function through a PROTAC Approach. *ACS Chem Biol* **2018,** *13* (10), 2862-2867.

342. Nunes, J.; McGonagle, G. A.; Eden, J.; Kiritharan, G.; Touzet, M.; Lewell, X.; Emery, J.; Eidam, H.; Harling, J. D.; Anderson, N. A., Targeting IRAK4 for Degradation with PROTACs. *ACS Med Chem Lett* **2019,** *10* (7), 1081-1085.

343. Gadd, M. S.; Testa, A.; Lucas, X.; Chan, K. H.; Chen, W.; Lamont, D. J.; Zengerle, M.; Ciulli, A., Structural basis of PROTAC cooperative recognition for selective protein degradation. *Nat Chem Biol* **2017,** *13* (5), 514-521.

344. Konstantinidou, M.; Li, J.; Zhang, B.; Wang, Z.; Shaabani, S.; Ter Brake, F.; Essa, K.; Domling, A., PROTACs- a game-changing technology. *Expert Opin Drug Discov* **2019,** *14* (12), 1255-1268.

345. Bartlett, D. W.; Gilbert, A. M., A kinetic proofreading model for bispecific protein degraders. *J Pharmacokinet Pharmacodyn* **2021,** *48* (1), 149-163.

346. Drummond, M. L.; Williams, C. I., In Silico Modeling of PROTAC-Mediated Ternary Complexes: Validation and Application. *J Chem Inf Model* **2019,** *59* (4), 1634-1644.

347. Nomura, D. K.; Maimone, T. J., Target Identification of Bioactive Covalently Acting Natural Products. *Curr Top Microbiol Immunol* **2019,** *420*, 351-374.

348. Ishida, T.; Ciulli, A., E3 Ligase Ligands for PROTACs: How They Were Found and How to Discover New Ones. *SLAS Discov* **2021,** *26* (4), 484-502.

349. Banik, S. M.; Pedram, K.; Wisnovsky, S.; Ahn, G.; Riley, N. M.; Bertozzi, C. R., Lysosome-targeting chimaeras for degradation of extracellular proteins. *Nature* **2020,** *584* (7820), 291-297.

350. Zhou, Y.; Teng, P.; Montgomery, N. T.; Li, X.; Tang, W., Development of Triantennary N-Acetylgalactosamine Conjugates as Degraders for Extracellular Proteins. *ACS Cent Sci* **2021,** *7* (3), 499-506.

351. Ahn, G.; Banik, S. M.; Miller, C. L.; Riley, N. M.; Cochran, J. R.; Bertozzi, C. R., LYTACs that engage the asialoglycoprotein receptor for targeted protein degradation. *Nat Chem Biol* **2021**.

352. Takahashi, D.; Moriyama, J.; Nakamura, T.; Miki, E.; Takahashi, E.; Sato, A.; Akaike, T.; Itto-Nakama, K.; Arimoto, H., AUTACs: Cargo-Specific Degraders Using Selective Autophagy. *Mol Cell* **2019,** *76* (5), 797-810 e10.

353. Li, Z.; Zhu, C.; Ding, Y.; Fei, Y.; Lu, B., ATTEC: a potential new approach to target proteinopathies. *Autophagy* **2020,** *16* (1), 185-187.

354. Li, Z.; Wang, C.; Wang, Z.; Zhu, C.; Li, J.; Sha, T.; Ma, L.; Gao, C.; Yang, Y.; Sun, Y., et al., Allele-selective lowering of mutant HTT protein by HTT-LC3 linker compounds. *Nature* **2019,** *575* (7781), 203-209.

355. Alabi, S.; Crews, C., Major Advances in Targeted Protein Degradation: PROTACs, LYTACs, and MADTACs. *J Biol Chem* **2021**, 100647.

356. Bond, M. J.; Crews, C. M., Proteolysis targeting chimeras (PROTACs) come of age: entering the third decade of targeted protein degradation. *RSC Chem Biol* **2021,** *2* (3), 725-742.

357. Conway, S. J., Bifunctional Molecules beyond PROTACs. *J Med Chem* **2020,** *63* (6), 2802-2806.

358. Siriwardena, S. U.; Munkanatta Godage, D. N. P.; Shoba, V. M.; Lai, S.; Shi, M.; Wu, P.; Chaudhary, S. K.; Schreiber, S. L.; Choudhary, A., Phosphorylation-Inducing Chimeric Small Molecules. *J Am Chem Soc* **2020,** *142* (33), 14052-14057.

359. Yamazoe, S.; Tom, J.; Fu, Y.; Wu, W.; Zeng, L.; Sun, C.; Liu, Q.; Lin, J.; Lin, K.; Fairbrother, W. J., et al., Heterobifunctional Molecules Induce Dephosphorylation of Kinases-A Proof of Concept Study. *J Med Chem* **2020,** *63* (6), 2807-2813.

360. Henning, N. J.; Boike, L.; Spradlin, J. N.; Ward, C. C.; Belcher, B.; Brittain, S. M.; Hesse, M.; Dovala, D.; McGregor, L. M.; McKenna, J. M., et al., Deubiquitinase-Targeting Chimeras for Targeted Protein Stabilization. *bioRxiv* **2021**, 2021.04.30.441959.

361. Costales, M. G.; Aikawa, H.; Li, Y.; Childs-Disney, J. L.; Abegg, D.; Hoch, D. G.; Pradeep Velagapudi, S.; Nakai, Y.; Khan, T.; Wang, K. W., et al., Small-molecule targeted recruitment of a nuclease to cleave an oncogenic RNA in a mouse model of metastatic cancer. *Proc Natl Acad Sci U S A* **2020,** *117* (5), 2406-2411.

362. Naro, Y.; Darrah, K.; Deiters, A., Optical Control of Small Molecule-Induced Protein Degradation. *J Am Chem Soc* **2020,** *142* (5), 2193-2197.

363. Gu, S.; Cui, D.; Chen, X.; Xiong, X.; Zhao, Y., PROTACs: An Emerging Targeting Technique for Protein Degradation in Drug Discovery. *Bioessays* **2018,** *40* (4), e1700247.

364. Raina, K.; Lu, J.; Qian, Y.; Altieri, M.; Gordon, D.; Rossi, A. M.; Wang, J.; Chen, X.; Dong, H.; Siu, K., et al., PROTAC-induced BET protein degradation as a therapy for castration-resistant prostate cancer. *Proc Natl Acad Sci U S A* **2016,** *113* (26), 7124-9.

365. Churcher, I., Protac-Induced Protein Degradation in Drug Discovery: Breaking the Rules or Just Making New Ones? *J Med Chem* **2018,** *61* (2), 444-452.

366. Mayer, G.; Heckel, A., Biologically active molecules with a "light switch". *Angew Chem Int Ed Engl* **2006,** *45* (30), 4900-21.

367. Yu, F.; White, S. B.; Zhao, Q.; Lee, F. S., HIF-1alpha binding to VHL is regulated by stimulus-sensitive proline hydroxylation. *Proc Natl Acad Sci U S A* **2001,** *98* (17), 9630-5.

368. Min, J. H.; Yang, H.; Ivan, M.; Gertler, F.; Kaelin, W. G., Jr.; Pavletich, N. P., Structure of an HIF-1alpha -pVHL complex: hydroxyproline recognition in signaling. *Science* **2002,** *296* (5574), 1886-9.

369. Hon, W. C.; Wilson, M. I.; Harlos, K.; Claridge, T. D.; Schofield, C. J.; Pugh, C. W.; Maxwell, P. H.; Ratcliffe, P. J.; Stuart, D. I.; Jones, E. Y., Structural basis for the recognition of hydroxyproline in HIF-1 alpha by pVHL. *Nature* **2002,** *417* (6892), 975-8.

370. Zengerle, M.; Chan, K. H.; Ciulli, A., Selective Small Molecule Induced Degradation of the BET Bromodomain Protein BRD4. *ACS Chem Biol* **2015,** *10* (8), 1770-7.

371. Ranhotra, H. S., The estrogen-related receptor alpha: the oldest, yet an energetic orphan with robust biological functions. *J Recept Signal Transduct Res* **2010,** *30* (4), 193-205.

372. Schmidt, R.; Geissler, D.; Hagen, V.; Bendig, J., Mechanism of photocleavage of (coumarin-4-yl)methyl esters. *J Phys Chem A* **2007,** *111* (26), 5768-74.

373. Nawrocki, S. T.; Griffin, P.; Kelly, K. R.; Carew, J. S., MLN4924: a novel first-in-class inhibitor of NEDD8-activating enzyme for cancer therapy. *Expert Opin Investig Drugs* **2012,** *21* (10), 1563-73.

374. Kraus, R. J.; Ariazi, E. A.; Farrell, M. L.; Mertz, J. E., Estrogen-related receptor alpha 1 actively antagonizes estrogen receptor-regulated transcription in MCF-7 mammary cells. *J Biol Chem* **2002,** *277* (27), 24826-34.

375. Kallen, J.; Schlaeppi, J. M.; Bitsch, F.; Filipuzzi, I.; Schilb, A.; Riou, V.; Graham, A.; Strauss, A.; Geiser, M.; Fournier, B., Evidence for ligand-independent transcriptional activation of the human estrogen-related receptor alpha (ERRalpha): crystal structure of ERRalpha ligand binding domain in complex with peroxisome proliferator-activated receptor coactivator-1alpha. *J Biol Chem* **2004,** *279* (47), 49330-7.

376. Schreiber, S. N.; Knutti, D.; Brogli, K.; Uhlmann, T.; Kralli, A., The transcriptional coactivator PGC-1 regulates the expression and activity of the orphan nuclear receptor estrogen-related receptor alpha (ERRalpha). *J Biol Chem* **2003,** *278* (11), 9013-8.

377. Watanabe, A.; Kinoshita, Y.; Hosokawa, K.; Mori, T.; Yamaguchi, T.; Honjo, H., Function of estrogen-related receptor alpha in human endometrial cancer. *J Clin Endocrinol Metab* **2006,** *91* (4), 1573-7.

378. Hatcher, J. M.; Wang, E. S.; Johannessen, L.; Kwiatkowski, N.; Sim, T.; Gray, N. S., Development of Highly Potent and Selective Steroidal Inhibitors and Degraders of CDK8. *ACS Med Chem Lett* **2018,** *9* (6), 540-545.

379. Winter, G. E.; Mayer, A.; Buckley, D. L.; Erb, M. A.; Roderick, J. E.; Vittori, S.; Reyes, J. M.; di Iulio, J.; Souza, A.; Ott, C. J., et al., BET Bromodomain Proteins Function as Master Transcription Elongation Factors Independent of CDK9 Recruitment. *Mol Cell* **2017,** *67* (1), 5-18 e19.

380. Lusic, H.; Deiters, A., A New Photocaging Group for Aromatic N-Heterocycles. *Synthesis* **2006,** *2006*, 2147-2150.

381. Bordwell, F. G., Equilibrium acidities in dimethyl sulfoxide solution. *Accounts of Chemical Research* **1988,** *21* (12), 456-463.

382. Ankenbruck, N.; Courtney, T.; Naro, Y.; Deiters, A., Optochemical Control of Biological Processes in Cells and Animals. *Angewandte Chemie International Edition* **2018,** *57*, 2-33.

383. Bradner, J. E.; Buckley, D. L.; Winter, G. E. Methods to Induce Targeted Protein Degradation Through Bifunctional Molecules. 2017.

384. Agbavwe, C.; Kim, C.; Hong, D.; Heinrich, K.; Wang, T.; Somoza, M. M., Efficiency, error and yield in light-directed maskless synthesis of DNA microarrays. *J Nanobiotechnology* **2011,** *9*, 57.

385. Reynders, M.; Trauner, D., Optical control of targeted protein degradation. *Cell chemical biology* **2021**.

386. Verma, S.; Manna, D., Controlling PROTACs with Light. *ChemMedChem* **2020,** *15* (14), 1258-1261.

387. Kounde, C. S.; Tate, E. W., Photoactive Bifunctional Degraders: Precision Tools To Regulate Protein Stability. *J Med Chem* **2020,** *63* (24), 15483-15493.

388. Xue, G.; Wang, K.; Zhou, D.; Zhong, H.; Pan, Z., Light-Induced Protein Degradation with Photocaged PROTACs. *J Am Chem Soc* **2019,** *141* (46), 18370-18374.

389. Kounde, C. S.; Shchepinova, M. M.; Saunders, C. N.; Muelbaier, M.; Rackham, M. D.; Harling, J. D.; Tate, E. W., A caged E3 ligase ligand for PROTAC-mediated protein degradation with light. *Chem Commun (Camb)* **2020,** *56* (41), 5532-5535.

390. Liu, J.; Chen, H.; Ma, L.; He, Z.; Wang, D.; Liu, Y.; Lin, Q.; Zhang, T.; Gray, N.; Kaniskan, H. U., et al., Light-induced control of protein destruction by opto-PROTAC. *Sci Adv* **2020,** *6* (8), eaay5154.

391. Pfaff, P.; Samarasinghe, K. T. G.; Crews, C. M.; Carreira, E. M., Reversible Spatiotemporal Control of Induced Protein Degradation by Bistable PhotoPROTACs. *ACS Cent Sci* **2019,** *5* (10), 1682-1690.

392. Jin, Y. H.; Lu, M. C.; Wang, Y.; Shan, W. X.; Wang, X. Y.; You, Q. D.; Jiang, Z. Y., Azo-PROTAC: Novel Light-Controlled Small-Molecule Tool for Protein Knockdown. *J Med Chem* **2020,** *63* (9), 4644-4654.

393. Reynders, M.; Matsuura, B. S.; Berouti, M.; Simoneschi, D.; Marzio, A.; Pagano, M.; Trauner, D., PHOTACs enable optical control of protein degradation. *Sci Adv* **2020,** *6* (8), eaay5064.

394. Fournier, L.; Gauron, C.; Xu, L.; Aujard, I.; Le Saux, T.; Gagey-Eilstein, N.; Maurin, S.; Dubruille, S.; Baudin, J. B.; Bensimon, D., et al., A blue-absorbing photolabile

protecting group for in vivo chromatically orthogonal photoactivation. *ACS Chem Biol* **2013,** *8* (7), 1528-36.

395. Remillard, D.; Buckley, D. L.; Paulk, J.; Brien, G. L.; Sonnett, M.; Seo, H. S.; Dastjerdi, S.; Wuhr, M.; Dhe-Paganon, S.; Armstrong, S. A., et al., Degradation of the BAF Complex Factor BRD9 by Heterobifunctional Ligands. *Angew Chem Int Ed Engl* **2017,** *56* (21), 5738-5743.

396. Heckler, M. M.; Thakor, H.; Schafer, C. C.; Riggins, R. B., ERK/MAPK regulates ERRgamma expression, transcriptional activity and receptor-mediated tamoxifen resistance in ER+ breast cancer. *FEBS J* **2014,** *281* (10), 2431-42.

397. Gong, F.; Chiu, L. Y.; Cox, B.; Aymard, F.; Clouaire, T.; Leung, J. W.; Cammarata, M.; Perez, M.; Agarwal, P.; Brodbelt, J. S., et al., Screen identifies bromodomain protein ZMYND8 in chromatin recognition of transcription-associated DNA damage that promotes homologous recombination. *Genes Dev* **2015,** *29* (2), 197-211.

398. Berkeley), K. L. U. C. Making Calcium Competent Cells. http://mcb.berkeley.edu/labs/krantz/protocols/calcium_comp_cells.pdf.

399. ThermoScientific Lipofectamine 2000 Transfection Protocol. https://www.thermofisher.com/us/en/home/references/protocols/cell-culture/transfection-protocol/lipofectamine-2000.html.

400. Khor, E.-S.; Noor, S. M.; Wong, P.-F., Expression of zTOR-associated microRNAs in zebrafish embryo treated with rapamycin. *Life Sciences* **2016,** *150*, 67-75.